Living Reviews in Relativity (2024)27:3
https://doi.org/10.1007/s41114-024-00049-6

REVIEW ARTICLE

Theoretical and experimental constraints for the equation of state of dense and hot matter

Rajesh Kumar · Veronica Dexheimer · Johannes Jahan · Jorge Noronha · Jacquelyn Noronha-Hostler · Claudia Ratti et al. (MUSES Collaboration) ***[full author details at the end of the article]***

Received: 20 April 2023 / Accepted: 22 April 2024

Abstract
This review aims at providing an extensive discussion of modern constraints relevant for dense and hot strongly interacting matter. It includes theoretical first-principle results from lattice and perturbative QCD, as well as chiral effective field theory results. From the experimental side, it includes heavy-ion collision and low-energy nuclear physics results, as well as observations from neutron stars and their mergers. The validity of different constraints, concerning specific conditions and ranges of applicability, is also provided.

Keywords Multi-messenger physics · Neutron star · Dense matter · Heavy-ion collisions

Contents

Extended author information available on the last page of the article

Published online: 05 June 2024

1 Introduction

Depending on conditions (thermodynamic variables), such as temperature and density, matter can appear in many forms (phases). Typical phases include solid, liquid, and gas; but many others can exist, such as plasmas, condensates, and superconducting phases (just to name a few). How matter transitions from one phase to another can also take many forms. A first-order phase transition is how water typically changes from solid to liquid or liquid to gas wherein the phase transition happens at a fixed temperature, free energy, and pressure, which leads to dramatic changes in certain thermodynamic properties (e.g., a jump in the density). At extremely large temperatures and pressures, for water, a crossover phase transition is reached between the liquid and gas phases: depending on what thermodynamic observable one looks at, the substance could look more like a liquid or a gas. In other words, the phase transition no longer takes place at a fixed temperature, free energy, and pressure, but rather across a range of them. Finally, bordering these two regimes, there exists a critical point that separates a crossover phase transition from a first-order one. To describe these different phases of matter, one requires an equation of state (EoS) that depends on the thermodynamic variables of the system. One should note, however, that the EoS is an equilibrium property, and, of course, out-of-equilibrium effects can also be quite relevant. For instance, imagine a body of water that is flowing and being cooled at the same time. In such a dynamical system, one also requires information about the transport coefficients in order to properly describe its behavior as it freezes.

In this work, we will concern ourselves with phases of matter that appear at high energy, relevant when studying the strong force. This is the force that binds together the nucleus, and leads to the generation of 99% of the visible matter in the universe. The theory that governs the strong force is quantum chromodynamics (QCD, Gross and Wilczek 1973; Politzer 1973). QCD describes the interactions of the smallest building blocks of matter (quarks and gluons). Quarks and gluons are normally not free (or “deconfined”) in Nature, but rather confined within hadrons. The latter comprise mesons (quark anti-quark pairs $q\bar{q}$), baryons (three-quark states qqq), or anti-baryons (three anti-quark states $\bar{q}\bar{q}\bar{q}$).[1] The quark content and their corresponding quantum numbers (see Table 1) yield the quantum numbers of the hadron itself. One can calculate the thermodynamic properties of strongly interacting matter using either lattice QCD in the non-perturbative regime, or perturbative QCD (pQCD) where the coupling is small (high temperatures and/or extremely high densities).

Protons (*uud* quark state), neutrons (*udd* quark state), and, in rare cases, hyperons (baryons with strange quark content) form nuclei, the properties of which depend on the number of nucleons A, as well as the number of protons Z and the number of neutrons $A - Z$ within the nucleus.[2] In principle, QCD also drives the properties of nuclei. However, in the vast majority of cases, it would not be convenient to calculate

[1] Several pentaquark ($qqqq\bar{q}$) and tetraquark ($qq\bar{q}\bar{q}$) states have also been observed in the past two decades but are not directly relevant to this work; we refer the reader to Chen et al. (2023) for an extended review of this topic.

[2] In the rare case of hypernuclei, one must also consider the number of hyperons H such that the total number of neutrons within the nucleus is $A - Z - H$.

Table 1 Summary table of quarks including flavor, mass, and quantum numbers (Workman et al. 2022)

Flavor	Mass (MeV)	Charge (e)	Baryon number	Spin	Isopsin (z-projection)	Strangeness
Up (u)	$2.16^{+0.49}_{-0.26}$	$+\frac{2}{3}$	$\frac{1}{3}$	$\frac{1}{2}$	$\frac{1}{2}\,(+\frac{1}{2})$	0
Down (d)	$4.67^{+0.48}_{-0.17}$	$-\frac{1}{3}$	$\frac{1}{3}$	$\frac{1}{2}$	$\frac{1}{2}\,(-\frac{1}{2})$	0
Strange (s)	$93.4^{+8.6}_{-3.4}$	$-\frac{1}{3}$	$\frac{1}{3}$	$\frac{1}{2}$	0	-1
Charm (c)	1270 ± 20	$+\frac{2}{3}$	$\frac{1}{3}$	$\frac{1}{2}$	0	0
Bottom (b)	4180^{+30}_{-20}	$-\frac{1}{3}$	$\frac{1}{3}$	$\frac{1}{2}$	0	0
Top (t)	$1.73 \times 10^5 \pm 300$	$+\frac{2}{3}$	$\frac{1}{3}$	$\frac{1}{2}$	0	0

the properties of nuclei or nuclear matter (beyond densities and temperatures at which nuclei dissolve into a soup of hadrons) directly from the Lagrangian of QCD, both because of the numerical challenges but also because it would not be the most effective way (it would be akin to calculating the properties of a lake from the microscopic interactions of H_2O molecules). The objective of this review article is to put together the constraints derived from fundamental theories (that are gauge invariant and renormalizable) and observations. For this reason, we do not discuss relativistic mean-filed models. We also opted not to incorporate the different approaches used to describe nuclear matter, and refer instead to an excellent review on this subject (Oertel et al. 2017). Two different approaches are generally used to obtain the equation of state of nuclear matter from these constraints: ab-initio many-body methods using realistic interactions (these include Green Function methods, variational and Monte Carlo methods, (Dirac)–Brueckner–Hartree–Fock calculations and an example is the well known Akmal, Pandharipande, and Ravenhall EoS (Akmal et al. 1998)) or phenomenological approaches based in density functional theories applying effective interactions, including relativistic mean-field models with meson exchange forces and non-relativistic Skyrme and Gogny forces, see Oertel et al. (2017) for a review. Using these methods, one can calculate thermodynamic quantities at low temperatures (on the MeV scale) and around nuclear saturation density, $n_{\rm sat}$, which represents the point on the saturation curve where the binding energy per nucleon in a nucleus is at its lowest, indicating a balance between the attractive and repulsive nuclear forces, therefore, maximal stability within the nuclear system (Haensel et al. 1981).

How can we solve QCD and study nuclear matter theoretically? How can we probe QCD and nuclear matter experimentally? What systems in Nature and in the laboratory are sensitive to quarks and gluons, hadrons, or nuclei? At large temperatures and vanishing net baryon densities $n_B = 0$ (i.e., the same amount of baryons/quarks and anti-baryons/anti-quarks), the conditions are the same as those of the early universe and can be reproduced in the laboratory, at the Large Hadron Collider (LHC, Citron et al. 2019) and at the Relativistic Heavy Ion Collider (RHIC, STAR Collaboration 2014; Cebra et al. 2014) for top center-of-mass beam energies $\sqrt{s_{NN}} = 200$ GeV. In equilibrium, lattice QCD can be used to calculate the EoS, which can be extended to finite n_B using expansion schemes up to baryon chemical potentials (over temperature) of about $\mu_B/T \sim 3.5$. Medium to low energy RHIC collisions explored in the Beam Energy Scan (BES) phase I and II ($\sqrt{s_{NN}} = 7.7 - 200$ GeV in collider mode), as well as existing and future fixed target experiments at RHIC (STAR Collaboration 2014; Cebra et al. 2014), SPS (Pianese et al. 2018), HADES (Galatyuk 2014, 2020), and FAIR (Friese 2006; Tahir et al. 2005; Lutz et al. 2009; Durante et al. 2019) can reach temperatures in the range $T \sim 50 - 350$ MeV and baryon chemical potentials $\mu_B \sim 20 - 800$ MeV, using a range of center of mass beam energies $\sqrt{s_{NN}} \sim 2 - 11$ GeV. Therefore, these low-energy experiments provide a significant amount of information that can also be used to infer the EoS (Dexheimer et al. 2021c; Lovato et al. 2022b; Sorensen et al. 2024). However, these systems are probed dynamically and may be far from equilibrium, so one must not consider the EoS extracted from heavy-ions as data in the typical sense, but rather as a posterior model that is sensitive to priors and systematic uncertainties that may exist in that model. In the high temperature and/or chemical potential limit, systematic methods such as perturbative resummations can be used to calculate the EoS analytically directly form the QCD Lagrangian.

Low-energy nuclear experiments provide methods to extract key properties of nuclei. Most stable nuclei are composed of "isospin-symmetric nuclear matter", i.e $Z = 0.5\,A$, such that the number of protons and neutrons are equal in the nucleus. For simplicity, one defines the charge fraction $Y_Q = Z/A$, which can also be related to the charge density n_Q (assuming a system of only hadrons, no leptons) over the baryon density n_B such that $Y_Q = n_Q/n_B$ as well. Then, for symmetric nuclear matter $Y_Q = 0.5$ and this is where most nuclear experiments provide information. However, heavy nuclei do become more neutron rich, such that $Y_Q \sim 0.4$. Note that, for the highest energies, heavy-ion experiments only probe $Y_Q = 0.5$ as the nuclei basically pass through each other, and the fireball left behind cannot create net isospin ($Y_Q \neq 0.5$) or strangeness ($Y_S = S/A = n_S/n_B \neq 0$) during the very brief time of the collision (on the order of ~ 10 fm/c or 10^{-23} s).

All thermodynamic properties change as Y_Q varies. This can be measured experimentally in low-energy nuclear experiments around $n_{\rm sat}$ through the determination of the symmetry energy $E_{\rm sym}$, which can be approximated as the difference between the energy per nucleon of $Y_Q = 0$ (pure neutron matter $E_{\rm PNM}$) and $Y_Q = 0.5$ matter (symmetric nuclear matter $E_{\rm SNM}$)[3]

$$E_{\rm sym} \equiv \frac{E_{\rm PNM} - E_{\rm SNM}}{N_B}. \tag{1}$$

The baryon number N_B is more comprehensive than A, as it also includes quarks, with $N_B = 1/3$. At saturation density, many other quantities can be determined such as the binding energy per nucleon, or the (in)compressibility of matter, in addition to $n_{\rm sat}$ itself. At small Y_Q, matter in neutron stars provides information about both

[3] The general definition of the symmetry energy is $E_{\rm sym} \equiv \frac{1}{2}\partial^2(E/N_B)/\partial\beta^2$, where E/N_B is the energy per baryon and $\beta \equiv (n_n - n_p)/(n_n + n_p)$ in terms of neutron stars or $\beta = 1 - 2\,Y_Q$ (Bombaci and Lombardo 1991; Haensel 1977; Muller-Kirsten et al. 1999). Equation (1), commonly found in the literature, only shows terms up to second order in the expansion.

nuclear and QCD matter at low temperatures and medium-to-high densities. Matter in this case is necessarily charge-neutral, as $Y_Q = Y_{lep}$, the charge fraction of leptons (electrons and muons). On the other hand, weak(-force) equilibrium ensures $\mu_Q = -\mu_e = -\mu_\mu$, meaning that the charge chemical potential, the difference between the chemical potential of protons and neutrons (in the absence of hyperons), or up and down quarks, equals the ones of electrons and muons.

At saturation densities, a neutron star's internal composition is primarily made up of nucleons and leptons. However, as the density increases, other baryonic species may appear due to the rapid rise in baryon chemical potential associated with a higher density and reduce the ground state energy of the dense nuclear matter phase by opening new Fermi channels. Due to the long time-scales involved (when compared to weak interactions), matter in neutron stars can also include particles with net strangeness, hyperons. Here on Earth, hyperons can be produced but are unstable and quickly decay in $\sim 10^{-8}$ seconds via weak interactions into protons and neutrons. In the high density regime in the core of neutron stars, hyperons cannot decay back to nucleons due to Pauli blocking, meaning that producing additional nucleons would increase the energy of the system (Joglekar et al. 2020; Blaschke et al. 2020). However, the appearance of hyperons softens the EoS of dense matter and lowers the maximum mass $M_{\max}$ of neutron stars predicted by a given theory, which is incompatible with the observations of massive stars, see Sect. 8. This mismatch between experimental observations and theoretical calculations is referred to as the hyperon puzzle (Bednarek et al. 2012; Buballa et al. 2014). To make them compatible, additional repulsion is needed in the theory so that the EoS becomes stiffer. This additional effect can be introduced through the following known mechanisms, (i) hyperon-hyperon interaction via exchange of short-range vector mesons (Rijken and Schulze 2016), (ii) three body repulsive hyperonic force (Lonardoni et al. 2015; Gerstung et al. 2020; Logoteta et al. 2019), (iii) higher-order vector interactions (Bodmer 1991; Dexheimer et al. 2021a), (iv) excluded volume for hadrons (Hagedorn 1983; Dexheimer et al. 2013), and (iii) a phase transition to quark matter at a density less than or around the hyperon threshold (Vidana et al. 2005).

On the other hand, the generation of heavier non-strange baryons (resonances) in the core of neutron stars is still an open question (Weissenborn et al. 2012). Initially (Glendenning 1985), it was argued that resonances appear at much higher densities beyond the density of a neutron star core and, thus, they are not relevant for nuclear astrophysics. Nevertheless, an early appearance of Δ-baryons at 2–3 $n_{\rm sat}$ was obtained in several works (Schürhoff et al. 2010; Drago et al. 2014; Li et al. 2018; Marquez et al. 2022). It was shown that, due to the isospin rearrangement that takes place when the Δ's appear, they do not produce an effect analogous to the hyperon puzzle and are able to replace baryons without clashing with $M_{\max}$ constraints, producing smaller stars in better agreement with observations (Dexheimer et al. 2021b).

2 Executive summary

In this work, we discuss theoretical and experimental constraints for dense and hot matter, including astrophysical observations. For theoretical constraints, we restrict ourselves to those that are derived directly from first principles in particular regimes, where lattice QCD or pQCD calculations are possible, as well as from χEFT also in a particular regime, where it can be considered as the low-energy theory of QCD. For experimental constraints, we focus on measurements and, whenever possible, avoid mentioning quantities inferred from data. For example, by using yields of identified particles in heavy-ion collisions, it is possible to infer the temperature and baryon chemical potential at the point of chemical freeze-out.[4] However, the extracted $\{T, \mu_B\}$ at fixed $\sqrt{s_{NN}}$ and centrality are dependent on a number of assumptions such as the particle list, decay channels, decay widths, how interactions are described (if at all), etc. Thus, we only provide the hadron yields measured directly from experiments and not the thermodynamic quantities inferred from them, which are model dependent.

In the case of experimental low-energy nuclear results, the use of quantities inferred from data is unavoidable. Due to the importance of those results, we discuss them, while highlighting relevant dependencies. For astrophysical observations, posteriors are extracted from a combination of measured data and modeling where the systematic uncertainties are carefully taken into account. Nonetheless, there are certain caveats when one considers these posteriors that we would be remiss not to discuss. This context is important for theorists to understand before making comparisons between tidal deformabilities posteriors extracted from gravitational waves, mass-radius posteriors from NICER X-ray observations, and mass and/or radius extractions from other types of X-ray observations.

2.1 Theoretical constraints: lattice QCD

At vanishing n_B or, equivalently (at finite temperature), $\mu_B = 0$, lattice QCD calculations reliably provide the EoS for $T \gtrsim 125$ MeV. They rely on solving QCD numerically on a very large grid of points in space and time. In this case, it has been determined that the change of phase between a hadron resonance gas (HRG) at low temperatures into a quark-gluon plasma at high temperatures is a smooth crossover. At finite μ_B, the exponential of the QCD action becomes complex and cannot be used as a weight for the configurations generated in Monte Carlo simulations, which is known as the sign problem (Troyer and Wiese 2005; Dexheimer et al. 2021c). However, expansions around $\mu_B = 0$ allow one to obtain the lattice QCD EoS up to a chemical potential dependent on temperature $\mu_B \sim 3.5\,T$ (Borsányi et al. 2021;

[4] Due to the rapid expansion and cooling of the quark-gluon plasma produced in heavy-ion collisions, at a point (chemical freeze-out) following the (pseudo)phase transition where quark and gluons have combined into hadrons, the particles become so far apart that chemical reactions are not longer possible. A second point (kinetic freeze-out) at even lower temperatures occurs (later in the reaction), where the particles become more dilute and kinetic reactions are no longer possible. It is generally believed that chemical freeze-out occurs near the quark deconfinement transition and can be used as a (close but not precise) proxy for the phase transition line.

Borsanyi et al. 2022). Furthermore, lattice QCD results can also constrain the hadronic spectrum through partial pressures (Alba et al. 2017) and provide insight into strangeness-baryon number interactions using cross-correlators (Bellwied et al. 2020). Despite these successes, the expanded lattice QCD EoS cannot reach temperatures and densities relevant to low-energy heavy-ion collisions and neutron stars.

2.2 Theoretical constraints: perturbative QCD

Although quarks are never truly free, due to asymptotic freedom, the coupling strength of the strong force (α_s) decreases logarithmically with energy and, more importantly, in a deconfined medium, Debye screening reduces the effective interaction between quarks and gluons. As a result, as the temperature and/or chemical potential(s) involved become large, one finds that perturbation theory becomes applicable and analytic calculations of the perturbative QCD (pQCD) EoS become reliable (Andersen et al. 2010a, b, 2011a, b; Mogliacci et al. 2013; Haque et al. 2014a, b; Haque and Strickland 2021; Ghiglieri et al. 2020). This occurs at $T \gtrsim 300$ MeV at $\mu_B = 0$ (Haque et al. 2014a, b; Haque and Strickland 2021) and at $n_B \gtrsim 40\ n_{\mathrm{sat}}$ at $T = 0$ (Andersen and Strickland 2002). In the latter case, note however that causality and stability bounds allow pQCD to be applied at lower densities (Komoltsev and Kurkela 2022). In practice, achieving agreement between perturbative QCD and lattice QCD requires resummations at all orders. The two main methods for accomplishing such resummations are effective field theory methods (Braaten and Nieto 1995, 1996a) and hard-thermal-loop perturbation theory (Andersen et al. 2002, 2004). Both resummation schemes have been extended to N2LO (next-to-next-to leading order) in their respective loop expansions at $\mu_B = 0$. At finite chemical potential, N2LO (Freedman and McLerran 1977a, b, c) and partial N3LO (next-to-next-to-next-to leading order) results are available (Gorda et al. 2018, 2021b, a).

2.3 Theoretical constraints: chiral effective field theory

Chiral effective field theory (χEFT) offers a systematic, model-independent framework for investigating the characteristics of hadronic systems at the low energies relevant for nuclear physics where the particle momentum is similar to the pion mass ($p \sim m_\pi$) with quantified uncertainties (Weinberg 1979; Epelbaum et al. 2009; Machleidt and Entem 2011; Drischler et al. 2021c). χEFT starts from the most general Lagrangian that is consistent with the symmetries, in particular the spontaneously broken chiral symmetry, of low-energy QCD with nucleons and pions as degrees of freedom. The theory offers an order-by-order expansion for two-nucleon and multi-nucleon interactions whose long-range features are governed by pion-exchange contributions constrained by chiral symmetry and whose short-distance details are encoded in a set of contact interactions with strengths fitted to two- and few-body scattering and bound-state data. Theoretical uncertainties can be estimated by examining the order-by-order convergence of the χEFT expansion, a feature that provides a crucial benefit over phenomenological approaches (Drischler

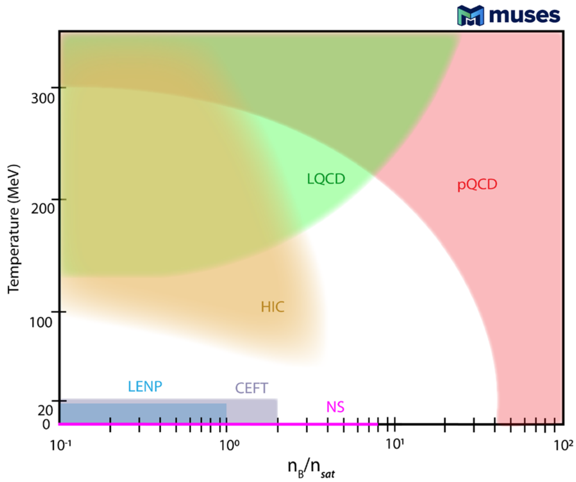

Fig. 1 Regions of the QCD phase diagram where constraints from heavy-ion collisions (HIC), lattice QCD (LQCD), perturbative QCD (pQCD), low-energy heavy-ion collisions (LENP), chiral effective field theory (χEFT), and astrophysics (neutron stars, NS) are available

et al. 2021c). Significant advances in the application of Bayesian statistical methods have led to robust uncertainty quantification in calculations of the EoS up to fourth order in the chiral expansion that are applicable in the range of $n_B \lesssim 2\ n_{\rm sat}$ (Hebeler et al. 2010; Sammarruca et al. 2015; Tews et al. 2018; Drischler et al. 2020).

2.4 QCD phase diagram

From a combination of lattice QCD results (at $T \geq 135$ MeV and $\mu_B/T \leq 3.5$), pQCD calculations (limits include $T \gtrsim 300$ MeV at $\mu_B/T \lesssim 1$ and at $n_B \gtrsim 40\ n_{\rm sat}$ at $T = 0$), and χEFT bands ($T \lesssim 20$ MeV and $n_B \lesssim 2\ n_{\rm sat}$) we now have three theoretical points of reference (or rather regimes) in the QCD phase diagram, see Fig. 1. Effective models —e.g., chiral models (Nambu and Jona-Lasinio 1961a, b; Hatsuda and Kunihiro 1994; Dexheimer and Schramm 2010; Motornenko et al. 2020) and holography (Rougemont et al. 2017; Critelli et al. 2017; Grefa et al. 2021, 2022; Demircik et al. 2022; Kovensky et al. 2023)—some describing the microscopic degrees of freedom and their interactions, are used to connect these regimes in the phase diagram and even propose entirely new phases of dense and hot matter. These models are fixed to be in agreement with theoretical and experimental (low-energy nuclear physics, heavy-ion collisions, and astrophysics) results in the relevant regimes.

2.5 Experimental constraints: heavy-ion collisions

In the laboratory, heavy-ion collisions probe finite temperatures in the range of $T \sim 50-650$ MeV, depending on the center of mass beam energy $\sqrt{s_{NN}}$, such that higher $\sqrt{s_{NN}}$ probe high temperatures and lower $\sqrt{s_{NN}}$ probe lower temperatures. The temperature and density of the system vary in space and time throughout the evolution, which is the hottest at early times. Depending on the choice of the experimental observables, one can obtain information at different temperatures and densities within the collisions. The final distribution of hadrons reflects the temperature and chemical potentials at chemical freeze-out (although certain momentum dependent observables are also sensitive to the kinetic freeze-out, see e.g. Adamczyk et al. 2017 for a comparison between chemical and kinetic freeze-out).

When temperatures are high enough (i.e., high $\sqrt{s_{NN}}$) for a quark-gluon plasma to be produced, such that hydrodynamics is a good dynamical description, lowering $\sqrt{s_{NN}}$ corresponds to a lower initial temperature, a lower freeze-out temperature, and a larger n_B. However, for very low beam energies, below $\sqrt{s_{NN}} \lesssim 4-7$ GeV, the hadron gas phase dominates, such that hadron transport models may be used. This then means that higher $\sqrt{s_{NN}}$ reaches larger n_B whereas lower $\sqrt{s_{NN}}$ reach a smaller range of n_B. The exact switching point from a quark-gluon plasma dominated- to hadronic-dominated dynamical description is unknown and still hotly debated within the community. The initial collision temperature T_0 is model-dependent, so we do not include estimates for it in this work. The freeze-out temperature, however, can be more directly extracted from experimental data (with certain caveats that we will explain here) using particle yields and assuming thermal equilibrium at freeze-out. Additionally, the emission of photons and lepton pairs (dileptons), which are immune to strong interactions and can traverse the QGP, can be used to extract average temperatures at different points in the heavy-ion collision evolution, which can be used to pin down the temperature evolution (Strickland 1994; Schenke and Strickland 2007; Martinez and Strickland 2008; Dion et al. 2011; Shen et al. 2014; Gale et al. 2015; Bhattacharya et al. 2016; Ryblewski and Strickland 2015; Paquet et al. 2016; Kasmaei and Strickland 2019, 2020). On the other hand, the extraction of n_B is more model dependent. If a QCD critical point exists, then susceptibilities of the pressure will diverge exactly at the critical point and may have non-trivial behavior in the surrounding critical region (Stephanov 2009; Parotto et al. 2020; Mroczek et al. 2021). In equilibrium, these would determine the cumulants of the distribution of protons, such as the kurtosis. Measurements of the kurtosis (Adam et al. 2021b; Abdallah et al. 2023b; Adamczewski-Musch et al. 2020c; Acharya et al. 2020a), 6th-order cumulants (Abdallah et al. 2021c), and fluctuations of light nuclei (Abdulhamid et al. 2023) exist from BES-I across a variety of beam energies with large statistical error bars. BES-II (Tlusty 2018) will significantly improve the measurement precision. However, the data has not yet been released.

Looking to the future, the Compressed Baryonic Matter (CBM) Experiment at FAIR (GSI, Germany) will be an experimental facility that will be dedicated to explore low beam energies in fixed target mode with high luminosity, i.e., with a high collision rate (Spies 2022). CBM (Lutz et al. 2009; Durante et al. 2019) will allow us to constrain the EoS at high μ_B and moderate temperatures. Eventually, from the wealth of experimental data in heavy-ion collisions, it will be possible to extract an EoS using model-to-data comparisons. However, that will require more sophisticated dynamical models that do not yet exist (Bluhm et al. 2020). It has already been identified that the azimuthal anisotropies of the momentum distribution of particles in collisions, otherwise known as flow harmonics, are sensitive to the EoS at these low beam energies (Danielewicz et al. 2002; Spieles and Bleicher 2020). However, there are still significant questions remaining about the correct dynamical model and other free parameters such as transport coefficients. Depending on the model assumptions, one can obtain radically different posteriors of the EoS, or find different EoSs consistent with the data at these beam energies (a few examples include comparing the different results and conclusions from Danielewicz et al. 2002; Spieles and Bleicher 2020; Schäfer et al. 2022; Shen and Schenke 2022; Oliinychenko et al. 2023). Thus, in this work, we will only include a discussion on some of the key experimental measurements but cannot yet clarify the precise implications of the data.

2.6 Experimental constraints: low-energy nuclear physics

At significantly lower beam energies (approaching the $T \rightarrow 0$ limit) there are a number of experiments that probe dense matter. These experiments study the properties of nuclei at (or near) saturation density. While most nuclei contain symmetric nuclear matter such that $Y_Q \sim 0.5$, heavy nuclei become more neutron-rich and may reach $Y_Q \sim 0.4$, while unstable nuclei close to the neutron drip line have much smaller values of Y_Q. However, neutron stars are composed of primarily asymmetric nuclear matter, with $Y_Q \sim 0.001 - 0.2$. Thus, one can use a Taylor series to expand between symmetric and asymmetric matter, known as the symmetry energy expansion. In this case, a few of its coefficients can be inferred from experimental measurements of, e.g., the neutron skin. Symmetric-matter properties include binding energy per nucleon, compressibility, and saturation density, and can also be inferred, together with the EoS. However, in this case there is model dependence which can be investigated by using different kinds of models.

In addition to the compressibility and the binding energy per nucleon, the effective mass of nucleons at saturation was shown to be important to study the nuclear EoS of hot stars (Raduta et al. 2021), the EoS of neutron stars with exotic particles at finite temperature (Raduta 2022), thermal effects in supernovae (Constantinou et al. 2015), and neutron-star mergers (see Raithel et al. 2019 and references therein). Nevertheless, the experimental determination of this quantity still includes large uncertainties and, therefore, will not be discussed in this review.

Beyond nucleons, properties of hyperons and Δ-baryons can also be determined for symmetric matter. The most useful observable to constrain effective models is optical potentials at n_{sat}, which provides the result of the balance between attractive and repulsive strong interactions. At finite temperature, there is also data concerning the critical point for the liquid–gas phase transition (Elliott et al. 2012), where nuclei turn into bulk hadronic matter.

2.7 Experimental constraints: astrophysics

The high baryon density inside neutron stars makes them a natural laboratory to understand strong interaction physics under conditions that are impossible to achieve in a laboratory setting. Neutron stars are the end-life of massive stars, which run out of fuel for fusion and collapse gravitationally, violently exploding as supernovae. As a result, the cores of the remnant neutron stars possess densities of the order of several times n_{sat}. Neutron stars are stratified according to density, with different

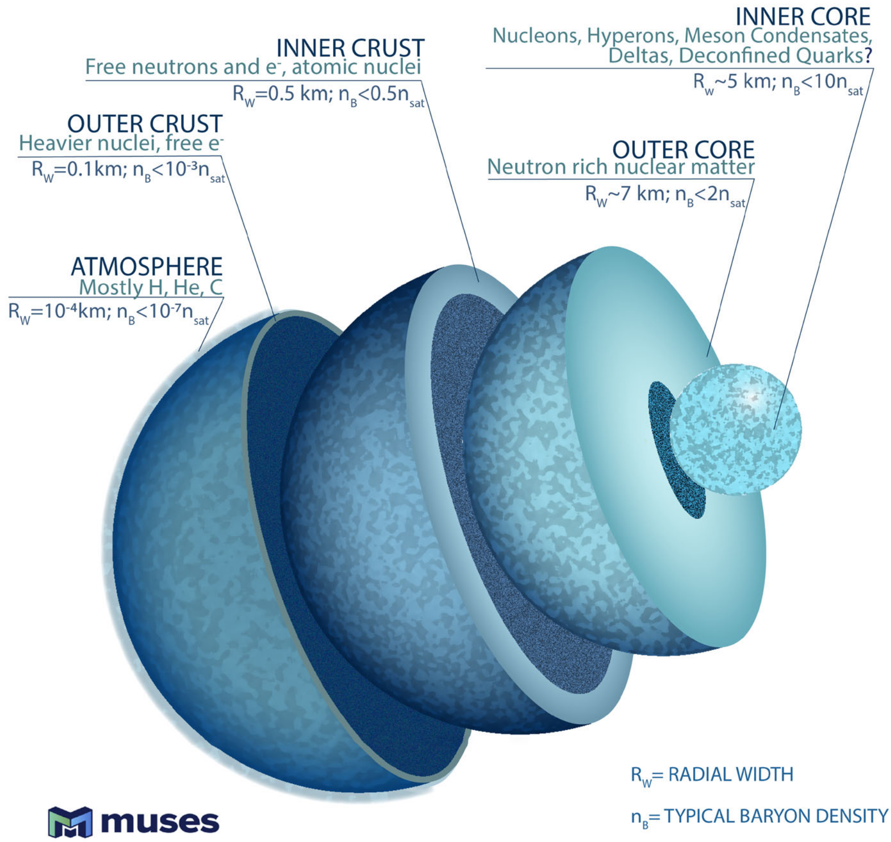

Fig. 2 Composition of a typical neutron star

types of co-existing phases categorized according to the radial coordinate (see Fig. 2). The outermost layer is the atmosphere, with a thickness of a few centimeters, which contains mostly hydrogen, helium, and carbon atoms. A little bit deeper, starts the outer crust with a layer of ^{56}Fe. Electrons disassociate from specific nuclei and, moving towards the center of the star, nuclei become neutron richer and more massive, such that at the transition to the inner crust the nucleus ^{118}Kr was determined as the most stable within several theoretical models (Ruester et al. 2006). There are, however, some models that may predict slightly larger nuclei at the outer-inner crust transition. In the inner crust, neutrons start to "drip out" of nuclei and, as a result, matter becomes a mixture of unbound electrons, unbound neutrons, and nuclei. At even higher densities in the outer core, above $\sim n_{\rm sat}$, matter turns into a neutron–rich "soup" with no isolated nuclei. Going deeper into higher densities for the inner core, at about 2 $n_{\rm sat}$, hyperons, Δ's, and meson condensates may appear and, eventually, deconfined quark matter may form. Regardless of the phase, fully evolved neutron stars fulfill chemical equilibrium and charge neutrality, either locally or globally, with mixtures of phases occurring in the latter case.

The EoS is related to microscopic equilibrium properties (pressure, energy density, etc.). Therefore, the nuclear EoS is not directly comparable to astrophysical observations, but it serves as an important input in calibrated models to calculate experimental observables, such as mass-radius relationships of compact stars. This is achieved by solving the Tolman–Oppenheimer–Volkoff (TOV) equations (Tolman 1939; Oppenheimer and Volkoff 1939), which are valid as long as rotational frequency (ν) and magnetic field (B) effects are not significant. These results can be compared with astrophysical observations from neutron-star electromagnetic emissions, usually radio and X-ray, and most recently, gravitational wave emission from neutron-star mergers. In particular, observations from the National Radio Astronomy Observatory's Green Bank Telescope (GBT, Demorest et al. 2010), NASA's Neutron Star Interior Composition Explorer (NICER, Gendreau et al. 2016; Baubock et al. 2015; Miller 2016; Özel et al. 2016), and NSF's Laser Interferometer Gravitational-wave Observatory (LIGO) together with Virgo (Abbott et al. 2017a, b; Gendreau et al. 2016) put strong constraints on the EoS (Gendreau et al. 2016; Annala et al. 2018). Many EoS models have been updated since these observations were made, to be in agreement with observations (Baym et al. 2018).

The most accurate neutron-star mass estimates come from the timing of radio pulsars in orbital systems with relativistic dynamical effects (Antoniadis et al. 2013; Cromartie et al. 2019; Fonseca et al. 2021b); they inform the EoS insofar as they set a lower bound on the maximum mass it must be able to support against gravitational collapse. The most reliable radius measurements stem from X-ray pulse profile modeling of rotating neutron stars (Miller et al. 2019; Riley et al. 2019a; Miller et al. 2021b; Riley et al. 2021a), and constrain the mass-radius relation predicted by the EoS. Meanwhile, gravitational-wave observations of merging neutron stars constrain the EoS via their tidal deformability (Abbott et al. 2017a, 2018, 2019, 2020a). If the gravitational waves are accompanied by a kilonova counterpart, as was the case for the binary neutron-star merger GW170817 (Abbott et al. 2017b), the lightcurve and spectrum of the electromagnetic emission, as well as its implications for the fate of the merger remnant, also inform the EoS (Bauswein et al. 2017; Margalit and Metzger 2017; Radice et al. 2018; Rezzolla et al. 2018; Ruiz et al. 2018; Shibata et al. 2017). Eventually, upgraded gravitational wave detectors will also be able to detect the post-merger signal (Carson et al. 2019) (the post-merger starts at the point where the two neutron stars touch). This signal is also sensitive to finite temperature effects that may even reach temperatures and densities similar to heavy-ion collisions (Adamczewski-Musch et al. 2019b), potential out-of-equilibrium effects due to the long-time scales associated with weak interactions (Alford et al. 2018, 2019; Alford and Harris 2019; Alford et al. 2021; Gavassino et al. 2021; Celora et al. 2022; Most et al. 2022) as well as deconfinement to quark matter (Bauswein et al. 2019; Most et al. 2019; Weih et al. 2020; Blacker et al. 2020; Tootle et al. 2022; Constantinou et al. 2021).

2.8 Organization of the paper

This review paper aims at compiling up-to-date constraints from high-energy physics, nuclear physics, and astrophysics that relate to the EoS and are, therefore, fundamental to the understanding of current and future data from heavy-ion collisions to gravitational waves, making them relevant to a very broad community. Additionally, precise knowledge of the dense and hot matter EoS can help physicists to look beyond the standard model either for dark matter, which may accumulate in or around neutron stars, or for modified theories of gravity.

The paper is organized as follows: we first discuss the theoretical constraints of lattice (Sect. 3) and perturbative QCD (Sect. 4), followed by χEFT (Sect. 5). Then, we discuss experimental constraints from heavy-ion collisions (Sect. 6), (isospin symmetric and asymmetric) low-energy nuclear physics (Sect. 7), and astrophysical observations (Sect. 8). We provide a future outlook in Sect. 9, since a significant amount of new data is anticipated over the next decade.

3 Theoretical constraints: lattice QCD

Lattice QCD is the most suitable method to study strong interactions around and above the deconfinement phase transition region in the QCD phase diagram, due to its non-perturbative nature (Drischler et al. 2021b). As discussed in the introduction, due to the sign problem, first-principles lattice QCD results for the EoS at finite μ_B are currently restricted. Since direct lattice simulations at $\mu_B = 0$ and imaginary μ_B are feasible, observables can be extrapolated using techniques involving zero or imaginary chemical potential simulations, i.e., analytical continuation, Taylor series and other alternative expansions. In this section, we present various constraints on the EoS, BSQ (baryon number, strangeness, and electric charge) susceptibilities, and partial pressures evaluated using lattice QCD.

3.1 Equation of state

In Borsanyi et al. (2014a) and Bazavov et al. (2014), the EoS was obtained in lattice QCD simulations at $\mu_B = 0$. It was found that the rigorous continuum extrapolation results for 2+1 quark flavors are perfectly compatible with previous continuum estimates based on coarser lattices (Aoki et al. 2006; Borsanyi et al. 2010). The obtained pressure, entropy density, and interaction measure are displayed in the left panel of Fig. 3 alongside the predictions of the hadron resonance gas (HRG) model (Venugopalan and Prakash 1992) at low temperatures and the Stefan–Boltzmann (or conformal) limit of a non-interacting massless quarks gas at high T. They show full agreement with HRG results in the hadronic phase, and reach about 75% of the Stefan–Boltzmann limit at $T \simeq 400$ MeV.

Furthermore, a Taylor series can be utilized to expand many observables to finite μ_B/T

$$\frac{p(T, \mu_B, \mu_Q, \mu_S)}{T^4} = \sum_{i,j,k} \frac{1}{i!j!k!} \chi_{ijk}^{BQS} \left(\frac{\mu_B}{T}\right)^i \left(\frac{\mu_Q}{T}\right)^j \left(\frac{\mu_S}{T}\right)^k \tag{2}$$

where the susceptibilities χ_{ijk}^{BQS} are defined as follows

$$\chi_{lmn}^{BSQ} = \frac{\partial^{l+m+n}(p/T^4)}{\partial(\mu_B/T)^l \partial(\mu_S/T)^m \partial(\mu_Q/T)^n}. \tag{3}$$

They were obtained from lattice QCD calculations up to $\mathcal{O}(\mu_B/T)^4$ for the full series of coefficients and up to $\mathcal{O}(\mu_B/T)^8$ for some of the coefficients. The range of applicability of the Taylor expansion has recently been extended from $\mu_B/T \leq 2$ (Guenther et al. 2017; Bazavov et al. 2017) to $\mu_B/T \leq 2.5$ (Bollweg et al. 2022). Isentropic trajectories in the $T - \mu_B$ plane have been extracted in Guenther et al. (2017), for which the starting points are the freeze-out parameters at different collision energies at RHIC (Alba et al. 2014). Strangeness neutrality and electric charge conservation were enforced by tuning the strange and electric charge chemical potentials, $\mu_S(\mu_B, T)$ and $\mu_Q(\mu_B, T)$, to reproduce the conditions $Y_S = 0$ and $Y_Q = 0.4$ (Guenther et al. 2017).

A new expansion scheme for extending the EoS of QCD to unprecedentedly large baryonic chemical potential up to $\mu_B/T < 3.5$ has been proposed recently (Borsányi et al. 2021). The drawbacks of the conventional Taylor expansion approach, such as the challenges involved in carrying out such an expansion with a constrained number of coefficients and the low signal-to-noise ratio for the coefficients themselves, are significantly reduced in this new scheme (Borsányi et al. 2021). In the hadronic phase, a good agreement is found for the thermodynamic variables with HRG model results. This scheme is based on the following identity

$$\frac{\chi_1^B(T, \mu_B)}{\mu_B/T} = \chi_2^B(T', 0) \tag{4}$$

with

$$T'(T, \mu_B) = T(1 + \kappa_2^{BB}(T)\left(\frac{\mu_B}{T}\right)^2 + \kappa_4^{BB}(T)\left(\frac{\mu_B}{T}\right)^4 + \mathcal{O}((\mu_B/T)^6. \tag{5}$$

The baryonic density as a function of the temperature for different values of μ_B/T

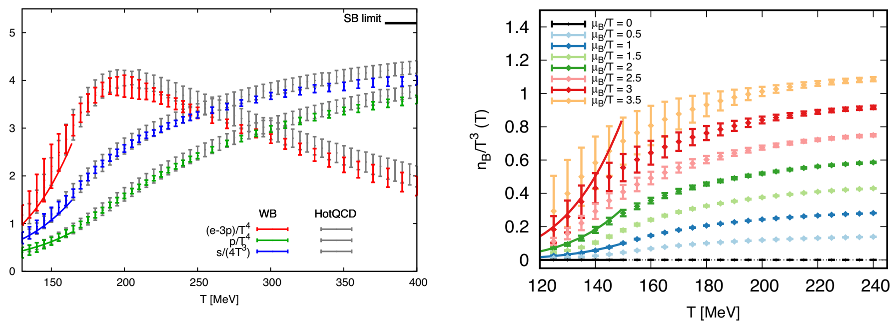

Fig. 3 Left: comparison between the lattice QCD EoS at $\mu_B = 0$ from the WB collaboration Borsanyi et al. (2014a) (colored points) and the HotQCD one (Bazavov et al. 2014) (gray points). Right: Baryonic density as a function of the temperature, for different values of μ_B/T. At low temperature, full lines show results from the HRG model. Images reproduced with permission from [left] Ratti (2018), copyright by IOP, and [right] from Borsányi et al. (2021), copyright by the author(s)

from Borsányi et al. (2021) is shown in the right panel of Fig. 3. This extrapolation method was then generalized to include the strangeness neutrality condition (Borsanyi et al. 2022), which requires $\mu_S \neq 0$. The extrapolation approach is devoid of the unphysical oscillations that afflict fixed order Taylor expansions at higher μ_B, even in the strangeness neutral situation. Effects beyond strangeness neutrality are estimated by computing the baryon-strangeness correlator to strangeness susceptibility ratio $\frac{\chi_{11}^{BS}}{\chi_2^S}$ (discussed in the following subsection) at finite real μ_B on the strangeness neutral line. This permits a leading order extrapolation in the ratio $R = \chi_1^S/\chi_1^B$ (Borsanyi et al. 2022).

3.2 BSQ susceptibilities

Fluctuations of different conserved charges have been postulated as a signal of the deconfinement transition because they are sensitive probes of quantum numbers and related degrees of freedom. In heavy-ion collisions, one needs to relate fluctuations of net baryon number, strangeness, and electric charge with the event-by-event fluctuations of particle species. Non-diagonal correlators of conserved charges, like fluctuations, are useful for studying the chemical freeze-out in heavy-ion collisions. In thermal equilibrium, these correlators may be estimated using lattice simulations, and linked to moments of event-by-event distributions of multiplicity (i.e., number of particles of a given species in some kinematic region, typically these are all charged particles) distributions. They are defined as derivatives of the pressure with respect to the chemical potentials according to Eq. (3). The quark number chemical potentials appear as parameters in the Grand Canonical partition function. The derivative of this function with respect to these chemical potentials yields the susceptibilities and the non-diagonal correlators of the quark flavors. Quark flavor chemical potentials can be related to the conserved charge ones through the following relationships: $\mu_u = \frac{1}{3}\mu_B + \frac{2}{3}\mu_Q$, $\mu_d = \frac{1}{3}\mu_B - \frac{1}{3}\mu_Q$, and $\mu_s = \frac{1}{3}\mu_B - \frac{1}{3}\mu_Q - \mu_S$.

For $T = 125 - 400$ MeV and at $\mu_B = \mu_S = \mu_Q = 0$, the Wuppertal-Budapest lattice QCD collaboration computed the non-diagonal (us) and diagonal (B,s,Q,I,u) susceptibilities for a system of 2+1 staggered quark flavors (Borsanyi et al. 2012), where I stands for isospin. Selected susceptibilities are shown in the left panel of Fig. 4. A Symanzik-improved gauge and a stout-link improved staggered fermion action were used in this analysis. The ratios of fluctuations were found, whose behavior may be recreated using hadronic observables, i.e. proxies, to compare either to lattice QCD findings or experimental observations (Bellwied et al. 2020).

Continuum extrapolated lattice QCD findings for $\chi_{2,2}^{u,s}$, $\chi_{2,2}^{u,d}$, $\chi_{1,1}^{u,d}$, χ_4^u, χ_4^B were presented in Bellwied et al. (2015). Second and fourth-order cumulants of conserved charges were constructed in a temperature range spanning from the QCD transition area to the region of resummed perturbation theory. It was found that, in the hadronic phase ($T \sim 130$ MeV), the HRG model predictions accurately reflect the lattice data, whereas in the deconfined region ($T \gtrsim 250$ MeV), a good agreement was found with three loop hard-thermal-loop (HTL) outcomes (Bellwied et al. 2015). Different diagonal and non-diagonal fluctuations of conserved charges are estimated up to

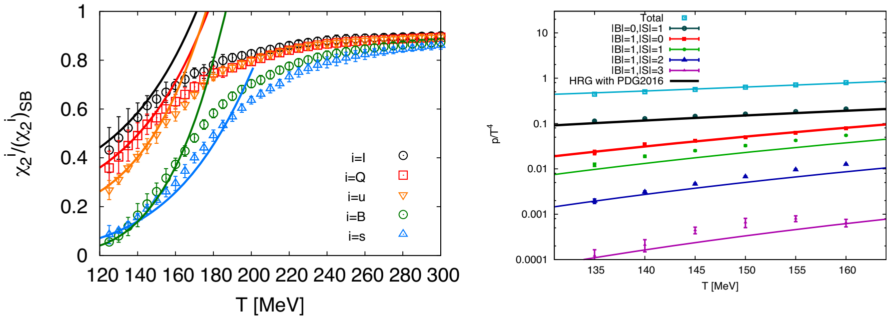

Fig. 4 Left: Baryon number, strange quark, electric charge, isospin number, and up quark susceptibilities as functions of the temperature at $\mu_B = 0$. Right: compilation of partial pressures for different hadron families as functions of the temperature. Images reproduced with permission from [left] Borsanyi et al. (2012), copyright by SISSA, and [right] from Alba et al. (2017), copyright by APS

sixth-order on a lattice size of $48^3 \times 12$ (Borsanyi et al. 2018). Higher-order fluctuations at zero baryon/charge/strangeness chemical potential are calculated. The ratios of baryon-number cumulants as functions of T and μ_B are derived from these correlations and fluctuations, which fulfill the experimental criteria of proton/baryon ratio and strangeness neutrality and in turn, describe the observed cumulants as functions of collision energy from the STAR collaboration (Borsanyi et al. 2018). Ratios of fourth-to-second order susceptibilities for light and strange quarks were presented in Bellwied et al. (2013).

3.3 Partial pressures

Under the assumption that the hadronic phase can be treated as an ideal gas of resonances, and using lattice simulations, the partial pressures of hadrons were determined with various strangeness and baryon number contents. To explain the difference between the results of the HRG model and lattice QCD for some of them, the existence of missing strange resonances was proposed (Bazavov et al. 2013b; Alba et al. 2017). Note that partial pressures are only possible within the hadron resonance gas phase because (i) they require hadronic degrees-of-freedom and (ii) they are applicable under the assumption that the pressure can be written as separable components by the quantum number of the hadrons, i.e.,

$$\begin{aligned} P(\hat{\mu}_B, \hat{\mu}_S) =& P_{00}^{BS} + P_{10}^{BS} \cosh(\hat{\mu}_B) + P_{01}^{BS} \cosh(\hat{\mu}_S) + P_{11}^{BS} \cosh(\hat{\mu}_B - \hat{\mu}_S) \\ &+ P_{12}^{BS} \cosh(\hat{\mu}_B - 2\hat{\mu}_S) + P_{13}^{BS} \cosh(\hat{\mu}_B - 3\hat{\mu}_S) \end{aligned} \tag{6}$$

where the coefficients P_{ij}^{BS} indicate the baryon number i and strangeness j of the family of hadrons for which the partial pressure is being isolated, and the dimensionless chemical potentials are written as $\hat{\mu} = \mu/T$. The calculations were made feasible by taking imaginary values of strange chemical potential in the simulations. For strange mesons, more interaction channels should be incorporated into the HRG model, in order to explain the lattice data (Alba et al. 2017). The right panel of Fig. 4 shows a compilation of these partial pressures.

3.4 Pseudo-phase transition line

In a crossover, there is no sudden jump in the first derivatives of the pressure. Nevertheless, a (chiral) pseudo-phase transition line can be calculated based on where the order parameters change more rapidly. The exact location of the QCD transition line is a hot topic of research in the field of strong interactions. The most recent results are contained in Borsanyi et al. (2020). The transition temperature, obtained from the chiral condensate and its susceptibility, as a function of the chemical potential can be parametrized as

$$\frac{T_c(\mu_B)}{T_c(\mu_B = 0)} = 1 - \kappa_2 \left(\frac{\mu_B}{T_c(\mu_B)}\right)^2 - \kappa_4 \left(\frac{\mu_B}{T_c(\mu_B)}\right)^4 + \ldots \tag{7}$$

The crossover or pseudo-critical temperature T_c has been determined with extreme accuracy and extrapolated from imaginary up to real $\mu_B \approx 300$ MeV. Additionally, the width of the chiral transition and the peak value of the chiral susceptibility were calculated along the crossover line. Both of them are constant functions of μ_B. This means that, up to $\mu_B = 300$ MeV, no sign of criticality has been observed in lattice results. In fact, at the critical point the height of the peak of the chiral susceptibility would diverge and its width would shrink. The small error reflects the most precise determination of the $T - \mu_B$ phase transition line using lattice techniques. Besides $T_c = 158 \pm 0.6$ MeV, the study provides updated results for the coefficients $\kappa_2 = 0.0153 \pm 0.0018$ and $\kappa_4 = 0.00032 \pm 0.00067$ (Borsanyi et al. 2020). Similar coefficients for the extrapolation of the transition temperature to finite strangeness, electric charge, and isospin chemical potentials were obtained in Bazavov et al. (2019), and are displayed in Table 2.

3.5 Limits on the critical point location

As mentioned in the previous subsection, in Borsanyi et al. (2020), by extrapolating the proxy for the transition width as well as the height of the chiral susceptibility peak from imaginary to real μ_B, the strength of the phase transition was evaluated and no indication of criticality was found up to $\mu_B \approx 300$ MeV. On the other hand, a phase transition temperature at $\mu_B = 0$ of $T_c = 132^{+3}_{-6}$ MeV was found in the chiral limit by the HotQCD collaboration using lattice QCD calculations with "rooted"

Table 2 Continuum-extrapolated values of κ_2^X and κ_4^X (with $\mu_Q = \mu_S = 0$ for $X = B$, $\mu_B = \mu_Q = 0$ for $X = S$ and $\mu_B = \mu_S = 0$ for $X = Q, I$) from Bazavov et al. (2019)

κ_2^B	κ_4^B	κ_2^S	κ_4^S	κ_2^Q	κ_4^Q	κ_2^I	κ_4^I
0.016(6)	0.001(7)	0.017(5)	0.004(6)	0.029(6)	0.008(1)	0.026(4)	0.005(7)

staggered fermions (Ding et al. 2019). This transition temperature is computed with two massless light quarks and a physical strange quark based on two unique estimators. Since the curvature of the phase diagram is negative, a critical point in the chiral limit would sit at a temperature smaller than this one. The expectation is that the temperature of the critical point at physical quark masses has to be smaller than the one of the critical point in the chiral limit, and therefore definitely smaller than $T_c = 132^{+3}_{-6}$ MeV.

4 Theoretical constraints: perturbative QCD

It is possible to compute analytically the QCD EoS directly from the QCD Lagrangian using finite temperature/density perturbation theory. However, in thermal and chemical equilibrium, when $T \gg \mu_i$ (with quark chemical potentials μ_i), one finds that the naive loop expansion of physical quantities is ill-defined and diverges beyond a given loop order, which depends on the quantity under consideration. In the calculation of QCD thermodynamics, this stems from uncanceled infrared (IR) divergences that enter the expansion of the partition function at three-loop order. These IR divergences are due to long-distance interactions mediated by static gluon fields and result in contributions that are non-analytic in the strong coupling constant $\alpha_s = g^2/4\pi$, e.g., $\alpha_s^{3/2}$ and $\log(\alpha_s)$, unlike vacuum perturbation expansions which involve only powers of α_s.

It is possible to understand at which perturbative order terms that are non-analytic in α_s appear by considering the contribution of non-interacting static gluons to a given quantity. For simplicity, we now discuss the case of $\mu_B = 0$ for this argument, but the same holds true at finite chemical potential. For the pressure of a gas of gluons one has $P_{\text{gluons}} \sim \int d^3p\, p f_B(E_p)$, where f_B denotes a Bose–Einstein distribution function and E_p is the energy of the in-medium gluons. The contributions from the momentum scales πT, gT and g^2T can be expressed as

$$P^{p\sim\pi T}_{\text{gluons}} \sim T^4 f_B(\pi T) \sim T^4 + \mathcal{O}(g^2)\,, \tag{8}$$

$$P^{p\sim gT}_{\text{gluons}} \sim (gT)^4 f_B(gT) \sim g^3 T^4 + \mathcal{O}(g^4)\,, \tag{9}$$

$$P^{p\sim g^2 T}_{\text{gluons}} \sim (g^2T)^4 f_B(g^2T) \sim g^6 T^4 \tag{10}$$

where we have used the fact that $f_B(E) \sim T/E$ if $E \ll T$. This fact is of fundamental importance, since it implies that when the energy/momentum are *soft*, corresponding to electrostatic contributions $p_{\text{soft}} \sim gT$, one receives an enhancement of $1/g$ compared to contributions from *hard* momenta, $p_{\text{hard}} \sim T$, due to the bosonic nature of the gluon. For *ultrasoft* (magnetostatic) momenta, $p_{\text{ultrasoft}} \sim g^2T$, the contributions are enhanced by $1/g^2$ compared to the naive perturbative order. As Eqs. (8)–(10) demonstrate, it is possible to generate contributions of the order $g^3 \sim \alpha_s^{3/2}$ from soft momenta and, in the case of the pressure, although perturbatively enhanced, ultrasoft momenta only start to play a role at order $g^6 \sim \alpha_s^3$.

Due to the infrared enhancement of electrostatic contributions, there is a class of diagrams called hard-thermal-loop (HTL) graphs that have soft external momenta and hard internal momenta that need to be resummed to all orders in the strong coupling (Braaten and Pisarski 1990a, b, c). There are now several schemes for carrying out such soft resummations (Arnold and Zhai 1994, 1995; Zhai and Kastening 1995; Braaten and Nieto 1995, 1996a; Kajantie et al. 1997; Andersen et al. 1999, 2000a, b; Blaizot et al. 1999a, b, 2001a, b; Andersen et al. 2002, 2004, 2010b, 2011c; Haque et al. 2014a, b). We note however, that even with such resummations, if one casts the result as a strict power series in the strong coupling constant the convergence of the perturbative series for the QCD free energy is quite poor. To address this issue, one must treat the soft sector non-perturbatively and re-sum contributions to all orders in the strong coupling constant. This can be done using effective field theory methods (Ghiglieri et al. 2020), approximately self-consistent two-particle irreducible methods (Blaizot et al. 1999a, b, 2001a, b), or the hard-thermal-loop perturbation theory reorganization of thermal field theory (Andersen et al. 1999, 2000b, 2002, 2004, 2010b, 2011c; Haque et al. 2014a, b).

Thus, the calculation of the QCD EoS requires all-orders resummation, which can be accomplished in a variety of manners. Despite the fact that different methods exist, they all rely fundamentally on the use of so-called hard-thermal- or hard-dense-loops, which self-consistently include the main physical effect of the generation of in-medium gluon and quark masses at the one-loop level. By reorganizing the perturbative calculation of the QCD EoS around the high-temperature hard-loop limit of quantum field theory, the convergence of the perturbative series can be extended to phenomenologically relevant temperatures and densities. Below we summarize the results that have been obtained and compared to lattice QCD calculations where available.

4.1 The resummed perturbative QCD EoS

The QCD EoS of deconfined quark matter at high chemical potential can be evaluated in terms of perturbative series in the running coupling constant α_s. As a result, the neutron-star EoS can be studied using the weak coupling expansion (Kurkela et al. 2014; Annala et al. 2018; Shuryak 1978; Zhai and Kastening 1995; Braaten and Nieto 1996a, b; Arnold and Zhai 1995, 1994; Toimela 1985; Kapusta 1979; Annala et al. 2020; Kurkela et al. 2014, 2010; Freedman and McLerran 1977b, c; Ecker and Rezzolla 2022a; Altiparmak et al. 2022; Ecker and Rezzolla 2022b). The EoS and trace anomaly of deconfined quark matter have been calculated to three-loop order using HTL perturbation theory framework at small μ_B and arbitrary T. Renormalization of the vacuum energy, the HTL mass parameters, and α_s eliminate all UV divergences. The three-loop results for the thermodynamic functions are observed to be in agreement with lattice QCD data for $T \gtrsim 2 - 3T_c$ after choosing a suitable mass parameter prescription (Andersen et al. 2011c). Furthermore, the QCD thermodynamic potential at nonzero temperature and

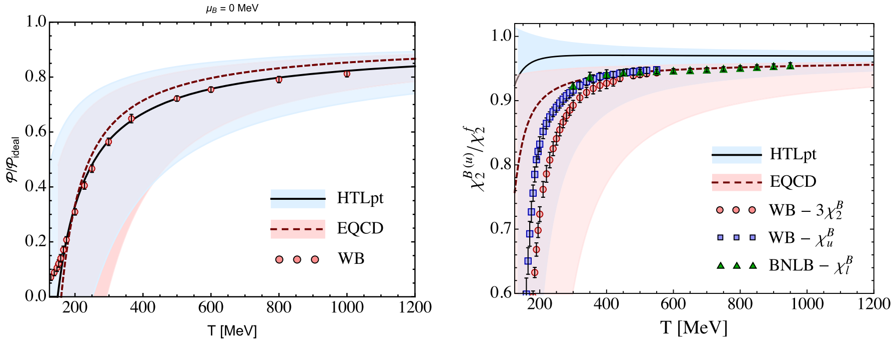

Fig. 5 Left: the resummed QCD pressure for $\mu_B = 0$ obtained using the three-loop EQCD and HTL perturbation theory results with lattice data from the Wuppertal-Budapest (WB) collaboration (Borsanyi et al. 2010). Right: the second-order light quark (and baryon) number susceptibilities. Lattice data are from the WB (Borsanyi 2013; Borsanyi et al. 2013) and BNLB collaborations (Bazavov et al. 2013a)

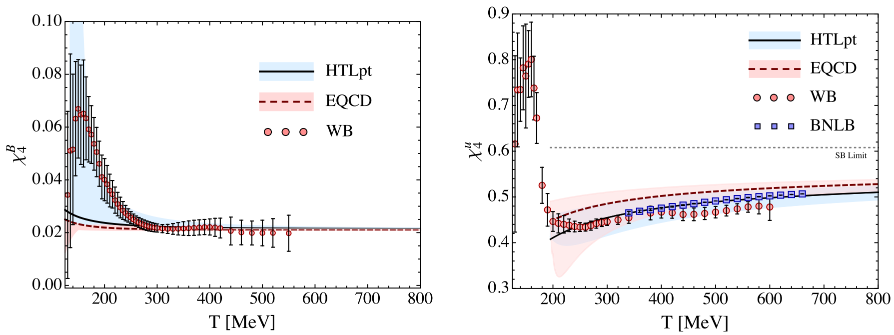

Fig. 6 Left: the 4th baryon number susceptibility. Right: the 4th light quark number susceptibility. Lattice data sources are the same as in Fig. 5

chemical potential(s) has been calculated using N2LO at three-loop HTL perturbation theory which was used further to calculate the pressure, entropy density, trace anomaly, energy density, and speed of sound, c_s, of the QGP (Haque et al. 2014b). These findings were found to be in very good agreement with the data obtained from lattice QCD using the central values of the renormalization scales. This is illustrated in Figs. 5 and 6, which present comparisons of the resummed perturbative results with lattice data for the pressure and fourth-order baryonic and light-quark susceptibilities. In these figures, HTLpt corresponds to the N2LO hard thermal loop perturbation theory calculation of the EoS and EQCD corresponds to a resummed N2LO electric QCD effective field theory calculation of the same. The shaded bands indicate the size of the uncertainty due to the choice of renormalization scale.

4.2 The curvature of the QCD phase transition line

In another study, for the second- and fourth-order curvatures of the QCD phase transition line, the N2LO HTL perturbation theory predictions were shown. In all

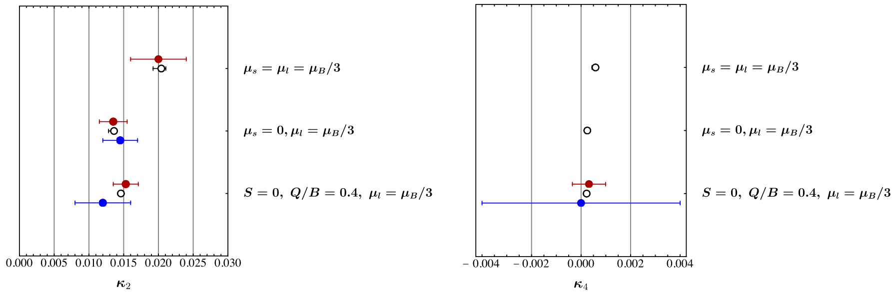

Fig. 7 Left: filled circles are lattice calculations of the quadratic curvature coefficient κ_2 (Cea et al. 2016; Bonati et al. 2015, 2018; Borsanyi et al. 2020; Bazavov et al. 2019), from top to bottom, respectively. Red-filled circles are results obtained using the imaginary chemical potential method and blue-filled circles are results obtained using Taylor expansions around $\mu_B = 0$. Black open circles are the N2LO HTL perturbation theory predictions. Right: filled circles are lattice calculations of quartic coefficient κ_4 from Borsanyi et al. (2020), Bazavov et al. (2019), from top to bottom, respectively. The error bars associated with the HTL perturbation theory predictions result from variations of the assumed renormalization scale

three situations, (i) $\mu_s = \mu_l = \mu_B/3$, (ii) $\mu_s = 0, \mu_l = \mu_B/3$, and (iii) $S = 0, Q/B = 0.4, \mu_l = \mu_B/3$, it was shown that N2LO HTL perturbation theory is compatible with the already available lattice computations of κ_2 and κ_4 as defined in Eq. (7) (Haque and Strickland 2021). This is illustrated in Fig. 7, which presents comparisons of the resummed perturbative results with lattice data for the coefficients κ_2 and κ_4.

4.3 Application at high density

Gorda et al. (2021b), at $T = 0$, calculated the N3LO contribution emerging from non-Abelian interactions among long-wavelength, dynamically screened gluonic fields using the weak-coupling expansion of the dense QCD EoS. In particular, they used the HTL effective theory to execute a comprehensive two-loop computation that is valid for long-wavelength, or soft, modes. In the plot of the EoS, unlike at high temperatures, the soft sector behaves well within cold quark matter, and the novel contribution reduces the renormalization-scale dependence of the EoS at high density (Gorda et al. 2021b). Working at exactly zero temperature is often a good approximation for fully evolved neutron stars but for the early stages of neutron-star evolution and neutron-star mergers, it is essential to incorporate temperature effects (Shen et al. 1998). However, the inclusion of finite temperature in high-μ_B quark matter gives rise to a technical difficulty for weak coupling expansions. It is no longer sufficient under this regime to handle simply the static sector of the theory nonperturbatively, but the $T = 0$ limit's accompanying technical simplifications are also unavailable. In the EoS plots (see Fig. 8), the breakdown of the weak coupling expansion is observed by a rapid increase in the uncertainty of the result with an increase in temperature for tiny values of μ_B (Kurkela and Vuorinen 2016).

The most up-to-date pQCD results at $T = 0$ and finite densities can be found in Gorda et al. (2021a). The EoS derived in these calculations was applicable starting at $n_B \sim 40\ n_{\rm sat}$ and above. However, there is an overall renormalization scale parameter,

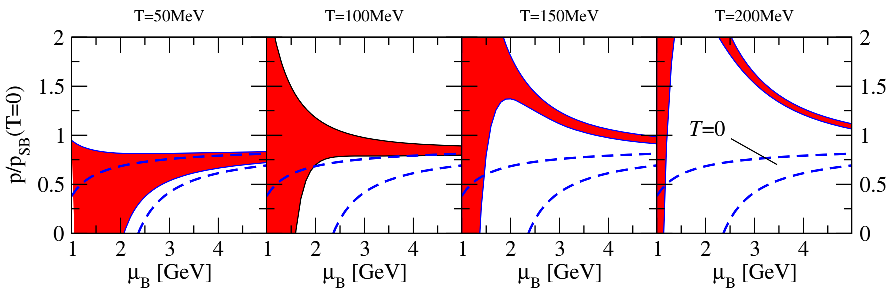

Fig. 8 EoS of deconfined quark matter as a function of μ_B at four different temperatures. The new result is shown by the red bands, with the widths resulting from a change in the renormalization scale $\tilde{\Lambda}$ (Kurkela and Vuorinen 2016). The corresponding $\mathcal{O}(g^4)$ result at absolute zero is shown by the dashed blue lines (Freedman and McLerran 1977c; Baluni 1978; Vuorinen 2003). Image reproduced with permission from Kurkela and Vuorinen (2016), copyright by the author(s)

X, that is unknown. One can extrapolate down to lower densities assuming that the speed of sound squared should be bounded by causality and stability, i.e., $0 \le c_s^2 \le 1$. The results were shown in Komoltsev and Kurkela (2022) where they varied X in the range $1 \le X \le 4$. The results of the constrained regime can be seen in Fig. 9. Various groups have then used these constraints in their neutron star EoS analyses (Marczenko et al. 2023; Somasundaram et al. 2023).

4.4 Transport coefficients at finite T and μ_B

The quark-gluon plasma probed in heavy-ion collisions is not in equilibrium and viscous effects from shear and bulk viscosities are important for the evolution of the system. At the moment it is not yet possible to reliably compute the shear and bulk viscosities using first principle calculations (Meyer 2011). However, it is possible to perform calculations of these coefficients in the weak-coupling limit of QCD. The shear viscosity η and relaxation time τ_π (the timescale within which the system

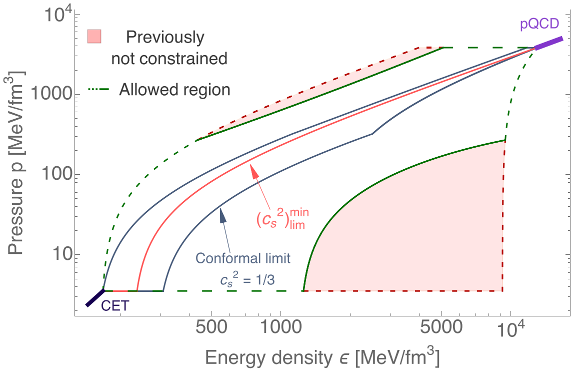

Fig. 9 The extracted EoS constraints from pQCD and χEFT(CET in the figure) as a function of energy density are shown (see Sect. 5 for details). The excluded regions are in pink. Image reproduced with permission from Komoltsev and Kurkela (2022), copyright by APS

relaxes towards its Navier–Stokes regime, Denicol and Rischke 2021) are usually related through

$$\tau_\pi = C \frac{\eta}{\varepsilon + p} \tag{11}$$

where C is a constant determined by the theory. Calculations of η/s in QCD have been completed up to NLO (next-to leading order, Ghiglieri et al. 2018a) and the constant C of the relaxation time at NLO (Ghiglieri et al. 2018b) for $\mu_B = 0$, as shown in Fig. 10.

Recently, the first calculations of shear viscosity at leading-log at finite μ_B were performed in QCD in Danhoni and Moore (2023), as shown in Fig. 11.

Note, however, that at finite μ_B the most natural dimensionless quantity involves the enthalpy ($w = \varepsilon + p$), such that $\eta T/w$ is the relevant quantity (the factor of T is to ensure that it remains dimensionless) to be used (Liao and Koch 2010). In the limit of vanishing baryon chemical potential, then

$$\lim_{\mu_B \to 0} \frac{\eta T}{\varepsilon + p} = \frac{\eta}{s} \tag{12}$$

such that these results should be smoothly connected regardless of μ_B. The relaxation time has not yet been calculated in QCD at finite μ_B. Finally we note that, in typical relativistic viscous hydrodynamics simulations performed in heavy-ion collisions, a number of other transport coefficients are also needed. For example, using perturbative QCD, the bulk viscosity has been computed in Arnold et al. (2006), conductivity and diffusion in Arnold et al. (2000), and some second-order transport coefficients can be found in York and Moore (2009). In practice, these perturbatively-

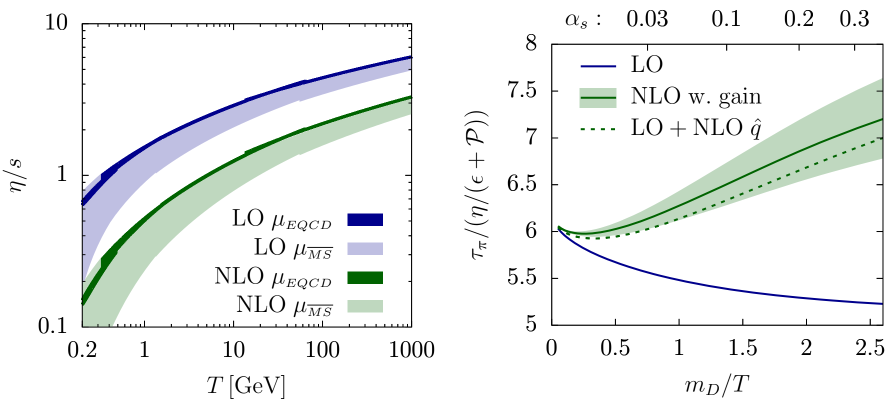

Fig. 10 Left: shear viscosity to entropy density ratio versus temperature derived from pQCD at LO (leading order) and NLO (next-to leading order) for two different choices of the running coupling for 3 flavors. Right: coefficient of the relaxation time for shear viscosity at leading order and next-to-leading order as a function of the Debye mass over temperature for QCD with 3 light flavors. Images reproduced with permission from [left] Ghiglieri et al. (2018a) and from [right] Ghiglieri et al. (2018b), copyright by the author(s)

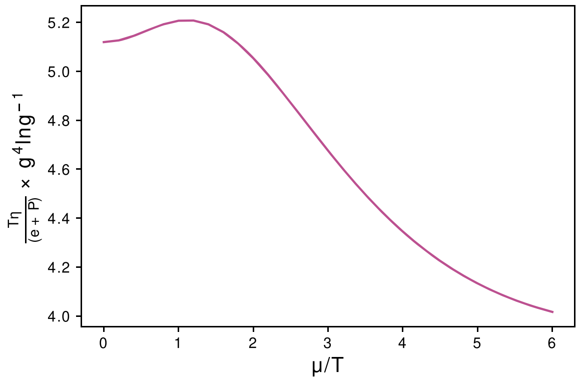

Fig. 11 Shear viscosity times temperature divided by the enthalpy versus chemical potential over temperature in 3 flavor QCD. Image reproduced with permission from Danhoni and Moore (2023), copyright by the author(s)

determined expressions are not the ones used in simulations, which often rely on simple formulas involving the transport coefficients determined from, for instance, kinetic theory models (Denicol et al. 2012, 2014) or holography (Kovtun et al. 2005; Finazzo et al. 2015; Rougemont et al. 2017; Grefa et al. 2022), see Everett et al. (2021).

5 Theoretical constraints: chiral effective field theory

In the opposite regime of low density and temperature, Chiral Effective Field Theory (χEFT) is used to calculate the EoS relevant around $n_B \sim n_{\rm sat}$ of neutron stars. For ab initio χEFT calculations, it is possible to study the EoS at arbitrary isospin asymmetry at both zero and nonzero temperature within a many-body perturbation theory (Drischler et al. 2014; Wellenhofer et al. 2016; Wen and Holt 2021; Somasundaram et al. 2021), or a many-body Brueckner–Hartree–Fock approach (Logoteta et al. 2016b, a). Recently, several benchmark calculations have been performed, considering the first and second generation of χEFT Norfolk NN and 3N interactions, to assess the possible error which is associated with the chosen method when solving the many-body Schrödinger equation (Piarulli et al. 2020; Lovato et al. 2022a). The authors have obtained a good agreement among the many-body techniques tested up to approximately the nuclear saturation density.

However, in practice it is convenient to first compute the EoS for symmetric nuclear matter ($Y_Q = 0.5$) and pure neutron matter ($Y_Q = 0$) and then interpolate between the two using the quadratic approximation for the isospin-asymmetry dependence of the EoS. From the density-dependent symmetry energy, one can extract the coefficients $E_{\rm sym}$, L, $K_{\rm sym}$ from χEFT calculations

$$E_{\rm NS} = E_{Y_Q=0.5} + N_B\left[E_{\rm sym,sat} + \frac{L_{\rm sat}}{3}\left(\frac{n_B}{n_{\rm sat}} - 1\right) + \frac{K_{\rm sym,sat}}{18}\left(\frac{n_B}{n_{\rm sat}} - 1\right)^2\right](1 - 2Y_Q)^2, \tag{13}$$

where $E_{\rm NS}$ is the ground-state energy at a given density and isospin asymmetry,

$E_{Y_Q=0.5}$ is the total energy for isospin-symmetric nuclear matter, $E_{\mathrm{sym,sat}} = \left(\frac{E_{Y_Q=0}-E_{Y_Q=0.5}}{N_B}\right)_{n_{\mathrm{sat}}}$ is the symmetry energy at saturation, $L_{\mathrm{sat}} = 3n_{\mathrm{sat}}\left(\frac{dE_{\mathrm{sym}}}{dn_B}\right)_{n_{\mathrm{sat}}}$ is the slope of the symmetry energy at saturation, and $K_{\mathrm{sym,sat}} = 9n_{\mathrm{sat}}^2\left(\frac{d^2E_{\mathrm{sym}}}{dn_B^2}\right)_{n_{\mathrm{sat}}}$ is the symmetry energy curvature at saturation. Using this expansion scheme, it is possible to obtain the neutron star outer core EoS with quantified uncertainties from χEFT. The properties of the low-density crust (Lim and Holt 2017; Grams et al. 2022) and the high-density inner core (Hebeler et al. 2010; Tews et al. 2018; Lim et al. 2021; Drischler et al. 2021a; Brandes et al. 2023) require additional modeling assumptions.

The energy per baryon of symmetric nuclear matter, $E_{Y_Q=0.5}/N_B$, and pure neutron matter, $E_{Y_Q=0}/N_B$, has been computed from χEFT at different orders in the chiral expansion and different approximations in many-body perturbation theory. As a representative example, in Holt and Kaiser (2017) the EoS was computed up to third order in many-body perturbation theory, including self-consistent second-order single-particle energies. Chiral nucleon–nucleon interactions were included up to N3LO, while three-body forces were included up to N2LO in the chiral expansion. Using the above approach, the authors gave error bands on the EoS (including $E_{\mathrm{sym,sat}}$ and slope parameter L_{sat}), taking into account uncertainties from the truncation of the chiral expansion and the choice of resolution scale in the nuclear interaction. The incorporation of third-order particle-hole ring diagrams (frequently overlooked in EoS computations) helped to reduce theoretical uncertainties in the neutron matter EoS at low densities, but beyond $n_B \gtrsim 2n_{\mathrm{sat}}$ the EoS error bars become large due to the breakdown in the chiral expansion. Recent advances in automated diagram and code generation have enabled studies at even higher orders in the many-body perturbation theory expansion (Drischler et al. 2021c, 2019). In the following we focus on selected results obtained in many-body perturbation theory and refer the reader to Lynn et al. (2019), Carlson et al. (2015), Gandolfi et al. (2020), Tews (2020), Rios (2020), Hagen et al. (2014) for comprehensive review articles on many-body calculations in the frameworks of quantum Monte Carlo, self-consistent Green’s functions method, and coupled cluster theory.

The left panel of Fig. 12 shows the correlation between the symmetry energy E_{sym} and slope parameter L at saturation for different choices of the high-momentum regulating scale (shown as different data points) and order in the chiral expansion (denoted by different colors) all calculated at 3rd order in many-body perturbation theory including self-consistent (SC) nucleon self-energies at second order (Holt and Kaiser 2017). The ellipses show the 95% confidence level at orders NLO, N2LO, and the N3LO* (where the star denotes that the three-body force is included only at N2LO) (Holt and Kaiser 2017). Interestingly, one finds that even EoS calculations performed at low order in the chiral expansion produce values of E_{sym} and L at saturation that tend to lie on a well-defined correlation line. The N3LO* (red) ellipse illustrates the range of symmetry energy $28\,\mathrm{MeV} < E_{\mathrm{sym,sat}} < 35\,\mathrm{MeV}$ and slope parameter $20\,\mathrm{MeV} < L_{\mathrm{sat}} < 65\,\mathrm{MeV}$, both of which are quite close to the findings of prior microscopic computations (Hebeler et al. 2010; Gandolfi et al. 2012) that also used neutron matter calculations plus the empirical saturation properties of

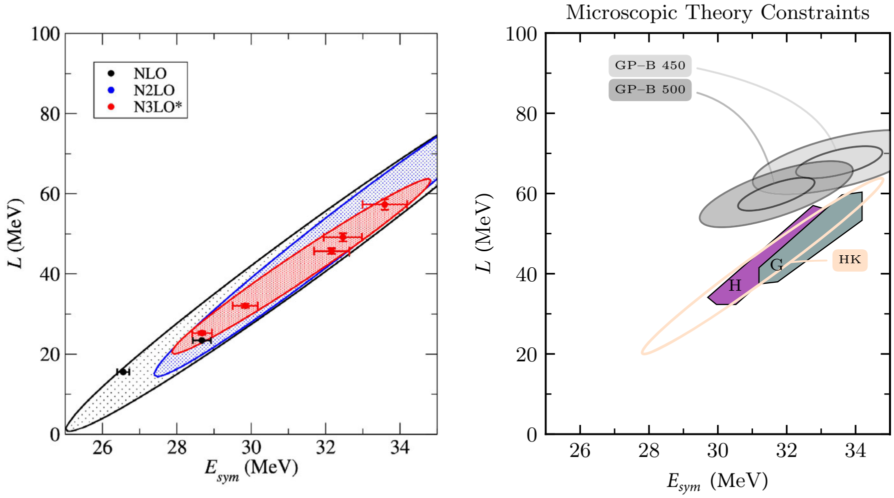

Fig. 12 Adapted from Holt and Kaiser (2017), Drischler et al. (2021c). Left: correlation between the symmetry energy E_{sym} and its slope, L at saturation, from χEFT calculations at different orders in the chiral expansion (Holt and Kaiser 2017). Right: microscopic constraints on the $E_{\mathrm{sym}} - L$ correlation from Hebeler et al. (2010), Gandolfi et al. (2012), Holt and Kaiser (2017), Drischler et al. (2020)

symmetric nuclear matter to deduce E_{sym} and L. All three sets of results are shown in the right panel of Fig. 12 and labeled 'H' (Hebeler et al. 2010), 'G' (Gandolfi et al. 2012), and 'HK' (Holt and Kaiser 2017) respectively. In contrast, a recent work (Drischler et al. 2020) that analyzed correlated χEFT truncation errors in the EoS for neutron matter and symmetric nuclear matter using Bayesian statistical methods found $E_{\mathrm{sym}} = 31.7 \pm 1.1$ MeV and $L = 59.8 \pm 4.1$ MeV at saturation, shown as 'GP-B 500' in the right panel of Fig. 12. The obtained value of E_{sym} was similar to those from Gandolfi et al. (2012), Hebeler et al. (2010), Holt and Kaiser (2017), but L was systematically larger. The results, however, are in good agreement with standard empirical constraints (Drischler et al. 2020; Li et al. 2019) discussed in Sect. 7.2.1.

Chiral effective field theory has also been employed to study the liquid–gas phase transition and thermodynamic EoS at low temperatures ($T < 25$ MeV) in isospin-symmetric nuclear matter (Wellenhofer et al. 2014). The EoS has been computed using χEFT nuclear potentials at resolution scales of 414, 450, and 500 MeV. The results from

Table 3 The N3LO contributions for binding energy per nucleon at saturation, saturation density, compressibility at saturation, and liquid–gas phase-transition critical values of temperature, density, and pressure at different resolution scales. Table adapted from Wellenhofer et al. (2014)

Resolution scale	$\frac{B}{A}$ (MeV)	$n_{\mathrm{sat}}(\mathrm{fm}^{-3})$	K(MeV)	T_c(MeV)	$n_c(\mathrm{fm}^{-3})$	$P_c(\mathrm{MeV/fm}^3)$
414 (M^*/M)	−15.79	0.171	223	17.4	0.066	0.33
450 (M^*/M)	−15.50	0.161	244	17.2	0.064	0.32
500 (no M^*/M)	−16.51	0.174	250	19.1	0.072	0.42

this study are tabulated in Table 3. In particular, the values of the liquid–gas critical endpoint in temperature, pressure, and density agree well with the empirical multifragmentation and compound nuclear decay experiments discussed in Sect. 7.3. In addition, at low densities and moderate temperatures, the pure neutron matter EoS is well described within the virial expansion in terms of neutron-neutron scattering phase shifts. The results from chiral effective field theory have been shown (Wellenhofer et al. 2015) to be in very good agreement with the model-independent virial EoS. Since finite-temperature effects are difficult to reliably extract empirically, chiral effective field theory calculations have been used to constrain the temperature dependence of the dense-matter EoS in recent tabulations Du et al. (2019, 2022) for astrophysical simulations.

6 Experimental constraints: heavy-ion collisions

Given that hot and dense matter can be created experimentally in heavy-ion collisions, constraints on its EoS can be extracted via experimental measurements obtained from such collisions. As explained previously in Sect. 2.5, we will especially focus in this paper on the data themselves, and avoid citing quantities inferred from the data, as the latter come with an associated model dependence. We will mention particle production yields and their ratios, as well as fluctuation observables of particle multiplicities. Then, we will review experimental results on flow harmonics, to end with Hanbury–Brown–Twiss (HBT) interferometry measurements, also referred to in the field as femtoscopy.

We remind the reader that, as a general rule of thumb, high center of mass energy collisions, $\sqrt{s_{NN}} \gtrsim 200$ GeV, are in the regime of the phase diagram where $\mu_B \ll T$, such that the numbers of particles and anti-particles are approximately equal (i.e., $n_B \sim 0$). As one lowers $\sqrt{s_{NN}}$, baryons are stopped within the collision such that higher n_B is reached. At sufficiently low beam energies, $\sqrt{s_{NN}} \lesssim 4-7$ GeV,[5] matter is dominated by the hadron gas phase, such that lowering $\sqrt{s_{NN}}$ leads to lower temperatures and lower n_B.

6.1 Particle yields

Particle production spectra are part of the simplest experimental observables used in heavy-ion collisions, to access thermodynamic properties and characteristics of the hot and dense matter. Starting with the integrated production yields of identified hadrons, they can be measured to help determine properties from the evolution of the system, in particular at chemical and kinetic freeze-out. These steps designate the ending of inelastic collisions between formed hadrons (what fixes the chemistry of the system) and in turn the ceasing of all elastic collisions (after which particles stream freely to the detectors) in the evolution of a heavy-ion collision. Statistical hadronization models (Hagedorn 1965; Dashen et al. 1969; Becattini and Passaleva 2002; Wheaton et al. 2011; Petran et al. 2014; Andronic et al. 2018, 2019; Vovchenko and Stoecker 2019) are fitted to these yields and ratios by varying over T

[5] Note that the exact beam energy where this occurs is still under debate.

and μ_B, in order to extract the respective chemical freeze-out values. Despite their ability to reproduce particle yields successfully, those models are limited in scope since they do not reproduce the dynamics of a collision and hinge on the assumption of thermal equilibrium, which is not necessarily achieved within the short time scales of heavy-ion collisions. Similar information can also be inferred for kinetic freeze-out, using a so-called blast-wave model (Schnedermann et al. 1993). The data from low transverse momentum particles (i.e., $p_T \lesssim 2-3$ GeV/c) measured at mid-rapidity (approximately transverse to the beam line direction) is used for statistical hadronization fits, because these particles spend the longest time within the medium (so they are more likely to be thermalized) and they have low enough momentum to avoid contributions from jet physics.

Measurement of yields for the most common light hadron species (namely $\pi^{\pm}$, $K^{\pm}$, $p/\overline{p}$) and strange hadrons ($\Lambda/\overline{\Lambda}$, $\Xi^-/\overline{\Xi}^+$ and $\Omega^-/\overline{\Omega}^+$) was achieved by STAR at RHIC and ALICE at the LHC. As part of the BES program, STAR has measured these hadron yields in Au+Au collisions at center-of-mass energies of $\sqrt{s_{NN}}$ =7.7, 11.5, 14.5, 19.6, 27, 39, 62.4 and 200 GeV (Abelev et al. 2009; Adamczyk et al. 2017; Adam et al. 2020b, d) and in U+U collisions at $\sqrt{s_{NN}} = 193$ GeV (Abdallah et al. 2023d). Motivated by results from the past SPS-experiment NA49 obtained from Pb+Pb collisions at $\sqrt{s_{NN}} < 20$ GeV (Alt et al. 2008), the NA61/SHINE experiment at CERN has conducted a scan in system-size and energy (in the same energy range as NA49). The diagram of all collided systems as a function of collision energy and nuclei is displayed in the left panel of Fig. 13. They published data for light hadrons in Ar+Sc (Acharya et al. 2021b) and Be+Be collisions (Acharya et al. 2021a) so far, while results from Xe+La and Pb+Pb collisions should become available in the next few years (Kowalski 2022). At LHC energies, the higher $\sqrt{s_{NN}}$ produces significantly more particles, allowing more precise measurements of the species. For this reason, the ALICE experiment has measured yields not only for light and (multi)strange hadrons, but also for light nuclei and hyper-nuclei, in Pb+Pb collisions at 2.76 TeV/A in particular (Abelev et al. 2013a, c, 2014a; Adam et al. 2016f; Acharya et al. 2018e; Adam et al. 2016a), and more recently in Pb+Pb collisions at 5.02 TeV/A too (Acharya et al. 2020c, 2023c), as well as Xe+Xe collisions at 5.44 TeV/A (Acharya et al. 2021e).

The yields of particle production can also be used as an indicator of the onset of deconfinement, notably thanks to the strangeness enhancement: strange quark-antiquark pairs are expected to be produced at a much higher rate in a hot and dense medium than in a hadron gas. Hence, one should expect in particular an increase of multi-strange baryons compared to light-quark-compound hadrons in collision systems where the QGP has been formed, which has been observed experimentally in heavy-ion collisions at several energies (Antinori et al. 2006; Abelev et al. 2008b, 2014a). Moreover, the distinctive non-monotonic behavior of the K^+/π^+ ratio as a function of the collision energy can also be considered as a sign of the onset of deconfinement, according to some authors (Gazdzicki and Gorenstein 1999; Poberezhnyuk et al. 2015). This so-called "horn" in the K^+/π^+ ratio has been notably observed in Pb+Pb (Afanasiev et al. 2002; Alt et al. 2008) and Au+Au collisions (Akiba et al. 1996; Ahle et al. 2000; Abelev et al. 2009, 2010b; Adamczyk

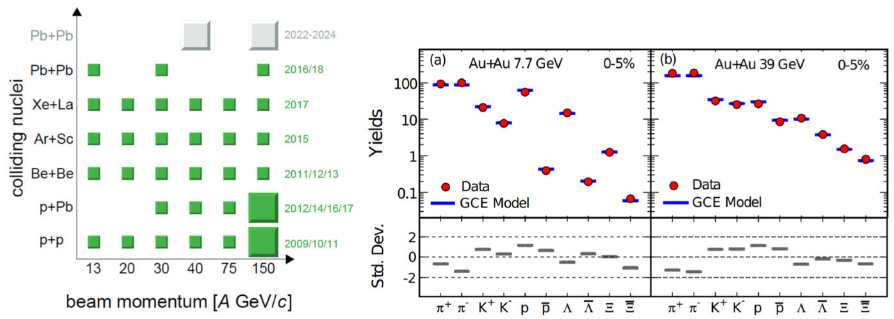

Fig. 13 Left: diagram of different collided systems as a function of collision energy. Right: yields of hadrons measured by STAR in central Au+Au collisions at 7.7 and 39 GeV/A, compared with results from a grand canonical statistical hadronization model. Images reproduced with permission from [left] Kowalski (2022), copyright by the author(s), and [right] Adamczyk et al. (2017), copyright by APS

et al. 2017), but absent from p+p data (Aduszkiewicz et al. 2017; Abelev et al. 2010b; Aamodt et al. 2011c; Abelev et al. 2014c) and Be+Be collisions results (Acharya et al. 2021a). Recent results from Ar+Sc collisions (Kowalski 2022) have, however, stirred up doubts regarding the interpretation of this observable, as the value of this ratio from such collision system is closer to the one measured in big systems, while no horn structure is seen, similar to small systems. All these results for different systems can be seen in Fig. 14.

6.2 Fluctuation observables

In heavy-ion collisions, observables measuring fluctuations are among the most relevant for the investigation of the QCD phase diagram. Within the assumption of thermodynamic equilibrium, cumulants of net-particle multiplicity distributions become directly related to thermodynamic susceptibilities, and can be compared to results from lattice QCD (see Sect. 3.2) to extract information on the chemical freeze-out line (Alba et al. 2014, 2015, 2020). Moreover, large, relatively long-range fluctuations are expected in the neighborhood of the conjectured QCD critical point, making fluctuation observables very promising signatures of criticality (Stephanov et al. 1999; Stephanov 2009; Athanasiou et al. 2010). It has also been proposed that the finite-size scaling of critical fluctuations could be employed to constrain the location of the critical point (Palhares et al. 2011; Fraga et al. 2010; Lacey 2015; Lacey et al. 2016). In Fraga et al. (2010), finite-size scaling arguments were applied to mean transverse-momentum fluctuations measured by STAR (Adams et al. 2005c, 2007) to exclude a critical point below $\mu_B \lesssim 450$ MeV.

Fluctuations of the conserved charges B, S, and Q are of particular importance. As mentioned already in Sect. 3.2, these fluctuations can be used to probe the deconfinement transition, as well as the location of the critical endpoint. Calculated via the susceptibilities expressed in Eq. (3), which can be evaluated via lattice QCD

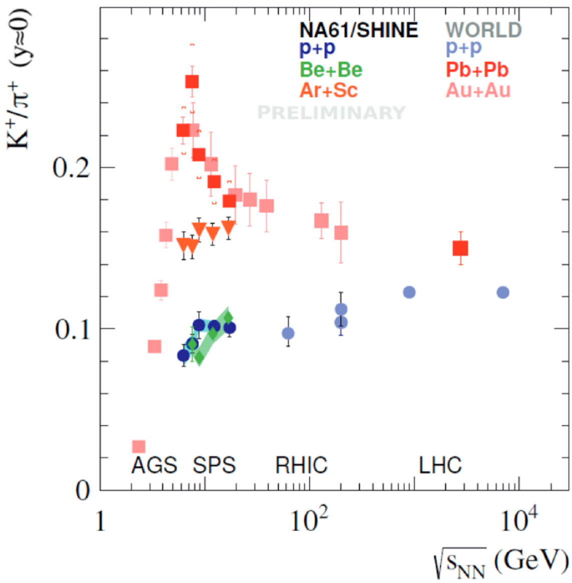

Fig. 14 Preliminary results for the ratio of K^+/π^+ yields at mid-rapidity as a function of the collision energy, compared for different collision systems. Image reproduced with permission from Kowalski (2022), copyright by the author (s)

simulations or HRG model calculations, they can also be related to the corresponding cumulants of conserved charges C^{BSQ}_{lmn},[6] following the relation

$$C^{BSQ}_{lmn} = VT^3 \times \chi^{BSQ}_{lmn} \tag{14}$$

with the volume V and temperature T of the system, and $l, m, n \in \mathbb{N}$ (Luo and Xu 2017). The cumulants are also theoretically related to the correlation length of the system ξ, which is expected to diverge in the vicinity of the critical endpoint. In particular, the higher order cumulants are proportional to higher powers of ξ, making them more sensitive to critical fluctuations (Stephanov et al. 1999; Stephanov 2009; Athanasiou et al. 2010).

In heavy-ion collisions, however, it is impossible to measure the fluctuations of conserved charges directly, because one cannot detect all produced particles (e.g., neutral particles are not always possible to measure, so that baryon number fluctuations do not include neutrons). Nevertheless, it is common to measure the cumulants of identified particles' net-multiplicity distributions, using some hadronic species as proxies for conserved charges (Koch et al. 2005). Net-proton distributions are used as a proxy for net-baryons (Aggarwal et al. 2010; Adam et al. 2019b; Abdallah et al. 2021b), net-kaons (Adamczyk et al. 2018c; Ohlson 2018; Adam et al. 2019c) or net-lambdas (Adam et al. 2020a) are used as a proxy for net-strangeness, and net-pions+protons+kaons (Adam et al. 2019c) has been recently used as a proxy for net-electric charge, instead of the actual net-charged unidentified hadron distributions. Mixed correlations have also been measured (Adam et al. 2019c),

[6] Note that such cumulants are often referred to as κ^{BSQ}_{lmn} in the literature; we used a different symbol here to avoid confusion with the κ coefficients of the pseudo-transition temperature parametrisation from lattice QCD in Sect. 3.4.

although alternative ones have been suggested, that would provide more direct comparisons to lattice QCD susceptibilities (Bellwied et al. 2020).

These net-particle cumulants can be used to construct ratios, as they are connected with usual statistic quantities characterizing the net-hadron distributions $N_\alpha = n_\alpha - n_{\bar{\alpha}}$ (with $n_{\alpha/\bar{\alpha}}$ being respectively the number of hadrons or anti-hadrons of hadronic specie α). Hence, relations between such ratios and the mean μ_α, variance σ_α, skewness S_α or kurtosis κ_α can be expressed as follows

$$\frac{\sigma_\alpha^2}{\mu_\alpha} = \frac{C_2^\alpha}{C_1^\alpha} = \frac{\langle(\delta N_\alpha)^2\rangle}{\langle N_\alpha\rangle} , \tag{15}$$

$$S_\alpha \sigma_\alpha = \frac{C_3^\alpha}{C_2^\alpha} = \frac{\langle(\delta N_\alpha)^3\rangle}{\langle(\delta N_\alpha)^2\rangle} , \tag{16}$$

$$\kappa_\alpha \sigma_\alpha^2 = \frac{C_4^\alpha}{C_2^\alpha} = \frac{\langle(\delta N_\alpha)^4\rangle}{\langle(\delta N_\alpha)^2\rangle} - 3\langle(\delta N_\alpha)^2\rangle , \tag{17}$$

$$\frac{\kappa_\alpha \sigma_\alpha}{S_\alpha} = \frac{C_4^\alpha}{C_3^\alpha} = \frac{\langle(\delta N_\alpha)^4\rangle - 3\langle(\delta N_\alpha)^2\rangle^2}{\langle(\delta N_\alpha)^3\rangle} , \tag{18}$$

with $\delta N_\alpha = N_\alpha - \langle N_\alpha\rangle$, and $\langle\,\rangle$ denoting an average over the number of events in a fixed centrality class at a specific beam energy (Luo and Xu 2017). These ratios allow for more direct comparisons to theoretical calculations of susceptibilities because the leading order dependence on volume and temperature cancels out (see Eq. (14)).

While direct comparisons between theoretically calculated susceptibilities and multi-particle cumulants have been made, certain caveats exist. First of all, these comparisons are only valid if the chosen particle species are good proxies for their respective conserved charge (see e.g. Chatterjee et al. 2016; Bellwied et al. 2020). Additionally, there are fundamental conceptual differences between the assumed in-equilibrium and infinite volume lattice QCD calculations on one side, and the highly dynamical, far-from-equilibrium, short-lived, and finite-size system created in heavy-ion collisions on the other side. While building cumulant ratios cancels the trivial dependence on volume and temperature, it does not prevent volume fluctuations that can affect the signal, especially for higher order cumulants (Gorenstein and Gazdzicki 2011; Konchakovski et al. 2009; Skokov et al. 2013; Luo and Xu 2017). Calculating the cumulants as a function of the centrality class will generally increase the signal, as the volume of systems varies within a single centrality class (Luo et al. 2013). Also known as the centrality bin-width effect, this artificial modification of the measured fluctuations can be minimized by using small centrality classes, and some correction methods (Sahoo et al. 2013; Gorenstein 2015). A second consequence is the fact that the finite size of the system limits the growth of ξ. The correlation length must be smaller than the size of the system itself and ξ is even smaller when the system is inhomogeneous (Stephanov et al. 1999). Because the system only approaches the critical point for a finite period of time, the growth of ξ would be consequently limited, restraining even more the size of measured fluctuations amplitude (Berdnikov and Rajagopal 2000; Hippert et al. 2016; Herold et al. 2016). Critical lensing effects may somewhat compensate for some of these effects by drawing more of the system towards the critical regime (Dore et al. 2022).

Finally, the width of the rapidity (angle with respect to the beam line) window in which particle cumulants are measured is important. The signal from critical fluctuations is expected to have a correlation range of $\Delta y \sim 1$, hence cumulants should be measured with particles in a rapidity of this order at least to be sensitive to criticality (Ling and Stephanov 2016). Another alternative is to use factorial cumulants $\hat{C}_n$ (also referred to as correlation functions), which can be expressed as linear combinations of cumulants C_n and are better suited for acceptance dependence studies because of their linear scaling with the rapidity acceptance (Ling and Stephanov 2016; Bzdak et al. 2017). Moreover, acceptance cuts may also affect fluctuation observables and, together with detection efficiency effects, contribute with spurious binomial fluctuations (Pruneau et al. 2002; Bzdak and Koch 2012; Garg et al. 2013; Karsch et al. 2016; Hippert and Fraga 2017). Resonance decays can also lead to spurious contributions, as has been discussed in Begun et al. (2006), Sahoo et al. (2013), Garg et al. (2013), Nahrgang et al. (2015), Bluhm et al. (2017), Mishra et al. (2016), Hippert and Fraga (2017).

6.2.1 Net-*p* fluctuations

Experimental collaborations commonly use the net-proton distribution as a proxy for the baryon number B, even though protons experience isospin randomization during the late stages of the collision (Kitazawa and Asakawa 2012b; Nahrgang et al. 2015). This process causes the original nucleon isospin distribution to be blurred and is due to the reactions $p + \pi^{0/-} \leftrightarrow \Delta^{+/0} \leftrightarrow n + \pi^{+/0}$ that nucleons undergo several times during the hadronic cascade. These reactions do not affect net-B fluctuations, but do affect net-proton fluctuations. Since protons are the only nucleons measured in the final state, isospin randomization has to be taken into account when comparing both quantities (Kitazawa and Asakawa 2012a).

The ALICE collaboration has published measurements of C_1^p and C_2^p net-proton cumulants and their ratios in Pb+Pb collisions at $\sqrt{s_{NN}} = 2.76$ TeV (Acharya et al. 2020a) and at $\sqrt{s_{NN}} = 5.02$ TeV C_3^p was also measured (Acharya et al. 2023b). As the system is created at almost vanishing baryonic chemical potential at such high energies, those cumulants can be compared to lattice QCD susceptibility results like the one discussed in Sect. 3.2, keeping in mind the subtleties of such comparison mentioned in the previous paragraph. However, no critical signal is expected in such collisions, they are mostly used to study correlation dynamics and the effect of global and local charge conservation (ALICE Collaboration 2022). Only higher-order cumulants, from C_6^p and beyond, are expected to exhibit $O(4)$ criticality (Friman et al. 2011; Almasi et al. 2019). At RHIC energies, the STAR experiment has measured net-proton (factorial) cumulants as one of the main objectives of the BES program, in Au+Au collisions from $\sqrt{s_{NN}} = 200$ GeV down to $\sqrt{s_{NN}} = 7.7$ GeV for cumulants up to C_4^p, and even down to $\sqrt{s_{NN}} = 3$ GeV for up to C_6^p (Abdallah et al. 2021b; Aboona et al. 2023b). One of the most interesting results is the energy dependence of

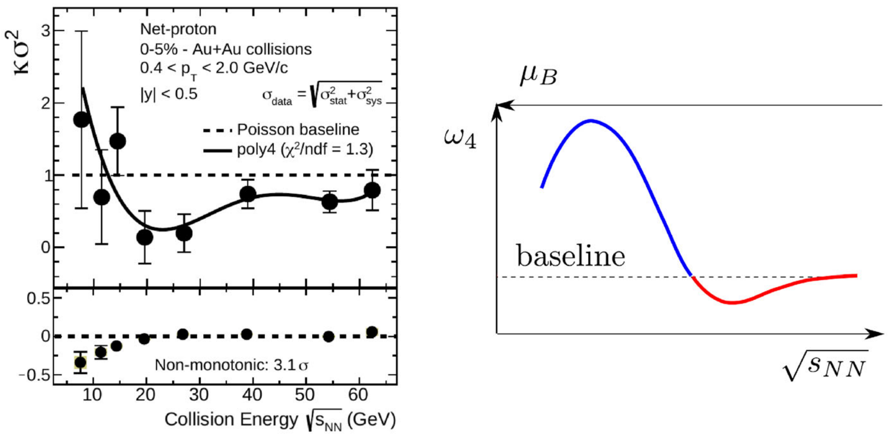

Fig. 15 Left: energy dependence of the $C_4/C_2(=\kappa\sigma^2)$ ratio from net-p distribution for $|y|<0.5$ and $0.4<p_T<2.0$ GeV/c, measured in 0–5% Au-Au collisions by the STAR collaboration. Image adapted from Abdallah et al. (2021b). Right: expected behavior of the $C_4/C_1(=\omega_4)$ ratio for net-p, in the case of a freeze-out line passing through the critical region near the critical endpoint. Image reproduced with permission from Bzdak et al. (2020), copyright by Elsevier

the C_4^p/C_2^p ratio, shown in the left panel of Fig. 15, which exhibits a non-monotonic behavior with a significance of 3.1σ towards low collision energies (Abdallah et al. 2021b). The right panel of Fig. 15 shows a theoretical calculation of one possible critical point from Stephanov (2011) using a 3D Ising model. Such non-monotonic behavior of the net-proton kurtosis, and more specifically the peak arising after the dip when going to lower energy, had been predicted as an effective sign of the existence a critical region in the phase diagram in Stephanov (2011)—later work (Mroczek et al. 2021, 2023a) has found exceptions to this using the same framework but incorporating all higher order terms, demonstrating that the peak in kurtosis is the most important signal for the critical point but the bump is not always present. Further investigations are already planned to enlighten this special result, by collecting more data in low-energy collisions and especially exploring energies below $\sqrt{s_{NN}}$ = 7.7 GeV in the BES-II program (Tlusty 2018). They will complete the results of the HADES collaboration, which published a complete analysis for net-p cumulants up to C_4^p, in Au+Au collisions at $\sqrt{s_{NN}}$ = 2.4 GeV (Adamczewski-Musch et al. 2020c).

6.2.2 Net-charged hadron fluctuations

Electric charge fluctuations are the easiest to measure experimentally, as charged particle distributions are accessible even without having to identify the detected particles. Both STAR (Adamczyk et al. 2014a) and PHENIX (Adare et al. 2016a) collaborations have published results of net-Q cumulants up to C_4^Q in Au+Au collisions from 7.7 to 200 GeV/A, shown for PHENIX in Fig. 16, with no evidence of a peak that could hint at the presence of a critical endpoint. The same net-Q cumulants have also been measured by the NA61/SHINE experiment in smaller

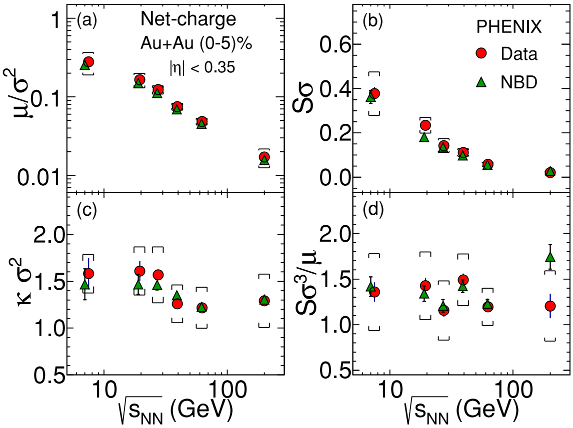

Fig. 16 Energy dependence of $\mu/\sigma^2 \sim C_1/C_2$, $S\sigma \sim C_3/C_2$, $\kappa\sigma^2 \sim C_4/C_2$ and $S\sigma^3/\mu \sim C_3/C_1$ for net-Q in central Au+Au collisions for particles with $0.3 < p_T < 2.0$ GeV and within $|\eta| < 0.35$, from the PHENIX collaboration. Data are compared with negative binomial-distribution (NBD). Image reproduced with permission from Adare et al. (2016a), copyright by APS

systems (Be+Be and Ar+Sc) for several collision energies within $5.1 \leq \sqrt{s_{NN}} \leq 17.3$ GeV, without any sign of criticality (Marcinek 2023). Combining net-p and net-Q fluctuations can be used to extract the T, μ_B at freeze-out for a specific $\sqrt{s_{NN}}$ and centrality class (normally central collisions of 0–5%). This has been done within a hadron resonance gas model where acceptance cuts and isospin randomization can be taken into account (Alba et al. 2014, 2015, 2020) but consistent results have also been found from lattice QCD susceptibilities as well (Borsanyi et al. 2014b) that cannot take those effects into account.

6.2.3 Net-K, net-Λ fluctuations

In the strangeness sector, net-kaon (specifically $K^{\pm}$) distributions are used as a proxy, since they are abundantly produced and easily reconstructed in heavy-ion collisions. Because all other strange particles carry baryon number, the resulting cumulants separated by particle species can provide varying results (Zhou et al. 2017). These cumulants have been measured extensively by the STAR experiment, again in Au+Au collisions from 7.7 to 200 GeV/A up to C_4^K (Adamczyk et al. 2018c), see Fig. 17. The ALICE collaboration has also published some preliminary results of C_1 and C_2 for net-K distributions, along with net-π and net-p results, in Pb+Pb collisions at 2.76 TeV/A (Ohlson 2018). Recently, net-Λ cumulants up to C_3^{Λ} order and their ratios have also been measured by the STAR experiment, in Au+Au collisions at $\sqrt{s_{NN}} = 19.6, 27, 39, 62.4$ and 200 GeV (Adam et al. 2020a). Note that Λ results inherently include contamination from Σ^0 baryons, which decay with a branching ratios of 100% via the channel $\Sigma^0 \rightarrow \Lambda + \gamma$ and cannot be discriminated from primary Λ production. Such results on event-by-event fluctuations of Λ baryons are important to investigate the interplay between baryon number and strangeness conservation at hadronization.

It was proposed in Bellwied et al. (2013) from lattice QCD that there may be a flavor hierarchy wherein strange particles freeze-out at a higher temperature than light particles. The idea relies on the change in the degrees of freedom in

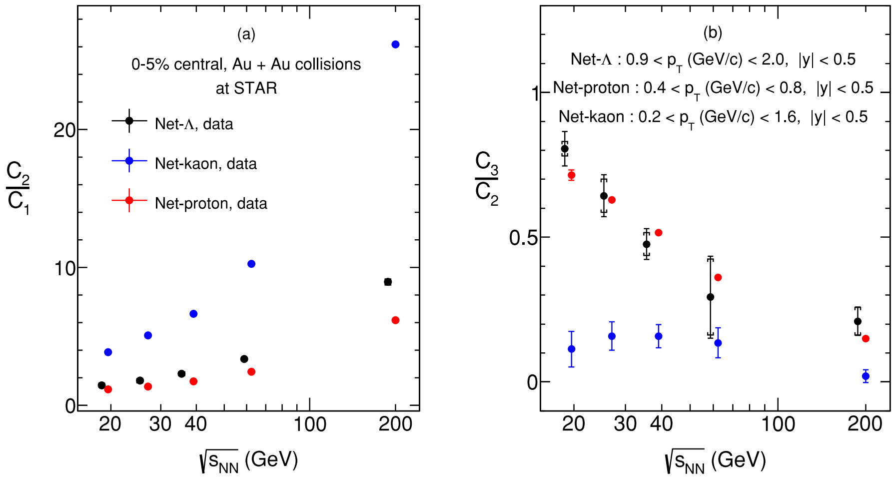

Fig. 17 Energy dependence of C_2/C_1 and C_3/C_2 for net-Λ, net-K and net-p within $|y| < 0.5$ in central Au+Au collisions, from the STAR collaboration. Image reproduced with permission from Adam et al. (2020a), copyright by APS

comparisons between various lattice susceptibilities for light and strange quarks to the hadron resonance gas model. The original lattice QCD paper suggested strange particles hadronize at $T \sim 10 - 15$ MeV higher temperatures than light particles. Using the net-K and net-Λ results, it has been shown from both a hadron resonance gas (Bellwied et al. 2019; Bluhm and Nahrgang 2019) and lattice QCD (Noronha-Hostler et al. 2016a) that a preference for a higher freeze-out temperature for strangeness is preferred (although the exact temperature is somewhat model dependent).

6.2.4 Mixed conserved charges

In addition to the so-called "diagonal" cumulants, i.e., cumulants of net-multiplicity distribution for hadronic species related to a single conserved charge, the STAR collaboration measured off-diagonal cumulants that represent correlations between different conserved charges (Koch et al. 2005; Majumder and Muller 2006). STAR extracted results for covariances, i.e. C_2 mixed-cumulants of net-Q, net-p, and net-K distributions (proxies for B and S respectively) and their ratios, from Au+Au collisions in the usual BES-I collision energy range $7.7 \leq \sqrt{s_{NN}} \leq 200$ GeV (Adam et al. 2019c). The full suite of experimental observables was $\sigma^{1,1}_{Q,p}$, $\sigma^{1,1}_{Q,K}$, $\sigma^{1,1}_{Q,K}$, $\sigma^{1,1}_{Q,p}/\sigma^2_p$, $\sigma^{1,1}_{Q,K}/\sigma^2_K$, $\sigma^{1,1}_{p,K}/\sigma^2_K$. While both $\sigma^{1,1}_{Q,p}/\sigma^2_p$ and $\sigma^{1,1}_{Q,K}/\sigma^2_K$ ratios show only a small collision energy dependence and no peculiar behavior, the $\sigma^{1,1}_{p,K}/\sigma^2_K$ ratio exhibits a global sign change around $\sqrt{s_{NN}} \sim 20$ GeV, as can be seen in Fig. 18. Even though not straightforward to interpret, this result might provide important insight into the onset of deconfinement. In Bellwied et al. (2020) it was argued that the current off-diagonal cumulants were not the best to reproduce lattice QCD due to

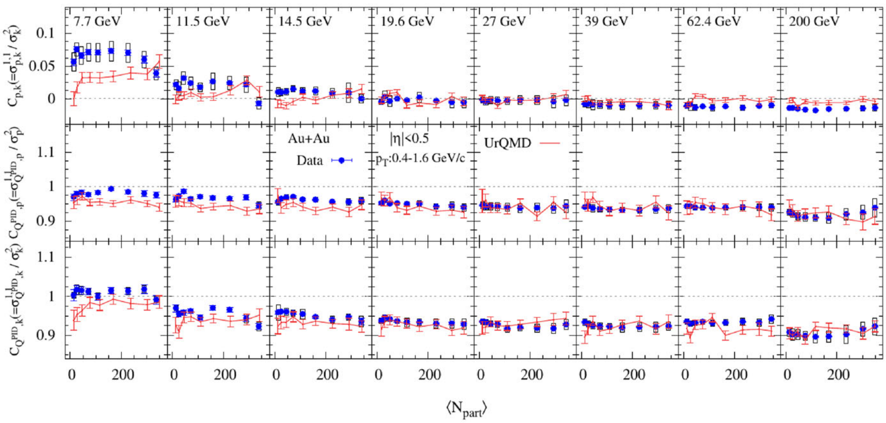

Fig. 18 From Adam et al. (2019c). Centrality dependence of covariance to variance ratios for net-Q, net-p, and net-K distributions in Au+Au collisions at different collision energies from the STAR collaboration, compared with results from ultra-relativistic quantum molecular dynamics (UrQMD) simulations

"missing" hadrons that could not be measured experimentally (e.g. neutrons). Thus, it was suggested to instead measure $\sigma^2_\Lambda/(\sigma^2_K + \sigma^2_\Lambda)$ and $\sigma^2_K/2(\sigma^2_\Lambda + \sigma^2_K)$ to assess, respectively, strange baryon correlations and strange electric charge correlations. These can be reconstructed using the data from Adam et al. (2020a, 2020d).

6.2.5 Summary of cumulant observables for conserved charge proxies

In terms of theoretical comparisons to these data points, each theoretical approach has its own caveats. In principle, lattice QCD only provides results for the infinite volume limit, it cannot account for decays, cannot account for limited particle species (i.e. effects like isospin randomization are missed), nor can it account for kinematic cuts. However, using partial pressures (Noronha-Hostler et al. 2016a) it is at least possible to capture fluctuations of certain hadronic species (i.e. kaons) more directly from lattice QCD. A hadron resonance gas approach does have the advantage of fitting lattice QCD very well at temperatures below $T \sim 150-165$ MeV (the exact temperature depends on the observable), can take into account isospin randomization and kinematic cuts, and can calculate quantities for specific particle species. However, a hadron resonance gas model is dependent on the particle list considered (incomplete particle lists can lead to misleading results) and cannot take into account dynamical effects or out-of-equilibrium effects. A third option is also often used, which are hadron transport codes like UrQMD (Bass et al. 1998; Bleicher et al. 1999) or SMASH (Weil et al. 2016; Hammelmann and Elfner 2023) that can take into account all the dynamical and out-of-equilibrium effects. However, transport models have the caveats that they cannot take into account decays and interactions of more than 2 bodies (i.e. $1 \rightarrow 3$ body decays are excluded, even though they are known to exist experimentally) and their connection to temperature is more tenuous.

In Table 4 we summarize the latest results from ALICE, STAR, HADES, and NA61/SHINE on all the cumulants for net-proton, net-charge, and net-strangeness.

Table 4 Summary of cumulant ratios of different particle species for which measurements have been published by experiments across several collision energies ($\sqrt{s_{NN}}$) and systems

Ratio	System	Experiment	$\sqrt{s_{NN}}$
C_2^p/C_1^p	Au+Au	HADES (Adamczewski-Musch et al. 2020c)	2.4 GeV
		STAR (Abdallah et al. 2021b)	7.7, 11.5, 14.5, 19.6, 27, 39, 54.4, 62.4, 200 GeV
$C_2^p/\langle p+\bar{p}\rangle$	Pb+Pb	ALICE (Acharya et al. 2020a, 2023b)	2.76, 5.02 TeV
C_3^p/C_1^p	Au+Au	PHENIX (Adare et al. 2016a)	7.7, 19.6, 27, 39, 62.4, 200 GeV
C_3^p/C_2^p	Au+Au	HADES (Adamczewski-Musch et al. 2020c)	2.4 GeV
		STAR (Abdallah et al. 2021b)	7.7, 11.5, 14.5, 19.6, 27, 39, 54.4, 62.4, 200 GeV
C_4^p/C_2^p	Au+Au	HADES (Adamczewski-Musch et al. 2020c)	2.4 GeV
		STAR (Aboona et al. 2023b; Abdallah et al. 2021b)	3, 7.7, 11.5, 14.5, 19.6, 27, 39, 54.4, 62.4, 200 GeV
C_5^p/C_1^p	Au+Au	STAR (Aboona et al. 2023b)	3, 7.7, 11.5, 14.5, 19.6, 27, 39, 54.4, 62.4, 200 GeV
C_6^p/C_2^p	Au+Au	STAR (Aboona et al. 2023b)	3, 7.7, 11.5, 14.5, 19.6, 27, 39, 54.4, 62.4, 200 GeV
C_2^Q/C_1^Q	Au+Au	PHENIX (Adare et al. 2016a)	7.7, 19.6, 27, 39, 62.4, 200 GeV
	Au+Au	STAR (Adamczyk et al. 2014a)	7.7, 11.5, 19.6, 27, 39, 62.4, 200 GeV
C_3^Q/C_1^Q	Au+Au	PHENIX (Adare et al. 2016a)	7.7, 19.6, 27, 39, 62.4, 200 GeV
C_3^Q/C_2^Q	Au+Au	PHENIX (Adare et al. 2016a)	7.7, 19.6, 27, 39, 62.4, 200 GeV
		STAR (Adamczyk et al. 2014a)	7.7, 11.5, 19.6, 27, 39, 62.4, 200 GeV
C_4^Q/C_2^Q	Au+Au	PHENIX (Adare et al. 2016a)	7.7, 19.6, 27, 39, 62.4, 200 GeV
		STAR (Adamczyk et al. 2014a)	7.7, 11.5, 19.6, 27, 39, 62.4, 200 GeV
C_2^K/C_1^K		STAR (Adamczyk et al. 2018c)	7.7, 11.5, 14.5, 19.6, 27, 39, 62.4, 200 GeV
C_3^K/C_2^K		STAR (Adamczyk et al. 2018c)	7.7, 11.5, 14.5, 19.6, 27, 39, 62.4, 200 GeV
C_4^K/C_2^K		STAR (Adamczyk et al. 2018c)	7.7, 11.5, 14.5, 19.6, 27, 39, 62.4, 200 GeV
C_2^Λ/C_1^Λ		STAR (Adam et al. 2020a)	19.6, 27, 39, 62.4, 200 GeV
C_3^Λ/C_2^Λ		STAR (Adam et al. 2020a)	19.6, 27, 39, 62.4, 200 GeV

We note that new results are anticipated later this year from STAR's Beam Energy Scan II program that will significantly reduce the error bars from BES I and also provide new beam energies in the fixed target regime i.e. between $\sqrt{s_{NN}} = 3 - 7.7$ GeV.

6.2.6 Other types of fluctuations

Other observables used to study two-particle correlations are the dynamical fluctuations, $\nu_{\rm dyn}$, which can be used in the case of incomplete particle detection, even though $\nu_{\rm dyn}$ intrinsically depends on multiplicity (Gavin and Kapusta 2002; Pruneau et al. 2002). Two-species correlations between proton, kaon, and pion distributions have been investigated by the NA49, STAR, and ALICE collaborations, in very central Pb+Pb and Au+Au collisions for $6.3 \leq \sqrt{s_{NN}} \leq 17.3$ GeV, $7.7 \leq \sqrt{s_{NN}} \leq 200$ GeV and $\sqrt{s_{NN}} = 2.76$ TeV, respectively (Anticic et al. 2014; Abdelwahab et al. 2015; Acharya et al. 2019d). The energy dependence of $\nu_{\rm dyn}[\pi, K]$ and $\nu_{\rm dyn}[p, K]$ from NA49 data, in particular, displays a strong variation below center-of-mass energy $\sqrt{s_{NN}} \sim 10$ GeV, as can be seen in Fig. 19. This could indicate a change in the production mechanism of such particles, hinting at differences in the phases probed in these collisions (Acharya et al. 2019d). The ALICE collaboration recently presented preliminary results on the system-size dependence of $\nu_{\rm dyn}[+,-]$ normalized by charged particle density to remove its intrinsic multiplicity dependence. The data collected from p+p, p+Pb, and Pb+Pb collisions at $\sqrt{s_{NN}} = 5.02$ TeV, and Xe+Xe collisions at $\sqrt{s_{NN}} = 5.44$ TeV display a decreasing trend with the size of collided systems that no model has been able to completely reproduce (Sputowska 2022).

Intensive and strongly intensive quantities can be used to investigate hadron number fluctuations, getting rid of the volume dependence and volume fluctuations, as proposed in Gorenstein and Gazdzicki (2011). Some of the results introduced earlier, like the scaled cumulants published by ALICE in Acharya et al. (2023b), STAR in Abdallah et al. (2021b) or NA61/SHINE in Marcinek (2023) are in fact intensive quantities by construction.

Scaled factorial moments $F_r(M)$ of order r can be used to study the presence of the critical endpoint or phase transition, as they are defined to be sensitive to large multiplicity fluctuations caused by criticality (Bialas and Peschanski 1986; Satz 1989; Bialas and Hwa 1991). They are defined as

$$F_r(M) = \frac{\left\langle \frac{1}{M^D} \sum_{i=1}^{M^D} n_i(n_i - 1)...(n_i - q + 1) \right\rangle}{\left\langle \frac{1}{M^D} \sum_{i=1}^{M^D} n_i \right\rangle^q} \tag{19}$$

with M^D the number of bins in which the D-dimensional momentum space is partitioned, n_i the multiplicity of particles of interest in the $i^{\rm th}$ bin, and r the order of the moment of interest (Wu et al. 2020). The NA61/SHINE collaboration has measured $F_2(M)$ for protons in central Pb+Pb and Ar+Sc collisions, and $F_{2,3,4}(M)$ for negatively charged hadrons at several energies below $\sqrt{s_{NN}} = 17$ GeV, showing no signal of any criticality in such systems (Adhikary 2022).

Fluctuations of the mean transverse momentum, as those of conserved quantities, would also diverge at the critical point in equilibrium and are expected to be enlarged in its vicinity (Stephanov et al. 1999). Mean transverse momentum correlations have

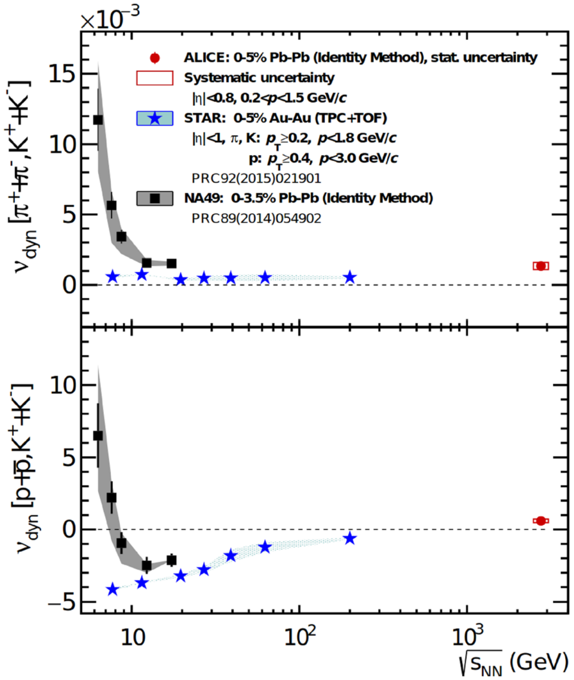

Fig. 19 Combined results from STAR measurements in central Au+Au collisions, and ALICE and NA49 measurements in central Pb+Pb collisions on the energy dependence of $\nu_{\rm dyn}[\pi, K]$ and $\nu_{\rm dyn}[p, K]$ (Acharya et al. 2019d)

been measured by the STAR collaboration, for beam energies of $\sqrt{s_{NN}} = 20, 62, 130$ and 200 GeV (Adams et al. 2005c, 2007).

6.3 Flow harmonics

Another important class of observables giving information about the dynamics of heavy-ion collisions and the EoS of nuclear matter are the flow harmonics v_n. They are the coefficients of the Fourier expansion of an N-particle triple-differential distribution

$$E\frac{d^3N}{d^3p} = \frac{1}{2\pi} \cdot \frac{d^2N}{p_T dp_T dy}\left(1 + 2\sum_{n=1}^{\infty} v_n . \cos\left(n(\phi - \Psi)\right)\right) \tag{20}$$

where E is the particle energy, $p_{(T)}$ its (transverse) momentum, y its rapidity, ϕ its azimuthal angle and Ψ the event plane angle. The flow coefficients are defined as $v_n = \langle \cos(n(\phi - \Psi)) \rangle$, $\langle \ldots \rangle$ denoting an average over many collision events (Voloshin and Zhang 1996; Poskanzer and Voloshin 1998). These flow coefficients measure the azimuthal anisotropies of particle distributions and are a signature of collective expansion, with v_2 measurements playing an important role in the conclusion that QGP formation was observed in Au+Au collisions at RHIC (Adcox et al. 2005; Back et al. 2005c; Adams et al. 2005b).

6.3.1 Measuring collective flow across $\sqrt{s_{NN}}$: event-plane versus multi-particle cumlant methods

While collective flow harmonics may initially appear deceptively simple as just a cos term, there are a number of subtle details that the reader must be aware of before making direct theory-to-experiment comparisons. There are two primary methods used to calculate v_n for low p_T particles (for the relevance to the EoS we will focus only on low p_T particles but at high p_T other technical details exist both on the theory and experimental side, some of which are discussed in Betz et al. (2017)). Before explaining the two methods, it is important to first understand that collective flow is not just a scalar quantity but rather it is a vector that contains both the magnitude of the flow v_n that is 0 for a circular event and 1 for the extreme of the corresponding shape (i.e. for elliptical flow, v_2, it would appear as a line) and the corresponding event-plane angle Ψ_n that is the direction of the flow vector. Then, the flow harmonic can be defined as the complex vector

$$V_n = v_n e^{in\Psi_n}. \tag{21}$$

To be clear, Ψ_n is the event plane angle reconstructed by the detector that includes all the usual caveats of having finite number of particles, acceptance cuts, and efficiencies. However, in principle, if all particles were measured to infinite precision one could rigorously define the underlying event plane Φ_n that is the actual event plane of the given event. Due to the previously mentioned detector effects, $\Psi_n \neq \Phi_n$ and the dispersion in this relationship can be defined as the resolution, R, for a specific flow harmonic

$$R(v_n) \equiv \langle e^{in(\Psi_n - \Phi_n)} \rangle \tag{22}$$

wherein the bracket $\langle \ldots \rangle$ indicates an averaging over a large ensemble of events.

At this point, we can discuss the two different methods for calculating flow harmonics. The first one is the **"event plane method"** (Poskanzer and Voloshin 1998), which was the first technique used to calculate flow harmonics. At that time it was assumed that dynamical fluctuations would have a negligible effect on the extraction of the event plane, such that v_n would essentially be the same for all events within a fixed centrality class. In this method, Ψ_n is determined from two or more subsets of particles (A and B, known as subevents) within a single event such that

$$\psi_n^{A,B} \equiv \frac{1}{n} \frac{\sum_{i\in A,B} w_i \sin(n\phi_i)}{\sum_{i\in A,B} w_i \cos(n\phi_i)} \tag{23}$$

where n is the number of particles considered and w_i is a relevant weight (such as energy or momentum). At this point, it is important to discuss the type of particles considered. The most standard flow measurements are all charged particles. However, it can be of interest to study the flow of *identified particles* such as protons, pions, or kaons. In that case, one "particle of interest", subevent A, is taken (e.g. kaons) and one "reference particle", subevent B, is taken from all charged particles. Because particles of interest tend to be rarer, in most cases only one particle of interest is considered rather than 2 (although exceptions exist). Next, the flow harmonic is determined via

$$v_n\{EP\} \equiv \frac{\langle \cos\left(\phi_n - \Psi_n^A\right)\rangle_{poi}}{\sqrt{\langle \cos\left(\phi_n - \Psi_n^A\right)\rangle}_{all}} \tag{24}$$

where the average in the numerator is only of particle of interest and the average in the denominator is over all charged particles.

The second method is the "multi-particle cumulant" method (Borghini et al. 2001c; Bilandzic et al. 2011, 2014) that correlates m number of particles. In this method (here we follow the formalism used in Luzum and Petersen 2014) one can correlate m particles such that

$$\langle m\rangle_{n_1,n_2,\ldots,n_m} \equiv \langle\langle \cos(n_1\phi^{a_1} + n_2\phi^{a_2} + \ldots + n_m\phi^{a_m})\rangle_m\rangle_{ev} \tag{25}$$

where averages over particles are indicated by the subscript m and averages over events are indicated by a subscript ev. While not shown here, often these averages also include weights (such as by multiplicity) when averaging over multiple events (we will revisit this concept later). At this point we should note that Eq. (25) leads to two distinct contributions that are flow v_n (single particle distribution) and non-flow $\delta_{n,p}$ (genuine p-particle correlations that arise from things like a $\rho \rightarrow \pi\pi$ decay). Because hydrodynamics leads to only flow, experimentalists use various methods to minimize non-flow in their data analysis. Returning to Eq. (25), a 2-particle correlation of all charged particles (i.e. with no particle of interest) leads to

$$v_n\{2\} \equiv \sqrt{\langle v_n^2\rangle_{ev} + \langle \delta_{2,2}\rangle_{ev}} \tag{26}$$

where one gets a contribution both from genuine flow and 2-particle correlations. In order to minimize the non-flow contribution, rapidity gaps are taken within the experiments. They remove decay and jet effects that occur close to each other in rapidity. Thus, after these cuts it is reasonable to assume that

$$v_n\{2\} \approx \sqrt{\langle v_n^2\rangle_{ev}} \tag{27}$$

such that in theoretical calculations one can directly calculate v_n for a single event and then take the root-mean-squared over many events to calculate $v_n\{2\}$. Notice that event-by-event flow fluctuations will also contribute to Eq. (27) and to multi-particle cumulants in general, and should be taken into account when comparing to hydrodynamic simulations.

Depending if one is in a high resolution limit (i.e. $v_n \gg 1/\sqrt{N}$ and $R \rightarrow 1$) or the low resolution limit (i.e. $v_n\sqrt{N} \ll 1$ and $R \rightarrow v_n\sqrt{N}$) the correct theoretical quantity to calculate varies (Luzum and Ollitrault 2013) such that

$$v_n\{EP\} \underset{\text{Highres}}{\longrightarrow} \langle v_n\rangle \tag{28}$$

$$v_n\{EP\} \underset{\text{Lowres}}{\longrightarrow} \sqrt{\langle v_n^2 \rangle}. \tag{29}$$

However, most calculations fall between the high and low resolution limits, leading to ambiguous comparisons to experimental data. Thus, only the multi-particle cumulant method that explicitly defines a two particle correlation as

$$v_n\{2\} \equiv \sqrt{\langle v_n^2 \rangle} \tag{30}$$

provides a method for unambiguous comparisons between theory and experiment.

Due to these uncertainties in the comparison between theory and experiment, only the multi-particle cumulant method ensures an apples-to-apples comparison (Luzum and Ollitrault 2013). However, currently multi-particle cumulants have not been adopted uniformly across $\sqrt{s_{NN}}$ but rather, at low energies the event-plane method is still used and at high-energies multi-particle cumulants are the standard. As explained in Luzum and Ollitrault (2013), this may lead to just a difference of few percentage points in the results, but for precision calculations that can lead to ambiguities.

An additional caveat when comparing high and low beam energies is the choice of event plane angle that is used in the experimental analysis. At high $\sqrt{s_{NN}}$, in the rare occasions in which the event-plane angle is used, the latter is always consistent with the flow harmonic such that v_2 is measured with Ψ_2, v_3 is measured with Ψ_3 and so on. However, at low beam energies all collective flow harmonics are measured with the event-plane method, relative to spectator reaction plane, Ψ_1 (Reisdorf et al. 2012). Thus, the interpretation of the flow harmonics is quite different than those measured at high $\sqrt{s_{NN}}$. At the time of writing, we are not aware of a systematic study within a theoretical model comparing the differences between these measurements across $\sqrt{s_{NN}}$. However, experiments have compared these methods and found differences between them (Bastid et al. 2005; Aamodt et al. 2011b).

Other caveats exist when comparing theory to experiment. The averaging over events, $\langle \ldots \rangle_{ev}$ normally is weighted by a certain factor W_i that is a function of the multiplicity, M, of a given event such that

$$\langle \ldots \rangle_{ev} \equiv \frac{\sum_i^{ev} \langle \ldots \rangle_i W_i}{\sum_i^{ev} W_i} \tag{31}$$

where for a two-particle correlation $W = M(M-1)$. The averaging in Eq. (31) biases experimental observables (within a fixed centrality class) to events with high multiplicities because events with large M have a large weight. Additionally, experiments often perform calculations in smaller centrality bins (e.g. 0.5%) which are then re-assembled into broader centrality bins such as ranges of 5% or 10% depending on the statistics. While these are minor effects, they do play a role at the few percent level, especially for correlations of 4+ particles (Gardim et al. 2017; Betz et al. 2017).

For the following sections, we will consider integrated flow harmonics, which include all particles in certain kinematic ranges in transverse momentum, p_T, and rapidity, y, or pseudorapidity, η. Later we will discuss differential flow, where one still integrates over (pseudo)rapidity but lets p_T vary. For the latter approach, the particle of interest is at a fixed p_T and the reference particles are taken across a much wider p_T range. For these calculations, a scalar product must be used

$$v_n\{SP\}(p_T) \equiv \frac{\langle v_n v_n(p_T) \cos n(\psi_n - \psi_n(p_T))\rangle}{\sqrt{\langle v_n^2\rangle}} \tag{32}$$

where $v_n(p_T)$ and $\psi_n(p_T)$ indicate the magnitude and angle of the flow harmonic at a fixed p_T. One can write a very similar equation integrating over p_T and instead varying (pseudo)rapidity.

6.3.2 Directed flow, v_1

Due to event-by-event fluctuations with rapidity, there are two contributions (Teaney and Yan 2011; Gardim et al. 2011) to directed flow (v_1)

$$v_1(y)e^{i\Psi_1(y)} = v_{1,even}(y)e^{i\Psi_{1,even}(y)} + v_{1,odd}(y)e^{i\Psi_{1,odd}(y)} \tag{33}$$

where $v_{1,even}(y) = v_{1,even}(-y)$, $\Psi_{1,even}(y) = \Psi_{1,even}(-y)$, and $\Psi_{1,odd}(y) = \Psi_{1,odd}(-y)$ such that they are even across rapidity, whereas $v_{1,odd}(-y) = -v_{1,odd}(y)$ such that it is odd in rapidity. Before the discovery of event-by-event fluctuations (i.e. if one assumes no initial state fluctuations) only $v_{1,odd}(y)$ is relevant. Thus, $v_{1,even}(y)$ is an entirely fluctuation-driven quantity.

Even though knowledge of $v_{1,even}(y)$ has existed for over a decade, it has been studied very little because issues related to momentum conservation make it difficult to perform meaningful comparisons between theory and experiment. On the other hand, $v_{1,odd}(y)$ has been used quite extensively at low $\sqrt{s_{NN}}$ to study the EoS. In fact, it is more common to consider the slope of directed flow with respect to the rapidity i.e. dv_1/dy, which is a notoriously difficult quantity to reproduce in theoretical calculations. Thus, from this point forward we will only consider $v_{1,odd}(y)$ and drop the "odd" sub-index for convenience.

Directed flow is expected to be sensitive to the EoS, in particular to the presence of a 1st order phase transition, or the compressibility of nuclear matter (Stoecker 2005; Reisdorf and Ritter 1997). For this reason, v_1 of charged particles has been measured in Pb+Pb collisions by the NA49 experiment at $\sqrt{s_{NN}} = 8.7$ GeV and $\sqrt{s_{NN}} = 17.3$ GeV (Alt et al. 2003) and by the ALICE experiment at $\sqrt{s_{NN}} = 2.76$ TeV (Abelev et al. 2013b). The same has been done in Au+Au collisions, from $\sqrt{s_{NN}} = 2$ GeV to $\sqrt{s_{NN}} = 8$ GeV by the E895 experiment (Liu et al. 2000), and at several collision energies within $7.7 \leq \sqrt{s_{NN}} \leq 200$ GeV by the PHOBOS experiment (Back et al. 2006), and by the STAR experiment for identified particles (Adamczyk et al. 2014b, 2018b). An interesting observation from these results is the discontinuous slope of the mid-rapidity proton directed flow as a function of the energy, exhibiting a minimum in the $\sqrt{s_{NN}} = 10 - 20$ GeV energy range, as displayed in Fig. 20. The interpretation of such results is still unclear though, despite the fact that it has been proposed as a sign for a 1st order phase transition, as no model can explain this behavior properly (Singha et al. 2016). At last, v_1 measurements have been achieved in asymmetric Au+Cu collisions at $\sqrt{s_{NN}} =$

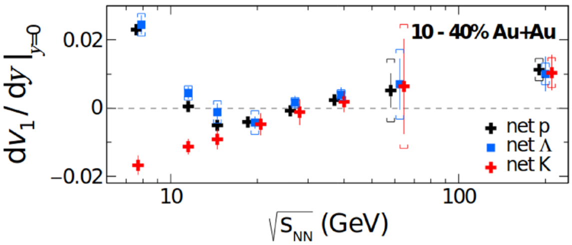

Fig. 20 Directed flow of net-p, Λ and K particle distributions at mid-rapidity as a function of the energy, for Au+Au collisions at intermediate centrality (10–40%). Image adapted from from Adamczyk et al. (2018b)

200 GeV too, for charged and identified particles by both PHENIX (Adare et al. 2016c) and STAR collaborations (Adamczyk et al. 2018a).

6.3.3 Elliptic flow, v_2

Elliptic flow, another name for the second flow harmonic v_2, characterises the ellipticity of the final-state particle momentum distribution, and is proportional to the initial spatial eccentricity of the collision system (Snellings 2011). A nonzero value of v_2 is naturally expected to arise due to the initial asymmetry of the colliding part of the system in non-central heavy-ion collisions, especially when going towards more peripheral events, where the almond shape of the overlapping region is accentuated. The pressure gradient, created by the very high initial energy density in the overlapping region, will hence convert the spatial anisotropies into momentum anisotropies while the system cools down (Snellings 2011). Using hydrodynamics or transport models, one can then extract the EoS (Pratt et al. 2015) and transport coefficients of the quark-gluon plasma like the shear viscosity over entropy ratio η/s (Bernhard et al. 2019), which are nevertheless highly model-dependent and thus out of the scope of this paper. Because the connection to the EoS is highly dependent on a number of other quantities such as the initial state amongst many others, we refer an interested reader to reviews, e.g. Heinz and Snellings (2013).

Elliptic flow has been measured by several collaborations at the LHC in Pb+Pb collisions at $\sqrt{s_{NN}} = 2.76$ TeV and $\sqrt{s_{NN}} = 5.02$ TeV for charged particles (Aad et al. 2012a; Chatrchyan et al. 2013, 2014b; Acharya et al. 2018d) and also for identified hadrons (Abelev et al. 2015; Acharya et al. 2018b), as well as in Xe+Xe collisions at $\sqrt{s_{NN}} = 5.44$ TeV (Acharya et al. 2018a; Aad et al. 2020; Sirunyan et al. 2019a). At collision energies of the BESI program, between $\sqrt{s_{NN}} = 7.7$ and 200 GeV, v_2 has also been extensively studied in Au+Au collision systems for both charged particles (Adler et al. 2002; Back et al. 2005b, a; Adamczyk et al. 2012; Adare et al. 2015a) and identified particles (Adler et al. 2001a; Adams et al. 2005d; Adamczyk et al. 2016b; Abdallah et al. 2023a) by the STAR, PHENIX and PHOBOS collaborations. Elliptic flow of smaller systems, namely Cu+Cu collisions at $\sqrt{s_{NN}} = 62.4$ and 200 GeV (Alver et al. 2007; Abelev et al. 2010a; Adare et al. 2015a), Ru+Ru and Zr+Zr collisions at $\sqrt{s_{NN}} = 200$ GeV (Sinha 2023) have been measured as well. In addition, v_2 data have also been extracted for the large, deformed system of U+U collisions at $\sqrt{s_{NN}} = 193$ GeV (Abdallah et al. 2021a). All of these results show two strong indicators of the common origin of produced particles from a moving fluid, namely the QGP. The first one is the mass ordering of the p_T-differential v_2 from identified hadrons at low p_T (<2 GeV), with lighter species exhibiting a larger v_2 than heavier ones (Abelev et al. 2010a; Adamczyk et al. 2013a). It can be understood by assuming that all particles originate from common cells of fluid with a given velocity, thus causing a shift of the v_2 signal in momentum due to the mass differences (Huovinen et al. 2001; Huovinen and Ruuskanen 2006). The second one is the so-called Number of Constituent Quarks (NCQ) scaling (Molnar and Voloshin 2003) at intermediate p_T (>1 GeV), namely the fact that all v_2 signals from different species match when plotted as a function of p_T or the reduced transverse mass, also called the transverse kinetic energy, $KE_T = m_T - m_0$, all of them divided by the number of valence quarks N_q ($= 2$ for mesons and $= 3$ for baryons) (Adare et al. 2007; Abelev et al. 2010a; Adamczyk et al. 2013a; Acharya et al. 2018b, 2021c). Assuming a common origin of the produced hadrons, this scaling shown in Fig. 21 illustrates that collectivity arises from quarks as degrees of freedom, before being translated into flow of the hadrons formed by quark coalescence (Fries et al. 2003; Molnar and Voloshin 2003). Such observations constitute, among other probes, a good indicator of the formation of a quark-gluon plasma. However, N_q scaling starts breaking down in minimum bias Au+Au collisions from $\sqrt{s_{NN}} = 11.5$ GeV and below, as can be seen in Fig. 21 with the v_2/N_q of ϕ mesons (although this interpretation is discussed in Hirano et al. (2008)).

At even lower beam energies of Au+Au collisions at $\sqrt{s_{NN}} = 3$ GeV, the v_2 measurements by the STAR experiment (Abdallah et al. 2022c) show no N_q scaling at all. This result tends to indicate the absence of efficient quark coalescence in the system created in such collisions, thus suggesting a dominance of the hadronic phase over deconfined partonic flow. Current hydrodynamic calculations can provide a reasonable match to experimental data down to $\sqrt{s_{NN}} = 7.7$ GeV (Shen and Schenke 2022) and $\sqrt{s_{NN}} = 4.3$ GeV (Schäfer et al. 2022). However, we point out that other effects may destroy N_q scaling that have not yet been explored at these energies in full (3+1)D relativistic viscous hydrodynamical simulations. For example, the existence of a critical point leads to critical fluctuations that may have dramatic effects on transport coefficients, which in turn affect collective flow (see Lovato et al. 2022b for further discussion on flow at these beam energies). We also caution that NCQ scaling is only approximate and expected to hold only at intermediate p_T (Molnar and Voloshin 2003). Precise NCQ scaling for $v_2\{2\}(p_T/N_q)/N_q$ is not observed even at LHC energies (Abelev et al. 2015; Acharya et al. 2018b, 2021c), so one must be careful when drawing conclusions from its absence. Overall, a much clearer scaling can be seen when plotting against KE_T/N_q (Adare et al. 2007; Abelev et al. 2015).

6.3.4 Triangular flow v_3 and beyond

Let us first discuss triangular flow before moving onto higher-order flow harmonics. The existence of triangular flow was not understood in the field of heavy-ion collisions for many years. In part, this occurred because experimentalists measured triangular flow with the wrong event plane angle (e.g. using Ψ_2 instead of Ψ_3,

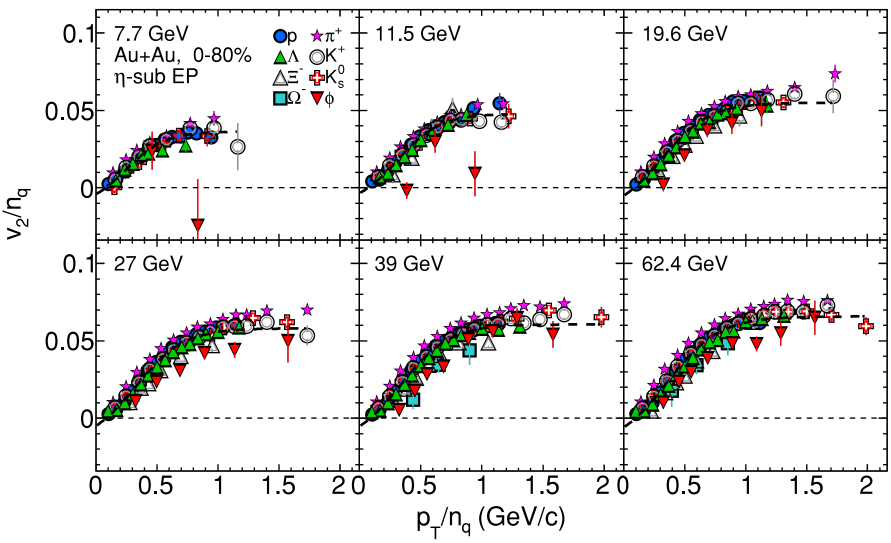

Fig. 21 NCQ scaling of the elliptic flow of identified hadrons (π^+, K^+, K_s^0, ϕ, p, Λ, Ξ^- and Ω^-) for 0–80% Au+Au collisions at $\sqrt{s_{NN}} = 7.7$, 11.5, 19.6, 27, 39 and 62.4 GeV. Image reproduced with permission from Adamczyk et al. (2013a), copyright by APS

leading to a result of $v_3(\Psi_2) = 0$). However, the key issue was that the importance of event-by-event fluctuations and how significantly they could affect flow harmonics was not understood. The calculations from Takahashi et al. (2009) of 2 particle correlations, were performed in the first theoretical framework to use event-by-event fluctuating initial conditions and was the only model able to reproduce the experimental results at the time. This made it possible for experimentalists to understand the significance of triangular flow and discover the correct method for calculating it (Alver and Roland 2010). This discovery of nonzero v_3 that can only arise from event-by-event fluctuating initial conditions led to a radical change in the field of heavy-ion collisions because many assumptions had to be changed, but it allowed for new ways to probe the QGP that did not exist previous to the discovery.

Higher-order flow harmonics, from v_3 and up to v_6, have also been measured in order to get complementary information concerning what can be already determined from $v_{1,2}$ results. As they require a rather high number of events to be measured with reasonable uncertainties, they have been measured almost exclusively at top energy of the BES program in Au+Au collisions, i.e., $\sqrt{s_{NN}} = 200$ GeV (Adare et al. 2016b; Adam et al. 2020c; Abdallah et al. 2022a), and also in Pb+Pb collisions at $\sqrt{s_{NN}} = 2.76$ TeV (Aamodt et al. 2011b; Aad et al. 2012a; Adam et al. 2016d; Chatrchyan et al. 2014a, b) and $\sqrt{s_{NN}} = 5.02$ TeV (Adam et al. 2016b; Aaboud et al. 2018; Acharya et al. 2020b), as well as in Xe+Xe collisions at $\sqrt{s_{NN}} = 5.44$ TeV (Acharya et al. 2018a; Aad et al. 2020). STAR (AuAu $\sqrt{s_{NN}} = 7.7 - 200$ GeV) has now measured the suppression of $v_3\{2\}$ at low beam energies (Adamczyk et al. 2016a) where a minimum is reached (but $v_3\{2\}$ does not precisely reach 0) whose results are still open for interpretation, see Fig. 22. Additionally, HADES has also

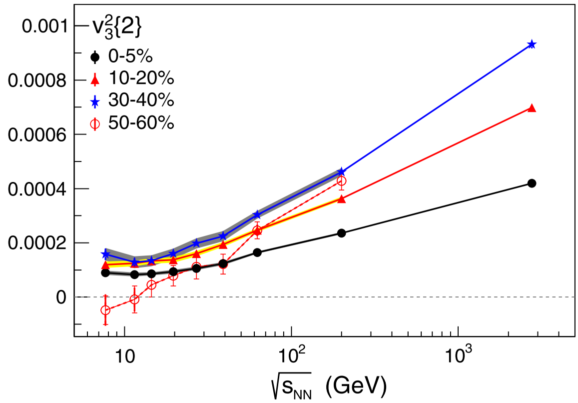

Fig. 22 All charged particles $v_3^2\{2\}$ from the STAR collaboration for various centralities in Au+Au collisions at $\sqrt{s_{NN}}$ = 7.7, 11.5, 19.6, 27, 39 and 62.4 GeV. Image reproduced with permission from Adamczyk et al. (2016a), copyright by APS

calculated higher-order flow harmonics at $\sqrt{s_{NN}} = 2.4$ GeV (Adamczewski-Musch et al. 2020a), albeit with the event-plane method with respect to the Ψ_1 event plane angle, see Fig. 23.

In the context of BESI, the STAR collaboration has performed a comprehensive analysis of 3-particle azimuthal anisotropy correlations $C_{m,n,m+n}$, between different harmonics m, n and $m+n$, over a wide range of multiplicities, transverse momenta, and energies from $\sqrt{s_{NN}} = 7.7\,\mathrm{GeV}$ to $200\,\mathrm{GeV}$ (Adamczyk et al. 2018d). The dependence displayed by results on the pseudo-rapidity differences between particles suggests the breaking of longitudinal boost invariance or dominance of unconventional non-flow contributions.

6.3.5 4+ particle flow cumulant observables

The multi-particle cumulant method used to extract $v_n\{2\}$ in Eq. (30) can be extended to cumulants of higher order, denoted $v_n\{2k\}$ (Borghini et al. 2001a, b, c; Bilandzic et al. 2011, 2014; Di Francesco et al. 2017; Moravcova et al. 2021). In general, measurements of $v_n\{2k\}$ depend on irreducible $2k$-particle correlations, so that non-collective contributions to v_n are suppressed by a combinatorial factor, which decreases with k. The four-particle $v_n\{4\}$, for instance, is given by

$$-v_n\{4\}^4 = \langle v_n^4 \rangle - 2\,\langle v_n^2 \rangle^2 \tag{34}$$

where 2-particle contributions are subtracted by the second term (see, for instance Giacalone et al. 2017).

Non-flow contributions set aside, differences between multi-particle cumulants are also sensitive to how the coefficients v_n fluctuate event-by-event (Aad et al. 2013, 2014b). In the regime in which these coefficients scale linearly with anisotropies of the initial state, i.e. $v_n \propto \varepsilon_n$ (Teaney and Yan 2011; Gardim et al. 2012, 2015; Niemi et al. 2013; Teaney and Yan 2012; Qiu and Heinz 2011; Betz et al. 2017), where ε_n quantifies the initial-state anisotropy, ratios between different cumulants depend only on fluctuations of the initial anisotropies, characterized by cumulants $\varepsilon_n\{2k\}$ (Ma et al. 2016; Giacalone et al. 2017). For instance,

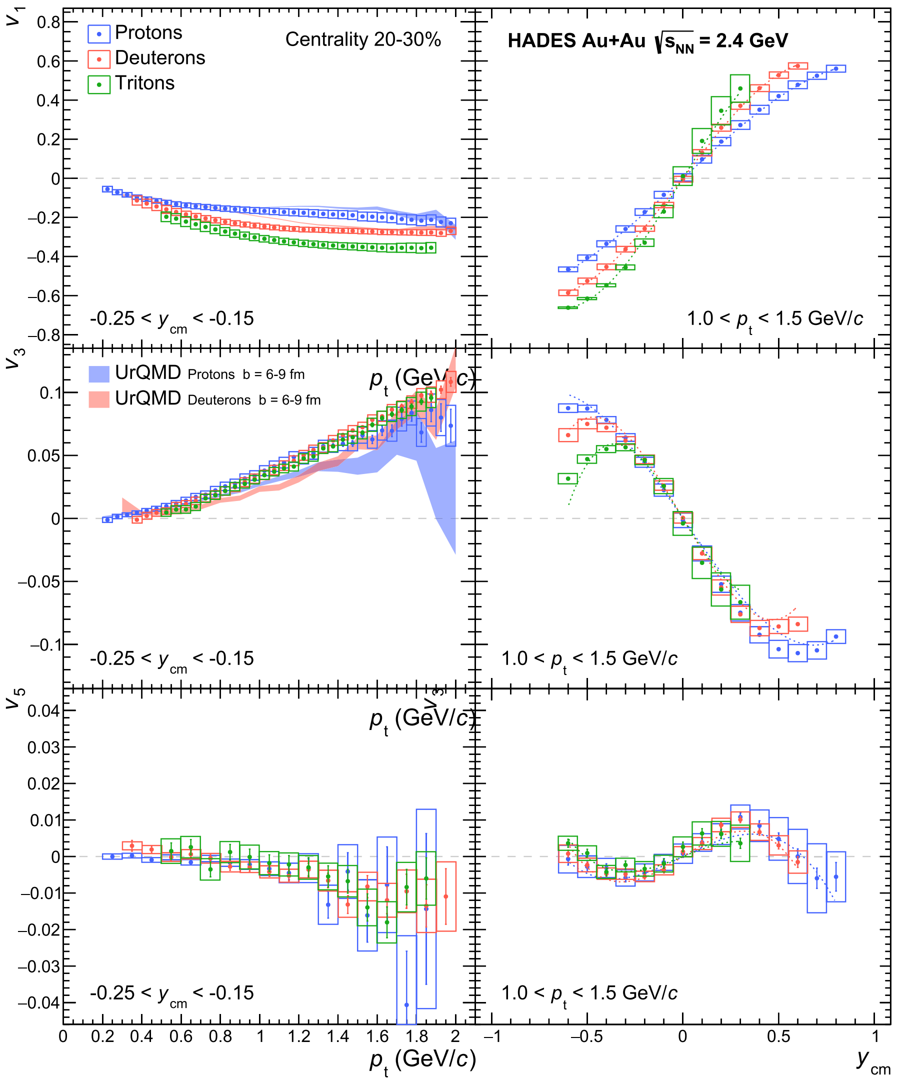

Fig. 23 All charged particles collective flow from HADES in Au+Au collisions at $\sqrt{s_{NN}} = 2.4$ GeV. Image reproduced with permission from Adamczewski-Musch et al. (2020a), copyright by APS

$$\frac{v_n\{2k\}}{v_n\{2\}} \approx \frac{\varepsilon_n\{2k\}}{\varepsilon_n\{2\}} \tag{35}$$

where the proportionality factor relating initial-state and flow anisotropy cancels out (Yan and Ollitrault 2014), so that multi-particle flow measurements can be employed to isolate information on initial-state fluctuations from information on the response of the medium (Giacalone et al. 2017; Bhalerao et al. 2019a, b). However, in peripheral collisions (Noronha-Hostler et al. 2016b), small systems (Sievert and Noronha-

Hostler 2019), differential flow (Hippert et al. 2020a), and to a much lesser extent lower beam energies (Rao et al. 2021) this linear scaling begins to break down, and it requires non-linear response as well. Multiparticle cumulants and fluctuations of flow coefficients have been measured at $\sqrt{s_{NN}} = 130$ GeV by the STAR collaboration (Adler et al. 2002), across BESI $\sqrt{s_{NN}} = 7.7 - 200$ GeV from the STAR collaboration (Abdallah et al. 2022b), and at $\sqrt{s_{NN}} = 2.76 - 5.02$ TeV by ATLAS, CMS and ALICE in Pb+Pb collisions (Aad et al. 2013, 2014b; Sirunyan et al. 2019b, 2018c; Acharya et al. 2018d), by ALICE, CMS, and ATLAS in p-Pb collisions (Abelev et al. 2014b; Khachatryan et al. 2015a, 2017; Sirunyan et al. 2018c; Aaboud et al. 2017b; Acharya et al. 2019b), and by ALICE in p+p and Xe+Xe collisions (Acharya et al. 2019b).

While multi-particle cumulants of a single flow coefficient can be used as proxies of its fluctuations, correlations between different coefficients can be studied with so-called symmetric cumulants (Bilandzic et al. 2014)

$$\mathrm{SC}(n,m) = \langle v_n^2 v_m^2 \rangle - \langle v_n^2 \rangle \langle v_m^2 \rangle \tag{36}$$

or normalized symmetric cumulants $\mathrm{sc}(m,n) = \mathrm{SC}(n,m)/(\langle v_n^2 \rangle \langle v_m^2 \rangle)$ (Bhalerao et al. 2011, 2019b; Moravcova et al. 2021), which can also be generalized to higher orders (Mordasini et al. 2020). For symmetric cumulants, it is important to ensure that multiplicity weighing and centrality binning are taken into account in order to reproduce experimental data (Gardim et al. 2017).

Normalized symmetric cumulants are related to event-plane correlations (Bhalerao et al. 2015a; Giacalone et al. 2016), which can be quantified by examining how combinations of event planes for different harmonics, $\Psi_{n_1,n_2,\ldots,n_k} \equiv a_1 \Psi_{n_1} + a_2 \Psi_{n_2} + \ldots + a_m \Psi_{n_k}$ fluctuate (Jia and Mohapatra 2013; Jia and Teaney 2013; Bhalerao et al. 2011; Qin and Muller 2012). Taking the Fourier series of the distribution $dN/d\Psi_{n_1,n_2,\ldots,n_k}$, one finds coefficients

$$V^j_{n_1,n_2,\ldots,n_k} \equiv \langle \cos\left(j\,\Psi_{n_1,n_2,\ldots,n_k}\right) \rangle \tag{37}$$

where n-fold symmetry of the event-plane angle Ψ_n requires that $a_i = n_i\, c_i$, $c_i \in \mathcal{Z}$, and invariance of correlations under global rotations imposes that $\sum_i n_i\, c_i = 0$. The event-plane correlations have been suggested as a method to possibly constrain viscous effects (Niemi et al. 2016).

The PHENIX collaboration has investigated event-plane correlations in Au+Au collisions at $\sqrt{s_{NN}} = 200$ GeV at RHIC (Adare et al. 2011). Results for symmetric cumulants and normalized symmetric cumulants in Au+Au collisions at center-of-mass energies of $\sqrt{s_{NN}} = 27$ GeV, 39 GeV, 54.4 GeV and 200 GeV were also published by STAR in Adam et al. (2018), Aboona et al. (2023a), where they are compared to LHC results. ATLAS and ALICE have performed measurements of event-plane correlations in Pb+Pb collisions at $\sqrt{s_{NN}} = 2.76$ TeV (Aad et al. 2014a; Acharya et al. 2017b), while ALICE, CMS, and ATLAS have published measurements of symmetric cumulants (Adam et al. 2016c; Sirunyan et al. 2018b; Aaboud et al. 2019; Acharya et al. 2021d).

6.3.6 Differential flow and scalar products

Another important tool for constraining QGP properties is the study of flow anisotropies *differentially* in transverse momentum p_T or (pseudo-rapidity η) (Luzum and Romatschke 2008; Schenke et al. 2012; Nijs et al. 2021). In theory this amounts to considering the p_T in Eq. (20), so that the flow coefficients become $v_n = v_n(p_T)$. In practice, this entails binning particles of interest according to their momenta. However, a good determination of the reference event plane ψ_n demands that particles of reference be defined over a wider and suitably chosen momentum range. The differential flow coefficients can thus be found from the scalar product of Eq. (32) (see e.g. Bilandzic et al. 2011 for details).

Flow harmonics in different p_T regions reveal different physics. In the low p_T region, differential flow observables allow for the investigation of the hydrodynamic response of the QGP as a function of transverse momentum. As discussed above, the mass ordering of elliptic flow at low p_T, with lighter particles presenting stronger flow, has been regarded as a signature of hydrodynamic expansion, while the NCQ scaling of flow harmonics at intermediate p_T has been viewed as a signature of quark coalescence (Huovinen et al. 2001; Molnar and Voloshin 2003; Gyulassy 2004; Gyulassy and McLerran 2005; Huovinen and Ruuskanen 2006; Adams et al. 2005d; Abelev et al. 2008a, a). At higher p_T, flow harmonics encode information on energy loss (Gyulassy et al. 2001; Wang 2001).

Differential flow harmonics have been measured for a variety of systems and beam energies. For Pb+Pb collisions, at the LHC differential flow measurements have been made at $\sqrt{s_{NN}} = 2.76$ TeV from ALICE (Aamodt et al. 2011b), CMS (Chatrchyan et al. 2012) and ATLAS (Aad et al. 2012b), and at $\sqrt{s_{NN}} = 5.02$ GeV from ALICE (Adam et al. 2016b; Acharya et al. 2018b, 2023a) and CMS (Sirunyan et al. 2018a, 2020). Measurements have also been performed at RHIC at high beam energies for Au+Au (Adams et al. 2005a; Adler et al. 2003; Afanasiev et al. 2009; Adler et al. 2004; Back et al. 2005a), Cu+Cu (Adare et al. 2015a) and Cu+Au (Adare et al. 2016c) collisions at $\sqrt{s_{NN}} = 200$ GeV and 62.4 GeV (Adare et al. 2015a), and Au+Au collisions at $\sqrt{s_{NN}} = 130$ GeV (Ackermann et al. 2001). A comprehensive analysis of p+Au, d+Au, Cu+Cu and Cu+Au collisions at $\sqrt{s_{NN}} =$ 200 GeV, as well as U+U collisions at $\sqrt{s_{NN}} = 193$ GeV, from the STAR collaboration can be found in Adam et al. (2019a). In the context of the BESI there have been measurements from $\sqrt{s_{NN}} = 7.7 - 200$ GeV (Adamczyk et al. 2013c, 2016b; Abelev et al. 2008a).

At very low beam energies, sometimes differential flow measurements are reported in terms of the transverse mass m_T such that this is related to p_T through

$$m_T = \sqrt{m^2 + p_T^2} \tag{38}$$

where m is the mass of the particle(s) considered. If only one particle species is considered in the flow, it is possible to translate between p_T-dependent flow and m_T-dependent flow. However, if multiple identified particles are considered, it is not possible to make this translation without more information from the experiment.

Fixed target measurements have been made at the STAR fixed target program for $\sqrt{s_{NN}} = 3$ GeV (Abdallah et al. 2022c) (in this work it was also normalized by the number of quarks such that $N_q = 2$ for mesons and $N_q = 3$ for baryons) for $\sqrt{s_{NN}} =$ 4.5 GeV (Adam et al. 2021a). At HADES, using Au-Au collisions at $\sqrt{s_{NN}} = 2.4$ GeV (Adamczewski-Musch et al. 2020a), differential flow was measured in terms of m_T. Differential flow provides a more stringent test for models of strongly interacting matter, with transport models, represented by SMASH (Mohs et al. 2022), currently unable to reproduce results from HADES (Kardan 2019)—although this may be fixed with further improvements (Sorensen et al. 2024).

An interesting consequence of the p_T dependence of flow coefficients is that one may investigate how anisotropies over different p_T ranges correlate with one another (Kikola et al. 2012; Gardim et al. 2013; Heinz et al. 2013). In particular, 2-particle correlations are given by the covariance matrix

$$V_{n\Delta}^{ab} \equiv V_{n\Delta}(p_T^a, p_T^b) = \langle V_n^*(p_T^a)\, V_n(p_T^b)\rangle \tag{39}$$

where $p_T^{(a,b)}$ denote the transverse momentum in two p_T bins a and b, and we generalize the complex $V_n = v_n\, e^{i\Psi_n}$ of Eq. (21) for differential flow. In the absence of flow fluctuations or non-flow effects, independent particle emission from the fluid implies that the covariance matrix "factorizes" as $V_{n\Delta}^{ab} = v_n(p_T^a)\, v_n(p_T^b)$. The breaking of this factorization can signal non-flow contributions (Kikola et al. 2012; Jia 2011; Adare 2011; Aad et al. 2012a) or, more interestingly, event-by-event flow fluctuations (Gardim et al. 2013), and can be quantified by the factorization-breaking coefficient

$$r_n(p_T^a, p_T^b) \equiv \frac{V_{n\Delta}(p_T^a, p_T^b)}{\sqrt{V_{n\Delta}(p_T^a, p_T^a)\, V_{n\Delta}(p_T^b, p_T^b)}} \leq 1 \tag{40}$$

with the inequality being saturated for the case of perfect factorization. The same coefficient can be defined for pseudo-rapidity instead of transverse-momentum bins. Equation (40) is such that, in the regime of linear response to initial anisotropies, the response of the medium cancels out and r_n is determined mainly by initial-state fluctuations. This coefficient, and its counterpart for η-differential flow, has been measured by CMS for both Pb+Pb collisions at $\sqrt{s_{NN}} = 2.76$ TeV and p-Pb collisions at $\sqrt{s_{NN}} = 5.02$ TeV (Khachatryan et al. 2015b; Sirunyan et al. 2017), and was found to be generally close to, yet below 1.

Factorization breaking can also be understood in terms of the spectral decomposition and principal component analysis of $V_{n\Delta}^{ab}$, with the case of perfect factorization corresponding to a single nonzero eigenvalue. The principal component analysis of flow fluctuations was proposed in Bhalerao et al. (2015b) as a more transparent alternative to r_n, and measured by CMS, in Pb+Pb collisions, at $\sqrt{s_{NN}} =$ 2.76 TeV (Sirunyan et al. 2017). However, it has been suggested that the original prescription for carrying out this measurement led to the contamination of subleading anisotropic flow modes by fluctuations of radial flow (Hippert et al. 2020b). Results from hydrodynamic simulations indicate that the factorization-breaking coefficient and subleading components of the PCA of $V_{n\Delta}$ are capable of probing initial-state fluctuations at smaller length-scales, compared to the initial transverse size of the system (Kozlov et al. 2014; Gardim et al. 2018; Hippert et al. 2020a).

6.4 HBT

Hanbury Brown–Twiss (HBT) interferometry (Heinz and Jacak 1999; Wiedemann and Heinz 1999; Lisa et al. 2005) provides a way to probe the space-time evolution of heavy-ion collisions using correlations between pairs of identical particles emitted from these collisions, such as pions or kaons.[7] By analyzing the resulting two-particle correlation functions at small relative momentum, one finds that their inverse widths (the 'HBT radii' R_{ij}^2) correspond to the average separation between the emission points of any two identical particles, and, therefore, provide a way of quantifying the space-time structure of the particle emission process. Insofar as the bulk of particle production occurs towards the end of the system's lifetime (Plumberg and Heinz 2015; Müller and Schäfer 2022), one expects that HBT measurements should be sensitive to the entire history of the fireball, and, therefore, should depend on the EoS as well.

This expectation turns out to be correct. Previous studies have established at least five different connections between HBT and the nuclear EoS. First, the space-time information extracted from HBT can be used to estimate the volume of the system at freeze out. The freeze-out volume can then be used to estimate the peak energy density and, thereby, obtain evidence for the onset of deconfinement (Heinz and Jacak 1999; Lisa et al. 2005). Second, the specific observables $R_o^2 - R_s^2$ and R_o/R_s are sensitive to the emission duration and rate of expansion of the collision system (Heinz and Jacak 1999; Pratt 2009; Adamczewski-Musch et al. 2019a); measuring these quantities as functions of the pair momentum K_T can constrain the existence or absence of a first-order phase transition at different beam energies and chemical potentials (Lisa et al. 2005; Li et al. 2023). For the same reason, these observables have also been identified as potential signatures of the QCD critical point, by analyzing their scaling with beam energy $\sqrt{s_{NN}}$ to signal a softening in the EoS (Lacey 2015). A third connection between HBT and the nuclear equation state uses the moments of collision-by-collision fluctuations in the HBT radii to isolate the geometric effects of critical fluctuations on the system's evolution (Plumberg and Kapusta 2017), and thereby provides an independent way of probing the QCD critical point. Fourth, HBT is sensitive to the speed of sound as a function of temperature. HBT measurements in different collision systems and beam energies (Au+Au at RHIC vs. Pb+Pb at the LHC) have been shown in a multi-observable Bayesian analysis (Pratt et al. 2015; Sangaline and Pratt 2016) to directly constrain a parameterized form of $c_s^2(T)$. Fifth, the multiplicity dependence of the HBT radii in different size collision systems—specifically, the slope of R_{ij} versus $(dN_{ch}/d\eta)^{1/3}$ in p+p, p+Pb, and Pb+Pb—may also reflect the influence of c_s^2 on the rate of the system's expansion (Plumberg 2020).

[7] The more general term *femtoscopy* typically may include, in addition to HBT, non-identical particle correlations and coalescence analyses as well, which may yield additional insights into the space-time dynamics of heavy-ion collisions (Lisa et al. 2005).

In addition to these examples, the global shape of the fireball at freezeout is sensitive to the EoS in at least two ways. First, the HBT radii can be analyzed experimentally as functions of the azimuthal pair emission angle Φ_K, which indicates the direction of a given particle pair's average momentum in the transverse plane. By expanding this azimuthal dependence in a Fourier series and studying the extracted coefficients as functions of $\sqrt{s_{NN}}$, one acquires sensitivity to the EoS via the freeze-out eccentricity ε_F (roughly, the normalized second-order Fourier coefficients of the R_{ij}^2), which measures the extent to which the initial elliptic geometry of the collision system is inverted by the subsequent dynamical expansion (Adamczyk et al. 2015; Adamczewski-Musch et al. 2020b). Second, one can also observe sensitivity to the EoS in the transition from prolate to oblate freezeout configurations, which is done by correlating transverse and longitudinal HBT radii as a function of collision energy. The resulting non-monotonic trend observed in the data (Adam et al. 2021a) is attributed to a transition from dynamical evolution dominated by nucleon stopping at low energies to boost-invariant evolution at higher energies.

HBT measurements have been carried out in a vast number of different collision systems and over a wide range of collision energies and particle species. We focus here on HBT with Bose-Einstein correlations, primarily using charged pion pairs. Important recent measurements include: azimuthally sensitive analyses in Pb+Pb at 2.76 TeV (Adamova et al. 2017; Acharya et al. 2018c), p+Pb at 5.02 TeV (ATLAS Collaboration 2017), Cu+Au and Au+Au (Lisa et al. 2000; Adams et al. 2004, 2005e; Adare et al. 2014; Khyzhniak 2020a), and Pb+Au at 40, 80, and 158 GeV (Adamová et al. 2003; Adamova et al. 2008). The majority of studies present results for azimuthally averaged analyses. At the LHC, HBT has been measured: by ALICE, in Pb+Pb at 2.76 TeV (Aamodt et al. 2011d), p+p at 0.9 and 7 TeV (Aamodt et al. 2011a; Acharya et al. 2019a); by CMS, in p+p, p+Pb, and Pb+Pb at various energies 0.9, 2.76, 5.02, and 7 TeV; and by ATLAS in p+Pb at 5.02 TeV (Aaboud et al. 2017a). At RHIC, STAR has further measured HBT: in U+U collisions at 193 GeV (Campbell 2018); in Au+Au at collision energies of $\sqrt{s_{NN}} = 4.5, 7.7, 9.2, 11.5, 19.6, 27, 39, 62.4, 130$, and 200 GeV (Adler et al. 2001b; Abelev et al. 2010b; Anson 2011; Adamczyk et al. 2015; Zbroszczyk 2022); in p+Au and d+Au at 200 GeV (Khyzhniak 2020b); and in p+p collisions at 200 GeV (Aggarwal et al. 2011). PHENIX has conducted measurements in d+Au and Au+Au at 200 GeV (Ajitanand et al. 2014) and in Au+Au at 7.9, 19.6, 27, 39, 62, and 200 GeV (Soltz 2014). Au+Au collisions have been further studied by the HADES collaboration at 2.4 GeV (Adamczewski-Musch et al. 2019a, 2020b; Greifenhagen 2020). The majority of analyses study two-pion correlations for statistical reasons, but HBT has also been studied for kaon pairs by various collaborations at both RHIC and the LHC (Adamczyk et al. 2013b; Nigmatkulov 2016; Acharya et al. 2017a, 2019c) and for multi-pion correlations in various systems (Adare et al. 2015b; Adam et al. 2016e).

7 Experimental constraints: low-energy nuclear physics

In the following section, we will review various empirical observations of constraints relevant to low-energy nuclear physics for isospin-symmetric and asymmetric matter.

7.1 Isospin symmetric matter at saturation density

As neutron stars are in many ways like giant nuclei with $\sim 10^{57}$ nucleons (Glendenning 1997), at densities which are typical of nuclei they should reproduce the same properties. Therefore, astrophysicists use laboratory measurements of nuclear experiments to calibrate neutron stars (or dense matter in general) properties. Low-energy laboratory conditions can be considered at $T \sim 0$ when describing fermions, as their order of chemical potential and mass are 10^5 times larger than the temperature of fully evolved neutron stars (10^{-2} MeV $\sim 10^8$ K) and even more when compared to laboratories. At effectively zero temperature, antifermions do not contribute and the relevant degrees of freedom at $n_{\rm sat}$ are nuclei (composed of neutrons and protons), which are approximately isospin symmetric, with charge fraction $Y_Q \sim 0.5$. The minimal condition on any dense matter theory is to reproduce the experimental results of zero temperature, isospin symmetric nuclear matter at saturation: saturation density $n_{\rm sat}$, binding energy per nucleon B/A, and compressibility K. Additionally, for models that contain exotic degrees of freedom, hyperon potentials U_H and Δ-baryon potential U_Δ can be used.

These empirical values are known within uncertainties and are extracted using extrapolation within phenomenological models, since infinite nuclear matter does not exist. Here, we enlist various empirical investigations of the above-mentioned properties. The values for the observables related to isospin-symmetric nuclear matter are summarized in Table 5, those related to exotic matter in Table 6.

Table 5 Experimental constraints related to isospin-symmetric nuclear matter at saturation

Constraints	Value	References
Saturation density, $n_{\rm sat}$ (fm^{-3})	0.17 ± 0.03	Haensel et al. (1981)
	$0.148 - 0.185$	Gross-Boelting et al. (1999)
	0.148 ± 0.0038	Adhikari et al. (2021)
Binding energy per nucleon, B/A (MeV)	-15.677	Myers and Swiatecki (1966)
	-16.24	Myers and Swiatecki (1996)
Compressibility, K_∞ (MeV)	240 ± 20	Colo et al. (2014), Todd-Rutel and Piekarewicz (2005), Colo et al. (2004), Agrawal et al. (2003)
	$210 - 270$	Khan and Margueron (2012)
	$251 - 315$	Stone et al. (2014)

Table 6 Empirical constraints related to isospin-symmetric exotic matter at saturation

Constraints	Value	References
Hyperon potentials (MeV)	$U_\Lambda = -28$	Inoue (2019), Millener et al. (1988)
	$U_\Lambda = -30$	Gal et al. (2016)
	$U_\Lambda = -26.7 \pm 1.7$	Friedman and Gal (2023)
	$U_\Sigma = 15$	Inoue (2019)
	$U_\Sigma = 10 - 50$	Gal et al. (2016)
	$U_\Xi = -14$	Gal et al. (2016)
	$U_\Xi = -21.9 \pm 0.7$	Friedman and Gal (2021)
	$U_\Xi = -4$	Inoue (2019)
Delta baryon potential (MeV)	$U_\Delta \sim U_N$	Horikawa et al. (1980)
	$U_\Delta(n_B) = -75 n_B(r)/n_{\rm sat}$	Koch and Ohtsuka (1985)
	$-90 < U_\Delta < -50$	Drago et al. (2014)

7.1.1 Saturation density

The saturation density (actually the number density, as it defines the number of baryons per volume) indicates that there is a size saturation in atomic nuclei, preventing them from expanding or collapsing as a result of the nuclear force's powerful attraction and repulsion. This is the most important constraint, as often other constraints are determined at this density (Fig. 24).

The simplest way to calculate a given number density is by dividing the number of baryons in a nucleus over the volume of the nucleus, as (Haensel et al. 1981)

$$n_{\rm sat} = \frac{A}{4\pi R^3/3} = \frac{3}{4\pi(R/A^{1/3})^3} = \frac{3}{4\pi R_0^3} = 0.17 \pm 0.03 \quad {\rm fm}^{-3} \tag{41}$$

where it was assumed that the value of the nuclear radius constant is $R = R_0 A^{1/3} = 1.04 - 1.17$ fm. The error bar reflects the uncertainty on R_0, obtained from electron scattering and μ-mesic atom experiments (Myers 1977).

Recently, in the elastic scattering of longitudinally polarized electrons extracted from ^{208}Pb, the PREX collaboration reported a precise measurement of the parity-violating asymmetry $A_{\rm PV}$ term (Adhikari et al. 2021), where the interior baryonic density at saturation was derived from the measured interior weak density n_W^0 i.e.

$$n_{\rm sat} = 0.1480 \pm 0.0038 \quad {\rm fm}^{-3}. \tag{42}$$

Here, the uncertainty contains both theoretical and experimental contributions.

7.1.2 Binding energy per nucleon at saturation

Binding energy (B) is the energy required to separate a nucleus, and is given by the semi-empirical mass formula

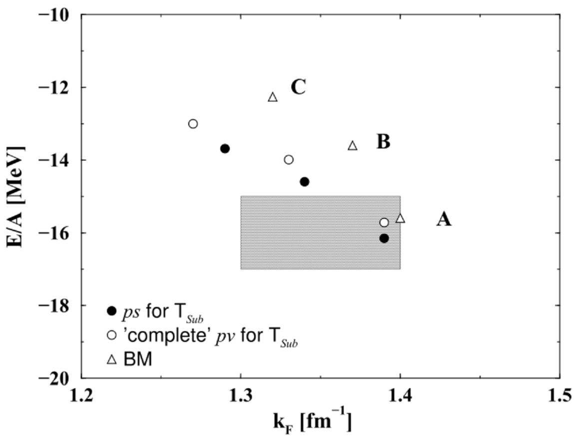

Fig. 24 Binding energy per nucleon (in this review, referred to as B/A) versus Fermi momentum k_f, with the shaded box representing saturation. The Bonn potentials shown via letters A, B, and C are used for bare nucleon–nucleon interaction. In addition, the three legends describe the T-matrix calculations using a subtraction scheme with the *ps* representation (top), the *pv* representation (middle), and Brockmann and Machleidt, *BM* (bottom) (Brockmann and Machleidt 1990). Image reproduced with permission from Gross-Boelting et al. (1999), copyright by Elsevier

$$B = a_v A - a_s A^{2/3} - a_c \frac{Z(Z-1)}{A^{1/3}} - a_a \frac{(N-Z)^2}{A} + \delta(A,Z) \tag{43}$$

where

$$\delta(A,Z) = \begin{cases} +a_p A^{-1/2} & \text{for even } Z, \text{ even } N \\ 0 & \text{for odd } Z, \text{ even } N \text{ or even } Z, \text{ odd } N \,. \\ -a_p A^{-1/2} & \text{for odd } Z, \text{ odd } N \end{cases} \tag{44}$$

In Eq. (43), the first term representing the volume effects (B_{vol}), the second term denoting the surface effects (B_{surf}), the third term describing the Coulomb interactions (B_{Coul}), the fourth term describing the effect of isospin asymmetry (B_{asym}), and the last term covering the effects of the pairing (B_{p}) (Martin and Shaw 2019). The exponent of A in the pairing term is derived from experimental binding-energy data. While it was previously commonly assumed to be $-3/4$, more recent experimental data suggest that a value closer to $-1/2$ is more accurate (Myers 1977). Furthermore, the coefficients for various terms are provided as $a_{\mathrm{v}} = 15.56$ MeV, $a_{\mathrm{s}} = 17.23$ MeV, $a_{\mathrm{c}} = 0.697$ MeV, $a_{\mathrm{a}} = 93.14$ MeV, and $a_{\mathrm{p}} = 12$ MeV. These values constitute one of the datasets employed to adjust the binding energy curve for $A > 20$ (Martin and Shaw 2019). Since there are no surface effects and Coulomb effects are also ignored in infinite isospin-symmetric nuclear matter, the net binding energy is approximated as the binding energy's volume term ($B \approx B_{vol}$). In Myers and Swiatecki (1966), the volume term of the binding energy per nucleon $B/A = -15.677$ MeV at $n_{\mathrm{sat}} = 0.16146$ fm^{-3} was obtained from a non-relativistic semi-empirical four-parameter mass formula with coefficients from the liquid-drop model using the experimental masses of 49 heavy nuclei. In addition, using experimental data from 1654 ground state masses of nuclei with N, Z $\geq$ 8, $B/A = -16.24$ MeV at $n_{\rm sat} = 0.16114$ fm^{-3} was obtained from non-relativistic semi-empirical four-parameter mass formula with coefficients from shell-corrected Thomas–Fermi model (Myers and Swiatecki 1996).

7.1.3 Compressibility at saturation

The incompressibility, usually referred to as compressibility, or compression modulus $K_\infty = 9 \frac{dP}{dn_B}\Big|_{n_{\rm sat}}$ of infinite nuclear matter at saturation is considered one of the vital constraints for dense matter, as it determines the stiffness of the EoS.[8] In finite nuclear systems, the isoscalar giant monopole resonance (ISGMR) establishes a direct empirical link between the finite nucleus compressibility, K_A and the centroid energy $E_{\rm ISGMR}$ (Colo et al. 2014),

$$E_{\rm ISGMR} = \sqrt{\frac{\hbar^2 K_A}{m\langle r^2\rangle_m}} \tag{45}$$

where $\left\langle r^2 \right\rangle_m$ is the mean square mass-radius in the ground state and m is the nucleon mass.

Furthermore, the finite compressibility can be expressed in terms of the liquid-drop mass formula (Blaizot 1980)

$$K_A = K_{\rm vol} + K_{\rm surf}A^{-1/3} + K_{\rm asym}\left(\frac{N-Z}{A}\right)^2 + K_{\rm Coul}\frac{Z^2}{A^{4/3}} \tag{46}$$

where $K_{\rm vol}$, $K_{\rm surf}$, $K_{\rm asym}$ and $K_{\rm Coul}$ define the volume, surface, asymmetry and Coulomb terms, respectively. The $K_{\rm vol}$ term is related to the nuclear matter properties such that $K_{\rm vol} \approx K_\infty$ (Blaizot 1980). Inelastic scattering of isoscalar probes can be used to determine the ISGMR strength distribution experimentally. The α particle has been the most widely used and emerges as effective probe for such observations. The discussion of ISGMR collective nucleon excitations from ^{90}Zr and ^{208}Pb nuclei suggests $K_\infty = 240 \pm 20$ MeV (Colo et al. 2014; Todd-Rutel and Piekarewicz 2005; Colo et al. 2004; Agrawal et al. 2003), but there might be a softening in this value caused by pairing (Cao et al. 2012; Vesely et al. 2012).

Khan and Margueron (2012) argue that properties of nuclei do not set constraints on the EoS at saturation density, but rather at an average density of ~ 0.11 fm^{-3}, that they design as crossing density. Considering that the giant monopole resonance of a chain of nuclei constrains the third derivative of the energy per unit of volume at this density, they arrive at $K_\infty = 230 \pm 40$ MeV with 17% uncertainty.

In another work, the authors reviewed in detail the methods of analysis of giant monopole resonance (GMR) data, as well as values obtained using different techniques and theories between 1961 and 2016 covering a range $K_\infty = 100-380$

[8] (R3 #14) At saturation density one can also write $K_\infty = 9\left[n_B^2 \frac{d^2E/A}{dn_B^2}\right]_{n_{sat}}$.

MeV (see references within Table 1 of Stone et al. (2014)), with a trend to higher values in relativistic than in non-relativistic mean-field models. Without any microscopic model assumptions, except (marginally) the Coulomb effect, $250 < K_\infty < 315$ MeV was obtained and it was shown that surface characteristics have a crucial influence in vibrating nuclei (Stone et al. 2014).

7.1.4 Hyperon potentials

In this section, we list various experimental results relevant to hyperon potentials. In relativistic models, the hyperon potential is defined as U_H = vector interaction+ scalar interaction, while in non-relativistic models it is defined as $U_H = E_H - T_H - m_H$, the difference between single-particle energy and kinetic energy (plus mass), both usually discussed at saturation. Although more constraining data exists for the potential of the Λ hyperon, data also exists for the Σ and Ξ potentials.

The analysis of data from the level spectra of Λ hypernuclei from π^+K^+ and $K^-\pi^-$ reactions produced at emulsion and bubble chambers showed that the single-particle energies of Λ-hypernuclei vary smoothly with number of nucleons A and are well reproduced considering the potential at nuclear saturation density $U(\Lambda - N) \equiv U_\Lambda = -28$ MeV (Millener et al. 1988). Considering a slightly different renormalization of the data obtained from the KEK 12-GeV PS and superconducting kaon spectrometer (SKS, Hasegawa et al. 1996), the value $U_\Lambda = -30$ MeV was obtained in Gal et al. (2016). In Shen et al. (2006), using a relativistic mean-field approach, in particular the TM1 model (Sugahara and Toki 1994), the data of Hasegawa et al. (1996) have been used to fit the σ-Λ coupling, while considering that the Λ-vector mesons couplings are determined from the SU(6) quark model. A Λ-hyperon potential in nuclear matter at saturation density equal to $U_\Lambda = -30$ MeV was obtained. Similar values, $U_\Lambda = -30$ to -32 MeV, have been obtained with other relativistic mean-field models using the same constraints (Fortin et al. 2018).

As discussed in Gal et al. (2016), measurements at KEK (the High Energy Accelerator Research Organization in Japan) of the Σ^- spectrum (Noumi et al. 2002; Saha et al. 2004) have indicated that the Σ-nucleon potential is strongly repulsive. A Σ potential in symmetric nuclear matter considered reasonable is of the order $U_\Sigma = 30 \pm 20$ MeV (Gal et al. 2016). Note that the Σ-hyperon is predicted by some models, such as the QMC model, not to appear in dense matter for the regime relevant for neutron stars (Stone et al. 2021).

Concerning the Ξ-nucleon potential, the measurement of ${}^{12}_{\Xi}$Be (Khaustov et al. 2000) was described with a Wood–Saxon potential of the order of $U_\Xi = -14$ MeV (Gal et al. 2016). The more recent Kiso event (Nakazawa et al. 2015) for ${}^{15}_{\Xi}$Ca, if interpreted as a $1p$ state, seems to indicate a deeper potential. Relativistic mean field models have been constrained by this measurement and a depth of the order of $U_\Xi = -15$ to -19 MeV was obtained (Fortin et al. 2020). Recently, considering five two-body Ξ capture events to two single Λ-hypernuclei obtained by KEK (Aoki et al. 2009; Nakazawa et al. 2015) and J-PARC (the Japan Proton Accelerator Research

Complex, Hayakawa et al. 2021), Friedman and Gal (2021) have calculated an attractive Ξ-nucleon interaction with a depth $U_\Xi \gtrsim 20$ MeV ($U_\Xi = 21.9 \pm 0.7$ MeV).

Note, however, that a much less attractive Ξ potential has been calculated by the HAL-QCD collaboration (Inoue 2019). Using hyperon interactions extracted from a (2+1) lattice QCD in Brueckner–Hartree–Fock (BHF) calculation with a statistical error of approximately ±2 MeV related with the QCD Monte Carlo simulation, the HAL QCD collaboration anticipated $U_\Lambda = -28$ MeV, $U_\Sigma = +15$ MeV, and $U_\Xi = -4$ MeV (Inoue 2019) at $n_{\rm sat}$, which agrees with $p - \Xi^-$ correlation functions from the ALICE collaboration using 3-momenta measured at $s = \sqrt{13}$ TeV (Fabbietti et al. 2021; ALICE Collaboration 2020).

In a recent study, Friedman and Gal (2023) conducted a direct optical potential analysis, examining the binding energies of both $1s_\Lambda$ and $1p_\Lambda$ states across the periodic table, covering nuclei from $A = 12$ to $A = 208$. This analytical approach relied on nuclear densities constrained by the charge root-mean-square (r.m.s.) radii. They investigated the three-body ΛNN (repulsive) interactions and found $U_\Lambda^{(3)} = 13.9 \pm 1.4$ MeV. The combined effect on U_Λ, computed as the sum of $U_\Lambda^{(2)}$ and $U_\Lambda^{(3)}$, was calculated to be -26.7 ± 1.7 MeV at the saturation density.

7.1.5 Δ-baryon potential

Here, we list the empirical observations of spin 3/2 Δ baryon-nucleon potential at saturation, which is a helpful quantity when constraining its values in dense matter models. As already discussed, Δ's can replace hyperons without softening the EoS as much, which can be a solution to the hyperon puzzle (Bednarek et al. 2012).

The introduction of a phenomenological Δ-nucleus spin-orbit interaction was used to improve the fit to the experimental π-nucleus angular distributions for $\pi - {}^{16}$O at 114 and 240 MeV, $\pi - {}^{4}$He at 220 and 260 MeV and $\pi - {}^{12}$C at 180 and 200 MeV (Horikawa et al. 1980). It was anticipated that the strength of the Δ-nucleus spin-orbit interaction term is similar (attractive) to the nucleon–nucleon one, i.e. $U_\Delta \approx U_N$ (Horikawa et al. 1980). In another study, the cross-section measurement of electron-nucleus scattering observed in 2.5 GeV Synchrotron at Bonn gives a density-dependent average binding potential $U_\Delta(n_B) \simeq -75\ n_B(r)/n_{\rm sat}$ MeV (Koch and Ohtsuka 1985). Furthermore, a range of uncertainty is estimated from the electron-nucleus, pion nucleus, scattering and photoabsorption experiments i.e. -30 MeV $+U_N < U_\Delta < U_N$, with $U_N \simeq -(50 - 60)$ MeV, which leads to the constraint -90 MeV $< U_\Delta < -50$ MeV (Drago et al. 2014).

7.2 Symmetry energy $E_{\rm sym}$ and derivative L

To translate between isospin symmetric matter and matter in neutron stars, with very low charge fraction, we make use of the symmetry energy $E_{\rm sym}$. The determination of the saturation density $E_{\rm sym}$, L, $K_{\rm sym}$, and J parameters is very challenging, and involves large experimental and theoretical efforts (Estee et al. 2021). At low densities, we have some fundamental understanding of the symmetry energy but, at large densities, the uncertainty becomes extremely large. At subsaturation densities, nuclear structure probes can generally confine the symmetry energy most effectively, whereas astronomical observations and heavy-ion collisions are two significant methods for constraining the symmetry energy from subsaturation to suprasaturation densities (Zhang and Chen 2015). The main source of uncertainty in the E_{sym} parameters are the poorly understood many-nucleon interactions.

Within nuclei, the distributions of neutrons and protons differ, and change with Z and A. As a result, nuclear property measurements, particularly for neutron-rich nuclei, hold promise for restricting nuclear symmetry energy parameters. It is shown that, in addition to the Fermi momentum and the isospin asymmetry parameter, the neutron skin thickness ($R_{\mathrm{skin}} = R_n - R_p$) of asymmetric semi-infinite nuclear matter is a function of the Coulomb energy, $E_{\mathrm{sym,sat}}$, L_{sat}, and $K_{\mathrm{sym,sat}}$ (see Suzuki 2022 and references therein). The neutron skin thickness of heavy nuclei such as ^{208}Pb has been shown to correspond linearly to the slope parameter L, which can also be written as $L = 3n_B \frac{dE_{\mathrm{sym}}}{dn_B}$, regulating the density dependence of E_{sym} around the saturation density n_{sat}. As a result, the high-accuracy measurement of R_{skin} is a significant limit on the density dependence of E_{sym} at subnormal densities.

7.2.1 E_{sym} and L at saturation

In this section, we review various experiments to determine the symmetry energy parameters at saturation density. Li et al. (2019) illustrated a comprehensive list of E_{sym} and L at saturation density from 28 model assessments of terrestrial nuclear tests and astrophysical data with the fiducial values of (31.6 ± 2.7) MeV and (58.9 ± 16) MeV, respectively (see Fig. 25). The SπRIT collaboration from the Radioactive Isotope Beam Factory (RIBF) at RIKEN measured the spectra of charged pions produced by colliding rare isotope tin (Sn) beams with isotopically enriched Sn targets to restrict their contributions at suprasaturation densities. The calculated slope of the symmetry energy is $(42 < L < 117)$ MeV using ratios of charged pion spectra observed at high transverse momentum (Estee et al. 2021). Furthermore, using the available experimental nuclear masses of heavy nuclei, E_{sym} was determined, which was employed further to extract $L = (50.0 \pm 15.5)$ MeV at $n_{\mathrm{sat}} = 0.16$ fm^{-3} (Fan et al. 2014). As discussed earlier, the thickness of the neutron skin of ^{208}Pb offers a strict laboratory restriction on the symmetry energy. Using the strong correlation between R_{skin} and L, the updated Lead Radius Experiment (PREX-II) reported a large $L = (106 \pm 37)$ MeV based on both theoretical and actual data, consistently overestimating present limits (Reed et al. 2021). In another PREX-II study, for ^{208}Pb the parity-violating asymmetry A_{PV} was studied using non-relativistic and relativistic energy density functionals (Reinhard et al. 2021). A neutron skin thickness of $R_{\mathrm{skin}}^{208} = (0.19 \pm 0.02)$ fm, and a small value of derivative $L = (54 \pm 8)$ MeV were obtained. Recent studies have considered both CREX and PREXI+II measurements in their analysis. In Lattimer (2023), the symmetry energy slope was determined to be $L = 53 \pm 13$ MeV. However, Reinhard et al. (2022) have shown the PREX and CREX measurements cannot be simultaneously described by nuclear models, defined in the framework of an energy density functional theory, which are also consistent with a

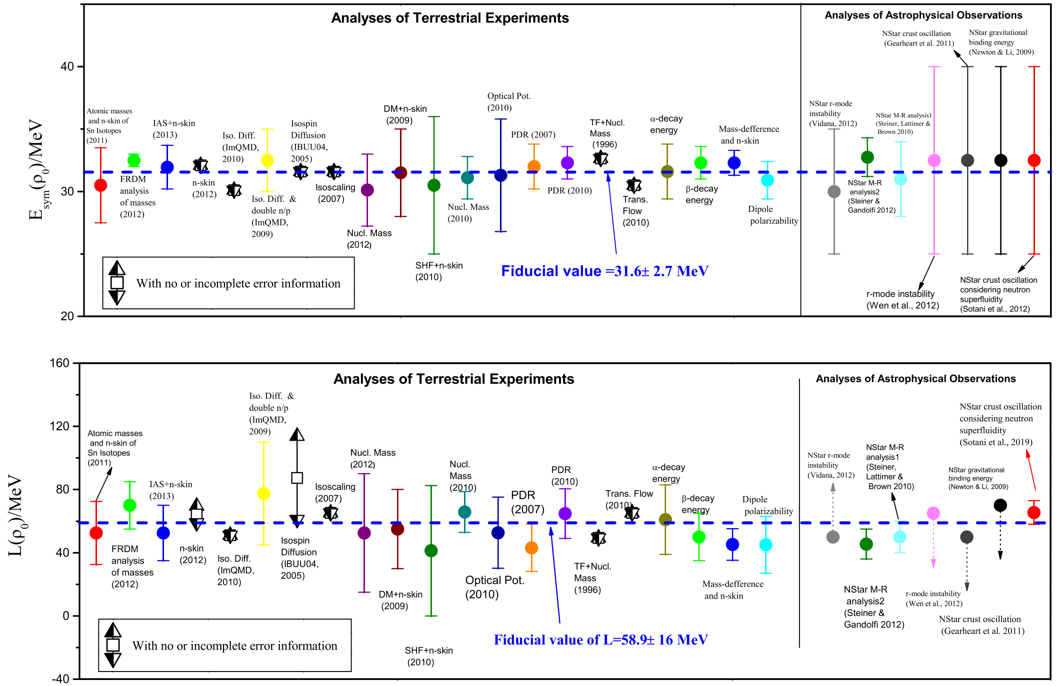

Fig. 25 Constraints on saturation values of the symmetry energy (upper panel) and slope (lower panel) at saturation from terrestrial and astrophysical experiments. Image reproduced with permission from Li et al. (2019), copyright by SIF/Springer

pool of global nuclear properties. The two panels of Fig. 25 are in line with earlier astrophysical estimates and show considerably lower values for the symmetry energy and its slope at saturation than those recently published using a specific set of relativistic energy density functionals to describe PREXII as in Reed et al. (2021).

7.2.2 E_{sym} and L below saturation

Constraining the symmetry energy parameters at subsaturation density also helps to restrict the EoS of the neutron-star matter. Here, we discuss experimental measurements for E_{sym} and L below saturation density. The moderate-temperature nuclear gases formed in the collisions of ^{64}Zn projectiles with ^{92}Mo and ^{197}Au target nuclei showed a large degree of α particle clustering at low densities. From isoscaling analyses of the yields of nuclei with $A \leq 4$, the temperature and density-dependent symmetry energy coefficients of these gases at densities $n_B = 0.01\ n_{\mathrm{sat}} - 0.05\ n_{\mathrm{sat}}$ were evaluated as $E_{\mathrm{sym}} = 9.03 - 13.6$ MeV (see Table 1 of Kowalski et al. 2007). From the measured excitation energies of the isovector giant quadrupole resonance (IVGQR) in ^{208}Pb, the symmetry-energy value $E_{\mathrm{sym}} = (23.3 \pm 0.6)$ MeV at $n_B = 0.1$ fm^{-3} was estimated (Roca-Maza et al. 2013). Furthermore, the magnitude of the symmetry energy $E_{\mathrm{sym}} = (26.65 \pm 0.20)$ MeV at a subsaturation cross density $n_B \approx 0.11$ fm^{-3} was determined by the binding energy difference ΔE between a heavy isotope pair (Zhang and Chen 2013). Using the available experimental nuclear masses of heavy nuclei $E_{\mathrm{sym,sat}}$ was determined, which was employed further to extract the density dependent symmetry-energy value, $E_{\mathrm{sym}} = (25.98 \pm 0.01)$ MeV and the derivative, $L = (49.6 \pm 6.2)$ MeV at $n_B = 0.11$ fm^{-3} (Fan et al. 2014). The magnitude of the symmetry energy E_{sym} at densities around $n_{\mathrm{sat}}/3$ was determined uniquely by the electric dipole polarizability α_{D} in ^{208}Pb. A stringent constraint of $E_{\mathrm{sym}} = (15.91 \pm 0.99)$ MeV was observed at $n_B = 0.05$ fm^{-3} and for the range $n_B = 0.02 - 0.11$ fm^{-3}, results are illustrated by the red band in Fig. 26 (Zhang and Chen 2015). In addition, the nuclear symmetry coefficients were extracted using

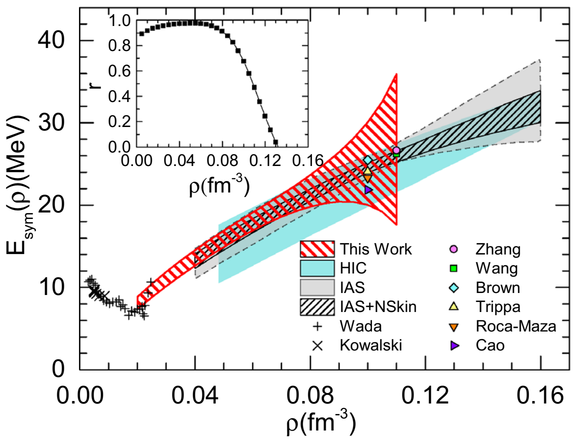

Fig. 26 Empirical constraints on symmetry energy versus baryon density. Image reproduced with permission from Zhang and Chen (2015), copyright by APS

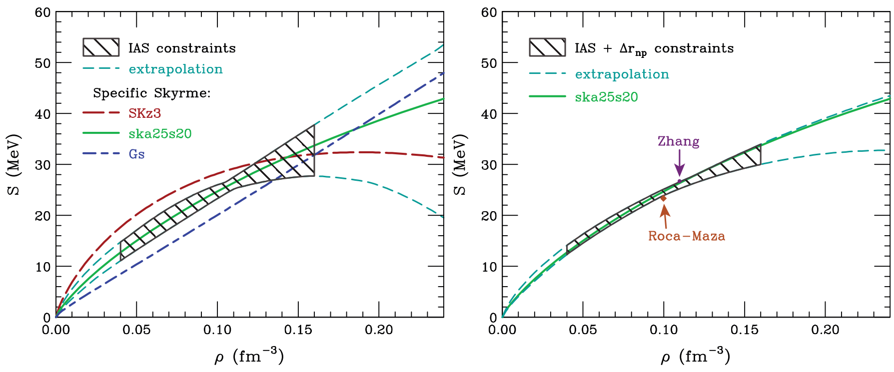

Fig. 27 Symmetry energy versus baryon density without (left:) and with (right:) neutron-skin constraints. Image reproduced with permission from Danielewicz and Lee (2014), copyright by Elsevier

Table 7 Empirical constraints related to isospin asymmetric matter for the symmetry energy and slope parameter

Constraints	Value	n_B	References
E_{sym} (MeV)	31.6 ± 2.7	n_{sat}	Li et al. (2019)
	9.03–13.6	$0.01-0.05$ fm^{-3}	Kowalski et al. (2007)
	15.91 ± 0.99	0.05 fm^{-3}	Zhang and Chen (2015)
	23.3 ± 0.6	0.1 fm^{-3}	Roca-Maza et al. (2013)
	26.65 ± 0.20	0.11 fm^{-3}	Zhang and Chen (2013)
	25.98 ± 0.01	0.11 fm^{-3}	Fan et al. (2014)
	32.20 ± 2.4	$0.04 \leq n_B$ (fm^{-3}) ≤ 0.13	Danielewicz and Lee (2014)
L (MeV)	58.16 ± 16	n_{sat}	Li et al. (2019)
	50 ± 15.5	n_{sat}	Fan et al. (2014)
	54 ± 8	n_{sat}	Reinhard et al. (2021)
	106 ± 37	n_{sat}	Reed et al. (2021)
	49.6 ± 6.2	0.11 fm^{-3}	Fan et al. (2014)

excitation energies to isobaric analog states (IAS) and charge invariance. A narrow constraint of $E_{sym} = 32.2 \pm 2.4$ MeV was obtained at saturation and for the range of density $(0.04 \lesssim n_B \lesssim 0.13)$ fm^{-3}, the behavior is illustrated in the left panel of Fig. 27. In addition, inclusion of the skin constraints narrows down the constraints for the same density range (see right panel of Fig. 27) and at saturation E_{sym} becomes (32.2 ± 1.1) MeV (Danielewicz and Lee 2014). Table 7 summarizes the empirical constraints on E_{sym} and L.

7.2.3 Correlation of symmetry energy and slope parameter

As discussed earlier, the symmetry energy and its slope play an important role in constraining the EoS of neutron-star matter. Thus, the correlation between both parameters can be useful to understand their interdependence. Lattimer and Steiner (2014) illustrate the experimentally determined values of $E_{\rm sym}$ and L parameters. Figure 28 contains different regimes coming from the observations of low-energy heavy-ion collisions, astrophysics, neutron skin, giant dipole resonance (GDR), isobaric analog states (IAS), and dipole polarizability.

7.2.4 Heavy-ion collision measurements of neutron skin of ^{197}Au and ^{238}U

Recently, from heavy-ion collisions it was discovered that it is possible to measure the nucleus charge radius by using the energy dependence of the Breit–Wheeler process (Wang et al. 2023). Additionally, the STAR experiment has also found the total matter radius determined using the diffractive photoproduction in ultra-peripheral collisions to observe a unique spin interference pattern in the angular distribution of $\rho \rightarrow \pi^+ + \pi^-$ decays (Abdallah et al. 2023c). Combining these two measurements, they found that for ^{197}Au there was a neutron skin of 0.17 ± 0.03 (stat.) ± 0.08 (syst.) fm and a for ^{238}U there was a neutron skin of 0.44 ± 0.05 (stat.) ±

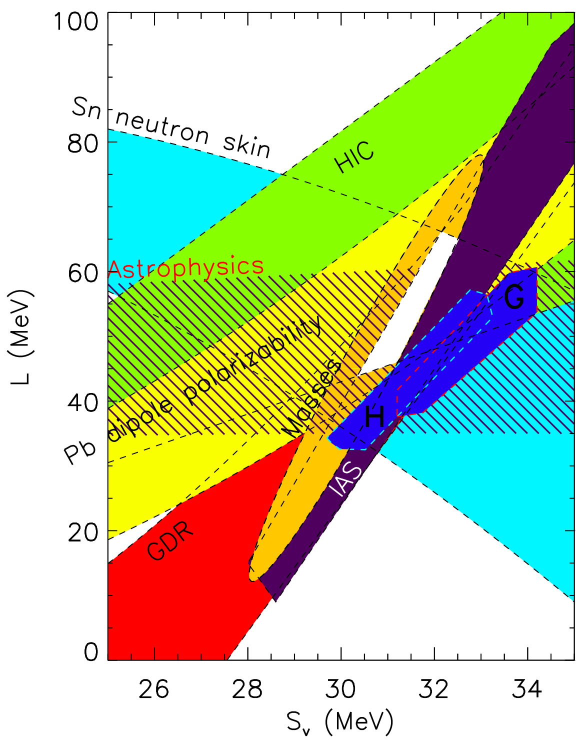

Fig. 28 Correlation between symmetry energy and slope at saturation. Image reproduced from Lattimer and Steiner (2014), copyright by SIF/ Springer

0.08 (syst.) fm (Abdallah et al. 2023c). To date these results have not yet been used in theoretical calculations but they do appear to be consistent with PREXII results.

7.3 Isospin-symmetric nuclear matter liquid–gas critical point

The similarity between nucleon–nucleon and Van der Waals interactions suggested the possibility of also having a liquid–gas phase transition in nuclear matter if the effects of Coulomb and limited size are ignored. If that is the case, the existence of a coexistence line associated with a first order transition stopping at a critical point is expected. Indeed in the liquid–gas phase diagram, the surface tension of a nucleus diminishes as its temperature rises, eventually disappearing at a point known as the critical point (Landau and Lifshitz 2000). The liquid–gas phase transition line divides two separate nuclear phases, i.e., nuclei (towards low density) and bulk matter (towards high density). In many models, if just nuclear matter is taken into account and Coulomb interactions are disregarded, this phase transition is anticipated as first-order (Soma and Bozek 2009; Fiorilla et al. 2012) whereas in astrophysical environments, the production of nuclei involves the Coulomb and other interactions that occur in finite nuclei, where some characteristics of the first order phase transition may be retained (Buyukcizmeci et al. 2013).

In this section, we review the different nuclear reaction experiments relevant to the liquid–gas phase diagram of symmetric nuclear matter. The critical temperature found in the studies on finite nuclei (Karnaukhov et al. 2003; Elliott et al. 2013; Natowitz et al. 2002; Karnaukhov et al. 2008) is in the range $T_c \approx 17 - 20$ MeV. In a study from empirical observations of limiting temperatures, the critical temperature of infinite nuclear matter was found to be $T_c = 16.6 \pm 0.86$ MeV (Natowitz et al. 2002). Also, in p + Au collisions at 8.1 GeV, the charge distribution of the intermediate mass fragments was analyzed in the framework of the statistical multifragmentation model, and the critical temperature was found to be $T_c = 20 \pm 3$ MeV (Karnaukhov et al. 2003). Furthermore, in another study, a critical temperature $T_c > 15$ MeV was anticipated for the nuclear liquid–gas phase transition from fission and multifragmentation data (see Fig. 29 for a list of T_c obtained from different studies (Karnaukhov et al. 2008)). In the latest study, six different sets of experimental data obtained from the Lawrence Berkeley National Laboratory 88-inch cyclotron, Indiana Silicon Sphere Collaboration and Equation of State Collaboration indicated that infinite nuclear matter has critical rms values for temperature $(T_c = 17.9 \pm 0.4)$ MeV, density $n_{Bc} = (0.06 \pm 0.01)$ fm^{-3}, and pressure $P_c = (0.31 \pm 0.07)$, MeV fm^{-3} (Elliott et al. 2013). The critical temperature is essentially a parameter that affects how quickly the surface tension falls when the nuclei heat up. The values mentioned in this work are useful to constrain nuclear matter models at finite temperature. They are summarized in Table 8.

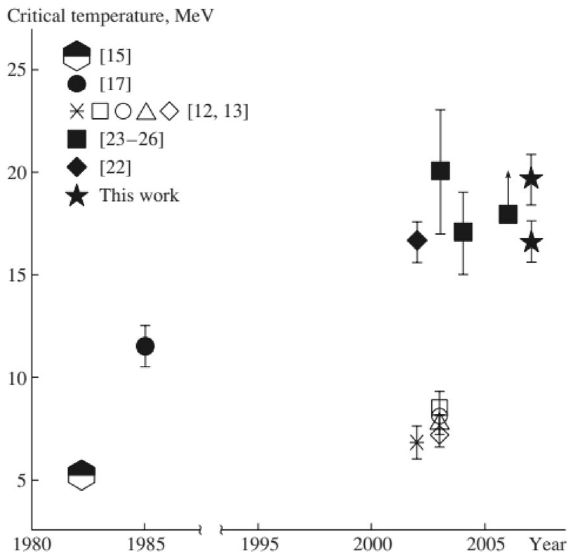

Fig. 29 Constraints on the critical temperature of the liquid–gas phase transition. Image reproduced with permission from Karnaukhov et al. (2008), copyright by Pleiades

Table 8 Empirical constraints for the critical temperature, pressure, and baryon density related to liquid–gas critical point

Constraints	Value	References
T_c (MeV)	16.6 ± 0.86	Natowitz et al. (2002)
	20 ± 3	Karnaukhov et al. (2003)
	>15	Karnaukhov et al. (2008)
	17.9 ± 0.4	Elliott et al. (2013)
P_c (MeV fm^{-3})	0.31 ± 0.07	Elliott et al. (2013)
n_{Bc} (fm^{-3})	0.06 ± 0.01	Elliott et al. (2013)

8 Observational constraints: astrophysics

Measurements of stellar masses, radii and tidal deformabilities play a central role in establishing a link between neutron stars' microscopic and macroscopic properties. These observables depend upon the internal structure and composition of the matter that makes up the neutron star. This microphysical information is relayed through the equations of stellar structure by the EoS, which cannot be directly measured in laboratory experiments at the densities, temperatures, and isospin asymmetries relevant for neutron star cores. In the astrophysical context, the EoS is probed by a variety of astronomical observations of neutron stars, particularly electromagnetic observations in the radio and X-ray bands, as well as gravitational waves from the coalescence of compact binaries. These probes assume general relativity is the correct description of nature, as otherwise, observables would also depend on the theory of gravity that is considered (see e.g. Yagi and Yunes 2013a, b).

Neutron stars, whether in isolation or in binaries systems, are described by the Einstein equations, which require, as input, the EoS to connect the pressure to the energy density and temperature inside the stars. When in isolation and when considering non-rotating stars, the Einstein equations reduce to the Tolman–Oppenheimer–Volkoff (TOV) equations (Tolman 1939; Oppenheimer and Volkoff 1939), whose solution determines the mass and radius of the non-rotating star for a given central energy density. Choosing a sequence of central densities yields a sequence of pairs of masses and radii, which together form a "mass-radius curve." For slowly-rotating stars, one can expand the Einstein equations in small rotation through the Hartle–Thorne approximation (R4 #17) (Hartle 1967; Paschalidis and Stergioulas 2017), and the solution to the expanded equations yields the moment of inertia at first order in rotation, the quadrupole moment and a mass correction at second order. When a neutron star is not in isolation, but instead is perturbed by some external object (like a binary companion), the perturbations can also be studied by solving the linearized Einstein equations about a neutron star background, which yields the tidal deformabilities of the star. In this way, one can construct various curves, including the mass-radius, moment of inertia-mass, quadrupole moment-mass, tidal deformability-mass, and so on, that represent neutron stars of various central densities. These curves can change shape depending on the EoS prescribed. Since one usually expects neutron stars to all be described by a unique EoS,[9] there is a single set of such curves that correctly describes Nature. Astrophysical observations can determine which set is the correct one, and thus, which is the correct EoS to describe neutron stars.

In the next subsections, we discuss one by one the empirical macroscopic constraints obtained from various astronomical observations. We provide summaries of current constraints with only brief explanations of the underlying measurements. See, e.g., Chatziioannou (2020) for a more thorough review.

It is important to remember that the densities relevant for the cores of neutron stars can certainly reach several times nuclear saturation density (see, e.g., Fig. 5 of Legred et al. (2021), Fig. 6 of Mroczek et al. (2023b), Fig. 7 of Pang et al. (2024), Fig. 5 of Koehn et al. (2024) for recent estimations), and connecting constraints from theoretical calculations and terrestrial experiments at lower densities (Sects. 5 and 7) to neutron star observations will almost certainly involve some extrapolation. The amount of freedom allowed in extrapolation schemes may be, but are not always, informed by physical models. Some care is, therefore, warranted when interpreting results combining low-density and high-density constraints as the conclusions often depend on the particular extrapolation scheme chosen. See, e.g., Essick et al. (2021b), Essick et al. (2021a), Legred et al. (2022) for more discussion.

8.1 Neutron-star maximum mass

The measurement of a neutron star's mass sets a lower bound on the mass above which the neutron star must undergo gravitational collapse to a black hole. Most observed neutron stars spin slowly compared with their Keplerian break-up rotation rate. Hence, mass observations are often used to bound the maximum mass

[9] There is also the possibility of a two-family scenario, where more than one distinct EoS is used to describe neutron stars (Drago et al. 2016)

achievable by cold, non-rotating neutron stars even though spin can support up to approximately $\sim 20\%$ additional mass (Breu and Rezzolla 2016).

The radio pulsar PSR J1614-2230 was the first massive pulsar to be measured with a mass close to two solar masses (Demorest et al. 2010). Recently, its mass was updated to $1.908^{+0.016}_{-0.016}\,M_\odot$ (Arzoumanian et al. 2018). The pulsar PSR J1614-2230 has a low mass companion and the determination of its mass was possible through the measurement of the Shapiro delay, a retardation effect of the pulse signal that originates on the curvature of the space-time close to the companion, and is given by (van Straten et al. 2001)

$$\Delta_S = 2r\ln[1 - s\cos(\phi - \phi_0)],$$

where $s = sin\, i$ with i the inclination angle, $r = Gm_2/c^3$ with m_2 the companion mass, ϕ is the orbital phase, and ϕ_0 is the phase where the pulsar is on the opposite side of the companion from Earth. The measurement of Δ_S allows the determination of the companion mass.

The record for the highest precisely and reliably measured neutron star mass currently belongs to the 2.8-ms radio pulsar (PSR) J0740+6620, which is likely orbiting an ultracool white-dwarf companion (Fonseca et al. 2021b). The data sets of this study are integrated pulse arrival-time measurements, obtained using the Canadian Hydrogen Intensity Mapping Experiment (CHIME) and 100-meter Green Bank Telescope (GBT). Timing solutions for PSR J0740+6620 were produced by the GBT and CHIME/Pulsar collaborations using narrow-band and wide-band times of arrival. While comparing the credible intervals of the Shapiro delay parameters across different dispersion measures (DM) evolution models, all calculated solutions were found to be statistically compatible with different DMX models at 68.3% credibility, with a 1% fluctuation in the credible intervals of the Shapiro delay. The Shapiro delay, also known as the gravitational time delay effect, is an increase in travel time of a signal when it passes near a massive object. The estimated mass of PSR J0740+6620 is $m_p = 2.08^{+0.07}_{-0.07}$ $\mathrm{M}_\odot$ (in solar masses) and of its companion is $m_c = 0.253^{+0.006}_{-0.005}\,M_\odot$ (Fonseca et al. 2021b) calculated at 1σ (68.3% credibility), which is consistent with the earlier observations of Cromartie et al. (2019) (posterior in Fonseca et al. 2021a).

The second-highest precisely and reliably measured pulsar mass belongs to PSR J0348+0432. For this pulsar, the mass is estimated to be $2.01 \pm 0.04\,M_\odot$ at 68.3% credibility based on a combination of radio timing of the pulsar and precise spectroscopy of the white dwarf companion, which has a mass of $m_c = 0.173 \pm 0.003\,M_\odot$ and is in a 2.46-h orbit around the pulsar (Antoniadis et al. 2013).

An *upper* limit on the maximum mass of nonrotating neutron stars has been placed, albeit with more substantial astrophysical uncertainties, using the properties of short gamma-ray bursts. These have long been assumed to be produced by the merger of two neutron stars, with the remnant either forming a black hole immediately or collapsing quickly to a black hole (e.g., Murguia-Berthier et al. 2014). Under this assumption, and working off of the mass distribution of double neutron star systems in our Galaxy, several authors proposed that the maximum mass $M_{\max}$ of a nonrotating neutron star was $\sim 2.3\,M_\odot$ (Bauswein et al. 2013; Lawrence

Table 9 Pulsar empirical constraints on the maximum mass of neutron stars. Pulsar timing constraints are less susceptible to modeling assumptions than current gravitational wave constraints

Neutron Star	$M_{\rm max}$ ($M_\odot$)	References
PSR J0740+6620	$\geq$ 2.08 ± 0.07	Fonseca et al. (2021b)
PSR J0348+0432	$\geq$ 2.01 ± 0.04	Antoniadis et al. (2013)

et al. 2015; Fryer et al. 2015). The gravitational wave and electromagnetic data from the binary neutron-star merger GW170817, for which it was possible to make a good estimate of the total mass, also led to an estimate of $M_{\rm max} \sim 2.2 - 2.3\, M_\odot$ (Margalit and Metzger 2017). The argument for rapid collapse to a black hole is that otherwise the rapidly spinning remnant will spin down and inject energy into the remnant, which has not been seen. A key but unproven assumption in this argument is that the merger process will generate strong and ultimately poloidal magnetic fields that will spin down the remnant.

Detailed modeling of the electromagnetic afterglow of GW170817 has led to other estimates of the maximum mass, e.g., $M_{\rm max} \simeq 2.16^{+0.17}_{-0.15}\, M_\odot$ (Rezzolla et al. 2018), $M_{\rm max} \simeq 2.16 - 2.28\, M_\odot$ Ruiz et al. (2018), $M_{\rm max} \simeq 2.13^{+0.17}_{-0.11}\, M_\odot$ (Shao et al. 2020), $M_{\rm max} \lesssim 2.3\, M_\odot$ (Shibata et al. 2019), $M_{\rm max} \simeq 2.21^{+0.12}_{-0.12}\, M_\odot$ (Nathanail et al. 2021), and if the assumption that the GW170817 event resulted in a black hole is relaxed, $M_{\rm max} \simeq 2.43^{+0.16}_{-0.12}\, M_\odot$ Ai et al. (2020). All of these estimates are subject to numerical and modeling uncertainties, but they are promising for the future. The empirical constraints on the maximum neutron-star mass are summarized in Table 9

There have also been several claims of heavier neutron stars. The discovery of black-widow pulsars with masses estimated as $2.13 \pm 0.04\, M_\odot$ (Romani et al. 2021) for PSR J1810+1744 and $2.35 \pm 0.17\, M_\odot$ (Romani et al. 2022) (68% confidence) for PSR J0952-0607 have been reported; however, these mass measurements are less secure (due to possible systematics) than the Shapiro delay-based measurements for PSR J0740+6620 and PSR J0348+0432. Moreover, the $2.59^{+0.08}_{-0.09}\, M_\odot$ secondary component of the compact binary merger GW190814 has been touted as a potential heavy neutron star because it is less massive than known black holes (Abbott et al. 2020b). However, its proximity in mass to the ostensible $2.7\, M_\odot$ black-hole remnant of GW170817, and the lack of any observed tidal effects or electromagnetic counterpart, have made people think that it may be more likely to be a black hole. However, this conclusion comes with some caveats. Tidal effects for such massive neutron stars are expected to be very small (Tan et al. 2020), and in fact, not observable with the sensitivity of ground interferometers when this event was detected (Abbott et al. 2020b). Moreover, the lack of an electromagnetic counterpart in the gamma range could be due to the short-gamma ray burst not being pointed toward Earth. An electromagnetic counterpart at other frequencies could have been missed due to the poor localization of the event in the sky through only the use of gravitational wave information. See de Sá et al. (2022) for a discussion on many

Table 10 Empirical constraints related to mass-radii from NICER

Neutron Star	$M(M_{\odot})$	Radius (km)	References
PSR J0030+0451	$1.34^{+0.15}_{-0.16}$	$12.71^{+1.14}_{-1.19}$	Riley et al. (2019a)
PSR J0740+6620	$2.072^{+0.067}_{-0.066}$	$12.39^{+1.30}_{-1.98}$	Riley et al. (2021a)
PSR J0030+0451	$1.44^{+0.15}_{-0.14}$	$13.02^{+1.24}_{-1.06}$	Miller et al. (2019)
PSR J0740+6620	$2.08^{+0.07}_{-0.07}$	$13.7^{+2.6}_{-1.5}$	Miller et al. (2021b)

candidates whose masses that lay inside the so called mass gap (between confirmed masses of neutron stars and black holes).

In another work, the authors used binary inclination i from lightcurve modeling and observed that J1810 offers a lower limit on the NS maximum mass of $2\,M_{\odot}$ at 99.7% credibility (Romani et al. 2021). A flat, but asymmetric, light-curve maximum and a deep, narrow minimum were observed in the spectrophotometry of the companion of PSR J1810+1744 measured by the Keck telescope. A hot pole, surface winds, and severe gravity darkening (GD) around the L_1 point are all indicated by the maximum, whereas the minimum denotes significant limb darkening and a low underlying temperature. Having the radial-velocity amplitude $K_C = 462.3 \pm 2.2$ km s^{-1} recorded by the Keck telescope provides a precise neutron star mass of $M_{NS} = 2.13 \pm 0.04\,M_{\odot}$, a value which is very relevant to the understanding of the dense-matter EoS (Romani et al. 2021).

8.2 Neutron-star mass-radius regions from NICER

NICER is a soft X-ray telescope mounted on the International Space Station (ISS) in 2017. The main aim of NICER is to determine masses and radii of neutron stars using pulse-profile modeling of neighboring rotation-powered millisecond pulsars. The NICER observations have played an important role in lowering the ambiguity in the EoS of high-density matter (1.5–5 n_{sat}) at zero temperature. See Table 10 for a summary of the results reported from NICER, which we now discuss in detail. A word of warning is due at this stage: the results presented in this table (and in other tables in this section) are a summary, and in particular, the reported masses and radius with error bars are not a square in probability space. Rather, these quantities correspond to the maximum likelihood points and the 90% confidence regions of the marginalized posterior after a careful Bayesian parameter estimation study. Two-dimensional posteriors on mass and radius are not squares, but rather complicated shapes due to the correlation between parameters.

Using Bayesian parameter estimation based on pulse-profile modeling of the NICER XTI event data for the isolated pulsar PSR J0030+0451, Miller et al. (2019) (posterior Bogdanov et al. 2019) reported a gravitational mass $M = 1.44^{+0.15}_{-0.14}\,M_{\odot}$ and a circumferential radius $R = 13.02^{+1.24}_{-1.06}$ km at 68% credibility. For the same data but using slightly different models and a different statistical sampler, Riley et al.

(2019a) found $M = 1.34^{+0.15}_{-0.16}\,M_\odot$ and $R = 12.71^{+1.14}_{-1.19}\,\mathrm{km}$ (posterior Riley et al. 2019b and raw data Steiner 2020).

The heavy binary pulsar PSR J0740+6620 has a NICER count rate only $\sim 5\%$ that of PSR J0030+0451 and thus NICER data alone are insufficient for precise measurements of the mass and radius. As a result, for this pulsar, radio data and X-ray data from the X-ray Multi-Mirror (XMM-Newton) satellite were analyzed jointly with the NICER data. Miller et al. (2021b) (posterior Miller et al. 2021a) found $M = 1.97 - 2.15\,M_\odot$ and $R = 12.21 - 16.33\,\mathrm{km}$, both at 68% credibility, whereas Riley et al. (2021a) (posterior Riley et al. 2021b) reported $M = 2.072^{+0.067}_{-0.066}\,M_\odot$ and $R = 12.39^{+1.30}_{-0.98}\,\mathrm{km}$.

The differences between the two results for PSR J0740+6620 (e.g., Miller et al. report a -1σ radius of 12.21 km, compared with Riley et al.'s estimate of 11.41 km) led the two groups to explore the reasons for the difference. As discussed in Miller et al. (2021b), the primary differences are as follows. First, Miller et al. (2021b) use a relative calibration between NICER and XMM-Newton that is consistent with the results of cross-calibration tests, whereas Riley et al. (2021a) assume a much broader range of possible cross-calibration factors. When Riley et al. (2021a) apply the same cross-calibration as Miller et al. (2021b), they find a -1σ radius of 11.75 km rather than 11.41 km, i.e., this accounts for almost half the difference from the 12.21 km -1σ radius of Miller et al. (2021b). Second, Riley et al. (2021a) have a hard prior upper bound on the radius of 16 km, whereas Miller et al. (2021b) allow the radius to be anything that fits the data. When Miller et al. (2021b) eliminate all solutions with $R > 16$ km, their -1σ radius drops to 12.06 km. The remaining difference, of 0.31 km (compared with the original 0.8 km), is likely to be primarily due to different choices of statistical samplers: Miller et al. (2021b) use the parallel-tempered Markov chain Monte Carlo code PT-emcee whereas Riley et al. (2021a) use the nested sampler MultiNest; Miller et al. (2021b) argue that at least in this specific case, MultiNest may underestimate the widths of the posteriors. More generally, there are many moving parts within such analyses and sometimes subtle choices on how data is analyzed or which data is analyzed can affect the resulting constraints; see Essick (2022) for an example related to data selection.

8.3 Other observational constraints on neutron star masses and radii

Quiescent low-mass X-ray binaries (QLMXBs) in globular clusters are promising objects for mass and radius constraints because (i) previous accretion events heat up the surface increasing their luminosity, (ii) their magnetic fields are expected (but not observed) to be relatively small, the magnetic field having been buried by the accretion, and (iii) the globular cluster permits a determination of the distance. There are several QLMXBs which have been used to obtain mass and radius constraints, see Steiner et al. (2018) for a recent analysis leading to neutron star radii between 10 and 14 km. However, there are still a significant number of potential systematics which may be important: (i) the magnetic field is not observed so the assumption of a small magnetic field is untested, (ii) the determination of the mass and radius requires a model of the neutron star atmosphere and the associated emergent X-ray spectrum,

(iii) the composition of the accreted material is not always known, (iv) the temperature is often presumed to be uniform over the entire surface, and (v) scattering by the interstellar medium leads to a reddening of the spectrum which is not fully known. A recent attempt (Al-Mamun et al. 2021) to search for systematic effects in QLMXB models compared QLMXBs to other mass and radius constraints (including those from LIGO/Virgo and NICER) and found no evidence for systematics that poison the QLMXB results. However, this result may change as the LIGO/Virgo constraints improve.

Within the supernova remnant HESS J1731-347, a star that is the centre compact object has been studied, according to Doroshenko et al. (2022), the mass and radius of this star is estimated to be $M = 0.77^{+0.20}_{-0.17} M_\odot$ and $R = 10.4^{+0.86}_{-0.78}$ km, respectively, which is based on the modeling of Gaia observations and X-ray spectrum. This result depends critically on the assumption that the entire surface of the star emits at the same temperature, based on the lack of clear modulation with the stellar rotation. With that assumption, and the assumption that the atmospheric effects of the stellar magnetic field can be neglected, a carbon atmosphere is favored over a hydrogen or a helium atmosphere. However, as shown by Alford and Halpern (2023), nonuniform emission is consistent with the data on several similar sources (and preferred for some). This means that hydrogen and helium atmospheres are possible, and these could imply standard masses well above one solar mass. According to their estimation, this star can be either the lightest neutron star ever discovered or a strange star with exotic EoS (Doroshenko et al. 2022). The examination of several SN explosions indicates that it is not feasible to form a neutron star (NS) with a mass less than approximately $1.17 M_\odot$ (Suwa et al. 2018), which begs the issue of what astronomical activity might result in such a small mass. Di Clemente et al. (2022) suggests that in the case of strange quark stars, masses of the order or less than one solar mass can be found and it is conceivable to construct a cogent astrophysical hypothesis that accounts for the object's mass, radius, and gradual cooling.

8.4 Neutron-star tidal deformability from gravitational waves

The phasing of the gravitational waves emitted during the inspiral of a compact binary system is sensitive to the tidal deformation experienced by each component as a result of its companion's non-uniform gravitational field. The size of the deformation is measured by the tidal deformability parameter (Flanagan and Hinderer 2008; Hinderer 2008), which depends on the neutron-star mass and the EoS. The tidal deformabilities of the individual neutron stars appear at leading order in the gravitational waveform as a mass-weighted average known as the chirp or binary tidal deformability, $\tilde{\Lambda}$ (Favata 2014; Wade et al. 2014), namely

$$\tilde{\Lambda} = \frac{16}{13}\left[\frac{(m_1 + 12m_2)m_1^4\Lambda_1 + (m_2 + 12m_1)m_2^4\Lambda_2}{(m_1 + m_2)^5}\right] \tag{47}$$

where m_1 and m_2 are the masses of the binary components and Λ_1 and Λ_2 are their (dimensionless) individual tidal deformabilities. Because an EoS predicts a unique

m–Λ relation, a measurement of $\tilde{\Lambda}$ and the binary masses helps to determine the EoS in a manner analogous to constraints on the m–R relation.

8.4.1 Extraction of $\tilde{\Lambda}$ from GW170817

The first measurement of $\tilde{\Lambda}$ was enabled by the detection of gravitational waves from the binary neutron-star merger GW170817 (Abbott et al. 2017a) by LIGO and Virgo. The binary tidal deformability was constrained simultaneously with the system's masses, spins and other source properties via Bayesian parameter estimation, in which a waveform model is compared against the data to produce a likelihood function over the waveform parameters (see e.g. Thrane and Talbot 2019). Because the tidal deformability is mass-dependent, and gravitational-wave measurements of the binary mass ratio and spins are correlated, the constraints on $\tilde{\Lambda}$ are sensitive to prior assumptions about spin. Assuming that both neutron stars in GW170817 had low spins, in keeping with the Galactic double neutron-star population (Burgay et al. 2003; Stovall et al. 2018), LIGO and Virgo measured $\tilde{\Lambda} = 300^{+500}_{-190}$ at 90% confidence; without this assumption, the constraint is $\tilde{\Lambda} \leq 630$ (Abbott et al. 2019). The joint constraints on $\tilde{\Lambda}$ and the binary masses are expressible in terms of a multi-dimensional posterior probability distribution, samples from which are available in the data release accompanying (Abbott et al. 2019).

As before, a word of caution is due at this stage. The measurements of the tidal deformabilities discussed above and below in this section result from a Bayesian parameter estimation study, and as such, they correspond to the maximum likelihood points and the 90% confidence region of the marginalized posterior. The posterior is multi-dimensional and covariances exist between the various parameters that enter the waveform model. Therefore, 2-dimensional confidence regions, like that for the chirp tidal deformability and the chirp mass, are not squares, but rather complicated shapes, which can be found in the papers we have referenced here.

The analysis of the signal (Abbott et al. 2019), and therefore, the tidal deformabilities reported above, do not require both of GW170817's compact objects to share the same EoS, implicitly leaving open the possibility that one of them is a black hole. Because of the kilonova and short gamma-ray burst counterparts to GW170817, however, it is reasonable to assume that the merger consisted of two neutron stars (De et al. 2018). The assumption that all neutron stars share the same EoS implicitly relates Λ_1 and Λ_2, since the EoS predicts a unique m–Λ relation. De et al. (2018) approximated this relation as $\Lambda_1 = \Lambda_2 {m_2}^6/{m_1}^6$, and used it to further constrain $\tilde{\Lambda} = 222^{+420}_{-138}$ at 90% confidence, assuming low neutron-star spins. An alternative to making such an approximation is to average over many different candidate EoSs drawn from a prior distribution: each EoS sample imposes an exact relation between Λ_1 and Λ_2, and the EoS uncertainty encoded in the prior distribution is propagated to $\tilde{\Lambda}$ by the averaging process. Of course, this approach requires modeling the EoS. Typically, this is done phenomenologically, either with a parameterization of the pressure-density relation—e.g., a spectral decomposition (Lindblom 2010)—or with a *Gaussian process* (Landry and Essick 2019)—i.e., a distribution over functions described by a mean function and a covariance kernel. Caveats exist here, however, because the choice of the functional form of the EoS may not include the entire phase space of possible equations of state that can be conceived from nuclear physics.

The EoS-averaging approach was taken by Essick et al. (2020), which modeled the EoS nonparametrically as a Gaussian process and found $\tilde{\Lambda} = 245^{+361}_{-160}$ (posterior median and 90% highest-probability-density credible region). The Gaussian process was constructed to explore the entire functional space of EoSs that obey causality (sound speed less than the speed of light) and thermodynamic stability (positive semidenfinite sound speed), subject to the requirement that the EoS support neutron star masses of at least $1.93\,M_\odot$ to account for the existence of heavy pulsars. For comparison, when using a spectral parameterization for the EoS, one find $\tilde{\Lambda} = 412^{+313}_{-262}$ for the posterior *median* and 90% credible regions. If one instead uses the global maximum of the posterior, one finds $\tilde{\Lambda} = 225^{+500}_{-75}$, which is similar to that found using Gaussian processes.

Electromagnetic observations of GW170817's kilonova counterpart have also been used to constrain the binary tidal deformability. However, these bounds depend on the assumed kilonova lightcurve model and are thus subject to sizeable systematic uncertainty: for example, $\tilde{\Lambda} \geq 197$ (90% confidence) (Coughlin et al. 2018), $120 < \tilde{\Lambda} < 1110$ (90% confidence) (Breschi et al. 2021), and $109 \leq \tilde{\Lambda} \leq 137$ (68% confidence) (Nicholl et al. 2021) was found. Unlike the gravitational-wave measurements of binary tidal deformability, $\tilde{\Lambda}$ does not appear directly as a parameter in the light curve model and it must therefore be constrained via correlations with other observables. As discussed in Radice et al. (2018), these constraints come with the possibility of large errors associated with uncertainties in the mass ratio of the system (Kiuchi et al. 2019).

8.4.2 Extraction of individual tidal deformabilities Λ_1 and Λ_2

The binary tidal deformability $\tilde{\Lambda}$ is the tidal parameter that is best constrained by gravitational-wave observations. However, it is the individual tidal deformability Λ that is directly determined by the EoS together with the equations of stellar structure. The relation between the individual tidal deformabilities Λ_1 and Λ_2 of each member of a compact binary and the system's binary tidal deformability is expressed in Eq. (47). Generally, the component masses m_1 and m_2 are constrained simultaneously with $\tilde{\Lambda}$ through the Bayesian parameter estimation of the gravitational-wave signal. Thus, we have one equation relating three tidal parameters: a measurement of $\tilde{\Lambda}$ only determines Λ_1 and Λ_2 up to a residual degeneracy. This degeneracy is broken by a tidal parameter $\delta\tilde{\Lambda}$ that appears at higher order in the gravitational waveform, but it is unfortunately not measurable with current detectors (Wade et al. 2014).

Nonetheless, this degeneracy is not an obstacle to translating measurements of $\tilde{\Lambda}$ into constraints on Λ_1 and Λ_2: it is simply the case that every combination of Λ_1 and Λ_2 that produces the same $\tilde{\Lambda}$ is equally likely. Thus, one can build up a posterior for

Λ_1 and Λ_2 by sampling in the individual tidal deformabilities, and assigning to each sample the likelihood of the $\tilde{\Lambda}$ it predicts (the likelihood is the ratio of the posterior probability to the prior probability). The result of this process for GW170817 is the posterior on the component tidal deformabilities illustrated in Fig. 10 of Abbott et al. (2019); notice that there is a direction in Λ_1–Λ_2 plane along which there is essentially no constraint due to the degeneracy.

One can break the degeneracy by introducing an additional layer of modeling that imposes a common EoS for both components of GW170817: this augments Eq. (47) with a second equation relating the individual tidal deformabilities. As in the case of $\tilde{\Lambda}$, this can be done either with an approximate relation connecting Λ_1 and Λ_2, or by averaging over an EoS prior distribution.

Using the Gaussian process-based EoS representation described above, Essick et al. (2020) mapped the binary tidal deformability measurement into constraints of $\Lambda_1 = 148^{+274}_{-125}$ and $\Lambda_2 = 430^{+519}_{-301}$ on the component tidal deformabilities, under the assumption of low neutron-star spins. Moreover, since each EoS sample from the Gaussian process prescribes an exact m–Λ relation, this approach allows the tidal deformability to be inferred at any mass scale. Essick et al. (2020) also constrained $\Lambda_{1.4} = 211^{+312}_{-137}$ (posterior median and 90% highest-probability-density credible region).

Alternatively, one can break the degeneracy with an approximate EoS-insensitive relation connecting the individual tidal deformabilities. The so-called binary Love relations (Yagi and Yunes 2016) fit the relation between two independent linear combinations of Λ_1 and Λ_2 to many candidate EoSs from nuclear theory. With the neutron stars' individual tidal deformabilities related by way of this EoS-insensitive relation (Chatziioannou et al. 2018), augmented with Gaussian white noise to account for the scatter in the fit, and Λ's mass dependence expanded in a series about $1.4\,M_\odot$, Abbott et al. (2018) reduced the joint constraint on binary masses and $\tilde{\Lambda}$ from GW170817 to an estimate of the tidal deformability of a $1.4\,M_\odot$ neutron star: $\Lambda_{1.4} = 190^{+390}_{-120}$ at the 90% credible level, in the low neutron-star spin scenario. The empirical constraints on the tidal deformability from GW170817 are summarized in Table 11.

The results for the extracted tidal deformability posteriors from GW170817 are shown in Fig. 30. While there is a lot of overlap for the posteriors of the EoS insensitive (universal relations), spectral EoS, and Gaussian Process EoS, they are not exactly the same and this may lead to incorrect conclusions when extracting the EoS unless one is careful. For instance, most nuclear physics EoS tend towards higher values of Λ for a given M. Thus, the EoS insensitive posterior may seem more restricting than the spectral EoS. However, since these are 90% confidence regions, all posteriors are actually statistically consistent with each other, and one cannot simply take the edge of one posterior to draw strong conclusions without a careful Bayesian parameter estimation study.

Table 11 Empirical constraints on the tidal deformability for GW170817 event from LIGO and Virgo

Tidal deformability	References	Confidence level
$\tilde{\Lambda} = 300^{+500}_{-190}$	Low spins (Abbott et al. 2019)	90%
$\tilde{\Lambda} \leq 630$	Minimal assumptions (Abbott et al. 2019)	90%
$\tilde{\Lambda} = 222^{+420}_{-138}$	Common EoS via analytic approximation (De et al. 2018)	90%
$\Lambda_{1.4} = 190^{+390}_{-120}$	Common EoS via binary Love relation (Abbott et al. 2018)	90%
$\tilde{\Lambda} = 245^{+361}_{-160}$	Common EoS via Gaussian process (Essick et al. 2020)	90%
$\Lambda_{1.4} = 211^{+312}_{-137}$	Common EoS via Gaussian process (Essick et al. 2020)	90%

8.4.3 Connecting tidal deformabilities to the mass-radius sequence

Because the neutron-star tidal deformability scales strongly with the stellar radius ($\Lambda \sim R^5/m^5$), and because R is an easily interpretable parameter, gravitational-wave measurements of Λ have often been translated into radius constraints in the literature. Nonetheless, we stress that gravitational waves from compact binaries do not directly measure the neutron star radius—the mapping from Λ to R necessarily involves additional modeling. This modeling can either be done at the level of the EoS (e.g. with a spectral or nonparametric EoS representation), or at the level of the mapping itself (e.g., with an EoS-insensitive relation between Λ and the stellar compactness m/R).

In Abbott et al. (2018), LIGO and Virgo mapped the joint posterior on component tidal deformabilities and masses from GW170817 (assuming a binary Love relation) into a posterior on m_1, m_2, R_1 and R_2 by adopting a spectral parameterization for the EoS. The original posterior was used to compute the likelihood of each spectral EoS

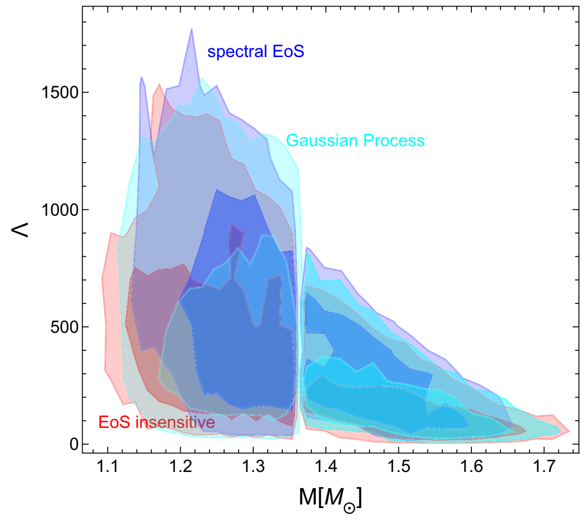

Fig. 30 Constraints on the tidal deformability using the universal relations (EOS insensitive), the spectral EOS and an EoS constructed from Gaussian Processes. The universal-relation constraint and spectral-EoS constraint are obtained using GW170817 data. The Gaussian Process constraint is obtained by combining GW170817, PSR 1614-2230, PSR 0348+0432, and PSR 0740+6620 (mass only) data. Shaded regions are shown at the 68% and 95% confidence regions

realization, and then for each component mass sample from the original posterior, the radius predicted by the EoS realization's mass-radius relation was assigned that likelihood. This procedure led to inferred radii of $R_1 = 11.9^{+1.4}_{-1.4}$ km and $R_2 = 11.9^{+1.4}_{-1.4}$ km.

LIGO and Virgo also implented an alternative approach that used an EoS-insensitive Λ–m/R relation. For each component mass and component tidal deformability sample from the original posterior, Λ was mapped to m/R using the relation from Yagi and Yunes (2017), and the radius was extracted using the sampled mass. The uncertainty in the EoS-insensitive relation fit was modeled as Gaussian white noise in the relation. This procedure led to inferred radii of $R_1 = 10.8^{2.0}_{-1.7}$ km and $R_2 = 10.7^{2.1}_{-1.5}$ km. The small differences versus the radius constraints with the spectral EoSs illustrate the systematic uncertainty that arises from the extra modeling required.

In De et al. (2018), a different EoS-insensitive relation was used to map from the tidal deformability measurement to a radius constraint. Imposing the common EoS assumption $\Lambda_1 = \Lambda_2 {m_2}^6/{m_1}^6$ described above and assuming that both neutron stars involved in GW170817 had the same radius R, the definition of the binary tidal deformability reduces to $\tilde{\Lambda} \propto (R/\mathcal{M})^6$, where $\mathcal{M} \equiv \eta^{3/5}(m_1 + m_2)$ is the chirp mass with $\eta \equiv m_1 m_2/(m_1 + m_2)^2$, in an EoS-insensitive relation that can be fit to a sample of various EoSs. The joint posterior on $\tilde{\Lambda}$ and $\mathcal{M}$ from GW170817 thus determines the common neutron-star radius, which was reported as $R = 10.7^{+2.1}_{-1.6}$ km at 90% confidence.

A summary of the resulting mass-radius constraints from both NICER and GW170817 can be see in Fig. 31. The heavier NICER pulsar (J0740+6620) has the highest posterior distribution that is centered nearly directly above the lighter NICER pulsar (J0030+0451) and the GW170817 extracted mass-radius posteriors. However,

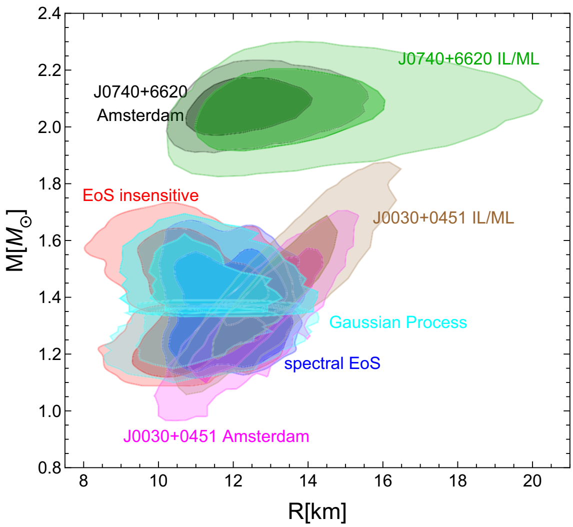

Fig. 31 Constraints on the mass-radius using the universal relations (EOS insensitive), the spectral EOS and an EoS sampled through Gaussian Processes. The universal-relation constraint and spectral-EoS constraint are obtained using GW170817 data. The Gaussian Process constraint is obtained by combining GW170817, PSR 1614-2230, PSR 0348+0432, and PSR 0740+6620 (mass only) data. NICER constraints from both the Amsterdam and Illinois/Maryland groups are show for both J0030+0451 and J0740+6620. Shaded regions show the 68% and 95% confidence region

there is some probability that heavier $M \sim 2M_\odot$ may bend to the right. The lighter constraints from J0030+0451 and GW170817 overlap in their posteriors as well, although GW170817 generally prefers a slightly smaller radius whereas J0030+0451's posterior prefers larger radii.

Different methods (EoS insensitive, spectral EoS and Gaussian processes) to obtain the posterior on the mass and radius with GW170817 may look different, but they all are statistically consistent with each other. In particular, we stress that one cannot use these posteriors, over-impose mass-radius curves computed with a given EoS and then determine whether the EoS is allowed or disallowed based on whether it overlaps with the contours or not. This is because each point on this plane, including those outside the 68% or the 95% confidence regions, actually has a posterior weight assigned to it (not shown in the figure). Therefore, comparison of the data to a given EoS needs to be done carefully in a Bayesian way. Overall, all posteriors are statistically consistent with each other at this time, and therefore, there is no tension between observations. Eventually, if future observations place better constraints on the mass-radius plane, one expects that a single EoS will be preferred by all data.

We emphasize that these radius constraints from GW170817 are merely approximate encapsulations of the information contained within the tidal deformability measurements reported above, which are directly constrained by the gravitational waves. When considering gravitational wave data, it is thus preferable to use the tidal deformability measurements to constrain the EoS.

8.4.4 GW190425, GW200105, and GW200115

Gravitational waves also yielded a constraint on tidal deformability in the binary neutron-star merger GW190425, but because this system was heavier (such that its $\tilde{\Lambda}$ is intrinsically smaller) and more distant (such that its signal-to-noise ratio was lower), the constraint is not competitive with GW170817. Similarly, GW200105 and GW200115 (Abbott et al. 2021) both likely contained neutron stars, but tidal effects were unmeasureably small in these systems due to the large masses of their companions and subsequent rapid orbital evolution through GW emission.

9 Outlook

In this work, we compiled various constraints coming from nuclear and astrophysics related to dense matter and neutron stars. We encapsulated up to date results from first principle theories and experimental observations. The usage of anticipated next-generation facilities and theoretical advancements are the most promising path for substantial improvement above current limitations. With enhanced sensitivity and expanded receiver bandwidths, several upcoming astrophysical radio observatories, including the dish Deep Synoptic Array, DSA-2000 (Hallinan et al. 2019), Canadian Hydrogen Observatory and Radio-transient Detector, CHORD (Vanderlinde et al. 2019), and the next-generation Very Large Array, ngVLA (Chatterjee 2018), will present significant opportunities in pulsar science. Also, we anticipate seeing more multi-messenger binary neutron-star merger detections in the coming years, the INTEGRAL, Fermi, Swift, and SVOM will observe merging binary neutron stars in conjunction with GW and electromagnetic data during the fourth LIGO-Virgo-KAGRA observing run which started on May, 2023 (Patricelli et al. 2022; Fletcher et al. 2023). Future detections of neutrinos from supernova explosions in our neighborhood will provide information about larger Y_Q at large densities and intermediate temperatures, while with future LIGO and NICER runs the post-merger signal of gravitation waves from neutron-star mergers will provide information about low Y_Q at large densities and large temperatures (Lovato et al. 2022b).

Several improvements are anticipated in the next phase of BES, thanks to the performance enhancements brought on by collider and detector modifications which will help to dig deeper into the high density regime of the QCD phase diagram. Constraining the EoS is not a simple task and significant work from different communities in nuclear and astrophysics is needed to achieve this. Within the nuclear physics community, the diverse models and theories, working in a different regime of QCD phase diagram are to be updated with the modern constraints so that we can have a unified EoS for nuclei, bulk baryonic and quark matter.

Acknowledgements The authors would like to thank Niseem Abdelrahman, Wei Li, Tetyana Galatyuk, and You Zhou for providing comments and assistance in finding the experimental references in this work. The MUSES collaboration is supported by NSF under OAC-2103680. Additional support for the collaboration members includes: DM is supported NSF Graduate Research Fellowship Program under Grant No. DGE - 1746047. JSSM is supported by Consejo Nacional de Ciencia y Tecnologia (CONACYT) under SNI Fellowship I1200/16/2020. CR is supported by NSF under Grants No. PHY-1654219, PHY-2208724, PHY-2116686. MGA is partly supported by DOE, Office of Science, Office of Nuclear Physics under Award No. DE-FG02-05ER41375. VD is supported by NSF under Grants PHY1748621 and NP3M PHY-2116686. MS is supported by DOE, Office of Science No DE-SC0013470. MCM is supported in part by NASA ADAP Grant 80NSSC21K0649. ML thanks the São Paulo Research Foundation (FAPESP) for support under Grants 2021/08465-9, 2018/24720-6, and 2017/05685-2, as well as the support of the Brazilian National Council for Scientific and Technological Development (CNPq). ERM acknowledges support as the John Archibald Wheeler Fellow at Princeton University (PCTS), and from the Institute for Advanced Study. SPH is supported by DOE Grant DE-FG02-00ER41132. PL is supported by the Natural Sciences & Engineering Research Council of Canada (NSERC). CP is supported by FCT (Fundação para a Ciência e a Tecnologia, I.P, Portugal) under Projects No. UIDP/-04564/-2020, No. UIDB/-04564/-2020 and 2022.06460.PTDC. SLS is supported by NSF Grant PHY-2006066 and NASA Grant 80NSSC17K0070, both to UIUC.

References

Aaboud M et al (2017a) Femtoscopy with identified charged pions in proton-lead collisions at $\sqrt{s_{NN}} = 5.02$ TeV with ATLAS. Phys Rev C 96(6):064908. https://doi.org/10.1103/PhysRevC.96.064908. arXiv:1704.01621 [hep-ex]

Aaboud M et al (2017b) Measurement of multi-particle azimuthal correlations in pp, p+Pb and low-multiplicity Pb+Pb collisions with the ATLAS detector. Eur Phys J C 77(6):428. https://doi.org/10.1140/epjc/s10052-017-4988-1. arXiv:1705.04176 [hep-ex]

Aaboud M et al (2018) Measurement of the azimuthal anisotropy of charged particles produced in $\sqrt{s_{NN}} = 5.02$ TeV Pb+Pb collisions with the ATLAS detector. Eur Phys J C 78(12):997. https://doi.org/10.1140/epjc/s10052-018-6468-7. arXiv:1808.03951 [nucl-ex]

Aaboud M et al (2019) Correlated long-range mixed-harmonic fluctuations measured in pp, p+Pb and low-multiplicity Pb+Pb collisions with the ATLAS detector. Phys Lett B 789:444–471. https://doi.org/10.1016/j.physletb.2018.11.065. arXiv:1807.02012 [nucl-ex]

Aad G et al (2012a) Measurement of the azimuthal anisotropy for charged particle production in $\sqrt{s_{NN}} = 2.76$ TeV lead-lead collisions with the ATLAS detector. Phys Rev C 86:014907. https://doi.org/10.1103/PhysRevC.86.014907. arXiv:1203.3087 [hep-ex]

Aad G et al (2012b) Measurement of the pseudorapidity and transverse momentum dependence of the elliptic flow of charged particles in lead-lead collisions at $\sqrt{s_{NN}} = 2.76$ TeV with the ATLAS detector. Phys Lett B 707:330–348. https://doi.org/10.1016/j.physletb.2011.12.056. arXiv:1108.6018 [hep-ex]

Aad G et al (2013) Measurement of the distributions of event-by-event flow harmonics in lead-lead collisions at $\sqrt{s_{NN}} = 2.76$ TeV with the ATLAS detector at the LHC. JHEP 11:183. https://doi.org/10.1007/JHEP11(2013)183. arXiv:1305.2942 [hep-ex]

Aad G et al (2014a) Measurement of event-plane correlations in $\sqrt{s_{NN}} = 2.76$ TeV lead-lead collisions with the ATLAS detector. Phys Rev C 90(2):024905. https://doi.org/10.1103/PhysRevC.90.024905. arXiv:1403.0489 [hep-ex]

Aad G et al (2014b) Measurement of flow harmonics with multi-particle cumulants in Pb+Pb collisions at $\sqrt{s_{\mathrm{NN}}} = 2.76$ TeV with the ATLAS detector. Eur Phys J C 74(11):3157. https://doi.org/10.1140/epjc/s10052-014-3157-z. arXiv:1408.4342 [hep-ex]

Aad G et al (2020) Measurement of the azimuthal anisotropy of charged-particle production in Xe+Xe collisions at $\sqrt{s_{NN}} = 5.44$ TeV with the ATLAS detector. Phys Rev C 101(2):024906. https://doi.org/10.1103/PhysRevC.101.024906. arXiv:1911.04812 [nucl-ex]

Aamodt K et al (2011a) Femtoscopy of pp collisions at $\sqrt{s} = 0.9$ and 7 TeV at the LHC with two-pion Bose–Einstein correlations. Phys Rev D 84:112004. https://doi.org/10.1103/PhysRevD.84.112004. arXiv:1101.3665 [hep-ex]

Aamodt K et al (2011b) Higher harmonic anisotropic flow measurements of charged particles in Pb–Pb collisions at $\sqrt{s_{NN}}$=2.76 TeV. Phys Rev Lett 107:032301. https://doi.org/10.1103/PhysRevLett.107.032301. arXiv:1105.3865 [nucl-ex]

Aamodt K et al (2011c) Production of pions, kaons and protons in pp collisions at $\sqrt{s} = 900$ GeV with ALICE at the LHC. Eur Phys J C 71:1655. https://doi.org/10.1140/epjc/s10052-011-1655-9. arXiv:1101.4110 [hep-ex]

Aamodt K et al (2011d) Two-pion Bose-Einstein correlations in central Pb–Pb collisions at $\sqrt{s_{NN}} = 2.76$ TeV. Phys Lett B 696:328–337. https://doi.org/10.1016/j.physletb.2010.12.053. arXiv:1012.4035 [nucl-ex]

Abbott BP et al (2017a) GW170817: observation of gravitational waves from a binary neutron star inspiral. Phys Rev Lett 119(16):161101. https://doi.org/10.1103/PhysRevLett.119.161101. arXiv:1710.05832 [gr-qc]

Abbott BP et al (2017b) Multi-messenger observations of a binary neutron star merger. Astrophys J Lett 848(2):L12. https://doi.org/10.3847/2041-8213/aa91c9. arXiv:1710.05833 [astro-ph.HE]

Abbott BP et al (2018) GW170817: measurements of neutron star radii and equation of state. Phys Rev Lett 121(16):161101. https://doi.org/10.1103/PhysRevLett.121.161101. arXiv:1805.11581 [gr-qc]

Abbott BP et al (2019) Properties of the binary neutron star merger GW170817. Phys Rev X 9(1):011001. https://doi.org/10.1103/PhysRevX.9.011001. arXiv:1805.11579 [gr-qc]

Abbott BP et al (2020a) GW190425: observation of a compact binary coalescence with total mass $\sim 3.4 M_{\odot}$. Astrophys J Lett 892(1):L3. https://doi.org/10.3847/2041-8213/ab75f5. arXiv:2001.01761 [astro-ph.HE]
Abbott R et al (2020b) GW190814: gravitational waves from the coalescence of a 23 solar mass black hole with a 2.6 solar mass compact object. Astrophys J Lett 896(2):L44. https://doi.org/10.3847/2041-8213/ab960f. arXiv:2006.12611 [astro-ph.HE]
Abbott R et al (2021a) Observation of gravitational waves from two neutron star-black hole coalescences. Astrophys J Lett 915(1):L5. https://doi.org/10.3847/2041-8213/ac082e. arXiv:2106.15163 [astro-ph.HE]
Abdallah M et al (2021b) Azimuthal anisotropy measurements of strange and multistrange hadrons in $U+U$ collisions at $\sqrt{s_{NN}}$ =193 GeV at the BNL Relativistic Heavy Ion Collider. Phys Rev C 103 (6):064907. https://doi.org/10.1103/PhysRevC.103.064907. arXiv:2103.09451 [nucl-ex]
Abdallah M et al (2021c) Cumulants and correlation functions of net-proton, proton, and antiproton multiplicity distributions in Au+Au collisions at energies available at the BNL relativistic heavy ion collider. Phys Rev C 104(2):024902. https://doi.org/10.1103/PhysRevC.104.024902. arXiv:2101.12413 [nucl-ex]
Abdallah M et al (2021d) Measurement of the sixth-order cumulant of net-proton multiplicity distributions in Au+Au collisions at $\sqrt{s_{NN}}$ = 27, 54.4, and 200 GeV at RHIC. Phys Rev Lett 127(26):262301. https://doi.org/10.1103/PhysRevLett.127.262301. arXiv:2105.14698 [nucl-ex]
Abdallah M et al (2022a) Centrality and transverse momentum dependence of higher-order flow harmonics of identified hadrons in Au+Au collisions at $\sqrt{s_{NN}}$ = 200 GeV. Phys Rev C 105(6):064911. https://doi.org/10.1103/PhysRevC.105.064911. arXiv:2203.07204 [nucl-ex]
Abdallah M et al (2022b) Collision-system and beam-energy dependence of anisotropic flow fluctuations. Phys Rev Lett 129(25):252301. https://doi.org/10.1103/PhysRevLett.129.252301. arXiv:2201.10365 [nucl-ex]
Abdallah MS et al (2022c) Disappearance of partonic collectivity in $\sqrt{s_{NN}}$ = 3 GeV Au+Au collisions at RHIC. Phys Lett B 827:137003. https://doi.org/10.1016/j.physletb.2022.137003. arXiv:2108.00908 [nucl-ex]
Abdallah M et al (2023a) Azimuthal anisotropy measurement of (multi)strange hadrons in Au+Au collisions at $\sqrt{S_{NN}}$ = 54.4 GeV. Phys Rev C 107(2):024912. https://doi.org/10.1103/PhysRevC.107.024912. arXiv:2205.11073 [nucl-ex]
Abdallah M et al (2023b) Higher-order cumulants and correlation functions of proton multiplicity distributions in $\sqrt{s_{NN}}$ = 3 GeV Au+Au collisions at the RHIC STAR experiment. Phys Rev C 107 (2):024908. https://doi.org/10.1103/PhysRevC.107.024908. arXiv:2209.11940 [nucl-ex]
Abdallah M et al (2023c) Tomography of ultrarelativistic nuclei with polarized photon-gluon collisions. Sci Adv 9(1):eabq3903. https://doi.org/10.1126/sciadv.abq3903. arXiv:2204.01625 [nucl-ex]
Abdallah MS et al (2023d) Pion, kaon, and (anti)proton production in U+U collisions at $\sqrt{s_{NN}}$ = 193 GeV measured with the STAR detector. Phys Rev C 107(2):024901. https://doi.org/10.1103/PhysRevC.107.024901. arXiv:2208.00653 [nucl-ex]
Abdelwahab NM et al (2015) Energy dependence of K/π, p/π, and K/p fluctuations in Au+Au collisions from $\sqrt{s_{\mathrm{NN}}}$ = 7.7 to 200 GeV. Phys Rev C 92(2):021901. https://doi.org/10.1103/PhysRevC.92.021901. arXiv:1410.5375 [nucl-ex]
Abdulhamid M et al (2023) Beam energy dependence of triton production and yield ratio ($\mathrm{N}_t \times \mathrm{N}_p/\mathrm{N}_d^2$) in Au+Au collisions at RHIC. Phys Rev Lett 130:202301. https://doi.org/10.1103/PhysRevLett.130.202301. arXiv:2209.08058 [nucl-ex]
Abelev BI et al (2008a) Centrality dependence of charged hadron and strange hadron elliptic flow from $\sqrt{s_{NN}}$ = 200 GeV Au + Au collisions. Phys Rev C 77:054901. https://doi.org/10.1103/PhysRevC.77.054901. arXiv:0801.3466 [nucl-ex]
Abelev BI et al (2008b) Enhanced strange baryon production in Au + Au collisions compared to p + p at $\sqrt{s_{NN}}$ = 200 GeV. Phys Rev C 77:044908. https://doi.org/10.1103/PhysRevC.77.044908. arXiv:0705.2511 [nucl-ex]
Abelev BI et al (2009) Systematic measurements of identified particle spectra in pp, d^+ Au and Au+Au collisions from STAR. Phys Rev C 79:034909. https://doi.org/10.1103/PhysRevC.79.034909. arXiv:0808.2041 [nucl-ex]
Abelev BI et al (2010a) Charged and strange hadron elliptic flow in Cu+Cu collisions at $\sqrt{s_{NN}}$ = 6.24 and 200 GeV. Phys Rev C 81:044902. https://doi.org/10.1103/PhysRevC.81.044902. arXiv:1001.5052 [nucl-ex]

Abelev BI et al (2010b) Identified particle production, azimuthal anisotropy, and interferometry measurements in Au+Au collisions at $\sqrt{s_{NN}}$ = 9.2 GeV. Phys Rev C 81:024911. https://doi.org/10.1103/PhysRevC.81.024911. arXiv:0909.4131 [nucl-ex]

Abelev B et al (2013a) Centrality dependence of π, K, p production in Pb–Pb collisions at $\sqrt{s_{NN}}$ = 2.76 TeV. Phys Rev C 88:044910. https://doi.org/10.1103/PhysRevC.88.044910. arXiv:1303.0737 [hep-ex]

Abelev B et al (2013b) Directed flow of charged particles at midrapidity relative to the spectator plane in Pb–Pb collisions at $\sqrt{s_{NN}}$=2.76 TeV. Phys Rev Lett 111(23):232302. https://doi.org/10.1103/PhysRevLett.111.232302. arXiv:1306.4145 [nucl-ex]

Abelev BB et al (2013c) K^0_S and Λ production in Pb–Pb collisions at $\sqrt{s_{NN}}$ = 2.76 TeV. Phys Rev Lett 111:222301. https://doi.org/10.1103/PhysRevLett.111.222301. arXiv:1307.5530 [nucl-ex]

Abelev BB et al (2014a) Multi-strange baryon production at mid-rapidity in Pb–Pb collisions at $\sqrt{s_{NN}}$ = 2.76 TeV. Phys Lett B 728:216–227. https://doi.org/10.1016/j.physletb.2014.05.052. [Erratum: Phys. Lett. B 734, 409–410 (2014)]. arXiv:1307.5543 [nucl-ex]

Abelev BB et al (2014b) Multiparticle azimuthal correlations in p-Pb and Pb–Pb collisions at the CERN Large Hadron Collider. Phys Rev C 90(5):054901. https://doi.org/10.1103/PhysRevC.90.054901. arXiv:1406.2474 [nucl-ex]

Abelev BB et al (2014c) Production of charged pions, kaons and protons at large transverse momenta in pp and Pb–Pb collisions at $\sqrt{s_{NN}}$ =2.76 TeV. Phys Lett B 736:196–207. https://doi.org/10.1016/j.physletb.2014.07.011. arXiv:1401.1250 [nucl-ex]

Abelev BB et al (2015) Elliptic flow of identified hadrons in Pb–Pb collisions at $\sqrt{s_{NN}}$ = 2.76 TeV. JHEP 06:190. https://doi.org/10.1007/JHEP06(2015)190. arXiv:1405.4632 [nucl-ex]

Aboona B et al (2023a) Beam energy dependence of the linear and mode-coupled flow harmonics in Au+Au collisions. Phys Lett B 839:137755. https://doi.org/10.1016/j.physletb.2023.137755. arXiv:2211.11637 [nucl-ex]

Aboona BE et al (2023b) Beam energy dependence of fifth and sixth-order net-proton number fluctuations in Au+Au collisions at RHIC. Phys Rev Lett 130(8):082301. https://doi.org/10.1103/PhysRevLett.130.082301. arXiv:2207.09837 [nucl-ex]

Acharya S et al (2017a) Kaon femtoscopy in Pb–Pb collisions at $\sqrt{s_{NN}}$ = 2.76 TeV. Phys Rev C 96(6):064613. https://doi.org/10.1103/PhysRevC.96.064613. arXiv:1709.01731 [nucl-ex]

Acharya S et al (2017b) Linear and non-linear flow modes in Pb–Pb collisions at $\sqrt{s_{NN}}$ = 2.76 TeV. Phys Lett B 773:68–80. https://doi.org/10.1016/j.physletb.2017.07.060. arXiv:1705.04377 [nucl-ex]

Acharya S et al (2018a) Anisotropic flow in Xe–Xe collisions at $\sqrt{s_{NN}}$ = 5.44 TeV. Phys Lett B 784:82–95. https://doi.org/10.1016/j.physletb.2018.06.059. arXiv:1805.01832 [nucl-ex]

Acharya S et al (2018b) Anisotropic flow of identified particles in Pb–Pb collisions at $\sqrt{s_{NN}}$ = 5.02 TeV. JHEP 09:006. https://doi.org/10.1007/JHEP09(2018)006. arXiv:1805.04390 [nucl-ex]

Acharya S et al (2018c) Azimuthally-differential pion femtoscopy relative to the third harmonic event plane in Pb–Pb collisions at $\sqrt{s_{NN}}$ = 2.76 TeV. Phys Lett B 785:320–331. https://doi.org/10.1016/j.physletb.2018.06.042. arXiv:1803.10594 [nucl-ex]

Acharya S et al (2018d) Energy dependence and fluctuations of anisotropic flow in Pb–Pb collisions at $\sqrt{s_{NN}}$ = 5.02 and 2.76 TeV. JHEP 07:103. https://doi.org/10.1007/JHEP07(2018)103. arXiv:1804.02944 [nucl-ex]

Acharya S et al (2018e) Production of ^{4}He and $^4\overline{\mathrm{He}}$ in Pb–Pb collisions at $\sqrt{s_{NN}}$ = 2.76 TeV at the LHC. Nucl Phys A 971:1–20. https://doi.org/10.1016/j.nuclphysa.2017.12.004. arXiv:1710.07531 [nucl-ex]

Acharya S et al (2019a) Event-shape and multiplicity dependence of freeze-out radii in pp collisions at $\sqrt{s}$ = 7 TeV. JHEP 09:108. https://doi.org/10.1007/JHEP09(2019)108. arXiv:1901.05518 [nucl-ex]

Acharya S et al (2019b) Investigations of anisotropic flow using multiparticle azimuthal correlations in pp, p-Pb, Xe–Xe, and Pb–Pb collisions at the LHC. Phys Rev Lett 123(14):142301. https://doi.org/10.1103/PhysRevLett.123.142301. arXiv:1903.01790 [nucl-ex]

Acharya S et al (2019c) One-dimensional charged kaon femtoscopy in p-Pb collisions at $\sqrt{s_{NN}}$ = 5.02 TeV. Phys Rev C 100(2):024002. https://doi.org/10.1103/PhysRevC.100.024002. arXiv:1903.12310 [nucl-ex]

Acharya S et al (2019d) Relative particle yield fluctuations in Pb–Pb collisions at $\sqrt{s_{NN}}$ = 2.76 TeV. Eur Phys J C 79(3):236. https://doi.org/10.1140/epjc/s10052-019-6711-x. arXiv:1712.07929 [nucl-ex]

Acharya S et al (2020a) Global baryon number conservation encoded in net-proton fluctuations measured in Pb–Pb collisions at $\sqrt{s_{\mathrm{NN}}}$ = 2.76 TeV. Phys Lett B 807:135564. https://doi.org/10.1016/j.physletb.2020.135564. arXiv:1910.14396 [nucl-ex]

Acharya S et al (2020b) Higher harmonic non-linear flow modes of charged hadrons in Pb–Pb collisions at $\sqrt{s_{\mathrm{NN}}}$ = 5.02 TeV. JHEP 05:085. https://doi.org/10.1007/JHEP05(2020)085. arXiv:2002.00633 [nucl-ex]

Acharya S et al (2020c) Production of charged pions, kaons, and (anti-)protons in Pb–Pb and inelastic pp collisions at $\sqrt{s_{NN}}$ = 5.02 TeV. Phys Rev C 101(4):044907. https://doi.org/10.1103/PhysRevC.101.044907. arXiv:1910.07678 [nucl-ex]

Acharya A et al (2021a) Measurements of $\pi^{\pm}$, $K^{\pm}$, p and $\bar{p}$ spectra in ^{7}Be+^{9}Be collisions at beam momenta from 19A to 150A GeV/c with the NA61/SHINE spectrometer at the CERN SPS. Eur Phys J C 81(1):73. https://doi.org/10.1140/epjc/s10052-020-08733-x. [Erratum: Eur. Phys. J. C 83, 90 (2023)]. arXiv:2010.01864 [hep-ex]

Acharya A et al (2021b) Spectra and mean multiplicities of π^{-} in central^{40}Ar+^{45}Sc collisions at 13A, 19A, 30A, 40A, 75A and 150A Ge V /c beam momenta measured by the NA61/SHINE spectrometer at the CERN SPS. Eur Phys J C 81(5):397. https://doi.org/10.1140/epjc/s10052-021-09135-3. arXiv:2101.08494 [hep-ex]

Acharya S et al (2021c) Anisotropic flow of identified hadrons in Xe–Xe collisions at $\sqrt{s_{\mathrm{NN}}}$ = 5.44 TeV. JHEP 10:152. https://doi.org/10.1007/JHEP10(2021)152. arXiv:2107.10592 [nucl-ex]

Acharya S et al (2021d) Measurements of mixed harmonic cumulants in Pb–Pb collisions at $\sqrt{s_{NN}}$ = 5.02 TeV. Phys Lett B 818:136354. https://doi.org/10.1016/j.physletb.2021.136354. arXiv:2102.12180 [nucl-ex]

Acharya S et al (2021e) Production of pions, kaons, (anti-)protons and ϕ mesons in Xe–Xe collisions at $\sqrt{s_{\mathrm{NN}}}$ = 5.44 TeV. Eur Phys J C 81(7):584. https://doi.org/10.1140/epjc/s10052-021-09304-4. arXiv:2101.03100 [nucl-ex]

Acharya S et al (2023a) Anisotropic flow and flow fluctuations of identified hadrons in Pb–Pb collisions at $\sqrt{s_{\mathrm{NN}}}$ = 5.02 TeV. JHEP 05:243. https://doi.org/10.1007/jhep05(2023)243. arXiv:2206.04587 [nucl-ex]

Acharya S et al (2023b) Closing in on critical net-baryon fluctuations at LHC energies: cumulants up to third order in Pb–Pb collisions. Phys Lett B 844:137545. https://doi.org/10.1016/j.physletb.2022.137545. arXiv:2206.03343 [nucl-ex]

Acharya S et al (2023c) Light (anti)nuclei production in Pb–Pb collisions at $\sqrt{s_{NN}}$ = 5.02 TeV. Phys Rev C 107(6):064904. https://doi.org/10.1103/PhysRevC.107.064904. arXiv:2211.14015 [nucl-ex]

Ackermann KH et al (2001) Elliptic flow in Au + Au collisions at $\sqrt{s_{NN}}$ = 130 GeV. Phys Rev Lett 86:402–407. https://doi.org/10.1103/PhysRevLett.86.402. arXiv:nucl-ex/0009011

Adam J et al (2016a) $^{3}_{\Lambda}\mathrm{H}$ and $^{3}_{\Lambda}\overline{\mathrm{H}}$ production in Pb–Pb collisions at $\sqrt{s_{\mathrm{NN}}}$ = 2.76 TeV. Phys Lett B 754:360–372. https://doi.org/10.1016/j.physletb.2016.01.040. arXiv:1506.08453 [nucl-ex]

Adam J et al (2016b) Anisotropic flow of charged particles in Pb–Pb collisions at $\sqrt{s_{NN}}$ = 5.02 TeV. Phys Rev Lett 116(13):132302. https://doi.org/10.1103/PhysRevLett.116.132302. arXiv:1602.01119 [nucl-ex]

Adam J et al (2016c) Correlated event-by-event fluctuations of flow harmonics in Pb–Pb collisions at $\sqrt{s_{\mathrm{NN}}}$ = 2.76 TeV. Phys Rev Lett 117:182301. https://doi.org/10.1103/PhysRevLett.117.182301. arXiv:1604.07663 [nucl-ex]

Adam J et al (2016d) Higher harmonic flow coefficients of identified hadrons in Pb–Pb collisions at $\sqrt{s_{\mathrm{NN}}}$ = 2.76 TeV. JHEP 09:164. https://doi.org/10.1007/JHEP09(2016)164. arXiv:1606.06057 [nucl-ex]

Adam J et al (2016e) Multipion Bose–Einstein correlations in pp, p-Pb, and Pb–Pb collisions at energies available at the CERN Large Hadron Collider. Phys Rev C 93(5):054908. https://doi.org/10.1103/PhysRevC.93.054908. arXiv:1512.08902 [nucl-ex]

Adam J et al (2016f) Production of light nuclei and anti-nuclei in pp and Pb–Pb collisions at energies available at the CERN Large Hadron Collider. Phys Rev C 93(2):024917. https://doi.org/10.1103/PhysRevC.93.024917. arXiv:1506.08951 [nucl-ex]

Adam J et al (2018) Correlation measurements between flow harmonics in Au+Au collisions at RHIC. Phys Lett B 783:459–465. https://doi.org/10.1016/j.physletb.2018.05.076. arXiv:1803.03876 [nucl-ex]

Adam J et al (2019a) Azimuthal harmonics in small and large collision systems at RHIC top energies. Phys Rev Lett 122(17):172301. https://doi.org/10.1103/PhysRevLett.122.172301. arXiv:1901.08155 [nucl-ex]

Adam J et al (2019b) Collision-energy dependence of p_t correlations in Au + Au collisions at energies available at the BNL Relativistic Heavy Ion Collider. Phys Rev C 99(4):044918. https://doi.org/10.1103/PhysRevC.99.044918. arXiv:1901.00837 [nucl-ex]

Adam J et al (2019c) Collision-energy dependence of second-order off-diagonal and diagonal cumulants of net-charge, net-proton, and net-kaon multiplicity distributions in Au + Au collisions. Phys Rev C 100 (1):014902. https://doi.org/10.1103/PhysRevC.100.014902. [Erratum: Phys. Rev. C 105, 029901 (2022)]. arXiv:1903.05370 [nucl-ex]

Adam J et al (2020a) Beam energy dependence of net- Λ fluctuations measured by the STAR experiment at the BNL Relativistic Heavy Ion Collider. Phys Rev C 102(2):024903. https://doi.org/10.1103/PhysRevC.102.024903. arXiv:2001.06419 [nucl-ex]

Adam J et al (2020b) Bulk properties of the system formed in $Au + Au$ collisions at $\sqrt{s_{\mathrm{NN}}}$ =14.5 GeV at the BNL STAR detector. Phys Rev C 101(2):024905. https://doi.org/10.1103/PhysRevC.101.024905. arXiv:1908.03585 [nucl-ex]

Adam J et al (2020c) Investigation of the linear and mode-coupled flow harmonics in Au+Au collisions at $\sqrt{s_{NN}}$ = 200 GeV. Phys Lett B 809:135728. https://doi.org/10.1016/j.physletb.2020.135728. arXiv:2006.13537 [nucl-ex]

Adam J et al (2020d) Strange hadron production in Au+Au collisions at $\sqrt{s_{\mathrm{NN}}}$ = 7.7, 11.5, 19.6, 27, and 39 GeV. Phys Rev C 102(3):034909. https://doi.org/10.1103/PhysRevC.102.034909. arXiv:1906.03732 [nucl-ex]

Adam J et al (2021a) Flow and interferometry results from Au+Au collisions at $\sqrt{s_{NN}}$ = 4.5 GeV. Phys Rev C 103(3):034908. https://doi.org/10.1103/PhysRevC.103.034908. arXiv:2007.14005 [nucl-ex]

Adam J et al (2021b) Nonmonotonic energy dependence of net-proton number fluctuations. Phys Rev Lett 126(9):092301. https://doi.org/10.1103/PhysRevLett.126.092301. arXiv:2001.02852 [nucl-ex]

Adamczewski-Musch J et al (2019a) Identical pion intensity interferometry in central Au + Au collisions at 1.23 A GeV. Phys Lett B 795:446–451. https://doi.org/10.1016/j.physletb.2019.06.047. arXiv:1811.06213 [nucl-ex]

Adamczewski-Musch J et al (2019b) Probing dense baryon-rich matter with virtual photons. Nat Phys 15 (10):1040–1045. https://doi.org/10.1038/s41567-019-0583-8

Adamczewski-Musch J et al (2020a) Directed, elliptic, and higher order flow harmonics of protons, deuterons, and tritons in Au+Au collisions at $\sqrt{s_{NN}}$ = 2.4 GeV. Phys Rev Lett 125:262301. https://doi.org/10.1103/PhysRevLett.125.262301. arXiv:2005.12217 [nucl-ex]

Adamczewski-Musch J et al (2020b) Identical pion intensity interferometry at $\sqrt{s_{\mathrm{NN}}}$ = 2.4 GeV. Eur Phys J A 56(5):140. https://doi.org/10.1140/epja/s10050-020-00116-w. arXiv:1910.07885 [nucl-ex]

Adamczewski-Musch J et al (2020c) Proton-number fluctuations in $\sqrt{s_{NN}}$ =2.4 GeV Au + Au collisions studied with the High-Acceptance DiElectron Spectrometer (HADES). Phys Rev C 102(2):024914. https://doi.org/10.1103/PhysRevC.102.024914. arXiv:2002.08701 [nucl-ex]

Adamczyk L et al (2012) Inclusive charged hadron elliptic flow in Au + Au collisions at $\sqrt{s_{NN}}$ = 7.7–39 GeV. Phys Rev C 86:054908. https://doi.org/10.1103/PhysRevC.86.054908. arXiv:1206.5528 [nucl-ex]

Adamczyk L et al (2013a) Elliptic flow of identified hadrons in Au+Au collisions at $\sqrt{s_{NN}}$ = 7.7–62.4 GeV. Phys Rev C 88:014902. https://doi.org/10.1103/PhysRevC.88.014902. arXiv:1301.2348 [nucl-ex]

Adamczyk L et al (2013b) Freeze-out dynamics via charged kaon femtoscopy in $\sqrt{s_{NN}}$ = 200 GeV central Au + Au collisions. Phys Rev C 88(3):034906. https://doi.org/10.1103/PhysRevC.88.034906. arXiv:1302.3168 [nucl-ex]

Adamczyk L et al (2013c) Observation of an energy-dependent difference in elliptic flow between particles and antiparticles in relativistic heavy ion collisions. Phys Rev Lett 110(14):142301. https://doi.org/10.1103/PhysRevLett.110.142301. arXiv:1301.2347 [nucl-ex]

Adamczyk L et al (2014a) Beam energy dependence of moments of the net-charge multiplicity distributions in Au+Au collisions at RHIC. Phys Rev Lett 113:092301. https://doi.org/10.1103/PhysRevLett.113.092301. arXiv:1402.1558 [nucl-ex]

Adamczyk L et al (2014b) Beam-energy dependence of the directed flow of protons, antiprotons, and pions in Au+Au collisions. Phys Rev Lett 112(16):162301. https://doi.org/10.1103/PhysRevLett.112.162301. arXiv:1401.3043 [nucl-ex]

Adamczyk L et al (2015) Beam-energy-dependent two-pion interferometry and the freeze-out eccentricity of pions measured in heavy ion collisions at the STAR detector. Phys Rev C 92(1):014904. https://doi.org/10.1103/PhysRevC.92.014904. arXiv:1403.4972 [nucl-ex]

Adamczyk L et al (2016a) Beam energy dependence of the third harmonic of azimuthal correlations in Au+Au collisions at RHIC. Phys Rev Lett 116(11):112302. https://doi.org/10.1103/PhysRevLett.116.112302. arXiv:1601.01999 [nucl-ex]

Adamczyk L et al (2016b) Centrality dependence of identified particle elliptic flow in relativistic heavy ion collisions at $\sqrt{s_{NN}}$=7.7-62.4 GeV. Phys Rev C 93(1):014907. https://doi.org/10.1103/PhysRevC.93.014907. arXiv:1509.08397 [nucl-ex]

Adamczyk L et al (2017) Bulk properties of the medium produced in relativistic heavy-ion collisions from the beam energy scan program. Phys Rev C 96(4):044904. https://doi.org/10.1103/PhysRevC.96.044904. arXiv:1701.07065 [nucl-ex]

Adamczyk L et al (2018a) Azimuthal anisotropy in Cu+Au collisions at $\sqrt{s_{_{NN}}}$ = 200 GeV. Phys Rev C 98(1):014915. https://doi.org/10.1103/PhysRevC.98.014915. arXiv:1712.01332 [nucl-ex]

Adamczyk L et al (2018b) Beam-energy dependence of directed flow of Λ, $\bar{\Lambda}$, $K^{\pm}$, K_s^0 and ϕ in Au+Au collisions. Phys Rev Lett 120(6):062301. https://doi.org/10.1103/PhysRevLett.120.062301. arXiv:1708.07132 [hep-ex]

Adamczyk L et al (2018c) Collision energy dependence of moments of net-kaon multiplicity distributions at RHIC. Phys Lett B 785:551–560. https://doi.org/10.1016/j.physletb.2018.07.066. arXiv:1709.00773 [nucl-ex]

Adamczyk L et al (2018d) Harmonic decomposition of three-particle azimuthal correlations at energies available at the BNL Relativistic Heavy Ion Collider. Phys Rev C 98(3):034918. https://doi.org/10.1103/PhysRevC.98.034918. arXiv:1701.06496 [nucl-ex]

Adamová D et al (2003) Beam energy and centrality dependence of two pion Bose–Einstein correlations at SPS energies. Nucl Phys A 714:124–144. https://doi.org/10.1016/S0375-9474(02)01369-6. arXiv:nucl-ex/0207005

Adamova D et al (2008) Azimuthal dependence of pion source radii in Pb+Au collisions at 158-A-GeV. Phys Rev C 78:064901. https://doi.org/10.1103/PhysRevC.78.064901. arXiv:0805.2484 [nucl-ex]

Adamova D et al (2017) Azimuthally differential pion femtoscopy in Pb–Pb collisions at $\sqrt{s_{\mathrm{NN}}} = 2.76$ TeV. Phys Rev Lett 118(22):222301. https://doi.org/10.1103/PhysRevLett.118.222301. arXiv:1702.01612 [nucl-ex]

Adams J et al (2004) Azimuthally sensitive HBT in Au + Au collisions at $\sqrt{s_{NN}}$ = 200 GeV. Phys Rev Lett 93:012301. https://doi.org/10.1103/PhysRevLett.93.012301. arXiv:nucl-ex/0312009

Adams J et al (2005a) Azimuthal anisotropy in Au+Au collisions at $\sqrt{s_{NN}}$ = 200 GeV. Phys Rev C 72:014904. https://doi.org/10.1103/PhysRevC.72.014904. arXiv:nucl-ex/0409033

Adams J et al (2005b) Experimental and theoretical challenges in the search for the quark gluon plasma: the STAR Collaboration's critical assessment of the evidence from RHIC collisions. Nucl Phys A 757:102–183. https://doi.org/10.1016/j.nuclphysa.2005.03.085. arXiv:nucl-ex/0501009

Adams J et al (2005c) Incident energy dependence of pt correlations at RHIC. Phys Rev C 72:044902. https://doi.org/10.1103/PhysRevC.72.044902. arXiv:nucl-ex/0504031

Adams J et al (2005d) Multi-strange baryon elliptic flow in Au + Au collisions at $\sqrt{s_{NN}}$ = 200 GeV. Phys Rev Lett 95:122301. https://doi.org/10.1103/PhysRevLett.95.122301. arXiv:nucl-ex/0504022

Adams J et al (2005e) Pion interferometry in Au+Au collisions at $\sqrt{s_{NN}}$ = 200 GeV. Phys Rev C 71:044906. https://doi.org/10.1103/PhysRevC.71.044906. arXiv:nucl-ex/0411036

Adams J et al (2007) The energy dependence of p_t angular correlations inferred from mean-p(t) fluctuation scale dependence in heavy ion collisions at the SPS and RHIC. J Phys G 34:451–466. https://doi.org/10.1088/0954-3899/34/3/004. arXiv:nucl-ex/0605021

Adare A (2011) Triggered di-hadron correlations in Pb–Pb collisions from the ALICE experiment. J Phys G 38:124091. https://doi.org/10.1088/0954-3899/38/12/124091. arXiv:1107.0285 [nucl-ex]

Adare A et al (2007) Scaling properties of azimuthal anisotropy in Au+Au and Cu+Cu collisions at s(NN) = 200-GeV. Phys Rev Lett 98:162301. https://doi.org/10.1103/PhysRevLett.98.162301. arXiv:nucl-ex/0608033

Adare A et al (2011) Measurements of higher-order flow harmonics in Au+Au collisions at $\sqrt{s_{NN}} = 200$ GeV. Phys Rev Lett 107:252301. https://doi.org/10.1103/PhysRevLett.107.252301. arXiv:1105.3928 [nucl-ex]

Adare A et al (2014) Azimuthal-angle dependence of charged-pion-interferometry measurements with respect to second- and third-order event planes in Au+Au collisions at $\sqrt{s_{NN}} = 200$ GeV. Phys Rev Lett 112(22):222301. https://doi.org/10.1103/PhysRevLett.112.222301. arXiv:1401.7680 [nucl-ex]
Adare A et al (2015a) Systematic study of azimuthal anisotropy in Cu + Cu and Au + Au collisions at $\sqrt{s_{NN}} = 62.4$ and 200 GeV. Phys Rev C 92(3):034913. https://doi.org/10.1103/PhysRevC.92.034913. arXiv:1412.1043 [nucl-ex]
Adare A et al (2015b) Systematic study of charged-pion and kaon femtoscopy in Au + Au collisions at $\sqrt{s_{NN}}$=200 GeV. Phys Rev C 92(3):034914. https://doi.org/10.1103/PhysRevC.92.034914. arXiv:1504.05168 [nucl-ex]
Adare A et al (2016a) Measurement of higher cumulants of net-charge multiplicity distributions in Au+Au collisions at $\sqrt{s_{NN}} = 7.7 - 200$ GeV. Phys Rev C 93(1):011901. https://doi.org/10.1103/PhysRevC.93.011901. arXiv:1506.07834 [nucl-ex]
Adare A et al (2016b) Measurement of the higher-order anisotropic flow coefficients for identified hadrons in Au+Au collisions at $\sqrt{s_{NN}} = 200$ GeV. Phys Rev C 93(5):051902. https://doi.org/10.1103/PhysRevC.93.051902. arXiv:1412.1038 [nucl-ex]
Adare A et al (2016c) Measurements of directed, elliptic, and triangular flow in Cu+Au collisions at $\sqrt{s_{NN}} = 200$ GeV. Phys Rev C 94(5):054910. https://doi.org/10.1103/PhysRevC.94.054910. arXiv:1509.07784 [nucl-ex]
Adcox K et al (2005) Formation of dense partonic matter in relativistic nucleus-nucleus collisions at RHIC: experimental evaluation by the PHENIX collaboration. Nucl Phys A 757:184–283. https://doi.org/10.1016/j.nuclphysa.2005.03.086. arXiv:nucl-ex/0410003
Adhikari D et al (2021) Accurate determination of the neutron skin thickness of ^{208}Pb through parity-violation in electron scattering. Phys Rev Lett 126(17):172502. https://doi.org/10.1103/PhysRevLett.126.172502. arXiv:2102.10767 [nucl-ex]
Adhikary H (2022) Search for the critical point of strongly interacting matter (intermittency analysis by NA61/SHINE at CERN SPS). EPJ Web Conf 274:06008. https://doi.org/10.1051/epjconf/202227406008. arXiv:2211.10504 [hep-ex]
Adler C et al (2001a) Identified particle elliptic flow in Au + Au collisions at $\sqrt{s_{NN}} = 130$ GeV. Phys Rev Lett 87:182301. https://doi.org/10.1103/PhysRevLett.87.182301. arXiv:nucl-ex/0107003
Adler C et al (2001b) Pion interferometry of $\sqrt{s_{NN}} = 130$ GeV Au+Au collisions at RHIC. Phys Rev Lett 87:082301. https://doi.org/10.1103/PhysRevLett.87.082301. arXiv:nucl-ex/0107008
Adler C et al (2002) Elliptic flow from two and four particle correlations in Au+Au collisions at $\sqrt{s_{NN}} = 130$ GeV. Phys Rev C 66:034904. https://doi.org/10.1103/PhysRevC.66.034904. arXiv:nucl-ex/0206001
Adler SS et al (2003) Elliptic flow of identified hadrons in Au+Au collisions at $\sqrt{s_{NN}} = 200$ GeV. Phys Rev Lett 91:182301. https://doi.org/10.1103/PhysRevLett.91.182301. arXiv:nucl-ex/0305013
Adler SS et al (2004) Measurement of nonrandom event by event fluctuations of average transverse momentum in $\sqrt{s_{NN}} = 200$ GeV Au+Au and p+p collisions. Phys Rev Lett 93:092301. https://doi.org/10.1103/PhysRevLett.93.092301. arXiv:nucl-ex/0310005
Aduszkiewicz A et al (2017) Measurements of $\pi^{\pm}$, $K^{\pm}$, p and $\bar{p}$ spectra in proton-proton interactions at 20, 31, 40, 80 and 158 GeV $/c$ with the NA61/SHINE spectrometer at the CERN SPS. Eur Phys J C 77(10):671. https://doi.org/10.1140/epjc/s10052-017-5260-4. arXiv:1705.02467 [nucl-ex]
Afanasiev SV et al (2002) Energy dependence of pion and kaon production in central Pb + Pb collisions. Phys Rev C 66:054902. https://doi.org/10.1103/PhysRevC.66.054902. arXiv:nucl-ex/0205002
Afanasiev S et al (2009) Systematic studies of elliptic flow measurements in Au+Au collisions at $\sqrt{s_{NN}} = 200$ GeV. Phys Rev C 80:024909. https://doi.org/10.1103/PhysRevC.80.024909. arXiv:0905.1070 [nucl-ex]
Aggarwal MM et al (2010) Higher moments of net-proton multiplicity distributions at RHIC. Phys Rev Lett 105:022302. https://doi.org/10.1103/PhysRevLett.105.022302. arXiv:1004.4959 [nucl-ex]
Aggarwal MM et al (2011) Pion femtoscopy in $p^{+}p$ collisions at $\sqrt{s} = 200$ GeV. Phys Rev C 83:064905. https://doi.org/10.1103/PhysRevC.83.064905. arXiv:1004.0925 [nucl-ex]
Agrawal BK, Shlomo S, Au VK (2003) Nuclear matter incompressibility coefficient in relativistic and nonrelativistic microscopic models. Phys Rev C 68:031304. https://doi.org/10.1103/PhysRevC.68.031304. arXiv:nucl-th/0308042
Ahle L et al (2000) Excitation function of K+ and pi+ production in Au + Au reactions at 2/A-GeV to 10/A-GeV. Phys Lett B 476:1–8. https://doi.org/10.1016/S0370-2693(00)00037-X. arXiv:nucl-ex/9910008

Ai S, Gao H, Zhang B (2020) What constraints on the neutron star maximum mass can one pose from GW170817 observations? Astrophys J 893(2):146. https://doi.org/10.3847/1538-4357/ab80bd. arXiv:1912.06369 [astro-ph.HE]

Ajitanand NN et al (2014) Comparison of the space-time extent of the emission source in d+Au and Au+Au collisions at $\sqrt{s_{NN}} = 200$ GeV. Nucl Phys A 931:1082–1087. https://doi.org/10.1016/j.nuclphysa.2014.08.054. arXiv:1404.5291 [nucl-ex]

Akiba Y et al (1996) Particle production in Au + Au collisions from BNL E866. Nucl Phys A 610:139C-152C. https://doi.org/10.1016/S0375-9474(96)00350-8

Akmal A, Pandharipande VR, Ravenhall DG (1998) The equation of state of nucleon matter and neutron star structure. Phys Rev C 58:1804–1828. https://doi.org/10.1103/PhysRevC.58.1804. arXiv:nucl-th/9804027

Al-Mamun M, Steiner AW, Nättilä J et al (2021) Combining electromagnetic and gravitational-wave constraints on neutron-star masses and radii. Phys Rev Lett 126(6):061101. https://doi.org/10.1103/PhysRevLett.126.061101. arXiv:2008.12817 [astro-ph.HE]

Alba P, Alberico W, Bellwied R et al (2014) Freeze-out conditions from net-proton and net-charge fluctuations at RHIC. Phys Lett B 738:305–310. https://doi.org/10.1016/j.physletb.2014.09.052. arXiv:1403.4903 [hep-ph]

Alba P, Bellwied R, Bluhm M et al (2015) Sensitivity of multiplicity fluctuations to freeze-out conditions in heavy ion collisions. Phys Rev C 92(6):064910. https://doi.org/10.1103/PhysRevC.92.064910. arXiv:1504.03262 [hep-ph]

Alba P et al (2017) Constraining the hadronic spectrum through QCD thermodynamics on the lattice. Phys Rev D 96(3):034517. https://doi.org/10.1103/PhysRevD.96.034517. arXiv:1702.01113 [hep-lat]

Alba P, Sarti VM, Noronha-Hostler J et al (2020) Influence of hadronic resonances on the chemical freeze-out in heavy-ion collisions. Phys Rev C 101(5):054905. https://doi.org/10.1103/PhysRevC.101.054905. arXiv:2002.12395 [hep-ph]

Alford JAJ, Halpern JP (2023) Do central compact objects have carbon atmospheres? Astrophys J 944 (1):36. https://doi.org/10.3847/1538-4357/acaf55. arXiv:2302.05893 [astro-ph.HE]

Alford MG, Harris SP (2019) Damping of density oscillations in neutrino-transparent nuclear matter. Phys Rev C 100(3):035803. https://doi.org/10.1103/PhysRevC.100.035803. arXiv:1907.03795 [nucl-th]

Alford MG, Bovard L, Hanauske M et al (2018) Viscous dissipation and heat conduction in binary neutron-star mergers. Phys Rev Lett 120(4):041101. https://doi.org/10.1103/PhysRevLett.120.041101. arXiv:1707.09475 [gr-qc]

Alford M, Harutyunyan A, Sedrakian A (2019) Bulk viscosity of baryonic matter with trapped neutrinos. Phys Rev D 100(10):103021. https://doi.org/10.1103/PhysRevD.100.103021. arXiv:1907.04192 [astro-ph.HE]

Alford M, Harutyunyan A, Sedrakian A (2021) Bulk viscosity from Urca processes: npeμ matter in the neutrino-trapped regime. Phys Rev D 104(10):103027. https://doi.org/10.1103/PhysRevD.104.103027. arXiv:2108.07523 [astro-ph.HE]

ALICE Collaboration (2020) Unveiling the strong interaction among hadrons at the LHC. Nature 588:232–238. https://doi.org/10.1038/s41586-020-3001-6. [Erratum: Nature 590, E13 (2021)]. arXiv:2005.11495 [nucl-ex]

ALICE Collaboration (2022) Letter of intent for ALICE 3: a next-generation heavy-ion experiment at the LHC. arXiv e-prints arXiv:2211.02491 [physics.ins-det]

Almasi G, Andronic A, Braun-Munzinger P et al (2019) Exploring chiral symmetry restoration in heavy-ion collisions with fluctuation observables. Nucl Phys A 982:295–298. https://doi.org/10.1016/j.nuclphysa.2018.10.044

Alt C et al (2003) Directed and elliptic flow of charged pions and protons in Pb + Pb collisions at 40-A-GeV and 158-A-GeV. Phys Rev C 68:034903. https://doi.org/10.1103/PhysRevC.68.034903. arXiv:nucl-ex/0303001

Alt C et al (2008) Pion and kaon production in central Pb + Pb collisions at 20-A and 30-A-GeV: evidence for the onset of deconfinement. Phys Rev C 77:024903. https://doi.org/10.1103/PhysRevC.77.024903. arXiv:0710.0118 [nucl-ex]

Altiparmak S, Ecker C, Rezzolla L (2022) On the sound speed in neutron stars. Astrophys J Lett 939(2):L34. https://doi.org/10.3847/2041-8213/ac9b2a. arXiv:2203.14974 [astro-ph.HE]

Alver B, Roland G (2010) Collision geometry fluctuations and triangular flow in heavy-ion collisions. Phys Rev C 81:054905. https://doi.org/10.1103/PhysRevC.82.039903. [Erratum: Phys. Rev. C 82, 039903 (2010)], arXiv:1003.0194 [nucl-th]

Alver B et al (2007) System size, energy, pseudorapidity, and centrality dependence of elliptic flow. Phys Rev Lett 98:242302. https://doi.org/10.1103/PhysRevLett.98.242302. arXiv:nucl-ex/0610037
Andersen JO, Strickland M (2002) The equation of state for dense QCD and quark stars. Phys Rev D 66:105001. https://doi.org/10.1103/PhysRevD.66.105001. arXiv:hep-ph/0206196
Andersen JO, Braaten E, Strickland M (1999) Hard thermal loop resummation of the free energy of a hot gluon plasma. Phys Rev Lett 83:2139–2142. https://doi.org/10.1103/PhysRevLett.83.2139. arXiv:hep-ph/9902327
Andersen JO, Braaten E, Strickland M (2000a) Hard thermal loop resummation of the free energy of a hot quark-gluon plasma. Phys Rev D 61:074016. https://doi.org/10.1103/PhysRevD.61.074016. arXiv:hep-ph/9908323
Andersen JO, Braaten E, Strickland M (2000b) Hard thermal loop resummation of the thermodynamics of a hot gluon plasma. Phys Rev D 61:014017. https://doi.org/10.1103/PhysRevD.61.014017. arXiv:hep-ph/9905337
Andersen JO, Braaten E, Petitgirard E et al (2002) HTL perturbation theory to two loops. Phys Rev D 66:085016. https://doi.org/10.1103/PhysRevD.66.085016. arXiv:hep-ph/0205085
Andersen JO, Petitgirard E, Strickland M (2004) Two loop HTL thermodynamics with quarks. Phys Rev D 70:045001. https://doi.org/10.1103/PhysRevD.70.045001. arXiv:hep-ph/0302069
Andersen JO, Strickland M, Su N (2010a) Gluon thermodynamics at intermediate coupling. Phys Rev Lett 104:122003. https://doi.org/10.1103/PhysRevLett.104.122003. arXiv:0911.0676 [hep-ph]
Andersen JO, Strickland M, Su N (2010b) Three-loop HTL gluon thermodynamics at intermediate coupling. JHEP 08:113. https://doi.org/10.1007/JHEP08(2010)113. arXiv:1005.1603 [hep-ph]
Andersen JO, Leganger LE, Strickland M et al (2011a) NNLO hard-thermal-loop thermodynamics for QCD. Phys Lett B 696:468–472. https://doi.org/10.1016/j.physletb.2010.12.070. arXiv:1009.4644 [hep-ph]
Andersen JO, Leganger LE, Strickland M et al (2011b) The QCD trace anomaly. Phys Rev D 84:087703. https://doi.org/10.1103/PhysRevD.84.087703. arXiv:1106.0514 [hep-ph]
Andersen JO, Leganger LE, Strickland M et al (2011c) Three-loop HTL QCD thermodynamics. JHEP 08:053. https://doi.org/10.1007/JHEP08(2011)053. arXiv:1103.2528 [hep-ph]
Andronic A, Braun-Munzinger P, Redlich K et al (2018) Decoding the phase structure of QCD via particle production at high energy. Nature 561(7723):321–330. https://doi.org/10.1038/s41586-018-0491-6. arXiv:1710.09425 [nucl-th]
Andronic A, Braun-Munzinger P, Friman B et al (2019) The thermal proton yield anomaly in Pb–Pb collisions at the LHC and its resolution. Phys Lett B 792:304–309. https://doi.org/10.1016/j.physletb.2019.03.052. arXiv:1808.03102 [hep-ph]
Annala E, Gorda T, Kurkela A et al (2018) Gravitational-wave constraints on the neutron-star-matter equation of state. Phys Rev Lett 120(17):172703. https://doi.org/10.1103/PhysRevLett.120.172703. arXiv:1711.02644 [astro-ph.HE]
Annala E, Gorda T, Kurkela A et al (2020) Evidence for quark-matter cores in massive neutron stars. Nature Phys 16(9):907–910. https://doi.org/10.1038/s41567-020-0914-9. arXiv:1903.09121 [astro-ph.HE]
Anson C (2011) Energy dependence of the freeze out eccentricity from the azimuthal dependence of HBT at STAR. J Phys G 38:124148. https://doi.org/10.1088/0954-3899/38/12/124148. arXiv:1107.1527 [nucl-ex]
Anticic T et al (2014) Phase-space dependence of particle-ratio fluctuations in Pb + Pb collisions from 20 A to 158 A GeV beam energy. Phys Rev C 89(5):054902. https://doi.org/10.1103/PhysRevC.89.054902. arXiv:1310.3428 [nucl-ex]
Antinori F et al (2006) Enhancement of hyperon production at central rapidity in 158-A-GeV/c Pb–Pb collisions. J Phys G 32:427–442. https://doi.org/10.1088/0954-3899/32/4/003. arXiv:nucl-ex/0601021
Antoniadis J et al (2013) A massive pulsar in a compact relativistic binary. Science 340:6131. https://doi.org/10.1126/science.1233232. arXiv:1304.6875 [astro-ph.HE]
Aoki Y, Fodor Z, Katz SD et al (2006) The equation of state in lattice QCD: with physical quark masses towards the continuum limit. JHEP 01:089. https://doi.org/10.1088/1126-6708/2006/01/089. arXiv:hep-lat/0510084
Aoki S et al (2009) Nuclear capture at rest of Ξ^- hyperons. Nucl Phys A 828:191–232. https://doi.org/10.1016/j.nuclphysa.2009.07.005
Arnold PB, Zhai CX (1994) The three loop free energy for pure gauge QCD. Phys Rev D 50:7603–7623. https://doi.org/10.1103/PhysRevD.50.7603. arXiv:hep-ph/9408276

Arnold PB, Cx Zhai (1995) The three loop free energy for high temperature QED and QCD with fermions. Phys Rev D 51:1906–1918. https://doi.org/10.1103/PhysRevD.51.1906. arXiv:hep-ph/9410360
Arnold PB, Moore GD, Yaffe LG (2000) Transport coefficients in high temperature gauge theories (I): leading-log results. JHEP 11:001. https://doi.org/10.1088/1126-6708/2000/11/001. arXiv:hep-ph/0010177
Arnold PB, Dogan C, Moore GD (2006) The bulk viscosity of high-temperature QCD. Phys Rev D 74:085021. https://doi.org/10.1103/PhysRevD.74.085021. arXiv:hep-ph/0608012
Arzoumanian Z et al (2018) The NANOGrav 11-year data set: high-precision timing of 45 millisecond pulsars. Astrophys J Suppl 235(2):37. https://doi.org/10.3847/1538-4365/aab5b0. arXiv:1801.01837 [astro-ph.HE]
Athanasiou C, Rajagopal K, Stephanov M (2010) Using higher moments of fluctuations and their ratios in the search for the QCD critical point. Phys Rev D 82:074008. https://doi.org/10.1103/PhysRevD.82.074008. arXiv:1006.4636 [hep-ph]
ATLAS Collaboration (2017) Azimuthal femtoscopy in central p+Pb collisions at $\sqrt{s_{\rm NN}} = 5.02$ TeV with ATLAS. In: Heinz U, Evdokimov O, Jacobs P (eds) The XXVI international conference on ultrarelativistic heavy-ion collisions, Chicago, United States Of America, 6–11 Feb 2017
Back BB et al (2005s) Centrality and pseudorapidity dependence of elliptic flow for charged hadrons in Au+Au collisions at $\sqrt{s_{NN}}$ = 200 GeV. Phys Rev C 72:051901. https://doi.org/10.1103/PhysRevC.72.051901. arXiv:nucl-ex/0407012
Back BB et al (2005b) Energy dependence of elliptic flow over a large pseudorapidity range in Au+Au collisions at RHIC. Phys Rev Lett 94:122303. https://doi.org/10.1103/PhysRevLett.94.122303. arXiv:nucl-ex/0406021
Back BB et al (2005c) The PHOBOS perspective on discoveries at RHIC. Nucl Phys A 757:28–101. https://doi.org/10.1016/j.nuclphysa.2005.03.084. arXiv:nucl-ex/0410022
Back BB et al (2006) Energy dependence of directed flow over a wide range of pseudorapidity in Au + Au collisions at RHIC. Phys Rev Lett 97:012301. https://doi.org/10.1103/PhysRevLett.97.012301. arXiv:nucl-ex/0511045
Baluni V (1978) Nonabelian gauge theories of Fermi systems: chromotheory of highly condensed matter. Phys Rev D 17:2092. https://doi.org/10.1103/PhysRevD.17.2092
Bass SA et al (1998) Microscopic models for ultrarelativistic heavy ion collisions. Prog Part Nucl Phys 41:255–369. https://doi.org/10.1016/S0146-6410(98)00058-1. arXiv:nucl-th/9803035
Bastid N et al (2005) First analysis of anisotropic flow with Lee-Yang zeroes. Phys Rev C 72:011901. https://doi.org/10.1103/PhysRevC.72.011901. arXiv:nucl-ex/0504002
Baubock M, Psaltis D, Ozel F (2015) Effects of spot size on neutron-star radius measurements from pulse profiles. Astrophys J 811(2):144. https://doi.org/10.1088/0004-637X/811/2/144. arXiv:1505.00780 [astro-ph.HE]
Bauswein A, Baumgarte TW, Janka HT (2013) Prompt merger collapse and the maximum mass of neutron stars. Phys Rev Lett 111(13):131101. https://doi.org/10.1103/PhysRevLett.111.131101. arXiv:1307.5191 [astro-ph.SR]
Bauswein A, Just O, Janka HT et al (2017) Neutron-star radius constraints from GW170817 and future detections. Astrophys J Lett 850(2):L34. https://doi.org/10.3847/2041-8213/aa9994. arXiv:1710.06843 [astro-ph.HE]
Bauswein A, Bastian NUF, Blaschke DB et al (2019) Identifying a first-order phase transition in neutron star mergers through gravitational waves. Phys Rev Lett 122(6):061102. https://doi.org/10.1103/PhysRevLett.122.061102. arXiv:1809.01116 [astro-ph.HE]
Baym G, Hatsuda T, Kojo T et al (2018) From hadrons to quarks in neutron stars: a review. Rep Prog Phys 81(5):056902. https://doi.org/10.1088/1361-6633/aaae14. arXiv:1707.04966 [astro-ph.HE]
Bazavov A, Ding HT, Hegde P et al (2013) Quark number susceptibilities at high temperatures. Phys Rev D 88(9):094021. https://doi.org/10.1103/PhysRevD.88.094021. arXiv:1309.2317 [hep-lat]
Bazavov A et al (2013) Strangeness at high temperatures: from hadrons to quarks. Phys Rev Lett 111:082301. https://doi.org/10.1103/PhysRevLett.111.082301. arXiv:1304.7220 [hep-lat]
Bazavov A et al (2014) Equation of state in (2+1)-flavor QCD. Phys Rev D 90:094503. https://doi.org/10.1103/PhysRevD.90.094503. arXiv:1407.6387 [hep-lat]
Bazavov A et al (2017) The QCD equation of state to $\mathcal{O}(\mu_B^6)$ from lattice QCD. Phys Rev D 95(5):054504. https://doi.org/10.1103/PhysRevD.95.054504. arXiv:1701.04325 [hep-lat]
Bazavov A et al (2019) Chiral crossover in QCD at zero and non-zero chemical potentials. Phys Lett B 795:15–21. https://doi.org/10.1016/j.physletb.2019.05.013. arXiv:1812.08235 [hep-lat]

Becattini F, Passaleva G (2002) Statistical hadronization model and transverse momentum spectra of hadrons in high-energy collisions. Eur Phys J C 23:551–583. https://doi.org/10.1007/s100520100869. arXiv:hep-ph/0110312

Bednarek I, Haensel P, Zdunik JL et al (2012) Hyperons in neutron-star cores and two-solar-mass pulsar. Astron Astrophys 543:A157. https://doi.org/10.1051/0004-6361/201118560. arXiv:1111.6942 [astro-ph.SR]

Begun VV, Gorenstein MI, Hauer M et al (2006) Multiplicity fluctuations in hadron-resonance gas. Phys Rev C 74:044903. https://doi.org/10.1103/PhysRevC.74.044903. arXiv:nucl-th/0606036

Bellwied R, Borsanyi S, Fodor Z et al (2013) Is there a flavor hierarchy in the deconfinement transition of QCD? Phys Rev Lett 111:202302. https://doi.org/10.1103/PhysRevLett.111.202302. arXiv:1305.6297 [hep-lat]

Bellwied R, Borsanyi S, Fodor Z et al (2015) Fluctuations and correlations in high temperature QCD. Phys Rev D 92(11):114505. https://doi.org/10.1103/PhysRevD.92.114505. arXiv:1507.04627 [hep-lat]

Bellwied R, Noronha-Hostler J, Parotto P et al (2019) Freeze-out temperature from net-kaon fluctuations at energies available at the BNL Relativistic Heavy Ion Collider. Phys Rev C 99(3):034912. https://doi.org/10.1103/PhysRevC.99.034912. arXiv:1805.00088 [hep-ph]

Bellwied R, Borsanyi S, Fodor Z et al (2020) Off-diagonal correlators of conserved charges from lattice QCD and how to relate them to experiment. Phys Rev D 101(3):034506. https://doi.org/10.1103/PhysRevD.101.034506. arXiv:1910.14592 [hep-lat]

Berdnikov B, Rajagopal K (2000) Slowing out-of-equilibrium near the QCD critical point. Phys Rev D 61:105017. https://doi.org/10.1103/PhysRevD.61.105017. arXiv:hep-ph/9912274

Bernhard JE, Moreland JS, Bass SA (2019) Bayesian estimation of the specific shear and bulk viscosity of quark-gluon plasma. Nat Phys 15(11):1113–1117. https://doi.org/10.1038/s41567-019-0611-8

Betz B, Gyulassy M, Luzum M et al (2017) Cumulants and nonlinear response of high p_T harmonic flow at $\sqrt{s_{NN}} = 5.02$ TeV. Phys Rev C 95(4):044901. https://doi.org/10.1103/PhysRevC.95.044901. arXiv:1609.05171 [nucl-th]

Bhalerao RS, Luzum M, Ollitrault JY (2011) Determining initial-state fluctuations from flow measurements in heavy-ion collisions. Phys Rev C 84:034910. https://doi.org/10.1103/PhysRevC.84.034910. arXiv:1104.4740 [nucl-th]

Bhalerao RS, Ollitrault JY, Pal S (2015a) Characterizing flow fluctuations with moments. Phys Lett B 742:94–98. https://doi.org/10.1016/j.physletb.2015.01.019. arXiv:1411.5160 [nucl-th]

Bhalerao RS, Ollitrault JY, Pal S et al (2015b) Principal component analysis of event-by-event fluctuations. Phys Rev Lett 114(15):152301. https://doi.org/10.1103/PhysRevLett.114.152301. arXiv:1410.7739 [nucl-th]

Bhalerao RS, Giacalone G, Guerrero-Rodríguez P et al (2019a) Relating eccentricity fluctuations to density fluctuations in heavy-ion collisions. Acta Phys Polon B 50:1165–1176. https://doi.org/10.5506/APhysPolB.50.1165. arXiv:1903.06366 [nucl-th]

Bhalerao RS, Giacalone G, Ollitrault JY (2019b) Primordial non-Gaussianity in heavy-ion collisions. Phys Rev C 100(1):014909. https://doi.org/10.1103/PhysRevC.100.014909. arXiv:1904.10350 [nucl-th]

Bhattacharya L, Ryblewski R, Strickland M (2016) Photon production from a nonequilibrium quark-gluon plasma. Phys Rev D 93(6):065005. https://doi.org/10.1103/PhysRevD.93.065005. arXiv:1507.06605 [hep-ph]

Bialas A, Hwa RC (1991) Intermittency parameters as a possible signal for quark-gluon plasma formation. Phys Lett B 253:436–438. https://doi.org/10.1016/0370-2693(91)91747-J

Bialas A, Peschanski RB (1986) Moments of rapidity distributions as a measure of short range fluctuations in high-energy collisions. Nucl Phys B 273:703–718. https://doi.org/10.1016/0550-3213(86)90386-X

Bilandzic A, Snellings R, Voloshin S (2011) Flow analysis with cumulants: direct calculations. Phys Rev C 83:044913. https://doi.org/10.1103/PhysRevC.83.044913. arXiv:1010.0233 [nucl-ex]

Bilandzic A, Christensen CH, Gulbrandsen K et al (2014) Generic framework for anisotropic flow analyses with multiparticle azimuthal correlations. Phys Rev C 89(6):064904. https://doi.org/10.1103/PhysRevC.89.064904. arXiv:1312.3572 [nucl-ex]

Blacker S, Bastian NUF, Bauswein A et al (2020) Constraining the onset density of the hadron-quark phase transition with gravitational-wave observations. Phys Rev D 102(12):123023. https://doi.org/10.1103/PhysRevD.102.123023. arXiv:2006.03789 [astro-ph.HE]

Blaizot JP (1980) Nuclear compressibilities. Phys Rep 64:171–248. https://doi.org/10.1016/0370-1573(80)90001-0

Blaizot JP, Iancu E, Rebhan A (1999a) Selfconsistent hard-thermal-loop thermodynamics for the quark-gluon plasma. Phys Lett B 470:181–188. https://doi.org/10.1016/S0370-2693(99)01306-4. arXiv:hep-ph/9910309
Blaizot JP, Iancu E, Rebhan A (1999b) The entropy of the QCD plasma. Phys Rev Lett 83:2906–2909. https://doi.org/10.1103/PhysRevLett.83.2906. arXiv:hep-ph/9906340
Blaizot JP, Iancu E, Rebhan A (2001a) Approximately selfconsistent resummations for the thermodynamics of the quark-gluon plasma: entropy and density. Phys Rev D 63:065003. https://doi.org/10.1103/PhysRevD.63.065003. arXiv:hep-ph/0005003
Blaizot JP, Iancu E, Rebhan A (2001b) Quark number susceptibilities from HTL resummed thermodynamics. Phys Lett B 523:143–150. https://doi.org/10.1016/S0370-2693(01)01316-8. arXiv:hep-ph/0110369
Blaschke D, Grigorian H, Röpke G (2020) Chirally improved quark Pauli blocking in nuclear matter and applications to quark deconfinement in neutron stars. Particles 3(2):477–499. https://doi.org/10.3390/particles3020033. arXiv:2005.10218 [nucl-th]
Bleicher M et al (1999) Relativistic hadron hadron collisions in the ultrarelativistic quantum molecular dynamics model. J Phys G 25:1859–1896. https://doi.org/10.1088/0954-3899/25/9/308. arXiv:hep-ph/9909407
Bluhm M, Nahrgang M (2019) Freeze-out conditions from strangeness observables at RHIC. Eur Phys J C 79(2):155. https://doi.org/10.1140/epjc/s10052-019-6661-3. arXiv:1806.04499 [nucl-th]
Bluhm M, Nahrgang M, Bass SA et al (2017) Impact of resonance decays on critical point signals in net-proton fluctuations. Eur Phys J C 77(4):210. https://doi.org/10.1140/epjc/s10052-017-4771-3. arXiv:1612.03889 [nucl-th]
Bluhm M et al (2020) Dynamics of critical fluctuations: theory—phenomenology—heavy-ion collisions. Nucl Phys A 1003:122016. https://doi.org/10.1016/j.nuclphysa.2020.122016. arXiv:2001.08831 [nucl-th]
Bodmer AR (1991) Relativistic mean field theory of nuclei with a vector meson selfinteraction. Nucl Phys A 526:703–721. https://doi.org/10.1016/0375-9474(91)90439-D
Bogdanov S et al (2019) Constraining the neutron star mass-radius relation and dense matter equation of state with NICER. I The millisecond pulsar X-ray data set. https://doi.org/10.5281/zenodo.3524457. Accessed 04 June 2022
Bollweg D, Goswami J, Kaczmarek O et al (2022) Taylor expansions and Padé approximants for cumulants of conserved charge fluctuations at nonvanishing chemical potentials. Phys Rev D 105 (7):074511. https://doi.org/10.1103/PhysRevD.105.074511. arXiv:2202.09184 [hep-lat]
Bombaci I, Lombardo U (1991) Asymmetric nuclear matter equation of state. Phys Rev C 44:1892–1900. https://doi.org/10.1103/PhysRevC.44.1892
Bonati C, D'Elia M, Mariti M et al (2015) Curvature of the chiral pseudocritical line in QCD: continuum extrapolated results. Phys Rev D 92(5):054503. https://doi.org/10.1103/PhysRevD.92.054503. arXiv:1507.03571 [hep-lat]
Bonati C, D'Elia M, Negro F et al (2018) Curvature of the pseudocritical line in QCD: Taylor expansion matches analytic continuation. Phys Rev D 98(5):054510. https://doi.org/10.1103/PhysRevD.98.054510. arXiv:1805.02960 [hep-lat]
Borghini N, Dinh PM, Ollitrault JY (2001a) A new method for measuring azimuthal distributions in nucleus-nucleus collisions. Phys Rev C 63:054906. https://doi.org/10.1103/PhysRevC.63.054906. arXiv:nucl-th/0007063
Borghini N, Dinh PM, Ollitrault JY (2001b) Flow analysis from cumulants: a Practical guide. In: International workshop on the physics of the quark gluon plasma. arXiv:nucl-ex/0110016
Borghini N, Dinh PM, Ollitrault JY (2001c) Flow analysis from multiparticle azimuthal correlations. Phys Rev C 64:054901. https://doi.org/10.1103/PhysRevC.64.054901. arXiv:nucl-th/0105040
Borsanyi S (2013) Thermodynamics of the QCD transition from lattice. Nucl Phys A 904–905:270c–277c. https://doi.org/10.1016/j.nuclphysa.2013.01.072. arXiv:1210.6901 [hep-lat]
Borsanyi S, Endrodi G, Fodor Z et al (2010) The QCD equation of state with dynamical quarks. JHEP 11:077. https://doi.org/10.1007/JHEP11(2010)077. arXiv:1007.2580 [hep-lat]
Borsanyi S, Fodor Z, Katz SD et al (2012) Fluctuations of conserved charges at finite temperature from lattice QCD. JHEP 01:138. https://doi.org/10.1007/JHEP01(2012)138. arXiv:1112.4416 [hep-lat]
Borsanyi S, Fodor Z, Katz SD et al (2013) Freeze-out parameters: lattice meets experiment. Phys Rev Lett 111:062005. https://doi.org/10.1103/PhysRevLett.111.062005. arXiv:1305.5161 [hep-lat]
Borsanyi S, Fodor Z, Hoelbling C et al (2014a) Full result for the QCD equation of state with 2+1 flavors. Phys Lett B 730:99–104. https://doi.org/10.1016/j.physletb.2014.01.007. arXiv:1309.5258 [hep-lat]

Borsanyi S, Fodor Z, Katz SD et al (2014b) Freeze-out parameters from electric charge and baryon number fluctuations: is there consistency? Phys Rev Lett 113:052301. https://doi.org/10.1103/PhysRevLett.113.052301. arXiv:1403.4576 [hep-lat]
Borsanyi S, Fodor Z, Guenther JN et al (2018) Higher order fluctuations and correlations of conserved charges from lattice QCD. JHEP 10:205. https://doi.org/10.1007/JHEP10(2018)205. arXiv:1805.04445 [hep-lat]
Borsanyi S, Fodor Z, Guenther JN et al (2020) QCD crossover at finite chemical potential from lattice simulations. Phys Rev Lett 125(5):052001. https://doi.org/10.1103/PhysRevLett.125.052001. arXiv:2002.02821 [hep-lat]
Borsányi S, Fodor Z, Guenther JN et al (2021) Lattice QCD equation of state at finite chemical potential from an alternative expansion scheme. Phys Rev Lett 126(23):232001. https://doi.org/10.1103/PhysRevLett.126.232001. arXiv:2102.06660 [hep-lat]
Borsanyi S, Guenther JN, Kara R et al (2022) Resummed lattice QCD equation of state at finite baryon density: strangeness neutrality and beyond. Phys Rev D 105(11):114504. https://doi.org/10.1103/PhysRevD.105.114504. arXiv:2202.05574 [hep-lat]
Braaten E, Nieto A (1995) Effective field theory approach to high temperature thermodynamics. Phys Rev D 51:6990–7006. https://doi.org/10.1103/PhysRevD.51.6990. arXiv:hep-ph/9501375
Braaten E, Nieto A (1996a) Free energy of QCD at high temperature. Phys Rev D 53:3421–3437. https://doi.org/10.1103/PhysRevD.53.3421. arXiv:hep-ph/9510408
Braaten E, Nieto A (1996b) On the convergence of perturbative QCD at high temperature. Phys Rev Lett 76:1417–1420. https://doi.org/10.1103/PhysRevLett.76.1417. arXiv:hep-ph/9508406
Braaten E, Pisarski RD (1990a) Calculation of the gluon damping rate in hot QCD. Phys Rev D 42:2156–2160. https://doi.org/10.1103/PhysRevD.42.2156
Braaten E, Pisarski RD (1990b) Resummation and gauge invariance of the gluon damping rate in hot QCD. Phys Rev Lett 64:1338. https://doi.org/10.1103/PhysRevLett.64.1338
Braaten E, Pisarski RD (1990c) Soft amplitudes in hot gauge theories: a general analysis. Nucl Phys B 337:569–634. https://doi.org/10.1016/0550-3213(90)90508-B
Brandes L, Weise W, Kaiser N (2023) Inference of the sound speed and related properties of neutron stars. Phys Rev D 107(1):014011. https://doi.org/10.1103/PhysRevD.107.014011. arXiv:2208.03026 [nucl-th]
Breschi M, Perego A, Bernuzzi S et al (2021) AT2017gfo: Bayesian inference and model selection of multicomponent kilonovae and constraints on the neutron star equation of state. Mon Not R Astron Soc 505(2):1661–1677. https://doi.org/10.1093/mnras/stab1287. arXiv:2101.01201 [astro-ph.HE]
Breu C, Rezzolla L (2016) Maximum mass, moment of inertia and compactness of relativistic stars. Mon Not R Astron Soc 459(1):646–656. https://doi.org/10.1093/mnras/stw575. arXiv:1601.06083 [gr-qc]
Brockmann R, Machleidt R (1990) Relativistic nuclear structure. 1: nuclear matter. Phys Rev C 42:1965–1980. https://doi.org/10.1103/PhysRevC.42.1965
Buballa M et al (2014) EMMI rapid reaction task force meeting on quark matter in compact stars. J Phys G 41(12):123001. https://doi.org/10.1088/0954-3899/41/12/123001. arXiv:1402.6911 [astro-ph.HE]
Burgay M et al (2003) An increased estimate of the merger rate of double neutron stars from observations of a highly relativistic system. Nature 426:531–533. https://doi.org/10.1038/nature02124. arXiv:astro-ph/0312071
Buyukcizmeci N et al (2013) A comparative study of statistical models for nuclear equation of state of stellar matter. Nucl Phys A 907:13–54. https://doi.org/10.1016/j.nuclphysa.2013.03.010. arXiv:1211.5990 [nucl-th]
Bzdak A, Koch V (2012) Acceptance corrections to net baryon and net charge cumulants. Phys Rev C 86:044904. https://doi.org/10.1103/PhysRevC.86.044904. arXiv:1206.4286 [nucl-th]
Bzdak A, Koch V, Strodthoff N (2017) Cumulants and correlation functions versus the QCD phase diagram. Phys Rev C 95(5):054906. https://doi.org/10.1103/PhysRevC.95.054906. arXiv:1607.07375 [nucl-th]
Bzdak A, Esumi S, Koch V et al (2020) Mapping the phases of quantum chromodynamics with beam energy scan. Phys Rep 853:1–87. https://doi.org/10.1016/j.physrep.2020.01.005. arXiv:1906.00936 [nucl-th]
Campbell JM (2018) Azimuthally sensitive pion femtoscopy in ultra-central U+U and Au+Au collisions at STAR. PhD thesis, The Ohio State University
Cao LG, Sagawa H, Colo G (2012) Microscopic study of the isoscalar giant monopole resonance in Cd, Sn and Pb isotopes. Phys Rev C 86:054313. https://doi.org/10.1103/PhysRevC.86.054313. arXiv:1206.6552 [nucl-th]

Carlson J, Gandolfi S, Pederiva F et al (2015) Quantum Monte Carlo methods for nuclear physics. Rev Mod Phys 87:1067. https://doi.org/10.1103/RevModPhys.87.1067. arXiv:1412.3081 [nucl-th]

Carson Z, Chatziioannou K, Haster CJ et al (2019) Equation-of-state insensitive relations after GW170817. Phys Rev D 99(8):083016. https://doi.org/10.1103/PhysRevD.99.083016. arXiv:1903.03909 [gr-qc]

Cea P, Cosmai L, Papa A (2016) Critical line of 2+1 flavor QCD: toward the continuum limit. Phys Rev D 93(1):014507. https://doi.org/10.1103/PhysRevD.93.014507. arXiv:1508.07599 [hep-lat]

Cebra D, Brovko SG, Flores CE, et al (2014) Coulomb effect in Au+Au and Pb+Pb collisions as a function of collision energy. arXiv e-prints arXiv:1408.1369 [nucl-ex]

Celora T, Hawke I, Hammond PC et al (2022) Formulating bulk viscosity for neutron star simulations. Phys Rev D 105(10):103016. https://doi.org/10.1103/PhysRevD.105.103016. arXiv:2202.01576 [astro-ph.HE]

Chatrchyan S et al (2012) Azimuthal anisotropy of charged particles at high transverse momenta in PbPb collisions at $\sqrt{s_{NN}} = 2.76$ TeV. Phys Rev Lett 109:022301. https://doi.org/10.1103/PhysRevLett.109.022301. arXiv:1204.1850 [nucl-ex]

Chatrchyan S et al (2013) Measurement of the elliptic anisotropy of charged particles produced in PbPb collisions at $\sqrt{s_{NN}}$=2.76 TeV. Phys Rev C 87(1):014902. https://doi.org/10.1103/PhysRevC.87.014902. arXiv:1204.1409 [nucl-ex]

Chatrchyan S et al (2014a) Measurement of higher-order harmonic azimuthal anisotropy in PbPb collisions at $\sqrt{s_{NN}} = 2.76$ TeV. Phys Rev C 89(4):044906. https://doi.org/10.1103/PhysRevC.89.044906. arXiv:1310.8651 [nucl-ex]

Chatrchyan S et al (2014b) Studies of azimuthal dihadron correlations in ultra-central PbPb collisions at $\sqrt{s_{NN}} = 2.76$ TeV. JHEP 02:088. https://doi.org/10.1007/JHEP02(2014)088. arXiv:1312.1845 [nucl-ex]

Chatterjee S (2018) Science with pulsar timing arrays and the ngVLA. In: Murphy EJ (ed) Science with a next generation very large array, ASP conference series, vol 517. Astronomical Society of the Pacific, p 751

Chatterjee A, Chatterjee S, Nayak TK et al (2016) Diagonal and off-diagonal susceptibilities of conserved quantities in relativistic heavy-ion collisions. J Phys G 43(12):125103. https://doi.org/10.1088/0954-3899/43/12/125103. arXiv:1606.09573 [nucl-ex]

Chatziioannou K (2020) Neutron star tidal deformability and equation of state constraints. Gen Relat Gravity 52(11):109. https://doi.org/10.1007/s10714-020-02754-3. arXiv:2006.03168 [gr-qc]

Chatziioannou K, Haster CJ, Zimmerman A (2018) Measuring the neutron star tidal deformability with equation-of-state-independent relations and gravitational waves. Phys Rev D 97(10):104036. https://doi.org/10.1103/PhysRevD.97.104036. arXiv:1804.03221 [gr-qc]

Chen HX, Chen W, Liu X et al (2023) An updated review of the new hadron states. Rep Prog Phys 86 (2):026201. https://doi.org/10.1088/1361-6633/aca3b6. arXiv:2204.02649 [hep-ph]

Citron Z, et al (2019) Report from working group 5: future physics opportunities for high-density QCD at the LHC with heavy-ion and proton beams. CERN Yellow Rep Monogr 7:1159–1410. https://doi.org/10.23731/CYRM-2019-007.1159, arXiv:1812.06772 [hep-ph]

Colo G, Van Giai N, Meyer J et al (2004) Microscopic determination of the nuclear incompressibility within the nonrelativistic framework. Phys Rev C 70:024307. https://doi.org/10.1103/PhysRevC.70.024307. arXiv:nucl-th/0403086

Colo G, Garg U, Sagawa H (2014) Symmetry energy from the nuclear collective motion: constraints from dipole, quadrupole, monopole and spin-dipole resonances. Eur Phys J A 50:26. https://doi.org/10.1140/epja/i2014-14026-9. arXiv:1309.1572 [nucl-th]

Constantinou C, Muccioli B, Prakash M et al (2015) Thermal properties of hot and dense matter with finite range interactions. Phys Rev C 92(2):025801. https://doi.org/10.1103/PhysRevC.92.025801. arXiv:1504.03982 [astro-ph.SR]

Constantinou C, Han S, Jaikumar P et al (2021) g modes of neutron stars with hadron-to-quark crossover transitions. Phys Rev D 104(12):123032. https://doi.org/10.1103/PhysRevD.104.123032. arXiv:2109.14091 [astro-ph.HE]

Coughlin MW et al (2018) Constraints on the neutron star equation of state from AT2017gfo using radiative transfer simulations. Mon Not R Astron Soc 480(3):3871–3878. https://doi.org/10.1093/mnras/sty2174. arXiv:1805.09371 [astro-ph.HE]

Critelli R, Noronha J, Noronha-Hostler J et al (2017) Critical point in the phase diagram of primordial quark-gluon matter from black hole physics. Phys Rev D 96(9):096026. https://doi.org/10.1103/PhysRevD.96.096026. arXiv:1706.00455 [nucl-th]

Cromartie HT et al (2019) Relativistic Shapiro delay measurements of an extremely massive millisecond pulsar. Nat Astron 4(1):72–76. https://doi.org/10.1038/s41550-019-0880-2. arXiv:1904.06759 [astro-ph.HE]

Danhoni I, Moore GD (2023) Hot and dense QCD shear viscosity at leading log. JHEP 02:124. https://doi.org/10.1007/JHEP02(2023)124. arXiv:2212.02325 [hep-ph]

Danielewicz P, Lee J (2014) Symmetry energy II: isobaric analog states. Nucl Phys A 922:1–70. https://doi.org/10.1016/j.nuclphysa.2013.11.005. arXiv:1307.4130 [nucl-th]

Danielewicz P, Lacey R, Lynch WG (2002) Determination of the equation of state of dense matter. Science 298:1592–1596. https://doi.org/10.1126/science.1078070. arXiv:nucl-th/0208016

Dashen R, Ma SK, Bernstein HJ (1969) S matrix formulation of statistical mechanics. Phys Rev 187:345–370. https://doi.org/10.1103/PhysRev.187.345

De S, Finstad D, Lattimer JM et al (2018) Tidal deformabilities and radii of neutron stars from the observation of GW170817. Phys Rev Lett 121(9):091102. https://doi.org/10.1103/PhysRevLett.121.091102. [Erratum: Phys. Rev. Lett. 121, 259902 (2018)]. arXiv:1804.08583 [astro-ph.HE]

Demircik T, Ecker C, Järvinen M (2022) Dense and hot QCD at strong coupling. Phys Rev X 12 (4):041012. https://doi.org/10.1103/PhysRevX.12.041012. arXiv:2112.12157 [hep-ph]

Demorest P, Pennucci T, Ransom S et al (2010) Shapiro delay measurement of a two solar mass neutron star. Nature 467:1081–1083. https://doi.org/10.1038/nature09466. arXiv:1010.5788 [astro-ph.HE]

Denicol G, Rischke DH (2021) Microscopic foundations of relativistic fluid dynamics. Lecture notes in physics, vol 990. Springer, Cham. https://doi.org/10.1007/978-3-030-82077-0

Denicol GS, Niemi H, Molnar E, et al (2012) Derivation of transient relativistic fluid dynamics from the Boltzmann equation. Phys Rev D 85:114047. https://doi.org/10.1103/PhysRevD.85.114047. [Erratum: Phys. Rev. D 91, 039902 (2015)], arXiv:1202.4551 [nucl-th]

Denicol GS, Jeon S, Gale C (2014) Transport coefficients of bulk viscous pressure in the 14-moment approximation. Phys Rev C 90(2):024912. https://doi.org/10.1103/PhysRevC.90.024912. arXiv:1403.0962 [nucl-th]

Dexheimer VA, Schramm S (2010) A novel approach to model hybrid stars. Phys Rev C 81:045201. https://doi.org/10.1103/PhysRevC.81.045201. arXiv:0901.1748 [astro-ph.SR]

Dexheimer V, Steinheimer J, Negreiros R et al (2013) Hybrid stars in an SU(3) parity doublet model. Phys Rev C 87(1):015804. https://doi.org/10.1103/PhysRevC.87.015804. arXiv:1206.3086 [astro-ph.HE]

Dexheimer V, Gomes RO, Klähn T et al (2021a) GW190814 as a massive rapidly rotating neutron star with exotic degrees of freedom. Phys Rev C 103(2):025808. https://doi.org/10.1103/PhysRevC.103.025808. arXiv:2007.08493 [astro-ph.HE]

Dexheimer V, Marquez KD, Menezes DP (2021b) Delta baryons in neutron-star matter under strong magnetic fields. Eur Phys J A 57(7):216. https://doi.org/10.1140/epja/s10050-021-00532-6. arXiv:2103.09855 [nucl-th]

Dexheimer V, Noronha J, Noronha-Hostler J et al (2021c) Future physics perspectives on the equation of state from heavy ion collisions to neutron stars. J Phys G 48(7):073001. https://doi.org/10.1088/1361-6471/abe104. arXiv:2010.08834 [nucl-th]

Di Clemente F, Drago A, Pagliara G (2022) Is the compact object associated with HESS J1731-347 a strange quark star? arXiv e-prints arXiv:2211.07485 [astro-ph.HE]

Di Francesco P, Guilbaud M, Luzum M et al (2017) Systematic procedure for analyzing cumulants at any order. Phys Rev C 95(4):044911. https://doi.org/10.1103/PhysRevC.95.044911. arXiv:1612.05634 [nucl-th]

Ding HT et al (2019) Chiral phase transition temperature in (2+1)-flavor QCD. Phys Rev Lett 123 (6):062002. https://doi.org/10.1103/PhysRevLett.123.062002. arXiv:1903.04801 [hep-lat]

Dion M, Paquet JF, Schenke B et al (2011) Viscous photons in relativistic heavy ion collisions. Phys Rev C 84:064901. https://doi.org/10.1103/PhysRevC.84.064901. arXiv:1109.4405 [hep-ph]

Dore T, Karthein JM, Long I et al (2022) Critical lensing and kurtosis near a critical point in the QCD phase diagram in and out of equilibrium. Phys Rev D 106(9):094024. https://doi.org/10.1103/PhysRevD.106.094024. arXiv:2207.04086 [nucl-th]

Doroshenko V, Suleimanov V, Pühlhofer G et al (2022) A strangely light neutron star within a supernova remnant. Nat Astron 6(12):1441–1451. https://doi.org/10.1038/s41550-022-01800-1

Drago A, Lavagno A, Pagliara G et al (2014) Early appearance of Δ isobars in neutron stars. Phys Rev C 90(6):065809. https://doi.org/10.1103/PhysRevC.90.065809. arXiv:1407.2843 [astro-ph.SR]

Drago A, Lavagno A, Pagliara G et al (2016) The scenario of two families of compact stars: 1. Equations of state, mass-radius relations and binary systems. Eur Phys J A 52(2):40. https://doi.org/10.1140/epja/i2016-16040-3. arXiv:1509.02131 [astro-ph.SR]

Drischler C, Soma V, Schwenk A (2014) Microscopic calculations and energy expansions for neutron-rich matter. Phys Rev C 89(2):025806. https://doi.org/10.1103/PhysRevC.89.025806. arXiv:1310.5627 [nucl-th]

Drischler C, Hebeler K, Schwenk A (2019) Chiral interactions up to next-to-next-to-next-to-leading order and nuclear saturation. Phys Rev Lett 122(4):042501. https://doi.org/10.1103/PhysRevLett.122.042501. arXiv:1710.08220 [nucl-th]

Drischler C, Furnstahl RJ, Melendez JA et al (2020) How well do we know the neutron-matter equation of state at the densities inside neutron stars? A Bayesian approach with correlated uncertainties. Phys Rev Lett 125(20):202702. https://doi.org/10.1103/PhysRevLett.125.202702. arXiv:2004.07232 [nucl-th]

Drischler C, Han S, Lattimer JM et al (2021a) Limiting masses and radii of neutron stars and their implications. Phys Rev C 103(4):045808. https://doi.org/10.1103/PhysRevC.103.045808. arXiv:2009.06441 [nucl-th]

Drischler C, Haxton W, McElvain K et al (2021b) Towards grounding nuclear physics in QCD. Prog Part Nucl Phys 121:103888. https://doi.org/10.1016/j.ppnp.2021.103888. arXiv:1910.07961 [nucl-th]

Drischler C, Holt JW, Wellenhofer C (2021c) Chiral effective field theory and the high-density nuclear equation of state. Annu Rev Nucl Part Sci 71:403–432. https://doi.org/10.1146/annurev-nucl-102419-041903. arXiv:2101.01709 [nucl-th]

Du X, Steiner AW, Holt JW (2019) Hot and dense homogeneous nucleonic matter constrained by observations, experiment, and theory. Phys Rev C 99(2):025803. https://doi.org/10.1103/PhysRevC.99.025803. arXiv:1802.09710 [nucl-th]

Du X, Steiner AW, Holt JW (2022) Hot and dense matter equation of state probability distributions for astrophysical simulations. Phys Rev C 105(3):035803. https://doi.org/10.1103/PhysRevC.105.035803. arXiv:2107.06697 [nucl-th]

Durante M et al (2019) All the fun of the FAIR: fundamental physics at the facility for antiproton and ion research. Phys Scr 94(3):033001. https://doi.org/10.1088/1402-4896/aaf93f. arXiv:1903.05693 [nucl-th]

Ecker C, Rezzolla L (2022a) A general, scale-independent description of the sound speed in neutron stars. Astrophys J Lett 939(2):L35. https://doi.org/10.3847/2041-8213/ac8674. arXiv:2207.04417 [gr-qc]

Ecker C, Rezzolla L (2022b) Impact of large-mass constraints on the properties of neutron stars. Mon Not R Astron Soc 519(2):2615–2622. https://doi.org/10.1093/mnras/stac3755. arXiv:2209.08101 [astro-ph.HE]

Elliott JB, Lake PT, Moretto LG, et al (2012) An experimental measurement of the coexistence curve and critical temperature, density and pressure of bulk nuclear matter. arXiv e-prints arXiv:1203.5132 [nucl-ex]

Elliott JB, Lake PT, Moretto LG et al (2013) Determination of the coexistence curve, critical temperature, density, and pressure of bulk nuclear matter from fragment emission data. Phys Rev C 87(5):054622. https://doi.org/10.1103/PhysRevC.87.054622

Epelbaum E, Hammer HW, Meissner UG (2009) Modern theory of nuclear forces. Rev Mod Phys 81:1773–1825. https://doi.org/10.1103/RevModPhys.81.1773. arXiv:0811.1338 [nucl-th]

Essick R (2022) Selection effects in periodic X-ray data from maximizing detection statistics. Astrophys J 927(2):195. https://doi.org/10.3847/1538-4357/ac517c. arXiv:2111.04244 [astro-ph.HE]

Essick R, Landry P, Holz DE (2020) Nonparametric inference of neutron star composition, equation of state, and maximum mass with GW170817. Phys Rev D 101(6):063007. https://doi.org/10.1103/PhysRevD.101.063007. arXiv:1910.09740 [astro-ph.HE]

Essick R, Landry P, Schwenk A et al (2021a) Detailed examination of astrophysical constraints on the symmetry energy and the neutron skin of Pb208 with minimal modeling assumptions. Phys Rev C 104(6):065804. https://doi.org/10.1103/PhysRevC.104.065804. arXiv:2107.05528 [nucl-th]

Essick R, Tews I, Landry P et al (2021b) Astrophysical constraints on the symmetry energy and the neutron skin of Pb208 with minimal modeling assumptions. Phys Rev Lett 127(19):192701. https://doi.org/10.1103/PhysRevLett.127.192701. arXiv:2102.10074 [nucl-th]

Estee J et al (2021) Probing the symmetry energy with the spectral pion ratio. Phys Rev Lett 126(16):162701. https://doi.org/10.1103/PhysRevLett.126.162701. arXiv:2103.06861 [nucl-ex]

Everett D et al (2021) Multisystem Bayesian constraints on the transport coefficients of QCD matter. Phys Rev C 103(5):054904. https://doi.org/10.1103/PhysRevC.103.054904. arXiv:2011.01430 [hep-ph]

Fabbietti L, Mantovani Sarti V, Vazquez Doce O (2021) Study of the strong interaction among hadrons with correlations at the LHC. Annu Rev Nucl Part Sci 71:377–402. https://doi.org/10.1146/annurev-nucl-102419-034438. arXiv:2012.09806 [nucl-ex]

Fan X, Dong J, Zuo W (2014) Density-dependent symmetry energy at subsaturation densities from nuclear mass differences. Phys Rev C 89(1):017305. https://doi.org/10.1103/PhysRevC.89.017305. arXiv:1403.2055 [nucl-th]

Favata M (2014) Systematic parameter errors in inspiraling neutron star binaries. Phys Rev Lett 112:101101. https://doi.org/10.1103/PhysRevLett.112.101101. arXiv:1310.8288 [gr-qc]

Finazzo SI, Rougemont R, Marrochio H et al (2015) Hydrodynamic transport coefficients for the non-conformal quark-gluon plasma from holography. JHEP 02:051. https://doi.org/10.1007/JHEP02(2015)051. arXiv:1412.2968 [hep-ph]

Fiorilla S, Kaiser N, Weise W (2012) Chiral thermodynamics of nuclear matter. Nucl Phys A 880:65–87. https://doi.org/10.1016/j.nuclphysa.2012.01.003. arXiv:1111.2791 [nucl-th]

Flanagan EE, Hinderer T (2008) Constraining neutron star tidal Love numbers with gravitational wave detectors. Phys Rev D 77:021502. https://doi.org/10.1103/PhysRevD.77.021502. arXiv:0709.1915 [astro-ph]

Fletcher C, et al (2023) A joint Fermi-GBM and Swift-BAT analysis of gravitational-wave candidates from the third gravitational-wave observing run. arXiv:2308.13666

Fonseca E, Cromartie HT, Pennucci TT, et al (2021a) Refined mass and geometric measurements of the high-mass PSR J0740+6620: probability density functions and their credible intervals. https://doi.org/10.5281/zenodo.4773599. Accessed 04 June 2022

Fonseca E et al (2021b) Refined mass and geometric measurements of the high-mass PSR J0740+6620. Astrophys J Lett 915(1):L12. https://doi.org/10.3847/2041-8213/ac03b8. arXiv:2104.00880 [astro-ph.HE]

Fortin M, Oertel M, Providência C (2018) Hyperons in hot dense matter: what do the constraints tell us for equation of state? Publ Astron Soc Austral 35:44. https://doi.org/10.1017/pasa.2018.32. arXiv:1711.09427 [astro-ph.HE]

Fortin M, Raduta AR, Avancini S et al (2020) Relativistic hypernuclear compact stars with calibrated equations of state. Phys Rev D 101(3):034017. https://doi.org/10.1103/PhysRevD.101.034017. arXiv:2001.08036 [hep-ph]

Fraga ES, Kodama T, Palhares LF, et al (2010) Finite-size effects and the search for the critical endpoint of QCD. PoS FACESQCD:017. https://doi.org/10.22323/1.117.0017. arXiv:1106.3887 [hep-ph]

Freedman BA, McLerran LD (1977) Fermions and gauge vector mesons at finite temperature and density. 1. Formal techniques. Phys Rev D 16:1130. https://doi.org/10.1103/PhysRevD.16.1130

Freedman BA, McLerran LD (1977a) Fermions and gauge vector mesons at finite temperature and density. 2. The ground state energy of a relativistic electron gas. Phys Rev D 16:1147. https://doi.org/10.1103/PhysRevD.16.1147

Freedman BA, McLerran LD (1977b) Fermions and gauge vector mesons at finite temperature and density. 3. The ground state energy of a relativistic quark gas. Phys Rev D 16:1169. https://doi.org/10.1103/PhysRevD.16.1169

Friedman E, Gal A (2021) Constraints on $\Xi-$ nuclear interactions from capture events in emulsion. Phys Lett B 820:136555. https://doi.org/10.1016/j.physletb.2021.136555. arXiv:2104.00421 [nucl-th]

Friedman E, Gal A (2023) Constraints from Λ hypernuclei on the ΛNN content of the Λ-nucleus potential. Phys Lett B 837:137669. https://doi.org/10.1016/j.physletb.2023.137669. arXiv:2204.02264 [nucl-th]

Fries RJ, Muller B, Nonaka C et al (2003) Hadronization in heavy ion collisions: recombination and fragmentation of partons. Phys Rev Lett 90:202303. https://doi.org/10.1103/PhysRevLett.90.202303. arXiv:nucl-th/0301087

Friese V (2006) The CBM experiment at GSI/FAIR. Nucl Phys A 774:377–386. https://doi.org/10.1016/j.nuclphysa.2006.06.018

Friman B, Karsch F, Redlich K et al (2011) Fluctuations as probe of the QCD phase transition and freeze-out in heavy ion collisions at LHC and RHIC. Eur Phys J C 71:1694. https://doi.org/10.1140/epjc/s10052-011-1694-2. arXiv:1103.3511 [hep-ph]

Fryer CL, Belczynski K, Ramirez-Ruiz E et al (2015) The fate of the compact remnant in neutron star mergers. Astrophys J 812(1):24. https://doi.org/10.1088/0004-637X/812/1/24. arXiv:1504.07605 [astro-ph.HE]

Gal A, Hungerford EV, Millener DJ (2016) Strangeness in nuclear physics. Rev Mod Phys 88(3):035004. https://doi.org/10.1103/RevModPhys.88.035004. arXiv:1605.00557 [nucl-th]

Galatyuk T (2014) HADES overview. Nucl Phys A 931:41–51. https://doi.org/10.1016/j.nuclphysa.2014.10.044

Galatyuk T (2020) Recent results from HADES. JPS Conf Proc 32:010079. https://doi.org/10.7566/JPSCP.32.010079
Gale C, Hidaka Y, Jeon S et al (2015) Production and elliptic flow of dileptons and photons in a matrix model of the quark-gluon plasma. Phys Rev Lett 114:072301. https://doi.org/10.1103/PhysRevLett.114.072301. arXiv:1409.4778 [hep-ph]
Gandolfi S, Carlson J, Reddy S (2012) The maximum mass and radius of neutron stars and the nuclear symmetry energy. Phys Rev C 85:032801. https://doi.org/10.1103/PhysRevC.85.032801. arXiv:1101.1921 [nucl-th]
Gandolfi S, Lonardoni D, Lovato A et al (2020) Atomic nuclei from quantum Monte Carlo calculations with chiral EFT interactions. Front Phys 8:117. https://doi.org/10.3389/fphy.2020.00117. arXiv:2001.01374 [nucl-th]
Gardim FG, Grassi F, Hama Y et al (2011) Directed flow at mid-rapidity in event-by-event hydrodynamics. Phys Rev C 83:064901. https://doi.org/10.1103/PhysRevC.83.064901. arXiv:1103.4605 [nucl-th]
Gardim FG, Grassi F, Luzum M et al (2012) Mapping the hydrodynamic response to the initial geometry in heavy-ion collisions. Phys Rev C 85:024908. https://doi.org/10.1103/PhysRevC.85.024908. arXiv:1111.6538 [nucl-th]
Gardim FG, Grassi F, Luzum M et al (2013) Breaking of factorization of two-particle correlations in hydrodynamics. Phys Rev C 87(3):031901. https://doi.org/10.1103/PhysRevC.87.031901. arXiv:1211.0989 [nucl-th]
Gardim FG, Noronha-Hostler J, Luzum M et al (2015) Effects of viscosity on the mapping of initial to final state in heavy ion collisions. Phys Rev C 91(3):034902. https://doi.org/10.1103/PhysRevC.91.034902. arXiv:1411.2574 [nucl-th]
Gardim FG, Grassi F, Luzum M et al (2017) Hydrodynamic predictions for mixed harmonic correlations in 200 GeV Au+Au collisions. Phys Rev C 95(3):034901. https://doi.org/10.1103/PhysRevC.95.034901. arXiv:1608.02982 [nucl-th]
Gardim FG, Grassi F, Ishida P et al (2018) Sensitivity of observables to coarse-graining size in heavy-ion collisions. Phys Rev C 97(6):064919. https://doi.org/10.1103/PhysRevC.97.064919. arXiv:1712.03912 [nucl-th]
Garg P, Mishra DK, Netrakanti PK et al (2013) Conserved number fluctuations in a hadron resonance gas model. Phys Lett B 726:691–696. https://doi.org/10.1016/j.physletb.2013.09.019. arXiv:1304.7133 [nucl-ex]
Gavassino L, Antonelli M, Haskell B (2021) Bulk viscosity in relativistic fluids: from thermodynamics to hydrodynamics. Class Quantum Gravity 38(7):075001. https://doi.org/10.1088/1361-6382/abe588. arXiv:2003.04609 [gr-qc]
Gavin S, Kapusta JI (2002) Kaon and pion fluctuations from small disoriented chiral condensates. Phys Rev C 65:054910. https://doi.org/10.1103/PhysRevC.65.054910. arXiv:nucl-th/0112083
Gazdzicki M, Gorenstein MI (1999) On the early stage of nucleus-nucleus collisions. Acta Phys Polon B 30:2705 arXiv:hep-ph/9803462
Gendreau KC, et al (2016) The Neutron star Interior Composition Explorer (NICER): design and development. In: den Herder JWA, Takahashi T, Bautz M (eds) Space Telescopes and instrumentation 2016: ultraviolet to gamma ray, vol 9905. International Society for Optics and Photonics. SPIE, pp 420–435. https://doi.org/10.1117/12.2231304
Gerstung D, Kaiser N, Weise W (2020) Hyperon-nucleon three-body forces and strangeness in neutron stars. Eur Phys J A 56(6):175. https://doi.org/10.1140/epja/s10050-020-00180-2. arXiv:2001.10563 [nucl-th]
Ghiglieri J, Moore GD, Teaney D (2018a) QCD shear viscosity at (almost) NLO. JHEP 03:179. https://doi.org/10.1007/JHEP03(2018)179. arXiv:1802.09535 [hep-ph]
Ghiglieri J, Moore GD, Teaney D (2018b) Second-order hydrodynamics in next-to-leading-order QCD. Phys Rev Lett 121(5):052302. https://doi.org/10.1103/PhysRevLett.121.052302. arXiv:1805.02663 [hep-ph]
Ghiglieri J, Kurkela A, Strickland M et al (2020) Perturbative thermal QCD: formalism and applications. Phys Rept 880:1–73. https://doi.org/10.1016/j.physrep.2020.07.004. arXiv:2002.10188 [hep-ph]
Giacalone G, Yan L, Noronha-Hostler J et al (2016) Symmetric cumulants and event-plane correlations in Pb + Pb collisions. Phys Rev C 94(1):014906. https://doi.org/10.1103/PhysRevC.94.014906. arXiv:1605.08303 [nucl-th]
Giacalone G, Noronha-Hostler J, Ollitrault JY (2017) Relative flow fluctuations as a probe of initial state fluctuations. Phys Rev C 95(5):054910. https://doi.org/10.1103/PhysRevC.95.054910. arXiv:1702.01730 [nucl-th]

Glendenning NK (1985) Neutron stars are giant hypernuclei? Astrophys J 293:470–493. https://doi.org/10.1086/163253
Glendenning NK (1997) Compact stars: nuclear physics, particle physics, and general relativity. Springer, New York. https://doi.org/10.1007/978-1-4684-0491-3
Gorda T, Kurkela A, Romatschke P et al (2018) Next-to-next-to-next-to-leading order pressure of cold quark matter: leading logarithm. Phys Rev Lett 121(20):202701. https://doi.org/10.1103/PhysRevLett.121.202701. arXiv:1807.04120 [hep-ph]
Gorda T, Kurkela A, Paatelainen R et al (2021a) Cold quark matter at N3LO: soft contributions. Phys Rev D 104(7):074015. https://doi.org/10.1103/PhysRevD.104.074015. arXiv:2103.07427 [hep-ph]
Gorda T, Kurkela A, Paatelainen R et al (2021b) Soft interactions in cold quark matter. Phys Rev Lett 127(16):162003. https://doi.org/10.1103/PhysRevLett.127.162003. arXiv:2103.05658 [hep-ph]
Gorenstein M (2015) New theoretical results on event-by-event fluctuations. PoS CPOD2014:017. https://doi.org/10.22323/1.217.0017. arXiv:1505.04135 [nucl-th]
Gorenstein MI, Gazdzicki M (2011) Strongly intensive quantities. Phys Rev C 84:014904. https://doi.org/10.1103/PhysRevC.84.014904. arXiv:1101.4865 [nucl-th]
Grams G, Margueron J, Somasundaram R et al (2022) Confronting a set of Skyrme and χ_{EFT} predictions for the crust of neutron stars: on the origin of uncertainties in model predictions. Eur Phys J A 58(3):56. https://doi.org/10.1140/epja/s10050-022-00706-w. arXiv:2203.11645 [nucl-th]
Grefa J, Noronha J, Noronha-Hostler J et al (2021) Hot and dense quark-gluon plasma thermodynamics from holographic black holes. Phys Rev D 104(3):034002. https://doi.org/10.1103/PhysRevD.104.034002. arXiv:2102.12042 [nucl-th]
Grefa J, Hippert M, Noronha J et al (2022) Transport coefficients of the quark-gluon plasma at the critical point and across the first-order line. Phys Rev D 106(3):034024. https://doi.org/10.1103/PhysRevD.106.034024. arXiv:2203.00139 [nucl-th]
Greifenhagen R (2020) Two-pion intensity-interferometry in non-central collisions of Au + Au @ 1.23 A GeV. Phys Part Nucl 51(3):288–292. https://doi.org/10.1134/S1063779620030132
Gross DJ, Wilczek F (1973) Ultraviolet behavior of nonabelian gauge theories. Phys Rev Lett 30:1343–1346. https://doi.org/10.1103/PhysRevLett.30.1343
Gross-Boelting T, Fuchs C, Faessler A (1999) Dirac structure of the nucleus-nucleus potential in heavy ion collisions. Prog Part Nucl Phys 42:65–74. https://doi.org/10.1016/S0146-6410(99)00061-7. arXiv:nucl-th/9812002
Guenther JN, Bellwied R, Borsanyi S et al (2017) The QCD equation of state at finite density from analytical continuation. Nucl Phys A 967:720–723. https://doi.org/10.1016/j.nuclphysa.2017.05.044. arXiv:1607.02493 [hep-lat]
Gyulassy M (2004) The QGP discovered at RHIC. In: NATO advanced study institute: structure and dynamics of elementary matter, pp 159–182. arXiv:nucl-th/0403032
Gyulassy M, McLerran L (2005) New forms of QCD matter discovered at RHIC. Nucl Phys A 750:30–63. https://doi.org/10.1016/j.nuclphysa.2004.10.034. arXiv:nucl-th/0405013
Gyulassy M, Vitev I, Wang XN (2001) High p(T) azimuthal asymmetry in noncentral A+A at RHIC. Phys Rev Lett 86:2537–2540. https://doi.org/10.1103/PhysRevLett.86.2537. arXiv:nucl-th/0012092
Haensel P (1977) Charge symmetry breaking nuclear forces and the properties of nuclear matter. J Phys G 3(3):373. https://doi.org/10.1088/0305-4616/3/3/012
Haensel P, Proszynski M, Kutschera M (1981) Uncertainty in the saturation density of nuclear matter and neutron star models. Astron Astrophys 102(3):299–302
Hagedorn R (1965) Statistical thermodynamics of strong interactions at high-energies. Nuovo Cim Suppl 3:147–186
Hagedorn R (1983) The pressure ensemble as a tool for describing the hadron—quark phase transition. Z Phys C 17:265. https://doi.org/10.1007/BF01578153
Hagen G, Papenbrock T, Hjorth-Jensen M et al (2014) Coupled-cluster computations of atomic nuclei. Rep Prog Phys 77(9):096302. https://doi.org/10.1088/0034-4885/77/9/096302. arXiv:1312.7872 [nucl-th]
Hallinan G, Ravi V, Weinreb S, et al (2019) The DSA-2000—a radio survey camera. Bull AAS 51(7). https://baas.aas.org/pub/2020n7i255. arXiv:1907.07648 [astro-ph.IM]
Hammelmann J, Elfner H (2023) Impact of hadronic interactions and conservation laws on cumulants of conserved charges in a dynamical model. Phys Rev C 107(4):044910. https://doi.org/10.1103/PhysRevC.107.044910. arXiv:2202.11417 [nucl-th]
Haque N, Strickland M (2021) Next-to-next-to leading-order hard-thermal-loop perturbation-theory predictions for the curvature of the QCD phase transition line. Phys Rev C 103(3):031901. https://doi.org/10.1103/PhysRevC.103.L031901. arXiv:2011.06938 [hep-ph]

Haque N, Andersen JO, Mustafa MG et al (2014a) Three-loop pressure and susceptibility at finite temperature and density from hard-thermal-loop perturbation theory. Phys Rev D 89(6):061701. https://doi.org/10.1103/PhysRevD.89.061701. arXiv:1309.3968 [hep-ph]
Haque N, Bandyopadhyay A, Andersen JO et al (2014b) Three-loop HTLpt thermodynamics at finite temperature and chemical potential. JHEP 05:027. https://doi.org/10.1007/JHEP05(2014)027. arXiv:1402.6907 [hep-ph]
Hartle JB (1967) Slowly rotating relativistic stars. 1. Equations of structure. Astrophys J 150:1005–1029. https://doi.org/10.1086/149400
Hasegawa T et al (1996) Spectroscopic study of (Lambda) B-10, (Lambda) C-12, (Lambda) Si-28, (Lambda) Y-89, (Lambda) La-139, and (Lambda) Pb-208 by the (pi+, K+) reaction. Phys Rev C 53:1210–1220. https://doi.org/10.1103/PhysRevC.53.1210
Hatsuda T, Kunihiro T (1994) QCD phenomenology based on a chiral effective Lagrangian. Phys Rept 247:221–367. https://doi.org/10.1016/0370-1573(94)90022-1. arXiv:hep-ph/9401310
Hayakawa SH et al (2021) Observation of Coulomb-assisted nuclear bound state of Ξ–N14 system. Phys Rev Lett 126(6):062501. https://doi.org/10.1103/PhysRevLett.126.062501. arXiv:2010.14317 [nucl-ex]
Hebeler K, Lattimer JM, Pethick CJ et al (2010) Constraints on neutron star radii based on chiral effective field theory interactions. Phys Rev Lett 105:161102. https://doi.org/10.1103/PhysRevLett.105.161102. arXiv:1007.1746 [nucl-th]
Heinz UW, Jacak BV (1999) Two particle correlations in relativistic heavy ion collisions. Annu Rev Nucl Part Sci 49:529–579. https://doi.org/10.1146/annurev.nucl.49.1.529. arXiv:nucl-th/9902020
Heinz U, Snellings R (2013) Collective flow and viscosity in relativistic heavy-ion collisions. Annu Rev Nucl Part Sci 63:123–151. https://doi.org/10.1146/annurev-nucl-102212-170540. arXiv:1301.2826 [nucl-th]
Heinz U, Qiu Z, Shen C (2013) Fluctuating flow angles and anisotropic flow measurements. Phys Rev C 87(3):034913. https://doi.org/10.1103/PhysRevC.87.034913. arXiv:1302.3535 [nucl-th]
Herold C, Nahrgang M, Yan Y et al (2016) Dynamical net-proton fluctuations near a QCD critical point. Phys Rev C 93(2):021902. https://doi.org/10.1103/PhysRevC.93.021902. arXiv:1601.04839 [hep-ph]
Hinderer T (2008) Tidal Love numbers of neutron stars. Astrophys J 677:1216–1220. https://doi.org/10.1086/533487. arXiv:0711.2420 [astro-ph]
Hippert M, Fraga ES (2017) Multiplicity fluctuations near the QCD critical point. Phys Rev D 96(3):034011. https://doi.org/10.1103/PhysRevD.96.034011. arXiv:1702.02028 [hep-ph]
Hippert M, Fraga ES, Santos EM (2016) Critical versus spurious fluctuations in the search for the QCD critical point. Phys Rev D 93(1):014029. https://doi.org/10.1103/PhysRevD.93.014029. arXiv:1507.04764 [hep-ph]
Hippert M, JaGP Barbon, Dobrigkeit Chinellato D et al (2020a) Probing the structure of the initial state of heavy-ion collisions with p_T -dependent flow fluctuations. Phys Rev C 102(6):064909. https://doi.org/10.1103/PhysRevC.102.064909. arXiv:2006.13358 [nucl-th]
Hippert M, Dobrigkeit Chinellato D, Luzum M et al (2020b) Measuring momentum-dependent flow fluctuations in heavy-ion collisions. Phys Rev C 101(3):034903. https://doi.org/10.1103/PhysRevC.101.034903. arXiv:1906.08915 [nucl-th]
Hirano T, Heinz UW, Kharzeev D et al (2008) Mass ordering of differential elliptic flow and its violation for phi mesons. Phys Rev C 77:044909. https://doi.org/10.1103/PhysRevC.77.044909. arXiv:0710.5795 [nucl-th]
Holt JW, Kaiser N (2017) Equation of state of nuclear and neutron matter at third-order in perturbation theory from chiral effective field theory. Phys Rev C 95(3):034326. https://doi.org/10.1103/PhysRevC.95.034326. arXiv:1612.04309 [nucl-th]
Horikawa Y, Thies M, Lenz F (1980) The Δ-nucleus spin-orbit interaction in π-nucleus scattering. Nucl Phys A 345:386–408. https://doi.org/10.1016/0375-9474(80)90346-2
Huovinen P, Ruuskanen PV (2006) Hydrodynamic models for heavy ion collisions. Annu Rev Nucl Part Sci 56:163–206. https://doi.org/10.1146/annurev.nucl.54.070103.181236. arXiv:nucl-th/0605008
Huovinen P, Kolb PF, Heinz UW et al (2001) Radial and elliptic flow at RHIC: further predictions. Phys Lett B 503:58–64. https://doi.org/10.1016/S0370-2693(01)00219-2. arXiv:hep-ph/0101136
Inoue T (2019) Hyperon forces from QCD and their applications. JPS Conf Proc 26:023018. https://doi.org/10.7566/JPSCP.26.023018
Jia J (2011) Measurement of elliptic and higher order flow from ATLAS experiment at the LHC. J Phys G 38:124012. https://doi.org/10.1088/0954-3899/38/12/124012. arXiv:1107.1468 [nucl-ex]

Jia J, Mohapatra S (2013) A method for studying initial geometry fluctuations via event plane correlations in heavy ion collisions. Eur Phys J C 73:2510. https://doi.org/10.1140/epjc/s10052-013-2510-y. arXiv:1203.5095 [nucl-th]

Jia J, Teaney D (2013) Study on initial geometry fluctuations via participant plane correlations in heavy ion collisions: part II. Eur Phys J C 73:2558. https://doi.org/10.1140/epjc/s10052-013-2558-8. arXiv:1205.3585 [nucl-ex]

Joglekar A, Raj N, Tanedo P et al (2020) Dark kinetic heating of neutron stars from contact interactions with relativistic targets. Phys Rev D 102(12):123002. https://doi.org/10.1103/PhysRevD.102.123002. arXiv:2004.09539 [hep-ph]

Kajantie K, Laine M, Rummukainen K et al (1997) 3-D SU(N) + adjoint Higgs theory and finite temperature QCD. Nucl Phys B 503:357–384. https://doi.org/10.1016/S0550-3213(97)00425-2. arXiv:hep-ph/9704416

Kapusta JI (1979) Quantum chromodynamics at high temperature. Nucl Phys B 148:461–498. https://doi.org/10.1016/0550-3213(79)90146-9

Kardan B (2019) Collective flow and correlations measurements with HADES in Au+Au collisions at 1.23 AGeV. Nucl Phys A 982:431–434. https://doi.org/10.1016/j.nuclphysa.2018.09.061. arXiv:1809.07821 [nucl-ex]

Karnaukhov VA et al (2003) Critical temperature for the nuclear liquid gas phase transition. Phys Rev C 67:011601. https://doi.org/10.1103/PhysRevC.67.011601. arXiv:nucl-ex/0302006

Karnaukhov VA et al (2008) Critical temperature for the nuclear liquid-gas phase transition (from multifragmentation and fission). Phys Atom Nucl 71:2067–2073. https://doi.org/10.1134/S1063778808120077. arXiv:0801.4485 [nucl-ex]

Karsch F, Morita K, Redlich K (2016) Effects of kinematic cuts on net-electric charge fluctuations. Phys Rev C 93(3):034907. https://doi.org/10.1103/PhysRevC.93.034907. arXiv:1508.02614 [hep-ph]

Kasmaei BS, Strickland M (2019) Dilepton production and elliptic flow from an anisotropic quark-gluon plasma. Phys Rev D 99(3):034015. https://doi.org/10.1103/PhysRevD.99.034015. arXiv:1811.07486 [hep-ph]

Kasmaei BS, Strickland M (2020) Photon production and elliptic flow from a momentum-anisotropic quark-gluon plasma. Phys Rev D 102(1):014037. https://doi.org/10.1103/PhysRevD.102.014037. arXiv:1911.03370 [hep-ph]

Khachatryan V et al (2015a) Evidence for collective multiparticle correlations in p-Pb collisions. Phys Rev Lett 115(1):012301. https://doi.org/10.1103/PhysRevLett.115.012301. arXiv:1502.05382 [nucl-ex]

Khachatryan V et al (2015b) Evidence for transverse momentum and pseudorapidity dependent event plane fluctuations in PbPb and pPb collisions. Phys Rev C 92(3):034911. https://doi.org/10.1103/PhysRevC.92.034911. arXiv:1503.01692 [nucl-ex]

Khachatryan V et al (2017) Evidence for collectivity in pp collisions at the LHC. Phys Lett B 765:193–220. https://doi.org/10.1016/j.physletb.2016.12.009. arXiv:1606.06198 [nucl-ex]

Khan E, Margueron J (2012) Constraining the nuclear equation of state at subsaturation densities. Phys Rev Lett 109:092501. https://doi.org/10.1103/PhysRevLett.109.092501. arXiv:1204.0399 [nucl-th]

Khaustov P et al (2000) Evidence of Xi hypernuclear production in the C-12(K-, K+)(Xi)Be-12 reaction. Phys Rev C 61:054603. https://doi.org/10.1103/PhysRevC.61.054603. arXiv:nucl-ex/9912007

Khyzhniak E (2020a) Azimuthally-differential pion femtoscopy in Cu + Au and Au + Au collisions at $\sqrt{s_{NN}} = 200$ GeV in the STAR experiment. Phys Part Nucl 51(3):270–273. https://doi.org/10.1134/S1063779620030168

Khyzhniak E (2020b) Pion femtoscopy in p+Au and d+Au collisions at $\sqrt{s_{NN}} = 200$ GeV in the STAR experiment. J Phys Conf Ser 1690(1):012130. https://doi.org/10.1088/1742-6596/1690/1/012130

Kikola D, Yi L, Esumi S et al (2012) Nonflow ‘factorization’ and a novel method to disentangle anisotropic flow and nonflow. Phys Rev C 86:014901. https://doi.org/10.1103/PhysRevC.86.014901. arXiv:1110.4809 [nucl-ex]

Kitazawa M, Asakawa M (2012a) Relation between baryon number fluctuations and experimentally observed proton number fluctuations in relativistic heavy ion collisions. Phys Rev C 86:024904. https://doi.org/10.1103/PhysRevC.86.024904. [Erratum: Phys. Rev. C 86, 069902 (2012)]. arXiv:1205.3292 [nucl-th]

Kitazawa M, Asakawa M (2012b) Revealing baryon number fluctuations from proton number fluctuations in relativistic heavy ion collisions. Phys Rev C 85:021901. https://doi.org/10.1103/PhysRevC.85.021901. arXiv:1107.2755 [nucl-th]

Kiuchi K, Kyutoku K, Shibata M et al (2019) Revisiting the lower bound on tidal deformability derived by AT 2017gfo. Astrophys J Lett 876(2):L31. https://doi.org/10.3847/2041-8213/ab1e45. arXiv:1903.01466 [astro-ph.HE]
Koch JH, Ohtsuka N (1985) Inclusive electron scattering from light nuclei at intermediate energies. Nucl Phys A 435:765–790. https://doi.org/10.1016/0375-9474(85)90187-3
Koch V, Majumder A, Randrup J (2005) Baryon-strangeness correlations: a diagnostic of strongly interacting matter. Phys Rev Lett 95:182301. https://doi.org/10.1103/PhysRevLett.95.182301. arXiv:nucl-th/0505052
Koehn H, et al (2024) An overview of existing and new nuclear and astrophysical constraints on the equation of state of neutron-rich dense matter. arXiv e-prints arXiv:2402.04172 [astro-ph.HE]
Komoltsev O, Kurkela A (2022) How perturbative QCD constrains the equation of state at neutron-star densities. Phys Rev Lett 128(20):202701. https://doi.org/10.1103/PhysRevLett.128.202701. arXiv:2111.05350 [nucl-th]
Konchakovski VP, Hauer M, Torrieri G et al (2009) Forward–backward correlations in nucleus-nucleus collisions: baseline contributions from geometrical fluctuations. Phys Rev C 79:034910. https://doi.org/10.1103/PhysRevC.79.034910. arXiv:0812.3967 [nucl-th]
Kovensky N, Poole A, Schmitt A (2023) Phases of cold holographic QCD: baryons, pions and rho mesons. SciPost Phys 15:162. https://doi.org/10.21468/SciPostPhys.15.4.162. arXiv:2302.10675 [hep-ph]
Kovtun P, Son DT, Starinets AO (2005) Viscosity in strongly interacting quantum field theories from black hole physics. Phys Rev Lett 94:111601. https://doi.org/10.1103/PhysRevLett.94.111601. arXiv:hep-th/0405231
Kowalski S (2022) Highlights from NA61/SHINE. PoS CPOD2021:002. https://doi.org/10.22323/1.400.0002
Kowalski S et al (2007) Experimental determination of the symmetry energy of a low density nuclear gas. Phys Rev C 75:014601. https://doi.org/10.1103/PhysRevC.75.014601. arXiv:nucl-ex/0602023
Kozlov I, Luzum M, Denicol G, et al (2014) Transverse momentum structure of pair correlations as a signature of collective behavior in small collision systems. arXiv e-prints arXiv:1405.3976 [nucl-th]
Kurkela A, Vuorinen A (2016) Cool quark matter. Phys Rev Lett 117(4):042501. https://doi.org/10.1103/PhysRevLett.117.042501. arXiv:1603.00750 [hep-ph]
Kurkela A, Romatschke P, Vuorinen A (2010) Cold quark matter. Phys Rev D 81:105021. https://doi.org/10.1103/PhysRevD.81.105021. arXiv:0912.1856 [hep-ph]
Kurkela A, Fraga ES, Schaffner-Bielich J et al (2014) Constraining neutron star matter with quantum chromodynamics. Astrophys J 789:127. https://doi.org/10.1088/0004-637X/789/2/127. arXiv:1402.6618 [astro-ph.HE]
Lacey RA (2015) Indications for a critical end point in the phase diagram for hot and dense nuclear matter. Phys Rev Lett 114(14):142301. https://doi.org/10.1103/PhysRevLett.114.142301. arXiv:1411.7931 [nucl-ex]
Lacey RA, Liu P, Magdy N, et al (2016) Finite-size scaling of non-Gaussian fluctuations near the QCD critical point. arXiv e-prints arXiv:1606.08071 [nucl-ex]
Landau LD, Lifshitz EM (2000) Statistical physics, 3rd edn. Butterworth-Heineman, Washington, DC
Landry P, Essick R (2019) Nonparametric inference of the neutron star equation of state from gravitational wave observations. Phys Rev D 99(8):084049. https://doi.org/10.1103/PhysRevD.99.084049. arXiv:1811.12529 [gr-qc]
Lattimer JM (2023) Constraints on nuclear symmetry energy parameters. Particles 6:30–56. https://doi.org/10.3390/particles6010003. arXiv:2301.03666 [nucl-th]
Lattimer JM, Steiner AW (2014) Constraints on the symmetry energy using the mass-radius relation of neutron stars. Eur Phys J A 50:40. https://doi.org/10.1140/epja/i2014-14040-y. arXiv:1403.1186 [nucl-th]
Lawrence S, Tervala JG, Bedaque PF et al (2015) An upper bound on neutron star masses from models of short gamma-ray bursts. Astrophys J 808:186. https://doi.org/10.1088/0004-637X/808/2/186. arXiv:1505.00231 [astro-ph.HE]
Legred I, Chatziioannou K, Essick R et al (2021) Impact of the PSR J0740+6620 radius constraint on the properties of high-density matter. Phys Rev D 104(6):063003. https://doi.org/10.1103/PhysRevD.104.063003. arXiv:2106.05313 [astro-ph.HE]
Legred I, Chatziioannou K, Essick R et al (2022) Implicit correlations within phenomenological parametric models of the neutron star equation of state. Phys Rev D 105(4):043016. https://doi.org/10.1103/PhysRevD.105.043016. arXiv:2201.06791 [astro-ph.HE]

Li JJ, Sedrakian A, Weber F (2018) Competition between delta isobars and hyperons and properties of compact stars. Phys Lett B 783:234–240. https://doi.org/10.1016/j.physletb.2018.06.051. arXiv:1803.03661 [nucl-th]

Li BA, Krastev PG, Wen DH et al (2019) Towards understanding astrophysical effects of nuclear symmetry energy. Eur Phys J A 55(7):117. https://doi.org/10.1140/epja/i2019-12780-8. arXiv:1905.13175 [nucl-th]

Li P, Steinheimer J, Reichert T et al (2023) Effects of a phase transition on two-pion interferometry in heavy ion collisions at $\sqrt{s_{\mathrm{NN}}} = 2.4 - 7.7$ GeV. Sci China Phys Mech Astron 66(3):232011. https://doi.org/10.1007/s11433-022-2041-8. arXiv:2209.01413 [nucl-th]

Liao J, Koch V (2010) On the fluidity and super-criticality of the QCD matter at RHIC. Phys Rev C 81:014902. https://doi.org/10.1103/PhysRevC.81.014902. arXiv:0909.3105 [hep-ph]

Lim Y, Holt JW (2017) Structure of neutron star crusts from new Skyrme effective interactions constrained by chiral effective field theory. Phys Rev C 95(6):065805. https://doi.org/10.1103/PhysRevC.95.065805. arXiv:1702.02898 [nucl-th]

Lim Y, Bhattacharya A, Holt JW et al (2021) Radius and equation of state constraints from massive neutron stars and GW190814. Phys Rev C 104(3):L032802. https://doi.org/10.1103/PhysRevC.104.L032802. arXiv:2007.06526 [nucl-th]

Lindblom L (2010) Spectral representations of neutron-star equations of state. Phys Rev D 82:103011. https://doi.org/10.1103/PhysRevD.82.103011. arXiv:1009.0738 [astro-ph.HE]

Ling B, Stephanov MA (2016) Acceptance dependence of fluctuation measures near the QCD critical point. Phys Rev C 93(3):034915. https://doi.org/10.1103/PhysRevC.93.034915. arXiv:1512.09125 [nucl-th]

Lisa MA, Pratt S, Soltz R et al (2005) Femtoscopy in relativistic heavy ion collisions. Annu Rev Nucl Part Sci 55:357–402. https://doi.org/10.1146/annurev.nucl.55.090704.151533. arXiv:nucl-ex/0505014

Lisa MA et al (2000) Azimuthal dependence of pion interferometry at the AGS. Phys Lett B 496:1–8. https://doi.org/10.1016/S0370-2693(00)01280-6. arXiv:nucl-ex/0007022

Liu H et al (2000) Sideward flow in Au + Au collisions between 2-A-GeV and 8-A-GeV. Phys Rev Lett 84:5488–5492. https://doi.org/10.1103/PhysRevLett.84.5488. arXiv:nucl-ex/0005005

Logoteta D, Bombaci I, Kievsky A (2016) Nuclear matter properties from local chiral interactions with Δ isobar intermediate states. Phys Rev C 94(6):064001. https://doi.org/10.1103/PhysRevC.94.064001. arXiv:1609.00649 [nucl-th]

Logoteta D, Bombaci I, Kievsky A (2016) Nuclear matter saturation with chiral three-nucleon interactions fitted to light nuclei properties. Phys Lett B 758:449–454. https://doi.org/10.1016/j.physletb.2016.05.042

Logoteta D, Vidana I, Bombaci I (2019) Impact of chiral hyperonic three-body forces on neutron stars. Eur Phys J A 55(11):207. https://doi.org/10.1140/epja/i2019-12909-9. arXiv:1906.11722 [nucl-th]

Lonardoni D, Lovato A, Gandolfi S et al (2015) Hyperon puzzle: hints from quantum Monte Carlo calculations. Phys Rev Lett 114(9):092301. https://doi.org/10.1103/PhysRevLett.114.092301. arXiv:1407.4448 [nucl-th]

Lovato A, Bombaci I, Logoteta D et al (2022a) Benchmark calculations of infinite neutron matter with realistic two- and three-nucleon potentials. Phys Rev C 105(5):055808. https://doi.org/10.1103/PhysRevC.105.055808. arXiv:2202.10293 [nucl-th]

Lovato A, et al (2022b) Long range plan: dense matter theory for heavy-ion collisions and neutron stars. arXiv e-prints arXiv:2211.02224 [nucl-th]

Luo X, Xu N (2017) Search for the QCD critical point with fluctuations of conserved quantities in relativistic heavy-ion collisions at RHIC : an overview. Nucl Sci Tech 28(8):112. https://doi.org/10.1007/s41365-017-0257-0. arXiv:1701.02105 [nucl-ex]

Luo X, Xu J, Mohanty B et al (2013) Volume fluctuation and auto-correlation effects in the moment analysis of net-proton multiplicity distributions in heavy-ion collisions. J Phys G 40:105104. https://doi.org/10.1088/0954-3899/40/10/105104. arXiv:1302.2332 [nucl-ex]

Lutz MFM, et al (2009) Physics performance report for PANDA: strong interaction studies with antiprotons. arXiv e-prints arXiv:0903.3905 [hep-ex]

Luzum M, Romatschke P (2008) Conformal relativistic viscous hydrodynamics: Applications to RHIC results at $\sqrt{s_{NN}} = 200$ GeV. Phys Rev C 78:034915. https://doi.org/10.1103/PhysRevC.78.034915. [Erratum: Phys. Rev. C 79, 039903 (2009)]. arXiv:0804.4015 [nucl-th]

Luzum M, Ollitrault JY (2013) Eliminating experimental bias in anisotropic-flow measurements of high-energy nuclear collisions. Phys Rev C 87(4):044907. https://doi.org/10.1103/PhysRevC.87.044907. arXiv:1209.2323 [nucl-ex]
Luzum M, Petersen H (2014) Initial state fluctuations and final state correlations in relativistic heavy-ion collisions. J Phys G 41:063102. https://doi.org/10.1088/0954-3899/41/6/063102. arXiv:1312.5503 [nucl-th]
Lynn JE, Tews I, Gandolfi S et al (2019) Quantum Monte Carlo methods in nuclear physics: recent advances. Annu Rev Nucl Part Sci 69:279–305. https://doi.org/10.1146/annurev-nucl-101918-023600. arXiv:1901.04868 [nucl-th]
Ma L, Ma GL, Ma YG (2016) Initial partonic eccentricity fluctuations in a multiphase transport model. Phys Rev C 94(4):044915. https://doi.org/10.1103/PhysRevC.94.044915. arXiv:1610.04733 [nucl-th]
Machleidt R, Entem DR (2011) Chiral effective field theory and nuclear forces. Phys Rep 503:1–75. https://doi.org/10.1016/j.physrep.2011.02.001. arXiv:1105.2919 [nucl-th]
Majumder A, Muller B (2006) Baryonic strangeness and related susceptibilities in QCD. Phys Rev C 74:054901. https://doi.org/10.1103/PhysRevC.74.054901. arXiv:nucl-th/0605079
Marcinek A (2023) Highlights from the NA61/SHINE experiment. Acta Phys Polon Supp 16:1-A8. https://doi.org/10.5506/APhysPolBSupp.16.1-A8. arXiv:2208.13823 [nucl-ex]
Marczenko M, McLerran L, Redlich K et al (2023) Reaching percolation and conformal limits in neutron stars. Phys Rev C 107(2):025802. https://doi.org/10.1103/PhysRevC.107.025802. arXiv:2207.13059 [nucl-th]
Margalit B, Metzger BD (2017) Constraining the maximum mass of neutron stars from multi-messenger observations of GW170817. Astrophys J Lett 850(2):L19. https://doi.org/10.3847/2041-8213/aa991c. arXiv:1710.05938 [astro-ph.HE]
Marquez KD, Pelicer MR, Ghosh S et al (2022) Exploring the effects of Δ baryons in magnetars. Phys Rev C 106(3):035801. https://doi.org/10.1103/PhysRevC.106.035801. arXiv:2205.09827 [astro-ph.HE]
Martin BR, Shaw G (2019) Nuclear and particle physics: an introduction. Wiley, New York
Martinez M, Strickland M (2008) Pre-equilibrium dilepton production from an anisotropic quark-gluon plasma. Phys Rev C 78:034917. https://doi.org/10.1103/PhysRevC.78.034917. arXiv:0805.4552 [hep-ph]
Meyer HB (2011) Transport properties of the quark-gluon plasma: a lattice QCD perspective. Eur Phys J A 47:86. https://doi.org/10.1140/epja/i2011-11086-3. arXiv:1104.3708 [hep-lat]
Millener DJ, Dover CB, Gal A (1988) Lambda nucleus single particle potentials. Phys Rev C 38:2700–2708. https://doi.org/10.1103/PhysRevC.38.2700
Miller MC (2016) The case for psr J1614–2230 as a NICER target. Astrophys J 822(1):27. https://doi.org/10.3847/0004-637X/822/1/27. arXiv:1602.00312 [astro-ph.HE]
Miller MC et al (2019) PSR J0030+0451 mass and radius from NICER data and implications for the properties of neutron star matter. Astrophys J Lett 887(1):L24. https://doi.org/10.3847/2041-8213/ab50c5. arXiv:1912.05705 [astro-ph.HE]
Miller MC, Lamb FK, Dittmann AJ, et al (2021a) NICER PSR J0740+6620 Illinois-Maryland MCMC samples. https://doi.org/10.5281/zenodo.4670689. Accessed 04 June 2022
Miller MC et al (2021b) The radius of PSR J0740+6620 from NICER and XMM-Newton data. Astrophys J Lett 918(2):L28. https://doi.org/10.3847/2041-8213/ac089b. arXiv:2105.06979 [astro-ph.HE]
Mishra DK, Garg P, Netrakanti PK et al (2016) Effect of resonance decay on conserved number fluctuations in a hadron resonance gas model. Phys Rev C 94(1):014905. https://doi.org/10.1103/PhysRevC.94.014905. arXiv:1607.01875 [hep-ph]
Mogliacci S, Andersen JO, Strickland M et al (2013) Equation of state of hot and dense QCD: resummed perturbation theory confronts lattice data. JHEP 12:055. https://doi.org/10.1007/JHEP12(2013)055. arXiv:1307.8098 [hep-ph]
Mohs J, Ege M, Elfner H et al (2022) Collective flow at SIS energies within a hadronic transport approach: influence of light nuclei formation and equation of state. Phys Rev C 105(3):034906. https://doi.org/10.1103/PhysRevC.105.034906. arXiv:2012.11454 [nucl-th]
Molnar D, Voloshin SA (2003) Elliptic flow at large transverse momenta from quark coalescence. Phys Rev Lett 91:092301. https://doi.org/10.1103/PhysRevLett.91.092301. arXiv:nucl-th/0302014
Moravcova Z, Gulbrandsen K, Zhou Y (2021) Generic algorithm for multiparticle cumulants of azimuthal correlations in high energy nucleus collisions. Phys Rev C 103(2):024913. https://doi.org/10.1103/PhysRevC.103.024913. arXiv:2005.07974 [nucl-th]
Mordasini C, Bilandzic A, Karakoç D et al (2020) Higher order symmetric cumulants. Phys Rev C 102(2):024907. https://doi.org/10.1103/PhysRevC.102.024907. arXiv:1901.06968 [nucl-ex]

Most ER, Papenfort LJ, Dexheimer V et al (2019) Signatures of quark-hadron phase transitions in general-relativistic neutron-star mergers. Phys Rev Lett 122(6):061101. https://doi.org/10.1103/PhysRevLett.122.061101. arXiv:1807.03684 [astro-ph.HE]
Most ER, Haber A, Harris SP, et al (2022) Emergence of microphysical viscosity in binary neutron star post-merger dynamics. arXiv e-prints arXiv:2207.00442 [astro-ph.HE]
Motornenko A, Steinheimer J, Vovchenko V et al (2020) Equation of state for hot QCD and compact stars from a mean field approach. Phys Rev C 101(3):034904. https://doi.org/10.1103/PhysRevC.101.034904. arXiv:1905.00866 [hep-ph]
Mroczek D, Nava Acuna AR, Noronha-Hostler J et al (2021) Quartic cumulant of baryon number in the presence of a QCD critical point. Phys Rev C 103(3):034901. https://doi.org/10.1103/PhysRevC.103.034901. arXiv:2008.04022 [nucl-th]
Mroczek D, Hjorth-Jensen M, Noronha-Hostler J et al (2023a) Mapping out the thermodynamic stability of a QCD equation of state with a critical point using active learning. Phys Rev C 107(5):054911. https://doi.org/10.1103/PhysRevC.107.054911. arXiv:2203.13876 [nucl-th]
Mroczek D, Miller MC, Noronha-Hostler J, et al (2023b) Nontrivial features in the speed of sound inside neutron stars. arXiv e-prints arXiv:2309.02345 [astro-ph.HE]
Müller B, Schäfer A (2022) Quark-hadron transition and entanglement. arXiv e-prints arXiv:2211.16265 [hep-ph]
Muller-Kirsten HJW, Ohta N, Zhou JG (1999) AdS(3) / CFT correspondence, Poincare vacuum state and grey body factors in BTZ black holes. Phys Lett B 445:287–295. https://doi.org/10.1016/S0370-2693(98)01465-8. arXiv:hep-th/9809193
Murguia-Berthier A, Montes G, Ramirez-Ruiz E et al (2014) Necessary conditions for short gamma-ray burst production in binary neutron star mergers. Astrophys J Lett 788:L8. https://doi.org/10.1088/2041-8205/788/1/L8. arXiv:1404.0383 [astro-ph.HE]
Myers W (1977) Droplet model of atomic nuclei. Plenum, New York
Myers WD, Swiatecki WJ (1966) Nuclear masses and deformations. Nucl Phys 81:1–60. https://doi.org/10.1016/S0029-5582(66)80001-9
Myers WD, Swiatecki WJ (1996) Nuclear properties according to the Thomas-Fermi model. Nucl Phys A 601:141–167. https://doi.org/10.1016/0375-9474(95)00509-9
Nahrgang M, Bluhm M, Alba P et al (2015) Impact of resonance regeneration and decay on the net-proton fluctuations in a hadron resonance gas. Eur Phys J C 75(12):573. https://doi.org/10.1140/epjc/s10052-015-3775-0. arXiv:1402.1238 [hep-ph]
Nakazawa K, et al (2015) The first evidence of a deeply bound state of Xi^{-}–^{14}N system. PTEP 2015 (3):033D02. https://doi.org/10.1093/ptep/ptv008
Nambu Y, Jona-Lasinio G (1961a) Dynamical model of elementary particles based on an analogy with superconductivity. I. Phys Rev 122:345–358. https://doi.org/10.1103/PhysRev.122.345
Nambu Y, Jona-Lasinio G (1961b) Dynamical model of elementary particles based on an analogy with superconductivity. II. Phys Rev 124:246–254. https://doi.org/10.1103/PhysRev.124.246
Nathanail A, Most ER, Rezzolla L (2021) GW170817 and GW190814: tension on the maximum mass. Astrophys J Lett 908(2):L28. https://doi.org/10.3847/2041-8213/abdfc6. arXiv:2101.01735 [astro-ph.HE]
Natowitz JB, Hagel K, Ma Y et al (2002) Limiting temperatures and the equation of state of nuclear matter. Phys Rev Lett 89:212701. https://doi.org/10.1103/PhysRevLett.89.212701. arXiv:nucl-ex/0204015
Nicholl M, Margalit B, Schmidt P et al (2021) Tight multimessenger constraints on the neutron star equation of state from GW170817 and a forward model for kilonova light-curve synthesis. Mon Not R Astron Soc 505(2):3016–3032. https://doi.org/10.1093/mnras/stab1523. arXiv:2102.02229 [astro-ph.HE]
Niemi H, Denicol GS, Holopainen H et al (2013) Event-by-event distributions of azimuthal asymmetries in ultrarelativistic heavy-ion collisions. Phys Rev C 87(5):054901. https://doi.org/10.1103/PhysRevC.87.054901. arXiv:1212.1008 [nucl-th]
Niemi H, Eskola KJ, Paatelainen R (2016) Event-by-event fluctuations in a perturbative QCD + saturation + hydrodynamics model: determining QCD matter shear viscosity in ultrarelativistic heavy-ion collisions. Phys Rev C 93(2):024907. https://doi.org/10.1103/PhysRevC.93.024907. arXiv:1505.02677 [hep-ph]
Nigmatkulov G (2016) Bose–Einstein correlations of charged kaons in p + p collisions with the STAR detector. J Phys Conf Ser 668(1):012073. https://doi.org/10.1088/1742-6596/668/1/012073

Nijs G, van der Schee W, Gürsoy U et al (2021) Bayesian analysis of heavy ion collisions with the heavy ion computational framework Trajectum. Phys Rev C 103(5):054909. https://doi.org/10.1103/PhysRevC.103.054909. arXiv:2010.15134 [nucl-th]

Noronha-Hostler J, Bellwied R, Gunther J, et al (2016a) Kaon fluctuations from lattice QCD. arXiv e-prints arXiv:1607.02527 [hep-ph]

Noronha-Hostler J, Yan L, Gardim FG et al (2016b) Linear and cubic response to the initial eccentricity in heavy-ion collisions. Phys Rev C 93(1):014909. https://doi.org/10.1103/PhysRevC.93.014909. arXiv:1511.03896 [nucl-th]

Noumi H et al (2002) Sigma nucleus potential in A = 28. Phys Rev Lett 89:072301. https://doi.org/10.1103/PhysRevLett.89.072301. [Erratum: Phys. Rev. Lett. 90, 049902 (2003)]

Oertel M, Hempel M, Klähn T et al (2017) Equations of state for supernovae and compact stars. Rev Mod Phys 89(1):015007. https://doi.org/10.1103/RevModPhys.89.015007. arXiv:1610.03361 [astro-ph.HE]

Ohlson A (2018) Measurements of the fluctuations of identified particles in ALICE at the LHC. PoS CPOD2017:031. https://doi.org/10.22323/1.311.0031. arXiv:1901.00709 [nucl-ex]

Oliinychenko D, Sorensen A, Koch V et al (2023) Sensitivity of Au+Au collisions to the symmetric nuclear matter equation of state at 2–5 nuclear saturation densities. Phys Rev C 108(3):034908. https://doi.org/10.1103/PhysRevC.108.034908. arXiv:2208.11996 [nucl-th]

Oppenheimer JR, Volkoff GM (1939) On massive neutron cores. Phys Rev 55:374–381. https://doi.org/10.1103/PhysRev.55.374

Özel F, Psaltis D, Arzoumanian Z et al (2016) Measuring neutron star radii via pulse profile modeling with NICER. Astrophys J 832(1):92. https://doi.org/10.3847/0004-637X/832/1/92. arXiv:1512.03067 [astro-ph.HE]

Palhares LF, Fraga ES, Kodama T (2011) Chiral transition in a finite system and possible use of finite size scaling in relativistic heavy ion collisions. J Phys G 38:085101. https://doi.org/10.1088/0954-3899/38/8/085101. arXiv:0904.4830 [nucl-th]

Pang PTH, Sivertsen L, Somasundaram R et al (2024) Probing quarkyonic matter in neutron stars with the Bayesian nuclear-physics multimessenger astrophysics framework. Phys Rev C 109(2):025807. https://doi.org/10.1103/PhysRevC.109.025807. arXiv:2308.15067 [nucl-th]

Paquet JF, Shen C, Denicol GS et al (2016) Production of photons in relativistic heavy-ion collisions. Phys Rev C 93(4):044906. https://doi.org/10.1103/PhysRevC.93.044906. arXiv:1509.06738 [hep-ph]

Parotto P, Bluhm M, Mroczek D et al (2020) QCD equation of state matched to lattice data and exhibiting a critical point singularity. Phys Rev C 101(3):034901. https://doi.org/10.1103/PhysRevC.101.034901. arXiv:1805.05249 [hep-ph]

Paschalidis V, Stergioulas N (2017) Rotating stars in relativity. Living Rev Relativ 20:7. https://doi.org/10.1007/s41114-017-0008-x. arXiv:1612.03050 [astro-ph.HE]

Patricelli B, Bernardini MG, Mapelli M et al (2022) Prospects for multimessenger detection of binary neutron star mergers in the fourth LIGO-Virgo-KAGRA observing run. Mon Not R Astron Soc 513(3):4159–4168. https://doi.org/10.1093/mnras/stac1167. [Erratum: Mon. Not. R. Astron. Soc. 514, 3395 (2022)]. arXiv:2204.12504 [astro-ph.HE]

Petran M, Letessier J, Rafelski J et al (2014) SHARE with CHARM. Comput Phys Commun 185:2056–2079. https://doi.org/10.1016/j.cpc.2014.02.026. arXiv:1310.5108 [hep-ph]

Pianese S, et al (2018) Design of the future high energy beam dump for the CERN SPS. In: 9th international particle accelerator conference. https://doi.org/10.18429/JACoW-IPAC2018-WEPMG004

Piarulli M, Bombaci I, Logoteta D et al (2020) Benchmark calculations of pure neutron matter with realistic nucleon–nucleon interactions. Phys Rev C 101(4):045801. https://doi.org/10.1103/PhysRevC.101.045801. arXiv:1908.04426 [nucl-th]

Plumberg C (2020) Hanbury-Brown-Twiss interferometry and collectivity in $p+p$, p+Pb, and Pb+Pb collisions. Phys Rev C 102(5):054908. https://doi.org/10.1103/PhysRevC.102.054908. arXiv:2008.01709 [nucl-th]

Plumberg C, Heinz U (2015) Interferometric signatures of the temperature dependence of the specific shear viscosity in heavy-ion collisions. Phys Rev C 91(5):054905. https://doi.org/10.1103/PhysRevC.91.054905. arXiv:1503.05605 [nucl-th]

Plumberg C, Kapusta JI (2017) Hydrodynamic fluctuations near a critical endpoint and Hanbury-Brown-Twiss interferometry. Phys Rev C 95(4):044910. https://doi.org/10.1103/PhysRevC.95.044910. arXiv:1702.01368 [nucl-th]

Poberezhnyuk RV, Gazdzicki M, Gorenstein MI (2015) Statistical model of the early stage of nucleus-nucleus collisions with exact strangeness conservation. Acta Phys Polon B 46(10):1991. https://doi.org/10.5506/APhysPolB.46.1991. arXiv:1502.05650 [nucl-th]

Politzer HD (1973) Reliable perturbative results for strong interactions? Phys Rev Lett 30:1346–1349. https://doi.org/10.1103/PhysRevLett.30.1346

Poskanzer AM, Voloshin SA (1998) Methods for analyzing anisotropic flow in relativistic nuclear collisions. Phys Rev C 58:1671–1678. https://doi.org/10.1103/PhysRevC.58.1671. arXiv:nucl-ex/9805001

Pratt S (2009) Resolving the HBT puzzle in relativistic heavy ion collision. Phys Rev Lett 102:232301. https://doi.org/10.1103/PhysRevLett.102.232301

Pratt S, Sangaline E, Sorensen P et al (2015) Constraining the equation of state of superhadronic matter from heavy-ion collisions. Phys Rev Lett 114:202301. https://doi.org/10.1103/PhysRevLett.114.202301. arXiv:1501.04042 [nucl-th]

Pruneau C, Gavin S, Voloshin S (2002) Methods for the study of particle production fluctuations. Phys Rev C 66:044904. https://doi.org/10.1103/PhysRevC.66.044904. arXiv:nucl-ex/0204011

Qin GY, Muller B (2012) Counting hot/cold spots in quark-gluon plasma. Phys Rev C 85:061901. https://doi.org/10.1103/PhysRevC.85.061901. arXiv:1109.5961 [hep-ph]

Qiu Z, Heinz UW (2011) Event-by-event shape and flow fluctuations of relativistic heavy-ion collision fireballs. Phys Rev C 84:024911. https://doi.org/10.1103/PhysRevC.84.024911. arXiv:1104.0650 [nucl-th]

Radice D, Perego A, Zappa F et al (2018) GW170817: joint constraint on the neutron star equation of state from multimessenger observations. Astrophys J Lett 852(2):L29. https://doi.org/10.3847/2041-8213/aaa402. arXiv:1711.03647 [astro-ph.HE]

Raduta AR (2022) Equations of state for hot neutron stars-II. The role of exotic particle degrees of freedom. Eur Phys J A 58(6):115. https://doi.org/10.1140/epja/s10050-022-00772-0. arXiv:2205.03177 [nucl-th]

Raduta AR, Nacu F, Oertel M (2021) Equations of state for hot neutron stars. Eur Phys J A 57(12):329. https://doi.org/10.1140/epja/s10050-021-00628-z. arXiv:2109.00251 [nucl-th]

Raithel CA, Özel F, Psaltis D (2019) Finite-temperature extension for cold neutron star equations of state. Astrophys J 875(1):12. https://doi.org/10.3847/1538-4357/ab08ea. arXiv:1902.10735 [astro-ph.HE]

Rao S, Sievert M, Noronha-Hostler J (2021) Baseline predictions of elliptic flow and fluctuations for the RHIC beam energy scan using response coefficients. Phys Rev C 103(3):034910. https://doi.org/10.1103/PhysRevC.103.034910. arXiv:1910.03677 [nucl-th]

Ratti C (2018) Lattice QCD and heavy ion collisions: a review of recent progress. Rep Prog Phys 81 (8):084301. https://doi.org/10.1088/1361-6633/aabb97. arXiv:1804.07810 [hep-lat]

Reed BT, Fattoyev FJ, Horowitz CJ et al (2021) Implications of PREX-2 on the equation of state of neutron-rich matter. Phys Rev Lett 126(17):172503. https://doi.org/10.1103/PhysRevLett.126.172503. arXiv:2101.03193 [nucl-th]

Reinhard PG, Roca-Maza X, Nazarewicz W (2021) Information content of the parity-violating asymmetry in Pb208. Phys Rev Lett 127(23):232501. https://doi.org/10.1103/PhysRevLett.127.232501. arXiv:2105.15050 [nucl-th]

Reinhard PG, Roca-Maza X, Nazarewicz W (2022) Combined theoretical analysis of the parity-violating asymmetry for Ca48 and Pb208. Phys Rev Lett 129(23):232501. https://doi.org/10.1103/PhysRevLett.129.232501. arXiv:2206.03134 [nucl-th]

Reisdorf W, Ritter HG (1997) Collective flow in heavy-ion collisions. Annu Rev Nucl Part Sci 47:663–709. https://doi.org/10.1146/annurev.nucl.47.1.663

Reisdorf W et al (2012) Systematics of azimuthal asymmetries in heavy ion collisions in the 1 A GeV regime. Nucl Phys A 876:1–60. https://doi.org/10.1016/j.nuclphysa.2011.12.006. arXiv:1112.3180 [nucl-ex]

Rezzolla L, Most ER, Weih LR (2018) Using gravitational-wave observations and quasi-universal relations to constrain the maximum mass of neutron stars. Astrophys J Lett 852(2):L25. https://doi.org/10.3847/2041-8213/aaa401. arXiv:1711.00314 [astro-ph.HE]

Rijken TA, Schulze HJ (2016) Hyperon-hyperon interactions with the Nijmegen ESC08 model. Eur Phys J A 52(2):21. https://doi.org/10.1140/epja/i2016-16021-6

Riley TE et al (2019a) A NICER view of PSR J0030+0451: millisecond pulsar parameter estimation. Astrophys J Lett 887(1):L21. https://doi.org/10.3847/2041-8213/ab481c. arXiv:1912.05702 [astro-ph.HE]

Riley TE, et al (2019b) A NICER view of PSR J0030+0451: nested samples for millisecond pulsar parameter estimation. https://doi.org/10.5281/zenodo.3386449. Accessed 04 June 2022

Riley TE et al (2021a) A NICER view of the massive Pulsar PSR J0740+6620 informed by radio timing and XMM-Newton spectroscopy. Astrophys J Lett 918(2):L27. https://doi.org/10.3847/2041-8213/ac0a81. arXiv:2105.06980 [astro-ph.HE]

Riley TE, et al (2021b) A NICER view of the massive pulsar PSR J0740+6620 informed by radio timing and XMM-Newton spectroscopy: nested samples for millisecond pulsar parameter estimation. https://doi.org/10.5281/zenodo.4697625. Accessed 04 June 2022

Rios A (2020) Green's function techniques for infinite nuclear systems. Front Phys 8:387. https://doi.org/10.3389/fphy.2020.00387. arXiv:2006.10610 [nucl-th]

Roca-Maza X, Brenna M, Agrawal BK et al (2013) Giant quadrupole resonances in 208Pb, the nuclear symmetry energy and the neutron skin thickness. Phys Rev C 87(3):034301. https://doi.org/10.1103/PhysRevC.87.034301. arXiv:1212.4377 [nucl-th]

Romani RW, Kandel D, Filippenko AV et al (2021) PSR J1810+1744: companion darkening and a precise high neutron star mass. Astrophys J Lett 908(2):L46. https://doi.org/10.3847/2041-8213/abe2b4. arXiv:2101.09822 [astro-ph.HE]

Romani RW, Kandel D, Filippenko AV et al (2022) PSR J0952−0607: the fastest and heaviest known galactic neutron star. Astrophys J Lett 934(2):L18. https://doi.org/10.3847/2041-8213/ac8007. arXiv:2207.05124 [astro-ph.HE]

Rougemont R, Critelli R, Noronha-Hostler J et al (2017) Dynamical versus equilibrium properties of the QCD phase transition: a holographic perspective. Phys Rev D 96(1):014032. https://doi.org/10.1103/PhysRevD.96.014032. arXiv:1704.05558 [hep-ph]

Ruester SB, Hempel M, Schaffner-Bielich J (2006) The outer crust of non-accreting cold neutron stars. Phys Rev C 73:035804. https://doi.org/10.1103/PhysRevC.73.035804. arXiv:astro-ph/0509325

Ruiz M, Shapiro SL, Tsokaros A (2018) GW170817, general relativistic magnetohydrodynamic simulations, and the neutron star maximum mass. Phys Rev D 97(2):021501. https://doi.org/10.1103/PhysRevD.97.021501. arXiv:1711.00473 [astro-ph.HE]

Ryblewski R, Strickland M (2015) Dilepton production from the quark-gluon plasma using (3+1)-dimensional anisotropic dissipative hydrodynamics. Phys Rev D 92(2):025026. https://doi.org/10.1103/PhysRevD.92.025026. arXiv:1501.03418 [nucl-th]

de Sá LM, Bernardo A, Bachega RRA et al (2022) Quantifying the evidence against a mass gap between black holes and neutron stars. Astrophys J 941(2):130. https://doi.org/10.3847/1538-4357/aca076. arXiv:2211.01447 [astro-ph.HE]

Saha PK et al (2004) Study of the sigma-nucleus potential by the (pi-, K+) reaction on medium-to-heavy nuclear targets. Phys Rev C 70:044613. https://doi.org/10.1103/PhysRevC.70.044613. arXiv:nucl-ex/0405031

Sahoo NR, De S, Nayak TK (2013) Baseline study for higher moments of net-charge distributions at energies available at the BNL Relativistic Heavy Ion Collider. Phys Rev C 87(4):044906. https://doi.org/10.1103/PhysRevC.87.044906. arXiv:1210.7206 [nucl-ex]

Sammarruca F, Coraggio L, Holt JW et al (2015) Toward order-by-order calculations of the nuclear and neutron matter equations of state in chiral effective field theory. Phys Rev C 91(5):054311. https://doi.org/10.1103/PhysRevC.91.054311. arXiv:1411.0136 [nucl-th]

Sangaline E, Pratt S (2016) Toward a deeper understanding of how experiments constrain the underlying physics of heavy-ion collisions. Phys Rev C 93(2):024908. https://doi.org/10.1103/PhysRevC.93.024908. arXiv:1508.07017 [nucl-th]

Satz H (1989) Intermittency and critical behavior. Nucl Phys B 326:613–618. https://doi.org/10.1016/0550-3213(89)90546-4

Schäfer A, Karpenko I, Wu XY et al (2022) Particle production in a hybrid approach for a beam energy scan of Au+Au/Pb+Pb collisions between $\sqrt{s_{\mathrm{NN}}} = 4.3$ GeV and $\sqrt{s_{\mathrm{NN}}} = 200.0$ GeV. Eur Phys J A 58(11):230. https://doi.org/10.1140/epja/s10050-022-00872-x. arXiv:2112.08724 [hep-ph]

Schenke B, Strickland M (2007) Photon production from an anisotropic quark-gluon plasma. Phys Rev D 76:025023. https://doi.org/10.1103/PhysRevD.76.025023. arXiv:hep-ph/0611332

Schenke B, Jeon S, Gale C (2012) Higher flow harmonics from (3+1)D event-by-event viscous hydrodynamics. Phys Rev C 85:024901. https://doi.org/10.1103/PhysRevC.85.024901. arXiv:1109.6289 [hep-ph]

Schnedermann E, Sollfrank J, Heinz UW (1993) Thermal phenomenology of hadrons from 200-A/GeV S+ S collisions. Phys Rev C 48:2462–2475. https://doi.org/10.1103/PhysRevC.48.2462. arXiv:nucl-th/9307020

Schürhoff T, Schramm S, Dexheimer V (2010) Neutron stars with small radii—the role of delta resonances. Astrophys J Lett 724:L74–L77. https://doi.org/10.1088/2041-8205/724/1/L74. arXiv:1008.0957 [astro-ph.SR]

Shao DS, Tang SP, Sheng X et al (2020) Estimating the maximum gravitational mass of nonrotating neutron stars from the GW170817/GRB 170817A/AT2017gfo observation. Phys Rev D 101 (6):063029. https://doi.org/10.1103/PhysRevD.101.063029. arXiv:1912.08122 [astro-ph.HE]

Shen C, Schenke B (2022) Longitudinal dynamics and particle production in relativistic nuclear collisions. Phys Rev C 105(6):064905. https://doi.org/10.1103/PhysRevC.105.064905. arXiv:2203.04685 [nucl-th]

Shen H, Toki H, Oyamatsu K et al (1998) Relativistic equation of state of nuclear matter for supernova and neutron star. Nucl Phys A 637:435–450. https://doi.org/10.1016/S0375-9474(98)00236-X. arXiv:nucl-th/9805035

Shen H, Yang F, Toki H (2006) Double-lambda hypernuclei in the relativistic mean-field theory. Prog Theor Phys 115:325–335. https://doi.org/10.1143/PTP.115.325. arXiv:nucl-th/0602046

Shen C, Heinz UW, Paquet JF et al (2014) Thermal photons as a quark-gluon plasma thermometer reexamined. Phys Rev C 89(4):044910. https://doi.org/10.1103/PhysRevC.89.044910. arXiv:1308.2440 [nucl-th]

Shibata M, Fujibayashi S, Hotokezaka K et al (2017) Modeling GW170817 based on numerical relativity and its implications. Phys Rev D 96(12):123012. https://doi.org/10.1103/PhysRevD.96.123012. arXiv:1710.07579 [astro-ph.HE]

Shibata M, Zhou E, Kiuchi K et al (2019) Constraint on the maximum mass of neutron stars using GW170817 event. Phys Rev D 100(2):023015. https://doi.org/10.1103/PhysRevD.100.023015. arXiv:1905.03656 [astro-ph.HE]

Shuryak EV (1978) Theory of hadronic plasma. Sov Phys JETP 47:212–219

Sievert MD, Noronha-Hostler J (2019) CERN Large Hadron Collider system size scan predictions for PbPb, XeXe, ArAr, and OO with relativistic hydrodynamics. Phys Rev C 100(2):024904. https://doi.org/10.1103/PhysRevC.100.024904. arXiv:1901.01319 [nucl-th]

Singha S, Shanmuganathan P, Keane D (2016) The first moment of azimuthal anisotropy in nuclear collisions from AGS to LHC energies. Adv High Energy Phys 2016:2836989. https://doi.org/10.1155/2016/2836989. arXiv:1610.00646 [nucl-ex]

Sinha P (2023) Elliptic flow of strange and multi-strange hadrons in isobar collisions at $\sqrt{s_{NN}}$ = 200 GeV at RHIC. EPJ Web Conf 276:03010. https://doi.org/10.1051/epjconf/202327603010. arXiv:2212.13039 [nucl-ex]

Sirunyan AM et al (2017) Principal-component analysis of two-particle azimuthal correlations in PbPb and *p* Pb collisions at CMS. Phys Rev C 96(6):064902. https://doi.org/10.1103/PhysRevC.96.064902. arXiv:1708.07113 [nucl-ex]

Sirunyan AM et al (2018a) Azimuthal anisotropy of charged particles with transverse momentum up to 100 GeV/ c in PbPb collisions at $\sqrt{s}_{NN}$=5.02 TeV. Phys Lett B 776:195–216. https://doi.org/10.1016/j.physletb.2017.11.041. arXiv:1702.00630 [hep-ex]

Sirunyan AM et al (2018b) Observation of correlated azimuthal anisotropy Fourier harmonics in *pp* and $p + Pb$ collisions at the LHC. Phys Rev Lett 120(9):092301. https://doi.org/10.1103/PhysRevLett.120.092301. arXiv:1709.09189 [nucl-ex]

Sirunyan AM et al (2018c) Pseudorapidity and transverse momentum dependence of flow harmonics in pPb and PbPb collisions. Phys Rev C 98(4):044902. https://doi.org/10.1103/PhysRevC.98.044902. arXiv:1710.07864 [nucl-ex]

Sirunyan AM et al (2019a) Charged-particle angular correlations in XeXe collisions at $\sqrt{s_{NN}} = 5.44$ TeV. Phys Rev C 100(4):044902. https://doi.org/10.1103/PhysRevC.100.044902. arXiv:1901.07997 [hep-ex]

Sirunyan AM et al (2019b) Non-Gaussian elliptic-flow fluctuations in PbPb collisions at $\sqrt{s_{NN}} = 5.02$ TeV. Phys Lett B 789:643–665. https://doi.org/10.1016/j.physletb.2018.11.063. arXiv:1711.05594 [nucl-ex]

Sirunyan AM et al (2020) Mixed higher-order anisotropic flow and nonlinear response coefficients of charged particles in PbPb collisions at $\sqrt{s_{\rm NN}}$ = 2.76 and 5.02 TeV. Eur Phys J C 80(6):534. https://doi.org/10.1140/epjc/s10052-020-7834-9. arXiv:1910.08789 [hep-ex]

Skokov V, Friman B, Redlich K (2013) Volume fluctuations and higher order cumulants of the net Baryon number. Phys Rev C 88:034911. https://doi.org/10.1103/PhysRevC.88.034911. arXiv:1205.4756 [hep-ph]
Snellings R (2011) Elliptic flow: a brief review. New J Phys 13:055008. https://doi.org/10.1088/1367-2630/13/5/055008. arXiv:1102.3010 [nucl-ex]
Soltz RA (2014) PHENIX beam energy scan results. Nucl Phys A 931:780–784. https://doi.org/10.1016/j.nuclphysa.2014.08.050
Soma V, Bozek P (2009) Thermodynamic properties of nuclear matter with three-body forces. Phys Rev C 80:025803. https://doi.org/10.1103/PhysRevC.80.025803. arXiv:0904.1169 [nucl-th]
Somasundaram R, Drischler C, Tews I et al (2021) Constraints on the nuclear symmetry energy from asymmetric-matter calculations with chiral *NN* and 3*N* interactions. Phys Rev C 103(4):045803. https://doi.org/10.1103/PhysRevC.103.045803. arXiv:2009.04737 [nucl-th]
Somasundaram R, Tews I, Margueron J (2023) Perturbative QCD and the neutron star equation of state. Phys Rev C 107(5):L052801. https://doi.org/10.1103/PhysRevC.107.L052801. arXiv:2204.14039 [nucl-th]
Sorensen A et al (2024) Dense nuclear matter equation of state from heavy-ion collisions. Prog Part Nucl Phys 134:104080. https://doi.org/10.1016/j.ppnp.2023.104080. arXiv:2301.13253 [nucl-th]
Spieles C, Bleicher M (2020) Effects of the QCD phase transition on hadronic observables in relativistic hydrodynamic simulations of heavy-ion reactions in the FAIR/NICA energy regime. Eur Phys J ST 229(22–23):3537–3550. https://doi.org/10.1140/epjst/e2020-000102-4. arXiv:2006.01220 [nucl-th]
Spies S (2022) HADES overview—recent results from Ag+Ag collisions at $\sqrt{s_{NN}}$ = 2.55 GeV measured by HADES. EPJ Web Conf 259:01007. https://doi.org/10.1051/epjconf/202225901007
Sputowska IA (2022) Event-by-event correlations and fluctuations with strongly intensive quantities in heavy-ion and. PoS CPOD2021:027. https://doi.org/10.22323/1.400.0027
STAR Collaboration (2014) Studying the phase diagram of QCD matter at RHIC. https://drupal.star.bnl.gov/STAR/starnotes/public/sn0598
Steiner AW (2020) Bayesian analysis of neutron star mass and radius observations. https://github.com/awsteiner/bamr/blob/main/data/nicer. Accessed 04 June 2022
Steiner AW, Heinke CO, Bogdanov S et al (2018) Constraining the mass and radius of neutron stars in globular clusters. Mon Not R Astron Soc 476(1):421–435. https://doi.org/10.1093/mnras/sty215. arXiv:1709.05013 [astro-ph.HE]
Stephanov MA (2009) Non-Gaussian fluctuations near the QCD critical point. Phys Rev Lett 102:032301. https://doi.org/10.1103/PhysRevLett.102.032301. arXiv:0809.3450 [hep-ph]
Stephanov MA (2011) On the sign of kurtosis near the QCD critical point. Phys Rev Lett 107:052301. https://doi.org/10.1103/PhysRevLett.107.052301. arXiv:1104.1627 [hep-ph]
Stephanov MA, Rajagopal K, Shuryak EV (1999) Event-by-event fluctuations in heavy ion collisions and the QCD critical point. Phys Rev D 60:114028. https://doi.org/10.1103/PhysRevD.60.114028. arXiv:hep-ph/9903292
Stoecker H (2005) Collective flow signals the quark gluon plasma. Nucl Phys A 750:121–147. https://doi.org/10.1016/j.nuclphysa.2004.12.074. arXiv:nucl-th/0406018
Stone JR, Stone NJ, Moszkowski SA (2014) Incompressibility in finite nuclei and nuclear matter. Phys Rev C 89(4):044316. https://doi.org/10.1103/PhysRevC.89.044316. arXiv:1404.0744 [nucl-th]
Stone JR, Dexheimer V, Guichon PAM et al (2021) Equation of state of hot dense hyperonic matter in the Quark-Meson-Coupling (QMC-A) model. Mon Not R Astron Soc 502(3):3476–3490. https://doi.org/10.1093/mnras/staa4006. arXiv:1906.11100 [nucl-th]
Stovall K et al (2018) PALFA discovery of a highly relativistic double neutron star binary. Astrophys J Lett 854(2):L22. https://doi.org/10.3847/2041-8213/aaad06. arXiv:1802.01707 [astro-ph.HE]
Strickland M (1994) Thermal photons and dileptons from nonequilibrium quark-gluon plasma. Phys Lett B 331:245–250. https://doi.org/10.1016/0370-2693(94)91045-6
Sugahara Y, Toki H (1994) Relativistic mean field theory for unstable nuclei with nonlinear sigma and omega terms. Nucl Phys A 579:557–572. https://doi.org/10.1016/0375-9474(94)90923-7
Suwa Y, Yoshida T, Shibata M et al (2018) On the minimum mass of neutron stars. Mon Not R Astron Soc 481(3):3305–3312. https://doi.org/10.1093/mnras/sty2460. arXiv:1808.02328 [astro-ph.HE]
Suzuki T (2022) The relationship of the neutron skin thickness to the symmetry energy and its slope. Science 2022(6):063D01. https://doi.org/10.1093/ptep/ptac083. arXiv:2204.11013 [nucl-th]

Tahir NA et al (2005) Proposal for the study of thermophysical properties of high-energy-density matter using current and future heavy-ion accelerator facilities at GSI Darmstadt. Phys Rev Lett 95:035001. https://doi.org/10.1103/PhysRevLett.95.035001
Takahashi J, Tavares BM, Qian WL et al (2009) Topology studies of hydrodynamics using two particle correlation analysis. Phys Rev Lett 103:242301. https://doi.org/10.1103/PhysRevLett.103.242301. arXiv:0902.4870 [nucl-th]
Tan H, Noronha-Hostler J, Yunes N (2020) Neutron star equation of state in light of GW190814. Phys Rev Lett 125(26):261104. https://doi.org/10.1103/PhysRevLett.125.261104. arXiv:2006.16296 [astro-ph.HE]
Teaney D, Yan L (2011) Triangularity and dipole asymmetry in heavy ion collisions. Phys Rev C 83:064904. https://doi.org/10.1103/PhysRevC.83.064904. arXiv:1010.1876 [nucl-th]
Teaney D, Yan L (2012) Non linearities in the harmonic spectrum of heavy ion collisions with ideal and viscous hydrodynamics. Phys Rev C 86:044908. https://doi.org/10.1103/PhysRevC.86.044908. arXiv:1206.1905 [nucl-th]
Tews I (2020) Quantum Monte Carlo methods for astrophysical applications. Front Phys 8:153. https://doi.org/10.3389/fphy.2020.00153
Tews I, Carlson J, Gandolfi S et al (2018) Constraining the speed of sound inside neutron stars with chiral effective field theory interactions and observations. Astrophys J 860(2):149. https://doi.org/10.3847/1538-4357/aac267. arXiv:1801.01923 [nucl-th]
Thrane E, Talbot C (2019) An introduction to Bayesian inference in gravitational-wave astronomy: parameter estimation, model selection, and hierarchical models. Publ Astron Soc Austral 36:e010. https://doi.org/10.1017/pasa.2019.2. [Erratum: Publ. Astron. Soc. Austral. 37, e036 (2020)]. arXiv:1809.02293 [astro-ph.IM]
Tlusty D (2018) The RHIC beam energy scan phase II: physics and upgrades. In: 13th conference on the intersections of particle and nuclear physics. arXiv:1810.04767
Todd-Rutel BG, Piekarewicz J (2005) Neutron-rich nuclei and neutron stars: a new accurately calibrated interaction for the study of neutron-rich matter. Phys Rev Lett 95:122501. https://doi.org/10.1103/PhysRevLett.95.122501. arXiv:nucl-th/0504034
Toimela T (1985) Perturbative QED and QCD at finite temperatures and densities. Int J Theor Phys 24:901. https://doi.org/10.1007/BF00671334. [Erratum: Int. J. Theor. Phys. 26, 1021 (1987)]
Tolman RC (1939) Static solutions of Einstein's field equations for spheres of fluid. Phys Rev 55:364–373. https://doi.org/10.1103/PhysRev.55.364
Tootle S, Ecker C, Topolski K et al (2022) Quark formation and phenomenology in binary neutron-star mergers using V-QCD. SciPost Phys 13:109. https://doi.org/10.21468/SciPostPhys.13.5.109. arXiv:2205.05691 [astro-ph.HE]
Troyer M, Wiese UJ (2005) Computational complexity and fundamental limitations to fermionic quantum Monte Carlo simulations. Phys Rev Lett 94:170201. https://doi.org/10.1103/PhysRevLett.94.170201. arXiv:cond-mat/0408370
van Straten W, Bailes M, Britton MC et al (2001) A test of general relativity from the three-dimensional orbital geometry of a binary pulsar. Nature 412:158–160. https://doi.org/10.1038/35084015. arXiv:astro-ph/0108254
Vanderlinde K, et al (2019) LRP 2020 whitepaper: the Canadian hydrogen observatory and radio-transient detector (CHORD). arXiv e-prints https://doi.org/10.5281/zenodo.3765414. arXiv:1911.01777 [astro-ph.IM]
Venugopalan R, Prakash M (1992) Thermal properties of interacting hadrons. Nucl Phys A 546:718–760. https://doi.org/10.1016/0375-9474(92)90005-5
Vesely P, Toivanen J, Carlsson BG et al (2012) Giant monopole resonances and nuclear incompressibilities studied for the zero-range and separable pairing interactions. Phys Rev C 86:024303. https://doi.org/10.1103/PhysRevC.86.024303. arXiv:1202.5617 [nucl-th]
Vidana I, Bombaci I, Parenti I (2005) Role of hyperons on the hadron-star to quark-star conversion mechanism. Nucl Phys A 754:345–349. https://doi.org/10.1016/j.nuclphysa.2005.02.081
Voloshin S, Zhang Y (1996) Flow study in relativistic nuclear collisions by Fourier expansion of Azimuthal particle distributions. Z Phys C 70:665–672. https://doi.org/10.1007/s002880050141. arXiv:hep-ph/9407282
Vovchenko V, Stoecker H (2019) Thermal-FIST: a package for heavy-ion collisions and hadronic equation of state. Comput Phys Commun 244:295–310. https://doi.org/10.1016/j.cpc.2019.06.024. arXiv:1901.05249 [nucl-th]

Vuorinen A (2003) The pressure of QCD at finite temperatures and chemical potentials. Phys Rev D 68:054017. https://doi.org/10.1103/PhysRevD.68.054017. arXiv:hep-ph/0305183

Wade L, Creighton JDE, Ochsner E et al (2014) Systematic and statistical errors in a Bayesian approach to the estimation of the neutron-star equation of state using advanced gravitational wave detectors. Phys Rev D 89(10):103012. https://doi.org/10.1103/PhysRevD.89.103012. arXiv:1402.5156 [gr-qc]

Wang XN (2001) Jet quenching and azimuthal anisotropy of large p(T) spectra in noncentral high-energy heavy ion collisions. Phys Rev C 63:054902. https://doi.org/10.1103/PhysRevC.63.054902. arXiv:nucl-th/0009019

Wang X, Brandenburg JD, Ruan L et al (2023) Collision-energy dependence of the Breit-Wheeler process in heavy-ion collisions and its application to nuclear charge radius measurements. Phys Rev C 107 (4):044906. https://doi.org/10.1103/PhysRevC.107.044906. arXiv:2207.05595 [nucl-th]

Weih LR, Hanauske M, Rezzolla L (2020) Postmerger gravitational-wave signatures of phase transitions in binary mergers. Phys Rev Lett 124(17):171103. https://doi.org/10.1103/PhysRevLett.124.171103. arXiv:1912.09340 [gr-qc]

Weil J et al (2016) Particle production and equilibrium properties within a new hadron transport approach for heavy-ion collisions. Phys Rev C 94(5):054905. https://doi.org/10.1103/PhysRevC.94.054905. arXiv:1606.06642 [nucl-th]

Weinberg S (1979) Phenomenological Lagrangians. Physica A 96(1–2):327–340. https://doi.org/10.1016/0378-4371(79)90223-1

Weissenborn S, Chatterjee D, Schaffner-Bielich J (2012) Hyperons and massive neutron stars: vector repulsion and SU(3) symmetry. Phys Rev C 85(6):065802. https://doi.org/10.1103/PhysRevC.85.065802. [Erratum: Phys. Rev. C 90, 019904 (2014)]. arXiv:1112.0234 [astro-ph.HE]

Wellenhofer C, Holt JW, Kaiser N et al (2014) Nuclear thermodynamics from chiral low-momentum interactions. Phys Rev C 89(6):064009. https://doi.org/10.1103/PhysRevC.89.064009. arXiv:1404.2136 [nucl-th]

Wellenhofer C, Holt JW, Kaiser N (2015) Thermodynamics of isospin-asymmetric nuclear matter from chiral effective field theory. Phys Rev C 92(1):015801. https://doi.org/10.1103/PhysRevC.92.015801. arXiv:1504.00177 [nucl-th]

Wellenhofer C, Holt JW, Kaiser N (2016) Divergence of the isospin-asymmetry expansion of the nuclear equation of state in many-body perturbation theory. Phys Rev C 93(5):055802. https://doi.org/10.1103/PhysRevC.93.055802. arXiv:1603.02935 [nucl-th]

Wen P, Holt JW (2021) Constraining the nonanalytic terms in the isospin-asymmetry expansion of the nuclear equation of state. Phys Rev C 103(6):064002. https://doi.org/10.1103/PhysRevC.103.064002. arXiv:2012.02163 [nucl-th]

Wheaton S, Cleymans J, Hauer M (2011) THERMUS. arXiv e-prints arXiv:1108.4588 [hep-ph]

Wiedemann UA, Heinz UW (1999) Particle interferometry for relativistic heavy ion collisions. Phys Rep 319:145–230. https://doi.org/10.1016/S0370-1573(99)00032-0. arXiv:nucl-th/9901094

Workman RL, et al (2022) Review of particle physics. PTEP 2022:083C01. https://doi.org/10.1093/ptep/ptac097

Wu J, Lin Y, Wu Y et al (2020) Probing QCD critical fluctuations from intermittency analysis in relativistic heavy-ion collisions. Phys Lett B 801:135186. https://doi.org/10.1016/j.physletb.2019.135186. arXiv:1901.11193 [nucl-th]

Yagi K, Yunes N (2013a) I-Love-Q. Science 341:365–368. https://doi.org/10.1126/science.1236462. arXiv:1302.4499 [gr-qc]

Yagi K, Yunes N (2013b) I-Love-Q relations in neutron stars and their applications to astrophysics, gravitational waves and fundamental physics. Phys Rev D 88(2):023009. https://doi.org/10.1103/PhysRevD.88.023009. arXiv:1303.1528 [gr-qc]

Yagi K, Yunes N (2016) Binary love relations. Class Quantum Grav 33(13):13LT01. https://doi.org/10.1088/0264-9381/33/13/13LT01. arXiv:1512.02639 [gr-qc]

Yagi K, Yunes N (2017) Approximate universal relations for neutron stars and quark stars. Phys Rep 681:1–72. https://doi.org/10.1016/j.physrep.2017.03.002. arXiv:1608.02582 [gr-qc]

Yan L, Ollitrault JY (2014) Universal fluctuation-driven eccentricities in proton–proton, proton–nucleus and nucleus–nucleus collisions. Phys Rev Lett 112:082301. https://doi.org/10.1103/PhysRevLett.112.082301. arXiv:1312.6555 [nucl-th]

York MA, Moore GD (2009) Second order hydrodynamic coefficients from kinetic theory. Phys Rev D 79:054011. https://doi.org/10.1103/PhysRevD.79.054011. arXiv:0811.0729 [hep-ph]

Zbroszczyk H (2022) STAR results on femtoscopy at the BES program. PoS CPOD2021:020. https://doi.org/10.22323/1.400.0020

Zhai Cx, Kastening BM (1995) The free energy of hot gauge theories with fermions through g^5. Phys Rev D 52:7232–7246. https://doi.org/10.1103/PhysRevD.52.7232. arXiv:hep-ph/9507380

Zhang Z, Chen LW (2013) Constraining the symmetry energy at subsaturation densities using isotope binding energy difference and neutron skin thickness. Phys Lett B 726:234–238. https://doi.org/10.1016/j.physletb.2013.08.002. arXiv:1302.5327 [nucl-th]

Zhang Z, Chen LW (2015) Electric dipole polarizability in ^{208}Pb as a probe of the symmetry energy and neutron matter around $\rho_0/3$. Phys Rev C 92(3):031301. https://doi.org/10.1103/PhysRevC.92.031301. arXiv:1504.01077 [nucl-th]

Zhou C, Xu J, Luo X et al (2017) Cumulants of event-by-event net-strangeness distributions in Au+Au collisions at $\sqrt{s_{\mathrm{NN}}}$ = 7.7–200 GeV from UrQMD model. Phys Rev C 96(1):014909. https://doi.org/10.1103/PhysRevC.96.014909. arXiv:1703.09114 [nucl-ex]

Authors and Affiliations

Rajesh Kumar[1] · Veronica Dexheimer[1] · Johannes Jahan[2] · Jorge Noronha[3] · Jacquelyn Noronha-Hostler[3] · Claudia Ratti[2] · Nico Yunes[3] · Angel Rodrigo Nava Acuna[2] · Mark Alford[4] · Mahmudul Hasan Anik[5] · Debarati Chatterjee[15] · Katerina Chatziioannou[6,7] · Hsin-Yu Chen[8,9] · Alexander Clevinger[1] · Carlos Conde[3] · Nikolas Cruz-Camacho[3] · Travis Dore[10] · Christian Drischler[11] · Hannah Elfner[12] · Reed Essick[13] · David Friedenberg[14] · Suprovo Ghosh[15] · Joaquin Grefa[2] · Roland Haas[3] · Alexander Haber[4] · Jan Hammelmann[16] · Steven Harris[17] · Carl-Johan Haster[18,19] · Tetsuo Hatsuda[20] · Mauricio Hippert[3] · Renan Hirayama[16] · Jeremy W. Holt[14] · Micheal Kahangirwe[2] · Jamie Karthein[21] · Toru Kojo[22] · Philippe Landry[23] · Zidu Lin[5] · Matthew Luzum[24] · Timothy Andrew Manning[3] · Jordi Salinas San Martin[3] · Cole Miller[25] · Elias Roland Most[26,27,28] · Debora Mroczek[3] · Azwinndini Muronga[29] · Nicolas Patino[3] · Jeffrey Peterson[1] · Christopher Plumberg[30] · Damien Price[2] · Constanca Providencia[31] · Romulo Rougemont[32] · Satyajit Roy[5] · Hitansh Shah[2] · Stuart Shapiro[3] · Andrew W. Steiner[5,33] · Michael Strickland[1] · Hung Tan[3] · Hajime Togashi[22] · Israel Portillo Vazquez[2] · Pengsheng Wen[14] · Ziyuan Zhang[4]

✉ Veronica Dexheimer
vdexheim@kent.edu

✉ Nico Yunes
nyunes@illinois.edu

1 Department of Physics, Kent State University, Kent, OH 44243, USA

2 Department of Physics, University of Houston, Houston, TX 77204, USA

3 University of Illinois at Urbana-Champaign, Urbana, IL 61801, USA

4 Department of Physics, Washington University, St. Louis, MO 63130, USA

[5] Department of Physics and Astronomy, University of Tennessee, Knoxville, Knoxville, TN 37996, USA

[6] Department of Physics, California Institute of Technology, Pasadena, CA 91125, USA

[7] LIGO Laboratory, California Institute of Technology, Pasadena, CA 91125, USA

[8] Department of Physics, The University of Texas at Austin, Robert A Welch Hall, 105 E 24th St, Austin, TX 78712, USA

[9] Department of Physics and Kavli Institute for Astrophysics and Space Research, Massachusetts Institute of Technology, 77 Massachusetts Ave, Cambridge, MA 02139, USA

[10] Department of Physics, Bielefeld University, 33615 Bielefeld, Germany

[11] Department of Physics and Astronomy and Institute of Nuclear and Particle Physics, Ohio University, Athens, OH 45701, USA

[12] GSI Helmholtz Centre for Heavy-Ion Research, Planckstr. 1, 64291 Darmstadt, Germany

[13] Perimeter Institute for Theoretical Physics, 31 Caroline Street North, Waterloo, ON N2L 2Y5, Canada

[14] Department of Physics and Astronomy and Cyclotron Institute, Texas A &M University, College Station, TX 77843, USA

[15] Inter-University Centre for Astronomy and Astrophysics, Pune University Campus, Pune 411007, India

[16] Frankfurt Institute for Advanced Studies, Ruth-Moufang-Strasse 1, 60438 Frankfurt am Main, Germany

[17] Institute for Nuclear Theory, University of Washington, Seattle, WA 98195, USA

[18] Department of Physics and Astronomy, University of Nevada, Las Vegas, 4505 South Maryland Parkway, Las Vegas, NV 89154, USA

[19] Nevada Center for Astrophysics, University of Nevada, Las Vegas, NV 89154, USA

[20] Interdisciplinary Theoretical and Mathematical Sciences Program (iTHEMS), RIKEN, Wako 351-0198, Japan

[21] Center for Theoretical Physics, Massachusetts Institute of Technology, Cambridge, MA 02139, USA

[22] Department of Physics, Tohoku University, Sendai 980-8578, Japan

[23] Canadian Institute for Theoretical Astrophysics, University of Toronto, Toronto, ON M5S 3H8, Canada

[24] Instituto de Física, Universidade de São Paulo, Rua do Matão, 1371, Butantã, São Paulo 05508-090, Brazil

[25] Department of Astronomy and Joint Space-Science Institute, University of Maryland, College Park, MD 20742, USA

[26] Theoretical Astrophysics, California Institute of Technology, Mailcode 350-17, Pasadena, CA 91125, USA

[27] Walter Burke Institute for Theoretical Physics, California Institute of Technology, Pasadena, CA 91125, USA

[28] School of Natural Sciences, Institute for Advanced Study, 1 Einstein Drive, Princeton, NJ 08540, USA

[29] Faculty of Science, Nelson Mandela University, Port Elizabeth, South Africa

[30] Natural Science Division, Pepperdine University, Malibu, CA 90263, USA

[31] CFisUC, Department of Physics, University of Coimbra, 3004-516 Coimbra, Portugal

[32] Instituto de Física, Universidade Federal de Goiás, Av. Esperança - Campus Samambaia, Goiânia, Goiás CEP 74690-900, Brazil

[33] Physics Division, Oak Ridge National Laboratory, Oak Ridge, TN 37830, USA